

UNISURV REPORT NO. S19, 1981

A GEODETIC BASIS FOR
RECOVERING OCEAN DYNAMIC INFORMATION
FROM SATELLITE ALTIMETRY

by

RICHARD COLEMAN

Received October, 1981

SCHOOL OF SURVEYING,
THE UNIVERSITY OF NEW SOUTH WALES,
P.O. BOX 1,
KENSINGTON, N.S.W. 2033, AUSTRALIA

National Library of Australia

Card No. and ISBN

0 85839 029 9

ABSTRACT.

Satellite altimeter data provides estimates of the height of the instantaneous ocean surface above a specific reference surface. For ocean dynamic studies, it is required to geometrically map (in concept) a level surface of the Earth's gravity field in ocean areas, the geoid, under circumstances where no direct measurements are made in relation to the geoid to better than $\pm 1-2$ m. The deviations of the ocean surface from the geoid are termed the sea surface topography (SST).

The development of geodetic techniques for the determination of global fields of SST to accuracies of at least ± 10 cm and its variations with time is essential in providing a reliable basis for monitoring ocean circulation on a synoptic basis, when used in conjunction with other remote sensed and/or surface data. A description is given of the available satellite remote sensing instruments and the basic data types from these instruments are assessed for their contributions to ocean dynamic information taking into account the relevant oceanographic and satellite time and space scales.

The determination of the SST is tackled in terms of three distinct constituents: the establishment of the time-invariant or quasi-stationary component, the non-tidal temporal component and the tidal component. Procedures and a set of relations between satellite determined gravity field models, satellite altimetry and surface gravity measurements are given for achieving these objectives.

It is shown that it is not possible to use the boundary value problem approach for determining the SST from sea surface heights above the reference figure because no data can be unambiguously related to the geoid at the desired level of precision without making unwarranted assumptions about the magnitude and distribution of the SST. The only data uncontaminated by the SST is the satellite determined gravity field model.

However, the time variations in the SST can be resolved at a precision sufficient to obtain ocean dynamic information since the constraint of needing a ± 10 cm marine geoid is eliminated. Using a 393 day span of GEOS-3 altimetry data, two techniques of analysis, regional sea surface models and overlapping passes, are used to demonstrate the potential of the altimetry data to monitor the movement of ocean eddies and current boundaries.

Under certain speculative assumptions, estimates of the SST maintaining the Gulf Stream are made and patterns of the geostrophic current are produced over this regional area. The estimated magnitudes of the satellite derived currents are in substantial agreement with oceanographic results but the general flow patterns are incoherent. The shortcomings are not in the altimetry data but in the best available gravity field and geoid models through the relevant wavelengths.

A solution procedure is also proposed for the recovery of ocean tide models using the altimetry data. Results from the analysis show that over regional extents limited information for the M2 tidal constituent can be recovered and the indications are encouraging enough to propose that possibilities exist for mapping complex ocean tide patterns covering several dominant tidal constituents.

The geodetic techniques proposed demonstrate the potential of the satellite altimeter as a tool with which to study the dynamics of the surface layer of the ocean. Sophisticated tracking support is not needed to track ocean eddies, provided 30 balanced passes of altimetry data are available per month in a $10^\circ \times 10^\circ$ area. A resolution of ± 20 cm can be expected in such a case. It is not possible to recover the quasi-stationary component of the SST at the present time unless one makes certain speculative assumptions. Gravity field improvements to 3 parts in 10^9 are needed before further advances in this area can be made.

TABLE OF CONTENTS

	Page
ABSTRACT	(iii)
TABLE OF CONTENTS	(v)
INDEX OF FIGURES AND TABLES	(xi)
ACKNOWLEDGEMENTS	(xiv)
1. INTRODUCTION	1
1.1 The Earth's Gravity Field and Ocean Dynamics	1
1.2 Ocean Dynamic Information from Satellite Altimetry	3
1.3 Synopsis of Contents	5
2. FUNDAMENTAL GEODETIC CONCEPTS	7
2.1 Introduction	7
2.1.1 Gravity	7
2.1.2 Coriolis Force	8
2.1.3 Geopotential	8
2.1.4 Equipotential or Level Surfaces	9
2.1.5 Reference Ellipsoid	9
2.1.6 Spheropotential	10
2.1.7 Disturbing Potential	10
2.1.8 Gravity Anomaly and Normal Gravity	11
2.1.9 Geoid Height and Orthometric Height	11
2.1.10 Height Anomaly and Normal Height	13
2.1.11 Dynamic Sea Surface Topography (SST)	15
2.2 A "Higher" Reference System	16
2.3 Basic Relations	18
2.4 Requirements for a High Precision Geoid	23
2.4.1 Preamble	23
2.4.2 Conceptual Definitions for a 10 cm Geoid	25
2.4.3 The Geoid in Four Dimensions	26
2.4.4 Reference System Requirements for Ocean Dynamics	27
2.4.4.1 Preliminary Considerations	27
2.4.4.2 Global Requirements	29
2.4.4.3 Regional Requirements	31
2.5 Determination of SST for Ocean Dynamic Studies	31

	Page
3. ON THE PROSPECTS FOR REMOTE SENSING	33
3.1 Introduction	33
3.2 Satellite Sensor Instruments	36
3.2.1 Radar Altimeter	36
3.2.1.1 Altimeter Design	37
3.2.1.2 Altimeter Geometry	41
3.2.1.3 Altimeter Measurements	45
3.2.2 Microwave Scatterometer	46
3.2.2.1 Scatterometer Design	47
3.2.2.2 Scatterometer Measurements	48
3.2.3 Microwave Radiometer	48
3.2.3.1 Radiometer Design	48
3.2.3.2 Radiometer Measurements	49
3.2.4 Synthetic Aperature Radar (SAR)	50
3.2.4.1 SAR Design	50
3.2.4.2 SAR Measurements	51
3.2.5 Visible and IR Radiometer (VIRR)	51
3.2.5.1 VIRR Design	51
3.2.5.2 VIRR Measurements	52
3.3 Oceanographic Instruments	53
3.4 Application of Satellite Data for Oceanographic Studies	55
3.4.1 Oceanography Time-Space Scales	56
3.4.2 Satellite Time-Space Scales	58
4. VARIABILITY OF THE OCEANS	63
4.1 Basic Hydrodynamics	63
4.1.1 Introduction	63
4.1.2 Geostrophic Flow	64
4.1.3 Non-Linear Terms in the Equations of Motion	66
4.2 The East Australian Current Area	68
4.2.1 Introduction	68
4.2.2 The EAC - to 1960	70
4.2.3 Merchant Ship Records	79
4.2.4 The EAC - to 1980	81
4.2.5 Theoretical Studies of the Dynamics of the EAC	90
4.2.6 Summary	92

	Page	
4.3	The Gulf Stream Area	93
4.3.1	Introduction	93
4.3.2	Variability of the Gulf Stream	93
4.3.2.1	Cold core eddies	94
4.3.2.2	Warm core eddies	98
4.3.2.3	Eastern eddies	99
5.	GRAVITY FIELD IMPROVEMENTS VIA THE BOUNDARY VALUE PROBLEM	100
5.1	Introduction	100
5.1.1	Background	100
5.1.2	Fundamental Relations	102
5.2	Relations Between the Gravity Anomaly, Height Anomaly and SST	108
5.2.1	A Basic Relation	108
5.2.2	Computational Possibilities	112
5.2.3	Possibilities for Model Improvement using Iterative Procedures	115
5.2.4	Discussion	119
5.3	The Function $M_1(\Psi)$ and its Characteristics on Surface Integration	122
5.3.1	Surface Sub-Divisions	123
5.3.2	Error Accumulation Patterns	130
5.3.3	Discussion	135
5.3.4	Truncation Function Representation of Distant Zone Effects	136
5.3.5	Conclusions	138
5.4	Criteria for Determining SST with Minimum Reliance on Gravity Data	139
5.4.1	Preamble	139
5.4.2	The Effect of Gravity Field Model Errors e_N	142
5.4.3	Relationship between Errors $dC_{\alpha nm}$ and $e_{N\alpha nm}$	144
5.4.4	Discussion	147
5.5	The Unification of Geodetic Levelling Networks	148
5.5.1	Description of the Problem	148
5.5.2	Determination of δW_j for the Continental Levelling Datums	150
5.5.3	Practical Possibilities in the Foreseeable Future	152
5.6	Conclusions	154

	Page
6. SENSING SURFACE OCEAN DYNAMICS USING SATELLITE ALTIMETRY	156
6.1 Recovering the Short wavelength Components of the SST	156
6.1.1 Introduction	156
6.1.2 Possibilities for Determining ζ_{qs}	156
6.1.3 Time Variations in the Short Wavelength SST	158
6.2 Geodetic Techniques for Studying Temporal Variations	159
6.2.1 Overlapping Pass Analysis	159
6.2.1.1 Basic Requirements	159
6.2.1.2 Analysis Techniques	160
6.2.2 Regional Sea Surface Models from Satellite Altimetry	164
6.2.2.1 Methodology	164
6.2.2.2 Refinement of Modelling Procedures	169
6.2.3 Alternate Techniques	171
6.3 East Australian Current Study	173
6.3.1 GEOS-3 Altimetry Data	173
6.3.2 Overlapping Pass Analysis	174
6.3.3 Regional Sea Surface Model Analysis	178
6.3.4 Correlation Studies	181
6.4 Gulf Stream Study	183
6.4.1 GEOS-3 Altimetry Data	183
6.4.2 Overlapping Pass Analyses	183
6.4.3 Regional Sea Surface Model Analysis	202
6.4.4 Correlations with Surface Ocean Data	207
6.4.4.1 Introduction	207
6.4.4.2 Overlapping Pass Correlations	217
6.4.4.3 Regional Sea Surface Model Correlations	218
6.4.4.4 Summary	220
6.4.5 Geostrophic Current Estimates	221
6.4.5.1 Requirements for Recovering the SST	221
6.4.5.2 Data Analysis Procedure	224
6.4.5.3 Results	225
6.4.5.4 Discussion	226

	Page
7. ON THE RECOVERY OF OCEAN TIDE MODELS	237
7.1 Ocean Tides	237
7.1.1 Introduction	237
7.1.2 Tidal Potential	239
7.2 Modelling of Ocean Tides	246
7.2.1 Laplace Tidal Equations	246
7.2.2 Satellite Altimetry Applications	248
7.3 Recovery of Regional Ocean Tide Models	249
7.3.1 Preamble	249
7.3.2 Altimeter Data Sets	253
7.3.2.1 GEOS-3 Altimetry Data Base - LAS79	254
7.3.2.2 Crossover Data Base - CROSSOVER	255
7.3.2.3 Overlap Data Base - OVERLAP	257
7.3.3 Problems to Be Considered for Ocean Tide Model Recovery	258
7.3.3.1 Introduction	258
7.3.3.2 GEOS-3 Orbital Errors	259
7.3.3.3 Sampling Distribution	261
7.3.4 Method of Analysis	262
7.3.5 Theoretical Tidal Model	263
7.3.6 Analysis of Data Available in the Sargasso Sea	264
7.3.6.1 Introduction	264
7.3.6.2 Results of SARG Data Set	265
7.3.6.3 Results for the FIVSARG Data Set	271
7.3.6.4 Results of the OVERLAP Data Set	272
7.3.6.5 Results for the CROSSOVER Data Set	274
7.3.7 Discussion	274
7.4 Recovery of Global Ocean Tide Models	275
7.4.1 Altimeter Data Sets	275
7.4.2 Modelling the Ocean Tide	276
7.5 Conclusions	278

	Page
8. CONCLUSIONS	280
8.1 Remote Sensing Capabilities	280
8.2 A 10 cm Marine Geoid	280
8.2.1 Preamble	280
8.2.2 A Geoid Definition Adequate for Ocean Dynamic Studies	283
8.2.3 Determinations using the GBVP Approach	284
8.3 Recovering Ocean Dynamic Information	286
8.3.1 Overlapping Pass Analysis	286
8.3.2 Regional Sea Surface Models	287
8.3.3 Discussion	289
8.4 Tide Model Recovery	289
8.5 Discussion	290
REFERENCES	292
APPENDICES	
APPENDIX A1	317
APPENDIX A2	321

INDEX OF FIGURES AND TABLES.

FIGURES.	Page.
2.1 Systems of Reference	20
2.2 The Influence of SST.	20
3.1 Altimeter Measurements.	40
3.2 Satellite Altimeter Geometry.	44
3.3 GEOS-3 Two Day Groundtrack.	61
3.4 Time/Space Scales.	62
4.1 Pattern of the EAC - 190 dyn. cm contours	75
4.2 Average Surface Dynamic Height Anomaly (1960-1979)	75
4.3 Variation of EAC Dynamic Heights as a Function of Position.	77
4.4 VHRR IR Image of the EAC Area.	83
4.5 Buoy Tracks - 1977	86
4.6 Formation of an Anticyclonic Eddy.	87
4.7 EAC and the Tasman Front.	89
5.1 Variations of the Inverse Operator $M_1(\psi)$ with ψ .	122
5.2 Effect of Systematic Error Correlations with Groundtrack in Quadratures Evaluations for a Single Annulus.	134
6.1 Offset in Longitude for Overlapping Passes as a Function of Time.	161
6.2 Overlapping Passes after Tilt and Bias Corrections	163
6.3 Distribution of GEOS-3 Altimetry Passes in the Coral and Tasman Seas and the Indian Ocean.	175
6.4 Model of Quasi-Stationary Sea Surface - Tasman and Coral Seas.	179
6.5 Discrepancies between Sea Surface Model SEP77 and Marsh GEM10 Detailed Gravimetric Geoid in Tasman & Coral Seas.	180
6.6 Sets of Overlapping Passes in the western North Atlantic	184
6.7 RMS Discrepancy as a Function of Pass Length.	191
6.8(a) Altimetry overlapping profiles, Set 1.	193
(b) Residuals of Fit for Rev. No. 2813.	193
6.9 Correlation of IR Imagery with GEOS-3 Altimetry Profiles - October 1975.	199

6.10 Correlation of IR Imagery with GEOS-3 Altimetry Profiles - April 1976.	200
6.11 Tracking a Gulf Stream Ring.	201
6.12 Distribution of GEOS-3 Altimeter Passes in the Sargasso Sea Test Area.	203
6.13 Variation of Monthly Sea Surface Heights as a Function of Position.	208
6.14 Discrepancies Between Average Sea Surface (Oriented on GEM9) and Marsh-Chang 5' Gravimetric Geoid.	209
6.15 Dynamic SSH Variations - July 1975.	210
6.16 Dynamic SSH Variations - August 1975.	211
6.17 Dynamic SSH Variations - September 1975.	212
6.18 Dynamic SSH Variations - October 1975.	213
6.19 Dynamic SSH Variations - April 1976.	214
6.20 Dynamic SSH Variations - May 1976.	215
6.21 Geostrophic Current - July 1975.	227
6.22 Geostrophic Current - August 1975.	228
6.23 Geostrophic Current - September 1975.	229
6.24 Geostrophic Current - October 1975.	230
6.25 Geostrophic Current - April 1976.	231
6.26 Geostrophic Current - May 1976.	232
6.27 Geostrophic Current - Epoch (May 75 - May 76).	233
6.28 Geostrophic Current - Epoch (GEM9).	234
6.29 Geostrophic Current - Epoch (GEM10B).	235
7.1 The Tide Producing Potential.	241
7.2 Vertical Section in the Orbital Plane.	241
7.3 Wallops Global CROSSOVER Data Set.	256
7.4(a) Mofjeld M2 Tide Model.	268
(b) Modified Mofjeld M2 Tide Model.	269
7.5 Satellite (GEM10) M2 Tide Model.	270
7.6 Satellite (Marsh-Chang) M2 Tide Model.	270
Al.1 Correlation of IR Imagery with GEOS-3 Altimetry Profiles - September 1975.	331
Al.2 Correlation of IR Imagery with GEOS-3 Altimetry Profiles - November 1975.	332
Al.3 Correlation of IR Imagery with GEOS-3 Altimetry Profiles - December 1975.	333

A2.1 Regional Model of Dynamic SST Variations - July 1975	335
A2.2 Regional Model of Dynamic SST Variations - August 1975	336
A2.3 Regional Model of Dynamic SST Variations - September 75	337
A2.4 Regional Model of Dynamic SST Variations - October 1975	338
A2.5 Regional Model of Dynamic SST Variations - November 75	339
A2.6 Regional Model of Dynamic SST Variations - April 1976	340
A2.7 Regional Model of Dynamic SST Variations - May 1976	341
A2.8 Regional Model of Dynamic SST Variations - June 1976	342
A2.9 Regional Model of Dynamic SST Variations - July 1976	343
A2.10 Regional Model of Dynamic SST Variations - August 1975	344

TABLES.

3.1 A Comparison of Altimeter Parameters.	38
3.2 Estimates of Time-Space Scales.	58
4.1 Equations of Motion at the Ocean Surface	69
5.1 Width ($d\psi$) of Annuli making 1 mGal Contributions to ($\Delta g_c + \gamma N_c''/\bar{R}$) as a Function of ψ .	126
5.2 Factors Affecting the Quadratures Evaluation of ($\Delta g_c + \gamma N_c''/\bar{R}$).	127
5.3 Strength of Signal in Computations of ($\Delta g_c + \gamma N_c''/\bar{R}$)	129
5.4 Near Zone Error Accumulation Patterns in the Quadratures Evaluation of ($\Delta g_c + \gamma N_c''/\bar{R}$).	133
5.5 Discrepancies Between Satellite Determined Gravity Field Models and Surface Gravity Anomalies (10^0 Area Means) as a Function of Distance from the Nearest Tracking Station.	141
6.1 Statistics for Overlapping Pass Sets - Australia.	176
6.2 Altimeter Performance.	182
6.3 Statistics for Overlapping Pass Sets - western North Atlantic.	185
6.4 Spectral Analysis of 32 Sets of Overlapping Passes in the western North Atlantic.	195
6.5 Regional Monthly Solutions for the Shape of the Sargasso Sea from GEOS-3 Altimetry.	204

6.6 Three Parameter Transformations of Regional Sea Surface Models to the GEM9 Datum.	206
6.7 Correlations Between Remote Sensed Cyclonic Eddies and Dynamic SSH's of Regional Models of the Sargasso Sea from GEOS-3 Altimetry.	219
7.1 Principal Tidal Waves.	245
7.2 Crossover Data Bank Statistics.	257
7.3 M2 Tidal Solutions using SARG Data Set.	266
7.4 M2 Tidal Solutions using OVERLAP Data Set.	273
7.5 M2 Tidal Solutions using CROSSOVER Data Set.	273
8.1 Sensor Capabilities.	281

ACKNOWLEDGEMENTS.

The stimulus and enjoyment derived from working with the late Associate Professor R.S.Mather cannot readily be expressed in words. This thesis is a tribute to R.S.M.

A great deal of appreciation is also due to the other members of the research group, Chris Rizos, Ewan Masters, Bernd Hirsch, Oscar Colombo and Karl Bretreger, for their company and enthusiasm for discussion.

I am grateful to Professor P.V. Angus-Leppan for his comments made during the preparation of this thesis.

The chance to work with the Geodynamics Branch at G.S.F.C. from mid-1977 to mid-1978 provided the opportunity to work in a stimulating research environment. In particular, thanks are due to Dr. David Smith, Barbara Putney, Carl Wagner and Frank Lerch. Steve Klosko of EG&G gave invaluable assistance during the visit. The author was supported by a Fulbright Travel Grant .

I wish also to express my thanks to Bob Cheney of G.S.F.C. for his valuable comments made during communication. Helpful discussions with the group at Fisheries and Oceanography, especially Bruce Hamon and Stuart Godfrey were appreciated. Dr. Richard Legeckis

of NOAA/NESS kindly provided prints of the NOAA-5 IR imagery.

The hospitality and ideal working condition at the Research School of Earth Sciences, A.N.U. enabled the completion of this thesis to be relatively painless.

I am indebted to Jane Prowse and Susan Pullan for their willing help in the typing of this thesis.

1. INTRODUCTION.

1.1. The Earth's Gravity Field and Ocean Dynamics.

Traditionally, the geoid has been considered as a datum level surface of the Earth's gravity field to which all elevations could be referred. The most physically obtainable level surface which had global relevance was that corresponding to mean sea level (MSL) which, if averaged at tide gauge stations for periods in excess of 1 year, was subject to variations less than ± 10 cm. Thus, by utilising the results of geodetic levelling, the spatial location of this datum level surface could be defined at different locations on land areas. However, it was recognised over 50 years ago (Bowie 1929) that discrepancies existed between the datum level surface established from levelling operations and that indicated by the tide gauge results, on the assumption that the latter defined a unique level surface.

Oceanographers have shown that these discrepancies are not unexpected as, on the basis of hydrostatic considerations, the free ocean surface does not lie on a unique equipotential surface of the Earth's gravity field. The departures of the ocean surface from an equipotential surface are called the sea surface topography (SST) with reported magnitudes of the order of $\pm 1-2$ m (e.g., Stommel 1964; Lisitzin 1974). A comparison of SST determinations from oceanic steric levelling and geodetic levelling/MSL values should be in agreement but for some, as yet, unaccountable reason the comparisons yield discrepancies significantly larger than the internal precision of either evaluation procedure. This problem is not tackled in this thesis but for a summary of results and conclusions related to the sea surface slope problem along the east coast of Australia reference is made to Coleman et al. (1979).

Physical geodesists have sought to formulate solutions of the geodetic boundary value problem (GBVP) in terms of surface integrals in order to incorporate the available geodetic measurements for defining a level surface of the Earth's gravity field, i.e., the geoid. For determinations of the geoid to precisions of 1 part in 10^6 , it can be assumed that MSL approximates the geoid. However, if it is required to use geodetic techniques for recovering ocean dynamic information, precisions of the order of ± 10 cm are required in the definition of the

marine geoid. To meet this accuracy criterion, it is necessary to formulate solutions of the GBVP to precisions of 1 part in 10^8 where the effect of the SST is taken into account.

The role of the gravity field for ocean dynamic applications is somewhat different from that in the solution of the GBVP. In the latter situation, it is desired to geometrically map a surface on which all measurements are made. For ocean dynamic studies, however, the shape of the bounding surface (the ocean) is known and the requirement is to spatially define a level surface of the Earth's gravity field (the geoid) in ocean areas under circumstances where no measurements have been directly made in relation to it.

The geodetic data available for the task of recovering ocean dynamic parameters of interest are:

- (i) surface gravity data measured on land and at sea
(usually confined to continental shelf areas),
- (ii) satellite altimetry data in ocean areas, and
- (iii) a gravity field model obtained from satellite orbital perturbation analysis.

It is therefore essential to consider a conceptual definition of the geoid that is adequate for the unambiguous definition of the SST using a combination of surface gravity, satellite altimetry and satellite tracking data. This is discussed in Section 2.4 together with the expected stability of the shape of the geoid over geodetic time scales.

The fundamental reasons for pursuing the arduous task of high precision geoid determinations using the GBVP approach are for: (1) the evaluation of the SST for applications in oceanography, and (2) the unification of world levelling datums with a resolution equivalent to that of first order geodetic levelling. This thesis primarily sets out to provide a geodetic basis for recovering ocean dynamic parameters of interest using the above data types. Thus, the basic requirements to be met are the following:

- (i) the definition of a datum level surface (the geoid) in ocean areas to a precision of at least ± 10 cm for all wavelengths of interest, and
- (ii) satellite orbit determinations such that the radial error of the altimeter-equipped spacecraft is held below the 10 cm level in regions where no direct satellite tracking coverage is available.

The development of remote sensing techniques for quantifying the ocean circulation is part of the Earth and Ocean Dynamics Program (EODAP) initiated by National Aeronautics and Space Administration (NASA) in 1972. Using data collected from near Earth satellites provides the only realistic means of achieving the objectives of this program. The provision of a geodetic basis for recovering oceanographic information from satellite altimetry data will considerably enhance the prospects for the synoptic monitoring of the dynamics of the air/sea interface and provide valuable new data for oceanographers. Such information will also be of considerable value in the areas of navigation, climatology, fishing, oceanic engineering and disaster prevention.

1.2. Ocean Dynamic Information from Satellite Altimetry.

The gravitationally stabilized Geodynamics Experimental Ocean Satellite (GEOS-3) spacecraft was launched in April 1975 with an orbital period of 101.79 minutes and an inclination of 115°. In addition to the usual instrumentation for accurate position fixing, GEOS-3 carried a 13.9 GHz radar altimeter for measuring the vertical distance to the ocean surface. Included in the design requirements for the altimeter in the short-pulse mode was a precision of ± 50 cm from averages over 0.1 second such that the correlation of random error in the averaging procedure was held below 0.33 (GEOS-C 1972).

As the spacecraft moves at approximately 7 km/sec, each data point has a finite footprint. If one is considering the local sea state, the analysis of 1 second averages imposes a 15 km limit on the shortest wavelength of information recoverable from GEOS-3 altimetry data of this type. However, from the spectral analysis of overlapping pass residuals (see Chapter 6), the minimum meaningful wavelength sensed by the altimeter is about 30-50 km given by the white noise in the spectrum at these wavelengths.

Figure 3.2 illustrates the relationship between the altimeter range h , the height N of the geoid, the height ζ of the ocean surface above the reference ellipsoid, and the SST (ζ_s). The last three quantities are related by the expression

$$\zeta_s = \zeta - N \quad (1.1)$$

Therefore, the heights ζ will contain variations due to altimeter errors, geoidal model and orbital uncertainties as well as the oceanographic signals (tidal and dynamic height).

The horizontal gradients of ζ_s are one of the factors influencing the circulation of the surface layer of the ocean through the basic hydrodynamic equations of motion (see equation 4.5). The other factors affecting the surface ocean circulation are the Earth's rotation, the horizontal atmospheric pressure gradients at the air/sea interface and the frictional forces acting on the surface layer.

The errors in the altimeter data must be held below $\pm 20 \text{ cm} / 10^2 \text{ km}$ if these data are to be used in mapping steady state currents (Mather 1978b). An improvement of a factor of 5 is needed if such data are to be used in determining the changes of ζ_s with time that are associated with variations in the surface circulation.

At first glance, it would appear that the signal-to-noise problems preclude the recovery of information related to ocean circulation from the GEOS-3 altimeter data. The GEOS-3 data base available for analysis covers the period from May 1975 to July 1976. The principal difficulties are the following :

(i) the data collected are banded in latitude, being between the latitudes 65°N and 65°S for the GEOS-3 satellite (see Figure 7.3). This, together with the absence of onboard recording facilities for GEOS-3 limits the available surface coverage to basically regional extents (e.g., see Mather et al. 1978b, Figures 4 to 7).

(ii) the altimetry measurements were recorded in the form of discrete passes never exceeding 9000 km in length. The acquisition areas and periods being governed by the location of transportable telemetry units.

(iii) the precision of the orbit determination was variable. The analysis of orbits based on Doppler tracking data indicated a root mean square (rms) radial error of $\pm 1.3 \text{ m}$ (Mather et al. 1978b). This figure reduces to $\pm 0.9 \text{ m}$ if the GEOS-3 ephemeris is based on primarily laser tracking data (Lerch et al. 1978b). The major source of error is the model of the Earth's gravity field used in orbit integration.

(iv) All data are related to the ocean surface and not the geoid. The only source of data at the present time that is unaffected by the SST is the disturbing potential of the Earth's gravity field obtained from satellite orbit analysis.

It is thus the aim of this thesis to investigate, under the principal difficulties listed above, a geodetic basis for the recovery

of ocean dynamic information using satellite altimetry data. Specifically, the following problems are investigated:

(i) Conceptual definitions of the geoid adequate for oceanographic applications at the ± 10 cm level and the stability in the shape of the geoid over geodetic time scales.

(ii) Review of the instrumentation available to quantify the dynamics of the surface layer of the ocean on a real time basis.

(iii) Formulation of procedures for determining the long wavelength components of the SST.

(iv) Techniques for studying the short wavelength components of the SST, specifically looking at the resolution of transient features such as ocean eddies.

(v) A solution procedure adequate for the recovery of ocean tidal information using satellite altimetry data.

1.3. Synopsis of Contents.

Fundamental definitions for the relevant geodetic terms are set out in Section 2.1. The concept of the "higher" reference system and the basic equations at the surface of measurement defining relations between the gravity anomaly, the height anomaly and the SST are given in Sections 2.2 and 2.3. The requirements for a high precision geoid are indicated in Section 2.4 detailing the definition for the geoid adequate for ocean dynamic studies and reference system requirements for both global and regional investigations. Section 2.5 looks at the possibilities of recovering different parts of the SST spectrum.

A detailed review of the satellite remote sensing instruments that may be used for oceanographic studies is set out in Section 3.2. The remote sensing instruments considered are the radar altimeter, the microwave scatterometer and radiometer, the synthetic aperture radar and the visible and infrared radiometer. The types of information obtained from each of these sensors as well as their accuracies is indicated. Section 3.3 gives a brief summary of some of the oceanographic instruments used to make "quasi-synoptic" measurements. The prospects for using the satellite data for ocean dynamic studies is documented in Section 3.4 with a comparison of the oceanographic and satellite time-space scales.

Section 4.1 discusses the basic hydrodynamic equations of motion at the air/sea interface and the neglected terms involved in assuming

that the ocean circulation is purely geostrophic. The remaining two sections in the Chapter give descriptions of the ocean variability in areas of interest where it is considered that the altimetry data will be useful in defining valuable new oceanographic information. The regional areas considered are the East Australian Current area (Section 4.2) and the Gulf Stream area (Section 4.3).

A geodetic basis for improving the definition of the gravity field model and determining the long wavelength SST using solutions of the GBVP is discussed in Chapter 5. The basic relations between the available input data are set out in Section 5.2 with an analysis of the requirements for the surface integration of the kernel function given in Section 5.3. An approach to solving the GBVP with minimum reliance on the surface gravity data is introduced in Section 5.4. Section 5.5 attempts to investigate the problem of unifying a global network of levelling datums to precisions of the order of 10 cm.

The basic techniques used to study the temporal variations in the SST are given in Section 6.2. The results obtained for the two regional ocean areas considered in Chapter 4 are summarized in Sections 6.3 and 6.4. Section 6.3 gives details of the analysis in the East Australian Current area while Section 6.4 highlights the information obtained for the Gulf Stream area.

Chapter 7 investigates the problem of recovering ocean tidal information using the altimeter data. The basic tidal theory is briefly set out in Section 7.1. Considerations of the Laplace tidal equations and the role of the altimetry data are given in Section 7.2. Results of the investigations using the GEOS-3 data base in the Sargasso Sea area can be found in Section 7.3. Section 7.4 introduces a solution procedure aimed at solving for the global ocean tides.

The conclusions and recommendations are presented in Chapter 8. This involves a discussion of the prospects of remote sensing the surface layer of the ocean using satellite altimetry data and the usefulness of this data for such studies.

2. FUNDAMENTAL GEODETIC CONCEPTS.

2.1. Introduction.

The purpose of this section is to introduce the basic fundamental quantities of physical geodesy and establish the relations that are to be used in subsequent Chapters.

2.1.1. Gravity.

In the following development, a geocentric Cartesian coordinate system is assumed with the X_3 axis coincident with the Earth's mean axis of rotation. The X_1 and X_2 axes complete the right-handed coordinate system.

Since the Earth and atmosphere have an uneven mass distribution, the gravitational force F_G varies with position and is given by the relation

$$F_G = G \iiint_V \frac{\rho}{r^2} dv \quad (2.1)$$

where ρ is the density distribution within the Earth,

G is the gravitational constant where $G=6.672 \times 10^{-11} \text{ m}^3 \text{ s}^{-2} \text{ kg}^{-1}$

(Moritz 1979),

r is the distance from the body, and

dv is an element of volume.

Considering a rotating Earth, the force acting on a body due to its rotation with the Earth is the centripetal force, F_Ω , where its magnitude is given by the relation

$$F_\Omega = \Omega^2 R \cos\phi \quad (2.2)$$

Here Ω is the angular velocity of rotation of the Earth,

R is the distance from the body to the geocentre, and

ϕ is the latitude of the body.

The force F_Ω is resolved in the direction perpendicular to the instantaneous axis of rotation.

If the Earth is also considered deformable, then the body will be subject to gravitational deviations, F_D . These deformation forces are

of the order 10^{-6} g (about 1 mGal).

The resultant of the gravitational, centripetal and deformation forces is the total force, g, or gravity, acting on the body. The gravity vector is given by

$$g = F_G - F_\Omega + F_D \quad (2.3)$$

where g has the units cm/s^2 (or Gal) and is directed towards the geocentre along the plumbline, or the vertical; its basic significance for geodetic and astronomic measurements is well known.

2.1.2. Coriolis Force.

Considering a rotating reference system, the Coriolis force also acts on a moving body. It is proportional to the velocity with respect to the Earth, so that it is zero for bodies resting on the Earth. Since in geodesy, most measuring instruments can be considered at rest relative to the Earth, the Coriolis force need not be considered. However, the Coriolis force is of fundamental importance in oceanography since the world's oceans are not at rest. The Coriolis force is denoted as

$$F_c = 2\Omega \sin\phi V_H \quad (2.4)$$

where V_H is the total velocity in the $X_1 X_2$ plane. The direction of F_c is orthogonal to the direction of the velocity V_H and to the right-hand side of the latter vector in the Northern Hemisphere.

2.1.3. Geopotential.

The gravitational potential is understood to be the work which is exerted to move a unit mass from a given point to a point of zero potential (i.e., to an infinitely distant point). The Earth's gravitational potential for a continuous distribution of mass over a volume v is given by the expression

$$W_G = G \iiint_v \frac{\rho}{r} dv \quad (2.5)$$

where all quantities have been defined in equation 2.1 .

The rotational potential is defined as

$$W_{\Omega} = \left(\frac{1}{2} \Omega^2 R^2 \cos^2 \phi \right) \quad (2.6)$$

where all quantities have also been previously defined.

The potential of gravity, W is termed the geopotential and is likewise the sum of the gravitation (W_G), rotation (W_{Ω}) and deformation (W_D) potentials.

$$W = W_G + W_{\Omega} + W_D \quad (2.7)$$

The gradient vector of the geopotential is gravity, or

$$\vec{g} = -\vec{\nabla} W \quad (2.8)$$

where

$$\vec{\nabla} = \frac{\partial}{\partial X_i} \vec{i} \quad (2.9)$$

the X_i axis system having unit vectors \vec{i} along the X_i axes. The negative sign in equation 2.8 indicates that the geopotential increases with distance from the geocentre.

2.1.4. Equipotential or Level Surfaces.

Equipotential surfaces are surfaces of constant geopotential. The force of gravity, directed along the plumbline, is everywhere perpendicular to an equipotential surface and therefore slightly curved in space. Geodetic measurements are predominantly taken with respect to this system of level surfaces that constitute the Earth's gravity field. A principal aim of physical geodesy is, therefore, to determine the location of the equipotential surfaces of the Earth's gravity field, or geops. The particular geop which most closely approximates mean sea level (MSL) is called the geoid.

2.1.5. Reference Ellipsoid.

Conventionally a simple mathematical figure is chosen to best fit the most physically obtainable equipotential surface, i.e., the geoid or

its approximation of MSL, since the level surfaces have irregular shapes.

The reference figure adopted is a biaxial symmetrical ellipsoid with its rotation axis co-linear with the axis of rotation of the Earth. The centre of the ellipsoid is at the geocentre and the ellipsoid will have the same mass and rotational characteristics as the Earth.

The reference ellipsoid and its normal gravity field are completely defined by four constants. The geometric parameters defining the ellipsoid are a , the semimajor axis and f , its flattening. The other parameters are physical constants, being the values of the angular velocity of the Earth's rotation, Ω and GM . Recommended values for these parameters are (Moritz 1979):

$$\begin{aligned} a &= 6\,378\,137 \text{ m} \quad (\text{exact}) \\ f^{-1} &= 298.247167427 \\ GM &= 398\,603 \text{ km}^3/\text{s}^{-2} \\ \Omega &= 7.2921151467 \times 10^{-5} \text{ rad/s} \quad (\text{exact}) \end{aligned}$$

Derived values of normal gravity at the equator (γ_e) and the spheropotential of the reference ellipsoid (U_0) can be found using formulae given in Heiskanen & Moritz (1967, Sections 2.7 - 2.10). This reference is hereafter referred to in the text as H & M.

2.1.6. Spheropotential.

The spheropotential is the total potential U of the normal gravity field, having gravitational (U_G) and rotational (U_Ω) components,

$$U = U_G + U_\Omega \quad (2.10)$$

Since the reference ellipsoid has a symmetrical mass-density distribution, the gravitational potential U_G varies only in latitude. The spheropotential of a gravitating, equipotential ellipsoid in the space exterior to its surfaces is given by relations in Mather (1971, p.85).

2.1.7. Disturbing Potential.

The disturbing potential of the solid Earth and oceans and the atmosphere is the difference between the actual gravity potential, W (geopotential) and the normal gravity potential, U (spheropotential) and

is denoted by (H & M 1967, p.82)

$$T = W - U \quad (2.11)$$

Combining equations 2.7 and 2.10, noting that $W_{\Omega} = U_{\Omega}$ and neglecting the deformation component of the geopotential, W_D gives

$$\vec{\nabla}^2 T = 0 \quad (2.12)$$

where $\vec{\nabla}^2$ is the Laplacian operator defined by

$$\vec{\nabla}^2 = \frac{\partial^2}{\partial X_1^2} + \frac{\partial^2}{\partial X_2^2} + \frac{\partial^2}{\partial X_3^2} \quad (2.13)$$

satisfying Laplace's equation, i.e., T is harmonic in the space exterior to the Earth and its atmosphere.

2.1.8. Gravity Anomaly and Normal Gravity.

The gravity anomaly, Δg at the surface of the Earth is defined as (H & M 1967, p.83)

$$\Delta g = g - \gamma \quad (2.14)$$

where g is the value of observed gravity, and γ is the normal or reference gravity of the reference ellipsoid.

The difference in direction between the gravity vector (plumbline) and the normal gravity vector is known as the deflection of the vertical (ζ_d).

Normal gravity is the gradient vector of the spheropotential,

$$\gamma = -\vec{\nabla} U \quad (2.15)$$

and can be computed using formulae found in H & M (1967, Sections 6.2, 6.3)

2.1.9. Geoid Height and Orthometric Height.

The separation between the geoid and the reference ellipsoid, along the normal to the ellipsoid, is called the geoid height or geoid

undulation (denoted by N). With respect to a best fitting reference ellipsoid, geoid height variations are of the order ± 100 m.

The orthometric height (H) is the linear distance along the curved vertical from the geoid to a point P on the surface of measurement, and is ordinarily obtained from geodetic levelling operations (see Bomford 1971, Chapter 3). Due to the non-parallelism of the level surfaces of the Earth's gravity field, the linear levelling increments dn , given by the difference of staff readings, are converted to potential differences dW . These latter potential differences are route independent. Thus,

$$dW = -g \, dn \quad (2.16)$$

where g is the observed value of gravity. If g is not available, it is conventional to use a computed value of normal gravity, γ .

For a point P , the geopotential difference between the point and the geoid is given by (H & M 1967, Section 4.1),

$$\Delta W_P = W_P - W_o = - \int_{\text{geoid}}^P g \, dn \quad (2.17)$$

the path of the integration being the levelling route from the datum level to the point, P .

The orthometric height at the point, P using equation 2.17 is given by (H & M 1967, Section 4.1)

$$H_P = - \frac{\Delta W_P}{\bar{g}} \quad (2.18)$$

where \bar{g} is the mean value of gravity along the vertical between P and the geoid. Since the density of material between the point P and the geoid is unknown, the value of \bar{g} is only an approximation given by:

$$\bar{g} = g - \left(\frac{1}{2} \frac{\partial \gamma}{\partial h} + 2\pi G \bar{\rho} \right) H \quad (2.19)$$

where $\partial \gamma / \partial h$ is the normal free air gravity gradient given by the relations (Mather 1971, Section 6.7),

$$\frac{\partial \gamma}{\partial h} = - \frac{2\gamma}{a} (1 + m + f - 2f \sin^2 \phi_c + O\{f^2\}) \quad (2.20)$$

Here a and f are the equatorial radius and flattening of the reference ellipsoid,

ϕ_c is the geocentric latitude of the point, and m is a parameter defined by the expression

$$m = \frac{a\Omega^2}{\gamma_e} \quad (2.21)$$

γ_e being the equatorial normal gravity on the ellipsoid. In most cases, equation 2.20 is approximated by

$$\frac{\partial \gamma}{\partial h} = 0.30855 H^{(m)} \quad \text{mgal} \quad (2.22)$$

The other quantities in equation 2.19 are G , the gravitational constant and $\bar{\rho}$, the average density between the geoid and P .

Assuming $\bar{\rho} = 2.67 \text{ g/cm}^3$, $G = 6.67 \times 10^{-11} \text{ m}^3 \text{ s}^{-2} \text{ kg}^{-1}$, and using equation 2.20,

$$\bar{g} \text{ (mgal)} = g \text{ (mgal)} + 0.0423 H \text{ (km)} \quad (2.23)$$

Thus, it is obvious that the orthometric height can never be precisely evaluated.

The height of the point P above the ellipsoid (see Figure 2.1) can be evaluated, given estimates of the orthometric height and geoid height as,

$$h = N + H \quad (2.24)$$

These quantities basically define the system of reference for the conventional Stokesian solution of the Geodetic Boundary Value Problem (GBVP).

2.1.10. Height Anomaly and Normal Height.

The ellipsoidal height may also be obtained by using the relation

$$h = \zeta + H^* \quad (2.25)$$

where ζ is the height anomaly (replacing the geoid height in equation 2.24), and

H^* is the normal height (replacing the orthometric height).

This system of reference, as proposed by Molodenskii in 1945 (Molodenskii et al. 1962), overcomes the problems made in assuming a

density distribution between the geoid and the Earth's surface. Molodenskii's formulation of the GBVP has been investigated in detail by Mather (1973a) for solutions of the height anomaly ζ to the order of 5 cm.

The normal height (see Figure 2.1) is the height of the spheropotential $U_Q (= U_0 + \Delta W)$ above the reference ellipsoid. The normal height, and hence the telluroid, can be determined by geodetic levelling data combined with gravity observations, by an analytical expression that is free of any assumptions about the density (H & M 1967, Section 8.3),

$$H^* = -\frac{\Delta W}{\gamma_0} \left(1 + \frac{\Delta W}{a\gamma_0} (1 + f + m - 2f \sin^2 \phi_c) \right) + \left(\frac{\Delta W}{a\gamma_0} \right)^2 \quad (2.26)$$

where γ_0 is the normal gravity on the reference ellipsoid at Q_0 , and

all other quantities have been defined previously in sub-section 2.1.9 .

The telluroid is defined as the locus of points $Q(\phi, \lambda, U_0 + \Delta W)$ which has the same difference in potential ΔW , in relation to the reference ellipsoid, as the difference in geopotential between the Earth's surface at P and the geoid (Hirvonen 1960) . At the point Q, ϕ and λ are the astronomically determined latitude and longitude. Thus, the telluroid is not a level surface of the Earth's gravity field but closely approximates the shape of the physical surface of the Earth.

The height anomaly is thus given by the expression

$$\zeta = h - H^* \quad (2.27)$$

and may be considered as the distance between the geopotential surface W and the corresponding spheropotential surface U at the point P. If $W_p = U_p$, then the ellipsoidal height would equal the normal height .

The geoid height can be related to the height anomaly by the expression (H & M 1967, Section 8.12),

$$N = \zeta + \left(\frac{\bar{g} - \bar{\gamma}}{\bar{\gamma}} \right) H \quad (2.28)$$

where \bar{g} is the mean gravity along the vertical between the geoid and the Earth's surface (equation 2.19),

$\bar{\gamma}$ is the mean normal gravity along the normal between the ellipsoid and the telluroid, and

H is the orthometric height above the geoid.

2.1.11. Dynamic Sea Surface Topography (SST).

Physical oceanographers, on the basis of temperature and salinity measurements and air pressure data have shown that the free ocean surface, neglecting periodic tidal and wind effects, does not lie along any equipotential surface of the Earth's gravity field (Sturges 1967; Montgomery 1969). The deviation of the free ocean surface from a level surface is termed the sea surface topography, or SST.

In a geodetic context, the SST is defined as the vertical displacement of the ocean surface above some specific reference surface in ocean areas. The term dynamic SST, denoted ζ_s , implies that the reference surface used is the geoid. The value of ζ_s in land areas is the height of MSL at the regional levelling datum above the geoid.

The stationary SST is the departure of MSL from the geoid with variations being of the order $\pm 1-2$ m (see Lisitzin 1974, Figure 30). The time varying component of ζ_s is of the order 1 m or less. A more detailed description of oceanographic time-space scales is given in sub-section 3.4.1. For geodetic definitions to 1 part in 10^6 , the SST can be ignored, i.e., the ocean surface is equivalent to the geoid.

However, the role of purely geodetic techniques in remote sensing ocean dynamics is to provide values of ζ_s from the altimeter data to accuracies of ± 10 cm to adequately quantify oceanographic features. To meet this requirement it is necessary to consider geodetic definitions to 1 part in 10^8 .

As seen in Figure 3.2, the SST can be determined, in concept quite simply, from satellite altimeter measurements as,

$$\zeta_s = \zeta - N \quad (2.29)$$

It is evident from this equation that the accuracy of the SST determination for ocean dynamic studies is dependent upon:

- (i) the radial position of the satellite orbit being defined to ± 10 cm for all wavelengths of interest,
- (ii) the geoid being defined in ocean areas with equivalent precision and wavelengths as in (i), and
- (iii) the radar altimeter measurement being at the decimetre level.

Considerations of (iii) are given in Chapter 3. Conceptual definitions of the geoid for solutions of the GBVP to 10 cm, a necessary prerequisite for ocean dynamic studies, are given in sub-section 2.4.

The later sections of this Chapter deal with other necessary requirements for resolutions of 1 in 10^8 in marine geoid determinations.

2.2. A "Higher" Reference System.

A system of reference in physical geodesy based on an equipotential ellipsoid with the same rotational characteristics and mass as the Earth, and the same volume as MSL, gives rise to the disturbing potential T at the surface of the Earth. The magnitude of T is of the order 10^2 kGal m. The corresponding height anomalies ζ do not exceed $\pm 10^2$ m.

A "higher" system of reference than that afforded by a rotating, gravitational, equipotential ellipsoid was proposed by Mather (1974b) that is equivalent to a precision of the order of 5 parts in 10^4 in ζ (± 5 cm). The spheropotential of the reference ellipsoid, conventionally equal to U_0 , has an additional gravitational potential model ΔU included in its definition where the spheropotential on the "higher" reference system is (Mather 1974b, p.92),

$$U = U_0 + \Delta U_s \quad (2.30)$$

and ΔU_s can be represented in geocentric spherical coordinates (R_e, ϕ, λ) by the relation,

$$\Delta U_s = \frac{GM}{R_e} \sum_{n=2}^{n'} \left(\frac{a}{R_e} \right)^n \sum_{m=0}^n \sum_{\alpha=1}^2 C_{\alpha nm}^* S_{\alpha nm}' \quad (2.31)$$

where R_e is the distance from the geocentre to the ellipsoid,

$S_{\alpha nm}$ are the surface spherical harmonic functions defined by

$$S_{1nm} = P_{nm}(\sin\phi) \cos m\lambda \quad ; \quad S_{2nm} = P_{nm}(\sin\phi) \sin m\lambda \quad (2.32)$$

Here $P_{nm}(\sin\phi)$ are the Legendre functions of degree n and order m (see H & M 1967, Section 1.11).

The harmonic coefficients $C_{\alpha nm}^*$ are equivalent to the coefficients $C_{\alpha nm}'$ except for the specific coefficients C_{120}^* , C_{140}^* and C_{160}^* . The coefficient $C_{120}^* = 0$ and C_{140}^* and C_{160}^* are corrected for the effect of the ellipsoidal flattening implied by the value of C_{120}' according to the relations (Mather 1978b, Appendix),

$$C_{140}^* = C_{140}' - \frac{\sin^4 \alpha}{5} \left[1 - \frac{4}{21} \frac{m' \sin \alpha}{q_2(\alpha)} \right] \quad (2.33)$$

$$C_{160}^* = C_{160}' - \frac{\sin^6 \alpha}{7} \left[\frac{2}{9} \frac{m' \sin \alpha}{q_2(\alpha)} - 1 \right] \quad (2.34)$$

The parameter m' is defined as

$$m' = a^3 \Omega^2 / GM \quad (2.35)$$

and α is given as

$$\begin{aligned} \sin \alpha &= (2f - f^2)^{\frac{1}{2}} \\ \cos \alpha &= 1 - f \end{aligned} \quad (2.36)$$

with

$$q_2(\alpha) = \frac{1}{2} (\alpha(3\cot^2 \alpha + 1) - 3\cot \alpha) \quad (2.37)$$

The coefficients $C_{\alpha nm}'$ are estimates of the spherical harmonic coefficients of the geopotential $C_{\alpha nm}$, as obtained from satellite orbit analysis, to some maximum degree n' . The coefficients $C_{\alpha nm}'$, together with constants a , GM and Ω , make up the geopotential or gravity field of the Earth (e.g., Goddard Earth Model (GEM) series).

The reference ellipsoid on the "higher" reference system is no longer an equipotential surface. The equipotential surface $U=U_0$, referred to as RS1 (see Mather 1974b, Figure 1), is irregular and now approximates the geoid to within ± 10 m. The height anomaly ζ' and the disturbing potential $T' (=T - \Delta U_s)$ on the "higher" reference system can be expected to be about 10% of their values for the telluroid-physical surface system shown in Figure 2.1 (i.e., ± 10 m and ± 10 kGal m respectively). However, a similar reduction in magnitude does not occur for gravity anomalies since gravity is heavily influenced by local mass anomalies and therefore unrepresented in the "higher" reference system unless n' was correspondingly large.

The subsequent mathematical formulations, relating to solutions of the GBVP, are with respect to the "higher" reference system. This means that the fundamental quantities and their relations defined in section 2.1 need to be modified. The necessary equations needed to satisfy the GBVP solution to ± 5 cm are set out in the next section, taking into account the effect of the atmosphere, the SST (ζ_s) and the "higher"

reference system.

2.3. Basic Relations.

With the launching of an altimeter onboard the GEOS-3 satellite in April 1975, the possibilities existed for utilising the altimeter data to make significant improvements in the definition of the Earth's gravity field . A far more ambitious undertaking is the definition of the SST . As mentioned in sub-section 2.1.11, the required resolution of geoid determinations for this latter purpose must be at the 10 cm level. A solution for the geoid to this precision in oceanic areas requires a re-examination of the solution of the GBVP to an equivalent precision in the height anomaly and an equivalent precision of $\pm 30 \mu\text{Gal}$ for gravity anomaly data. The fundamental relations required to achieve this are given below and an attempt to define the SST from a solution of the GBVP, without making unwarranted assumptions about the nature of the SST, is given in Chapter 5.

It is necessary to formulate the disturbing potential, in terms of Green's third identity (see H & M 1967, p.11) so that Laplace's equation is satisfied without approximation on the surface of measurement and exterior to it, when considering solutions of the GBVP which attempt to define ζ to ± 5 cm (Mather 1973a). Such a potential is T'' which is harmonic in the space on and exterior to the surface of measurement and is given by

$$T'' = T' - V \quad (2.38)$$

where T'' is the potential of the solid Earth and oceans,

T' is the potential of the solid Earth, oceans and atmosphere on the "higher" reference system, and

V is the potential of the atmosphere (see Anderson et al. 1975 for further details).

This step is necessary to ensure the mathematical validity of expressions involving spherical harmonic representations. Spherical harmonic expressions relate quantities on the surface of the sphere, but the geodetic observations are made at or near the irregular surface of the Earth. Thus, the use of the orthogonal properties of surface harmonics is restricted to the surface of a sphere and only where such expansions exist. The minimum sphere to which this applies is the

Brillouin sphere which is concentric with the reference ellipsoid and the centre of mass of the solid Earth and oceans such that all topography is included within it (Mather 1973a). Expressions on the Brillouin sphere are denoted by an overbar.

A solution of the GBVP which considered the effect of the stationary SST was proposed by Mather (1975b). Attempts to recover ζ_s using solutions of the GBVP are discussed further in Chapter 5. The existence of stationary SST affects the determination of the height anomaly ζ in two distinct ways:

- (i) creating systematic errors in the gravity anomaly data set due to assumptions made in the relations between the geoid and regional elevation datums, and
- (ii) the geometry of the GBVP according to Molodenskii, as indicated in Figure 2.1, is altered. This requires new relationships to be obtained between the geoid height N and the height anomaly ζ (see equation 2.28) .

The effect of (i) is to cause systematic errors of 0.3-0.6 mGal in the gravity anomaly values, with half wavelengths of the order of 500-1000 km, based on the average extent of continental levelling networks. These errors would introduce uncertainties of the order $\pm 15-50$ cm in determinations of geoid height/ height anomaly values by quadratures evaluations (Rizos 1980, Section 2.3.5).

The revised geometry of Molodenskii's problem is illustrated in Figure 2.2 showing the effect of the SST ($= \delta W_d$ in potential units). From geodetic levelling in relation to an offset datum, the normal height H^* defines the height of the point Q" above the ellipsoid. In order to preserve the geometry implied by equation 2.25, the height anomaly is the distance from the Earth's surface to the altered telluroid. This means that in ocean areas, the height anomaly is identical to the sea surface height (SSH) derived from satellite altimetry. The relationship between the "altered" height anomaly and the geoid height is now :

$$N = \zeta + \left(\frac{\bar{g}-\bar{\gamma}}{\bar{\gamma}} \right) H + \frac{\delta W}{\bar{\gamma}} \quad (2.39)$$

In ocean areas, equation 2.39 becomes,

$$N = \zeta + \frac{\delta W}{\bar{\gamma}} \quad (2.40)$$

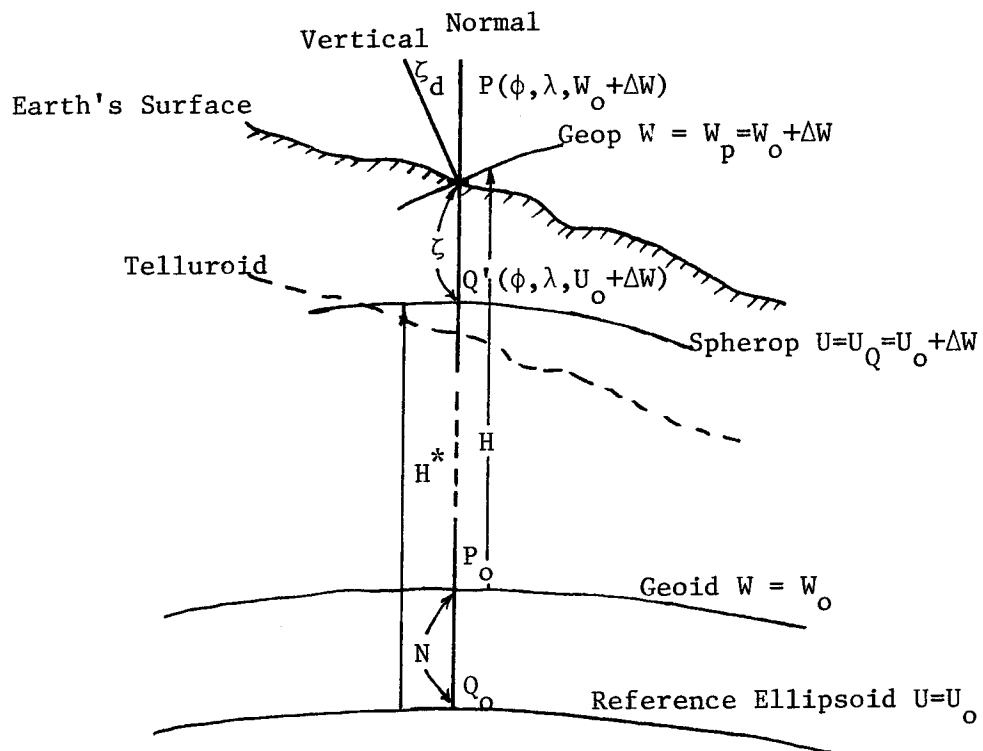


Figure 2.1 Systems of Reference.

H^* = Normal Height H = Orthometric Height
 ζ = Height Anomaly N = Geoid Height

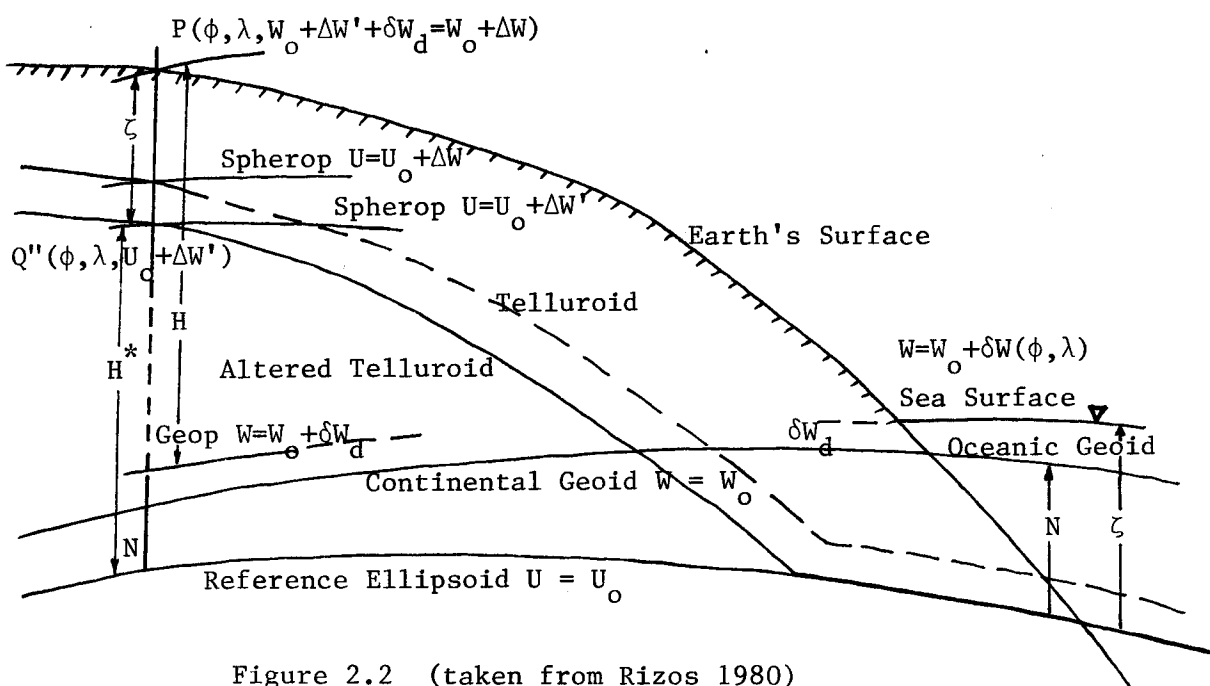


Figure 2.2 (taken from Rizos 1980)

The Influence of SST.

The relationship between the disturbing potential T' , the Earth's geopotential W and the normal potential U at the point P on the Earth's surface is (using equation 2.11),

$$T'_p = W_p - U_p \quad (2.41)$$

where U_p is the spheropotential on the "higher" reference system.

It can be seen from Figure 2.2 noting that the "higher" reference system is being used that,

$$\begin{aligned} T'_p &= (W_o + \Delta W' + \delta W) - (U_o + \Delta W' + \zeta' \frac{\partial U}{\partial h}) \\ &= (W_o - U_o) + \delta W + \gamma_p \zeta' \end{aligned} \quad (2.42)$$

or

$$\zeta' = \frac{1}{\gamma_p} (T'_p - (W_o - U_o) - \delta W) \quad (2.43)$$

where $\Delta W'$ is the geopotential difference between the point P and the MSL datum,

δW is the difference in potential between the sea surface/ MSL datum and the geoid, such that

$$\delta W \text{ is defined by } \begin{array}{ll} -g \zeta_{sd} & \text{on land} \\ -g \zeta_s & \text{at sea} \end{array} \quad (2.44)$$

In equation 2.44, ζ_{sd} is the height of the MSL datum above the geoid and ζ_s is the SST in the open oceans.

$\partial U / \partial h$, in equation 2.42, is the radial derivative of the spheropotential along the spherop normal defined by

(equation 2.15),

$$-\frac{\partial U}{\partial h} = \gamma \quad (2.45)$$

Thus, the disturbing potential of the solid Earth and oceans, referred to the "higher" reference system, is

$$T'' = (W_o - U_o) + \delta W + \gamma \zeta' - V + O\{10^{-3} T''\} \quad (2.46)$$

The gradient of the disturbing potential can be obtained by

differentiating along the spherop normal through P giving,

$$\begin{aligned} \left(\frac{\partial T'}{\partial h}\right)_P &= \left(\frac{\partial W}{\partial h}\right)_P - \left(\frac{\partial U}{\partial h}\right)_P \\ &= -\Delta g' + \zeta' \left(\frac{\partial \gamma}{\partial h}\right)_P + \frac{1}{2} g_p \zeta_d^2 + O\{10^{-4}\Delta g\} \end{aligned} \quad (2.47)$$

where ζ_d is the deflection of the vertical at the point P, and the pseudo gravity anomaly is defined as (Mather 1974b, p.96),

$$\Delta g' = \Delta g - \delta \gamma \quad (2.48)$$

Here Δg is the gravity anomaly deduced from surface measurements (equation 2.14), and

$\delta \gamma$ is the change in the normal gravity from the equipotential ellipsoid to the "higher" reference system given by (Mather 1974b, p.95),

$$\delta \gamma = \gamma \sum_{n=2}^{n'} (n-1) C_{\alpha n m}^* S_{\alpha n m} + O\{f\delta \gamma\} \quad (2.49)$$

The term "pseudo" is used to differentiate this quantity from the ground level gravity anomaly Δg . Note that the pseudo gravity anomaly can only be evaluated from satellite determined gravity field models.

Using equations 2.38, 2.42 and 2.47 and the definition of the vertical gradient of normal gravity (Mather 1973a, p.29), it follows that at the surface of measurement,

$$\begin{aligned} \frac{\partial T''}{\partial h} &= \frac{\partial T'}{\partial h} - \frac{\partial V}{\partial h} = -\Delta g' - \delta g_a - \frac{2T''}{R} (1 + c_\phi) + \frac{1}{2} g \zeta_d^2 \\ &\quad + \frac{2}{R} (W_o - U_o) + \frac{2\delta W}{R} \end{aligned} \quad (2.50)$$

where R is the distance from the centre of mass of the solid Earth and oceans,

c_ϕ is a parameter defined as

$$c_\phi = 1 + m + f - 3f \sin^2 \phi_c \quad (2.51)$$

δg_a is the atmospheric effect on the gravity anomaly observed at the surface of the Earth ($=\partial V/\partial h + 2V/R$) (see Anderson et al. 1975 for details).

These fundamental equations provide a basis for the complete definition of the GBVP for the case of the "higher" reference system which incorporates the global characteristics of the Earth's gravity

field.

2.4. Requirements for a High Precision Geoid.

2.4.1. Preamble.

For over a century it has been known that the mean surface of the oceans approximated a level surface of the Earth's gravity field. Thus, it was conventional in geodetic practice to assume that the geoid was synonymous with the directly observable MSL defined by tide gauge readings at the regional levelling datum. Hence the role of the geoid was strictly a passive one, being only as a datum for geodetic levelling.

It was also recognised about 50 years ago (Bowie 1929) that discrepancies existed between the elevations of coastal tide gauges established by geodetic levelling and the elevations indicated by the tide gauge zeros, on the assumption that the latter defined a unique level surface. In other words, the MSL surface defined by more than one tide gauge did not lie along a unique level surface of the Earth's gravity field. The departure of the mean ocean surface from a level surface at the tide gauge site is the coastal SST. The magnitude of this coastal SST, implied from geodetic levelling, is not consistent with SST derived from meteorological and oceanographic data in open oceans. The literature investigating the discrepancy between geodetic and oceanographic estimates has been quite substantial in recent years. The problem has yet to be satisfactorily resolved but the general consensus at the present time is that there are unknown systematic errors in the geodetic levelling data (Anderson 1979; Coleman et al. 1979; Rizos 1980; Kumar & Soler 1981).

It is obvious that the classical definition of the geoid is inadequate for geodetic considerations at the ± 10 cm level. The interest in attempting the rather arduous task of defining a high precision geoid has been generated in the last 10 years with the concepts of satellite oceanography proposed in Kaula (1970). The requirements for a high precision geoid may be stated as:

- (i) the determination of the SST, and
- (ii) the unification of the regional levelling datums in the context of the datum level surface - the geoid.

Geodetic techniques are therefore required to determine the marine geoid to 10 cm in relation to a specified reference figure. This task involves computing the geoid-ellipsoid separation (N) by some technique. The types of data available for determining the shape of the geoid in the foreseeable future are the following :

- (i) gravity data measured at the surface of the Earth -
 these data are usually expressed as gravity anomalies that are related to a regional levelling datum in land areas. The precision sought in the values of Δg for determining a high precision geoid is $\pm 30 \mu\text{Gal}$.
- (ii) Tracking data from ground stations and synchronous satellites to near-Earth altimeter satellites -
 the orbital perturbations can be analysed to determine the disturbing potential T of the Earth's gravity field to some degree n' . An important point to note is that this data type is the only one unaffected by the SST, assuming that the tidal effects are adequately modelled in the orbit integration. The resolution required when using the "higher" reference system is that the disturbing potential T" has no terms with wavelengths greater than 1 (equivalent to n'), where 1 is estimated to be about 10^3 km.
- (iii) the location of the instantaneous ocean surface ζ above the reference surface, derived from satellite altimetry data -
 it can be seen from equation 2.40 that the value of ζ contains the signature of the SST. In addition, the geometry of the orbital plane (see Figure 3.2) shows that values of ζ from altimetry are directly influenced by errors in orbit determination where the orbital errors will be predominantly of long wavelength and subject to large uncertainties in regions where tracking data are inadequate. It is required to define ζ to ± 10 cm in the radial component of position for adequate SST studies.

There are a number of techniques available for the computation of the geoid-ellipsoid separation. They may be categorised into the following methods :

- (1) Astrogeodetic methods,
- (2) Passive satellite methods,
- (3) Active satellite methods,
- (4) Gravimetric methods, and

(5) Combination methods.

A thorough description of these methods, their underlying principles, deficiencies and practicability for marine geoid determinations at the ± 10 cm level has been given in Rizos (1980, Section 2.3) . However, only a formulation of the GBVP for the recovery of the long wave features of the SST, using all three data types outlined above, is discussed in this thesis.

2.4.2. Conceptual Definitions for a 10 cm Geoid.

For definitions of the geoid to 1 part in 10^8 , the relationship between the satellite observed MSL and the level surface of the Earth's gravity field should be quantified. Satellite altimetry data are likely to be collected over finite time periods of about 1-5 years and provide discontinuous samples of ζ in oceanic regions. Such sampling distributions of ζ could be averaged over some $n^\circ \times m^\circ$ surface area and be used to obtain a definitive geoid for a particular epoch (i.e., the time span of the observation period) . However, ambiguity can occur in the selection of a particular level surface as the geoid depending upon how the altimetry data are used to sample MSL as a function of position.

A number of definitions for the geoid have already been proposed (Mather 1975c, 1978c; Lelgemann 1976) and it is evident that the choice of a particular level surface is arbitrary, the definition chosen being determined by its practical utility. Three possible definitions given by Mather (1978c) are set out below :

"The geoid, for a selected epoch of measurement, is that level surface of the Earth's gravity field in relation to which the average non-tidal SST

- (1) is zero as sampled globally in ocean regions (Oceanic definition).
- (2) has no zero degree harmonic in solutions of the GBVP (BVP definition).
- (3) has zero mean as sampled at all the world's levelling datums (Geodetic definition) ."

In definition (1), 70% of the data for its definition comes from radar altimetry. At regional levelling datums, oceanographically derived values of ζ_s can be incorporated, provided distorting coastal shelf effects are considered, to ensure unique definition at the 10 cm level.

For the BVP definition, oceanic areas are sampled as for definition (1), but land areas are represented by values of ζ_{sd} at the

regional datum for elevations used in the compilation of gravity anomalies. Considerable aliasing of determined ζ_{sd} values may occur if errors in the "higher" reference system with wavelengths greater than the smallest dimension of the area served by the datum are not modelled in the computation (Mather et al. 1978c). This definition implies that there is no zero degree term in ζ_s . However complete global sampling is required for the realisation of definition (2) .

The data available for the Geodetic definition are restricted to land areas where geodetic levelling networks connect to the regional levelling datum. As such, this definition has no relevance for studies pertaining to the definition of a marine geoid to 10 cm .

Therefore, the favoured definition of the geoid for ocean dynamic studies is the Oceanic definition since no assumptions need be made concerning the pattern of SST on a global basis. This definition also implies that an estimate of the potential of the geoid (W_0) can be obtained using satellite altimetry data. Details of these studies are given in Mather et al. (1978c), Mather & Rizos (1979) and Rizos (1980). Definition (1) is likely to give a more representative level surface than the other two definitions with the presently available altimetry data distributions. The condition of best fit using this definition is that of equal volume.

2.4.3. The Geoid in Four Dimensions.

Having adopted a definition for the geoid, its validity is dependent on its stability over long periods of time. In the case of a real deformable Earth, the spatial position of the level surfaces will undergo changes on a wide variety of time scales due to a number of different phenomena.

The dominant factor causing changes in the radial component of geoidal position with time is the tidal potential (see equation 7.7) . But it is impractical to deal with phenomena which cause position variations with periods shorter than about 1-5 years (i.e., an epoch of observation) other than as corrections to observations or as modelling parameters in a solution procedure. Thus, the effect of short period phenomena that affect the shape of the geoid, such as Earth and ocean tides and tidal loading, would have to be eliminated from observations by modelling.

Interest is therefore focused on those phenomena causing secular

variations in the shape of the geoid over geodetic time scales (say, up to 10^2 years). Secular variations in the radial position of the geoid, referenced to a selected equipotential surface, are of three types (Mather & Larden 1978) :

- (i) Variations in the definition (i.e., nett volume changes), e.g., global mean secular variation in MSL estimated at 3 cm/100 years (Mather 1974d, Appendix).
- (ii) Variations in the shape of the geoid as a function of position, and
- (iii) Changes in the geopotential W_0 of the geoid.

The study by Mather and Larden and other investigations by Mather et al. (1977a;1979a) indicated that geoid height changes as a result of secular phenomena over geodetic time scales of 100 years can be considered negligible at the 10 cm level. However, these studies did not adequately account for tectonic phenomena, such as stress waves, which would create additional noise at measurement sites. But, it is still considered valid for ocean dynamic studies to assume that the geoid is time-invariant over time scales of up to 50 years.

2.4.4. Reference System Requirements for Ocean Dynamics.

2.4.4.1. Preliminary Considerations.

With the introduction of satellite altimetry data into the information matrix available for quantifying studies of the circulation of the oceans, it is possibly an opportune time to review the requirements of reference systems for oceanography. The requirements for systems of reference in geodesy and ocean dynamic studies should be framed in accordance with the same requirements imposed on the definition of the geoid, i.e., 1 part in 10^8 . Techniques promising this precision are predominantly based on observations made on the surface of the Earth to extraterrestrial sources/transponders.

To date, the spatial precision with which a system of reference is defined in physical oceanography does not appear to be a crucial factor, being largely due to data acquisition from ship cruises lacking continuity in space and time. Precisions of the order 1 in 10^4 (approximately 0.5 to 1 km in horizontal position) appear adequate for monitoring the spatial variability of the ocean surface on a global

scale.

Global ocean circulation models published in the oceanographic literature (Reid 1961; Lisitzin 1974; Wyrтки 1975; Levitus & Dort 1977) are usually assembled from a series of sporadic surveys and each global model may use a different vertical reference level. The choice, therefore, appears to have a rather subjective basis as there is an inability to be able to define a unique system of reference (see Fomin 1964).

The role of purely geodetic techniques in remote sensing ocean dynamics is primarily that of providing values of sea surface departures from a datum level surface using the radar altimetry data. Geodetic techniques are able to circumvent the problem of making ad hoc assumptions such as the level of no motion, and possess the ability to determine absolutely the ocean circulation. It is possible to formulate a four dimensional, geocentric frame of reference for sub-surface ocean dynamics, in addition to providing information for modelling the dynamics of the surface layers of the ocean (Mather 1975a, 1978a).

The global oceans are a fluid system which vary over a broad range of space and time scales (see sub-section 3.4.1). Recent results from oceanographic experiments such as MODE and POLYMODE suggest that to be able to monitor the global oceans, with adequate resolution for forecasting abilities, requires measurements on the appropriate small spatial scales and long time scales - e.g., an eddy or current ring, such as seen in the Gulf Stream, may have horizontal extents of 300 km and move this distance in 30 days. Sampling of the oceans using satellite based instruments therefore provides the only viable proposition for achieving the necessary density and time distributions.

The requirement for determining changes in SST for monitoring ocean circulation is the definition of the radial component of the geocentric location of the instantaneous sea surface. This necessitates the definition of the geometry of the ocean geoid in Earth space. Here Earth space is defined as the space which has the same rotational and orbital motion as the Earth, with the rotational characteristics derived from a specified network of geodetic observatories .

With the exception of geodetic levelling, all procedures that can be used for position determinations to 1 part in 10^8 are related to the Earth's instantaneous axis of rotation, while ocean geoid determinations and measurements from orbiting satellites are related to the instantaneous geocentre. It is obvious then that a system of reference

related to the instantaneous axis of rotation of the Earth and the instantaneous geocentre is required for the stated accuracy standards.

Geodetic determinations of SST, as previously stated, should be at the ± 10 cm level if they are to play a useful role in defining oceanographic phenomena of interest. The signatures of oceanographic interest that are able to be detected at the present time by satellite altimetry are:

(i) intermediate period phenomena (between 10 and 100 days) such as eddies, short period currents, etc. Results can be found in a number of references - Huang et al. 1978; Douglas & Gaborski 1979; Leitao et al. 1979a; Mather et al. 1980; Gordon & Baker 1980; Cheney & Marsn 1980b; Coleman 1980; Wunsch & Gaposchkin 1980.

(ii) quasi-stationary phenomena - see Mather et al. (1979b).

This sub-division lends itself to the following discussion on the need for reference systems in oceanography as the phenomena at (i) would best be studied over regional areas and the quasi-stationary component would usually be viewed on a global basis.

2.4.4.2. Global Requirements.

Geodetic reference systems must be able to define vertical position without ambiguity at the $\pm 1-2$ cm level for ocean circulation studies over long periods of time. On the assumption that adequate 10 cm tracking systems are available, it is necessary to model the phenomena listed below to meet the cited accuracy level :

- (1) the effect of plate motions on tracking station coordinates,
- (2) the radial deformation of the Earth due to Earth and ocean tides,
- (3) the motion of the geocentre in relation to the network of tracking stations (see Stolz 1976a, 1976b; Stolz & Larden 1979 for estimates of geocentre displacement),
- (4) models for polar motion, precession and nutation, and
- (5) the relation of Cartesian coordinate systems, based on the instantaneous axis of rotation in Earth space, to an inertial reference system.

A proposal for handling these problems has been described in Mather (1974c). Such a proposed system requires an absolute frame of reference in four dimensions.

However, considerations of a four dimensional system of reference for ocean dynamics are not attempted in this thesis since the remote

sensed data available for analysis does not warrant the sophistication of these concepts. Nor is it envisaged to be necessary, in the foreseeable future, at least not until remote sensing of ocean surface circulation on a quantitative basis has become a reality.

It is therefore proposed that an inertial, three dimensional, Cartesian coordinate system be used over a defined epoch (usually a satellite mission) for future global studies. One such geocentric reference system, commensurate with orbital analysis processing and entirely adequate for ocean dynamic requirements, is a Cartesian coordinate system X_1 , with the X_3 axis passing through the CIO pole and the X_1X_3 plane being that of zero longitude, implicit in the system of time maintained by the Bureau International de l'Heure. The CIO pole is defined as the mean position of the Earth's pole of rotation for the epoch 1900.0 to 1905.0 .

The radial component of the orbital position needs to be defined at the 10 cm level since any errors will directly affect the SST values. A network of at least 25 globally distributed, laser tracking stations is desirable to obtain the necessary information for SST determinations (Mather 1974b). In practice, however, the realisation of a system of reference for global circulation studies is only as good as the available tracking data provided the geodetic concepts outlined above are enforced. A major problem in the determination of a global field of SST is the lack of tracking coverage with adequate precision. Present coverages are banded in latitude, being from $\pm 65^\circ$ for GEOS-3 and $\pm 72^\circ$ for SEASAT-1 . Compounded with this is the fact that the determination of SST by geodetic means has the problem that none of the data observed at the surface of the Earth are related to the geoid to better than $\pm 1-2$ m . Thus, formulations of the GBVP have to overcome the problem of making unwarranted assumptions about the magnitude and distribution of the SST.

Improved geopotential models, with resolutions at wavelengths short enough for practical significance in ocean dynamic studies (at least 500 km), are not envisaged in the near future. The desired resolution may be attained from the planned GRAVSAT mission due for launch in 1984. The present resolution of the latest Goddard geopotential model, PGS-4, that used 10 cm laser tracking data and altimetry data in its compilation to degree and order 30, appears to have an rms radial accuracy of the order ± 70 cm (Lerch et al. 1980) .

2.4.4.3. Regional Requirements.

To quantify ocean surface circulation, the basic Lagrangian equations of motion can be established in relation to coordinate systems rigidly connected to Earth space (Mather 1976). Over regional extents, such as the Gulf Stream area, the non-tidal dynamic equations at the air/sea interface can be represented conveniently in a local, topographic Cartesian coordinate system for any circulation studies (Coleman 1980).

In studying the temporal variations of the short wavelength SST, such as the movement of eddies and the main current axis, assertions about the nature of the geoid are not required as the prerequisite of needing a high precision geoid is avoided. Solution techniques, such as those set out in Chapter 6, have been based on the assumption that the long wavelength orbital errors may be removed by a first order polynomial and wavelengths of interest in the SST may be recovered without any difficulty. However, only limited parts of the spectrum of ocean phenomena can be viewed using these techniques.

If the quasi-stationary component of the SST is required for determining the basic geostrophic motion, problems of having an adequate 10 cm geoid are still present and to date no definitive studies have been made without speculating as to the nature of the errors in the SST.

In conclusion, it seems at the present time that to proceed with ocean dynamic studies of a definitive nature, analysis is restricted to regional areas in which local Cartesian coordinate systems are suitable for these studies.

2.5. Determination of SST for Ocean Dynamic Studies.

In classical formulations of the GBVP, the solutions purport to determine the shape of a bounding surface at which the measurements were made. This involves the combination of results from geodetic levelling, to determine the normal or orthometric height, and gravimetric computations to define the height anomaly or geoid height. However, with satellite altimetry observations in ocean areas and three dimensional position determinations from observations to satellites, the geometry of the Earth's surface can be easily defined at the sub-metre precision.

For ocean dynamic applications, the situation is somewhat

different in that it is required, in concept, to determine the shape of a level surface (the "geoid") in ocean areas where no direct measurements have been made in relation to it. Thus, procedures need to be found to obtain the SST from solutions of the GBVP without making any assumptions as to the nature of the SST.

The major task to be tackled initially is the definition of the dynamic SST, ζ_s , through wavelengths of interest for quantifying dynamics of the surface layer of the oceans. It is considered appropriate to investigate ζ_s in five distinct constituents, due to the nature of the oceanographic time-space scales and the present resolution of gravity field models, according to the relation

$$\begin{aligned}\zeta_s &= (\zeta_{ql} + \zeta_{nl}) + (\zeta_{qs} + \zeta_{ns}) + \zeta_t \\ &= \zeta_{sl} + \zeta_{ss} + \zeta_t\end{aligned}\tag{2.52}$$

where the subscripts have the following significance:

- (1) Primary - q is the time invariant or quasi-stationary component,
n is the non-tidal temporal component, and
t is the tidal component.

- (2) Secondary - ℓ represents long wavelength contributions, and
s represents the shorter wavelength contributions.

Contributions of long wavelength (ζ_{ql} and ζ_{nl}) are the components of the SST with wavelengths longer than those in the Earth's gravity field which perturb the altimeter-equipped spacecraft by amounts greater than the noise level of the tracking systems available. This limiting wavelength (\bar{l}) is estimated at about 1000 km for satellites having altitudes of the order 800 km and being tracked by a global network of 10 cm tracking stations. The short wavelength components (ζ_{qs} and ζ_{ns}) represent the SST components with wavelengths shorter than \bar{l} .

A formulation of the GBVP for recovery of the long wave features of the SST, considered to be a more recoverable part of the SST spectrum in the first instance, is outlined in Chapter 5. Attempts to obtain ocean dynamic information of the SST spectrum with wavelengths less than 1000 km are given in Chapter 6. The recovery of ocean tidal information using satellite altimetry has been investigated in Chapter 7.

3. ON THE PROSPECTS FOR REMOTE SENSING.

3.1. Introduction.

The possibilities for making global observations from satellites of the surface of the ocean for oceanographic studies were proposed some 10 years ago (Kaula 1970). However, it has only been in the past several years that the quality, type, and amount of satellite data have allowed the process of acquiring information from spacecraft platforms to resemble true "remote" measurement. As a result, it is now possible under certain conditions to study the dynamics of the ocean surface. Ocean dynamics is concerned with circulation and the physical state of the ocean surface in which fluxes of momentum, moisture and heat acting at the air/sea interface primarily drive the dynamic processes. The surface manifestations of these energy couplings between the atmosphere and oceans are the observable quantities, from spacecraft sensors, that are required to formulate information on ocean dynamics in conjunction with in-situ measurements. This Chapter looks briefly at the satellite sensors available for the task of extracting parameters of interest for ocean dynamic studies and reviews some of the results from satellite missions. Information is specifically directed at prospects of remote sensing phenomena on a planetary scale, corresponding roughly to the large scale circulation in the ocean and its variability. Detailed oceanographic information on the dynamics of the areas to be studied using satellite remote sensed data has been set out in Sections 4.2 and 4.3.

The relevant general objectives, set out at the Williamstown Meeting (Kaula 1970), for the application of space techniques to solid Earth and ocean dynamics studies were:

- (i) measurement of spatial variations of the geoid to ± 10 cm,
- (ii) measurement of MSL on a global basis to ± 10 cm,
- (iii) measurement of the time variations in the geoid to ± 5 cm.

In 1972, the National Aeronautical and Space Administration (NASA) put forward a comprehensive program which had, as one of its goals, the use of satellites for the collection of information which would lead to an improved understanding of ocean dynamics (NASA 1972). This Earth and Ocean Dynamics Applications Program (EODAP) set out a number of major Applications objectives, with those relevant to the study of ocean

dynamics being:-

- (i) development and validation of means of predicting the general ocean circulation, surface currents, and their transport of mass, heat and nutrients;
- (ii) development and validation of methods for synoptic monitoring and predicting of transient surface phenomena, including the magnitudes and geographical distributions of sea state, storm surges, swell, surface winds, etc with the emphasis on identifying existing and potential hazards;
- (iii) refinement of the global geoid.

Some aspects of (i) and (ii) are discussed in Chapters 6 and 7 with reference to the GEOS-3 altimetry data available. The results represent some of the first obtained in which altimetry data were used to recover surface ocean dynamic information. Some theoretical considerations of (iii) are given in Chapter 5.

The basic objectives set out above are still to be met but much progress has been made in the intervening years. A number of review papers related to satellite sensing of ocean surface dynamics have been published covering a broad range of aspects (Apel 1972,1976,1980; Hanson 1972; Szekiolda 1976; Schanda 1976; Maul 1977; Stewart 1978; Huang 1979; Gower 1980). Some of these aspects will be mentioned in the following sections.

Remote sensing instruments may be either active or passive sensors. However the basic problem of remote sensing techniques lies in the fact that all observations are made at the surface of the ocean or within a thin layer at the surface. The actual surface of the ocean involved in the interaction of electromagnetic energy depends on skin-depth. In the infra-red (IR) region of the spectrum, this skin-depth is of the order tens of micrometers (McAlister and McLeish 1969), for visible regions tens of meters and in the microwave region several centimeters.

This limitation of sensing only the surface layer appears restrictive at first glance but in fact the measurements are valuable since nearly all the dynamic processes in the oceans are controlled by the boundary conditions at the air/sea interface. Of secondary importance to ocean circulation is the oceanic convection arising from small variations in water density - namely, thermohaline currents. The present understanding of upper ocean dynamics has been adequately summarized in texts such as Stern (1975), Phillips (1977), Kraus (1977)

and Monin et al. (1977) and therefore no quantitative details are set out in this Chapter.

The principles of remote sensing are based on the different responses of a given sensor to the ocean surface changes. It is convenient to subdivide these changes into two types:

- (i) Geometric - changes in the surface relief of the oceans resulting from a number of sources such as geostrophic adjustments of the density field in current systems such as the Kuroshio, Gulf Stream; tides; large frontal movements; surface waves of various wavelengths generated by wind interaction.
- (ii) Physical Properties - changes in the physical characteristics of the ocean environs such as temperature and salinity changes caused by current movement; water colour changes due to variation of water masses or sediment content.

Given that these surface changes have been converted from the satellite engineering units to plausible geophysical parameters via adequate theoretical algorithms (see Hayne et al. 1977 and Stanley & Dwyer 1980 for GEOS-3 sensor algorithm descriptions), a number of techniques are available to monitor the ocean surface changes. The most important of these various techniques, used on the GEOS-3, SEASAT-1 and NOAA environmental satellites, involve the analysis of the following signals:

- (1) Radar ranging,
- (2) Return radar waveform,
- (3) Backscattering strength; and
- (4) Radiation strength.

A full description of these measurement techniques and the specific sensors are given in the next section. It should be noted that each sensor may give information on more than one data type.

The following basic data types are assessed to provide the only basis for the synoptic monitoring of the oceans, on both global and regional scales, in the foreseeable future: (1) Distance from the spacecraft to the ocean surface sampling a finite element of surface area (footprint) estimated at having 2-12 km sides, using a pulse-radar altimeter, (2) The small scale roughness of the ocean surface on either side of the groundtrack as measured by a microwave scatterometer giving wind vector estimates, (3) The thermal emission of the oceans sensed by an infra-red (IR) and visible radiometer, over finite footprints of

about 5 km square, (4) An imaging radar which scans off nadir to provide data on ocean wave spectra, (5) Ocean surface temperature and wind speed estimates based on microwave radiometer measurements.

It is therefore of interest to look more closely at these sources of data to clarify a number of points related to the usefulness of remote sensed data for ocean dynamic studies. The points to be noted are the likely resolution of each data type, the oceanographic feature of interest sensed by the different spacecraft instruments, and the possible limitations when attempting to infer ocean dynamic behaviour at the air/sea interface.

3.2. Satellite Sensor Instruments.

The five instruments mentioned above, the radar altimeter, microwave scatterometer and radiometer, visible and IR radiometer and the synthetic aperture imaging radar (SAR) are evaluated in terms of their accuracy and contribution to oceanographic information. The radar altimeter is analysed in some detail as the data from this sensor is used exclusively in this thesis to extract ocean dynamic information. Data from other sensors are used to verify the altimeter results. A description of the other sensors is also given below as well as results of the individual sensor's performance pertaining to the recovery of ocean dynamic information.

3.2.1. Radar Altimeter.

Initial assessments of the application of radar altimeters to oceanography were made by Greenwood et al. (1969a; 1969b) and a history of radar altimetry is given by McGoogan et al. (1974). To date, three separate generation satellite radar altimeters have been flown onboard satellite missions. The first altimeter experiment was carried out from mid 1973 to February, 1974 during the Skylab SL-2, SL-3 and SL-4 missions. The Skylab S-193 altimeter was an initial test design, primarily for obtaining radar measurements for designing an improved altimeter before the launching of the Geodynamics Experimental Ocean Satellite (GEOS). GEOS-3 was launched on April 9, 1975 and carried the first globally applied altimeter system designed for oceanographic purposes. The third generation altimeter was launched onboard SEASAT-1 on 26 June, 1978 as part of an ocean dedicated satellite instrumentation

system and represented the first attempt to achieve 10 cm precision from orbit.

3.2.1.1. Altimeter Design.

Early contributions to the mathematical modelling of the received radar waveform are given in Moore & Williams (1957) and Godbey (1965). The potential of pulse-limited radar altimeters for measuring ocean waveheight has been discussed in detail by numerous investigators (Barrick 1972; Miller & Hayne 1972; Shapiro et al. 1972; Walsh 1974). Walsh et al. (1978) evaluated the performance of a pulse-limited altimeter from measurements onboard an aircraft at a 3 km altitude, following the results from the GEOS-3 mission. cursory details of the design fundamentals of the altimeter are discussed below but further information is available in the stated references.

Radar altimeters onboard low-orbiting satellites (altitudes of approximately 800 km) have the capability of measuring the mean height of the ocean surface, the roughness of this surface and the ocean waveheight. A pulse is transmitted from the satellite and is radiated in a spherical shell whose intersection with the ocean surface defines an instantaneous illuminated area or footprint. The footprint size is a function of the antenna beamwidth and satellite altitude and a comparison of these parameters for the three generation altimeter designs, as well as other altimeter design parameters is given in Table 3.1.

Detailed studies of the measurement of the ocean reflected pulse shape from radar measurements were made by Shapiro et al. (1972), Miller and Hayne (1972) and Barrick (1972). The latter two analyses used linear scattering theory of geometrical optics and assumed that the incident microwave energy was, on average, reflected back equally for all elements of the ocean surface. This is not quite the case as the troughs of ocean waves tend to reflect more strongly than do the crests, causing a height bias of the order of 5% of the significant waveheight (SWH) (Jackson 1979). SWH, denoted as $H_{1/3}$, is the average of the heights from crest to trough of the one-third highest waves in a long sequence of waves observed at a point. The SWH is related to the SSH standard deviation (σ_{SSH}) by the relation $\sigma_{SWH} = 4\sigma_{SSH}$ (Neumann & Pierson 1966, p.351)

Under the assumption of uniform reflectivity, the actual shape of

Table 3.1.

A Comparison of Altimeter Parameters

	Skylab	GEOS-3 (intensive)	SEASAT-1
Mean Altitude (km)	435	840	800
Mean Inclination (°)	50	115	108
Antenna Beamwidth (°)	1.5	2.6	1.6
Frequency (GHz)	13.9	13.9	13.5
Pulsewidth -uncompressed	10 ns	1.2 μ s	3.2 μ s
Pulsewidth -compressed	10 ns	12.5 ns	3.125 ns
Repetition Frequency (Hz)	250	100	1020
Footprint Diameter (km)	8	3.6	1.7
Altitude Precision (rms)	< 1 m	< 50 cm	< 10 cm
Sample & hold gates	8	16	60
Peak RF Power (kw)	2	2	2.5
Average RW Power (W)	0.05	0.24	6.5

the return waveform is proportional to the area of the footprint at any given time. For the simplified case of a quasi-calm sea, the return waveform shape will approximate a ramp function. With increasing waveheight, the rise time of the step is lengthened and assuming Gaussian statistics apply for the SSH and transmitted pulse shape data, the average return waveform can be modelled as a repeated convolution of three functions, two of which describe the ocean surface features with the third representing altimeter effects (Walsh 1979). The first of these functions is the average impulse response of the quasi-calm, "flat" sea as mentioned above. The second function involved is the radar-observed SSH probability density function or ocean surface roughness function. The system point-target response is the third term, which incorporates the altimeter waveshape, as sampled at the receiver by the waveform sample and hold gates, and tracking jitter effects on the return waveform.

Non-Gaussian ocean wave statistics for the reflection of radar pulses from the sea surface have been put forward by Jackson (1979). The theory predicts, for non-linear seas, that the net impulse response at vertical incidence is approximately given by the waveheight probability density function with the mean displaced below the true MSL. The amount of displacement is equal to the waveheight skewness coefficient times the rms SSH (σ_{SSH}) and is on the order of 20% of σ_{SSH} . This result confirms the observed negative sea state bias first determined from observational evidence by Shapiro et al. (1972) .

The fundamental design of the altimeter system is given in Figure 3.1 showing the instrument processor involved. The basic parameters measured by the radar altimeter are the two way ranging between the radar and the ocean surface, the pulse-by-pulse waveform shape, and the peak power returned. There are four parameters that need to be resolved in order to determine the leading edge of the averaged returned waveform (Fedor et al. 1979). The leading edge is of prime importance for distinguishing the basic measurements of altitude and waveheight. The required parameters are the mean time of returned signal arrival from which the altitude is derived, the rise time of the leading edge from which SWH is estimated, the plateau amplitude of the waveform, and the average noise level (jitter).

The altitude of the altimeter above the instantaneous electromagnetic mean sea surface (IEMSS) is determined by measuring the time interval between the transmission and reception of the radiated

Altimeter Measurements

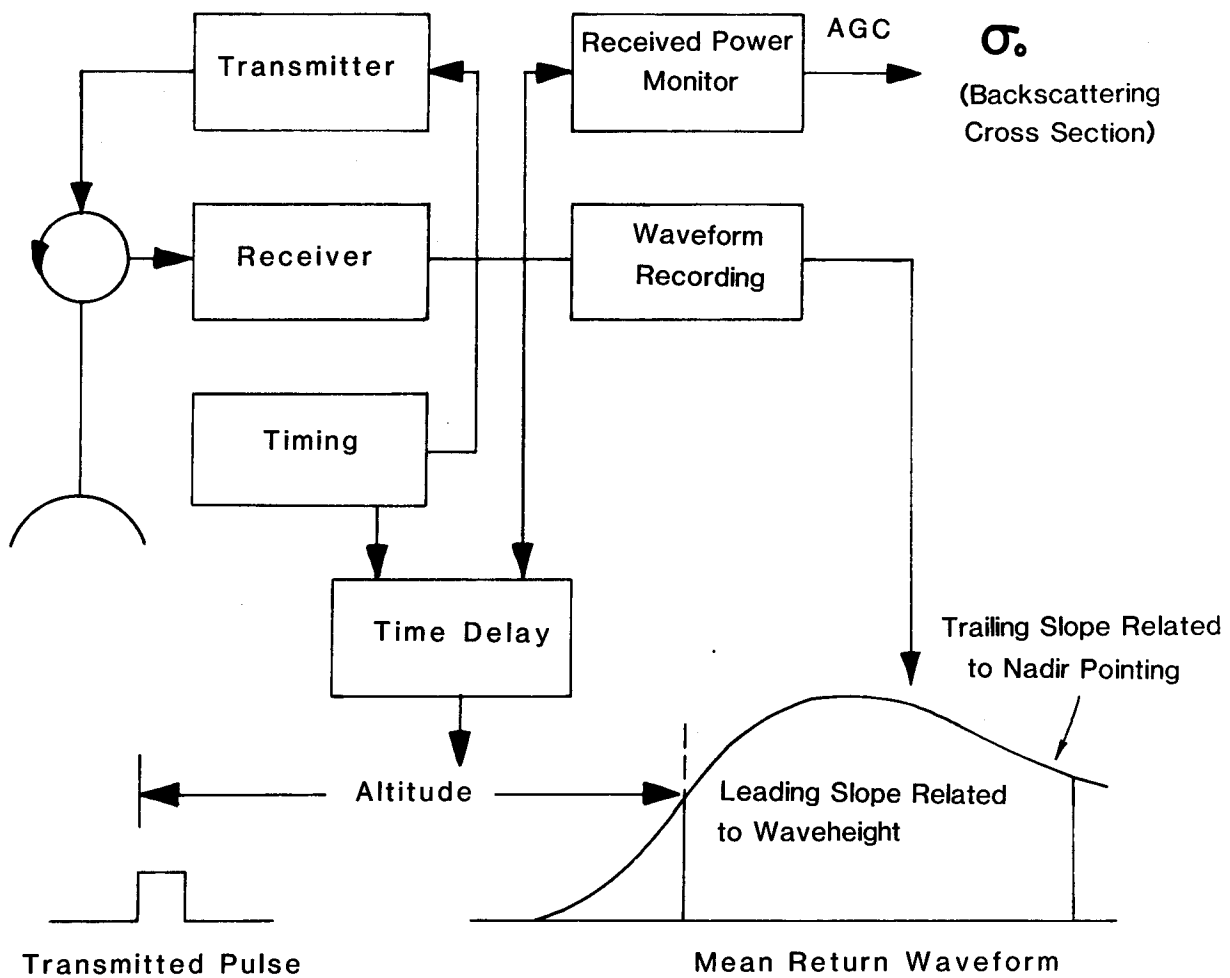


Figure 3.1

(from Tapley et al., 1979a)

pulse allowing for the internal time delay of the pulse propagation from transmitter to antenna and back to receiver and taking into account the shape of the leading edge of the returning pulse. The altimeter's repetition frequency sets the number of pulses emitted per second (see Table 3.1). The IEMSS can be related to the MSL if the relationship between the radar mean return point and the mean sea height is known, i.e. the SWH (see paragraph 3.2.1.2 for more details).

The SWH is estimated from the average pulse shape using information on the leading edge discriminated by the sample and hold gates of the backscattered waveform recorder. For complete details of SWH estimation, see Rufenach and Alpers (1978), Miller & Priester (1978), Gower (1979), Priester & Miller (1979) and Parsons (1979). It is also possible to infer surface wind speeds using the surface scattering cross-section per unit area at normal incidence, denoted σ_0 (Brown & Curry 1977; Brown 1979). The higher wind speeds result in a rougher surface and an attendant lowering of the backscatter cross-section.

For the GEOS-3 altimeter, six different algorithms were tested for extracting SWH data and a comparison of results is given in Fedor et al. (1979). It was concluded from these studies that for 1 sec averages, with SWH's in the range 4 to 8 m, the accuracy of the altimeter was ± 50 cm or 10% of the SWH, whichever was larger. The SEASAT-1 altimeter has improved altimeter design aspects to satisfy the specified 10 cm accuracy requirement. The general design characteristics are discussed and an initial assessment of the altimeter's performance is given in Townsend (1980). Hayne (1980) gives a detailed description of the return waveform analysis procedure for the SEASAT-1 altimeter.

The receiver automatic gain control (AGC) is necessary to normalise the mean detected return pulses for acquisition and tracking. The AGC voltage is a source of information on the reflectivity of the ocean surface, which can be related to wind stress (Hammond et al. 1977) and rain cells (Parsons 1976).

3.2.1.2. Altimeter Geometry.

The basic altimeter measurement can provide estimates of the height anomaly, ζ , but there are potentially a large number of sources of error that could influence the accurate determination of this

latter quantity. The majority of the possible corrections to reduce the raw altimeter measurement to an accurate ζ estimate are indicated in Figure 3.2. These "corrections" are:

(1) Geometric distance - the distance between the centre of gravity of the satellite and the antenna electrical centre. This correction is a constant and thus will have no influence on determinations of the temporal variations in the ocean. The only effect that this correction will have is on determinations of the shape of the global MSL (Mather & Rizos 1979), i.e. the value of W_0 . In the case of GEOS-3, this correction was estimated as 3.55 m (Martin & Butler 1977) and for SEASAT-1, the centre of gravity correction was 6.04 m (Tapley et al. 1979a).

(2) Propagation Effects - corrections need to be applied to the altimeter measurement due to tropospheric and ionospheric refraction effects. The transmission time of the altimeter signal is lengthened by passing through the atmosphere. For a nadir pointing satellite, the total refractive error due to propagation through the troposphere is approximately 2.3 m (Dickinson et al. 1970). The major portion of this correction is due to the dry tropospheric error, the wet tropospheric error being about 10% of the former. At the frequencies operated onboard GEOS-3 and SEASAT-1 (see Table 3.1), the refractive bias at zenith, due to ionospheric effects, is below 10 cm (Dickson et al. 1970). The tropospheric corrections will vary according to fluctuations in the surface pressure field but these errors can be held at the 10 cm level if monthly averages of surface pressure are used (Goad & Martin 1977). Global ionospheric models are sufficient to reduce the ionospheric effects to the centimetre level. There are also ionospheric and tropospheric refraction effects on the satellite orbit since the tracking measurements propagate through the atmosphere. This has been discussed by Goad and Martin (1977) and it is usual for models to be used in the orbit analysis to account for these effects.

(3) Attitude correction - this alias has been largely catered for since the spacecraft is stabilized to within $\pm 1^\circ$ of the vertical and the returned altimeter waveform is discriminated onboard the satellite, by the waveform recorder, for the trailing slope of the returned signal (see Figure 3.1). Some problems will occur, however, for very rough seas.

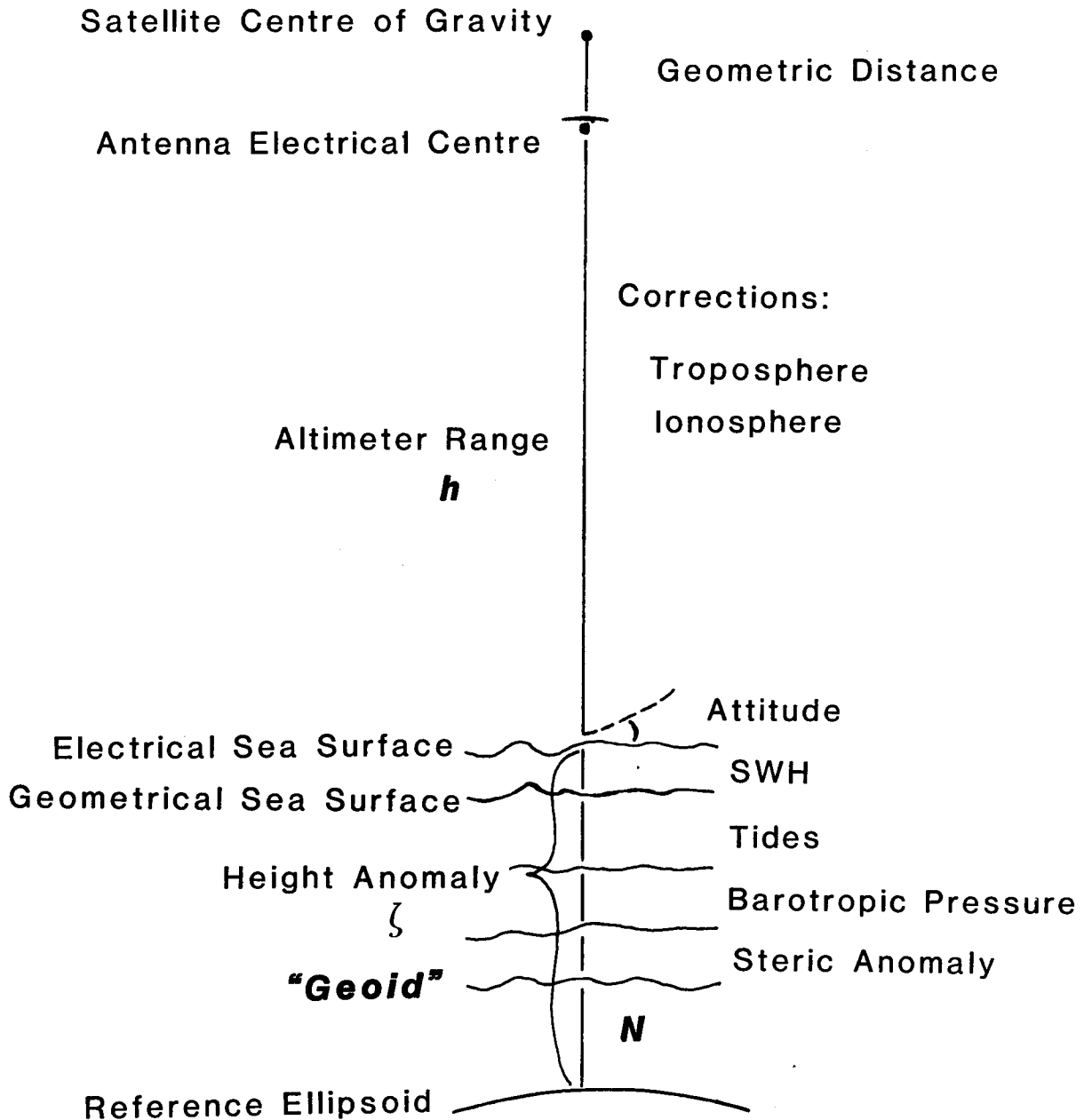
(4) SWH - this correction is required to relate the IEMSS to the geometrical sea surface. The slope of the leading edge of the returned

waveform determines the height of the waves and consequently the SWH (see paragraph 3.2.1.1 for more details). However, the bias caused by more energy being reflected from the wave troughs than wave crests is required for high precision ocean dynamic studies. As stated above the bias is of the order of 5% of the SWH (Jackson 1979). For very rough seas, the SWH is about 3 m (Barrick 1972, Table 12.1)) giving a bias of about 15 cm. This correction must always be subtracted from the altimeter measurements. It is considered however, that the process of averaging over, say, monthly time scales and at the resolution of the GEOS-3 altimeter ($\pm 20-30$ cm), the SWH bias term can be neglected at the present time.

(5) Tides - the altimeter measurement will contain the signature of the total geocentric tide (ocean tide plus the body and loading tides) as the surface responds to tidal influences. Reference is made to Figure 7.2 to see the effect of the body and loading tides on the altimeter measurements. The altimeter measurement can be corrected for the ocean tides using empirical models (e.g., Schwiderski 1980) at about the 10 cm level and for the body tide and ocean load response via equations 7.23 and 7.24 respectively. At the present time, tidal elevations cannot be determined from altimetry data with adequate precision, as discussed in Chapter 7, but the possibilities exist in future years for this to be achieved. The correction for tides has not been applied in the development set out in Chapter 6 as much of the tidal information in the open ocean is of long wavelength, and is thus largely removed when invoking corrections for tilt along an altimeter profile. The tidal signature is also reduced by taking averages in an $n^\circ \times n^\circ$ square over the period of interest when constructing the regional surface models (see sub-section 6.2.2).

(6) Atmospheric Pressure Effects - the ocean surface may respond isostatically to variations in the atmospheric pressure, usually referred to as the "inverted barometer" effect. This effect has been defined by Lambeck (1980) as "the increase in the atmospheric pressure, over and above the mean pressure over the entire ocean surface" and its magnitude is taken as an increase (decrease) of 1 cm of the ocean surface for a decrease (increase) of 1 mbar in atmospheric pressure. Pressure variations account for about 6% of the total sea level variance (Wunsch 1972). However, studies by Hamon (1962b, 1966) indicated that the barometric factor (sea level change/atmospheric pressure change) was less than 1 on the east coast of Australia and greater than 1 on the

Satellite Altimeter Geometry



(from Tapley et al., 1979a)

Figure 3.2

west coast. Robinson (1964) proposed an explanation based on the theory of shelf waves but Crepon (1973) suggested that the mechanism responsible for this effect was geostrophic adjustment of the ocean surface. Along individual profiles, the atmospheric pressure correction would appear largely as a constant bias and would be removed in the processing discussed in (5). Thus, no correction has been made for the atmospheric pressure response.

For quantitative ocean dynamic studies, the above corrections can be sufficiently modelled or neglected at the 10 cm level. Most of the corrections have been taken care of in the altimeter data pre-processing. The terms that need attention for ocean dynamic studies are the SWH bias and the tidal effects. No mention has been made here of the orbital errors which influence the position of the satellite and hence the radial altimeter measurement. Orbital errors for the GEOS-3 satellite are discussed in sub-section 7.3.3.

3.2.1.3. Altimeter Measurements.

The major attraction of satellite remote sensing instruments such as the altimeter is the potential ability of these systems to provide useful, new quantitative information about the ocean and its surface circulation over spatial and time distributions impossible to duplicate by conventional means. The type of information that can be extracted from the mean altimeter return waveform for ocean dynamic studies has been mentioned in paragraph 3.2.1.1. In summary, these direct and indirect measurements are:

- (i) the altitude of the satellite above the ocean surface,
- (ii) SWH estimates, and
- (iii) ocean surface roughness and surface wind speed.

The altimeter has also been applied to remote sensing of land and sea features (Miller 1977) and monitoring continental ice sheets (Brooks 1979).

The relative accuracy of the altimeter has improved by an order of magnitude since the Skylab mission where the resolution was approximately ± 60 cm (McGoogan et al. 1974). Results for the GEOS-3 mission, using overlapping pass analyses, suggested levels of $\pm 20-30$ cm for the altimeter repeatability (see Chapter 6). Initial results for the SEASAT-1 altimeter (Tapley et al. 1979a; Townsend 1980; Brammer & Sailor 1980) give accuracy estimates of about ± 10 cm, in accordance

with the original performance requirements. The SWH estimates from SEASAT-1 are reliable at the ± 50 cm level for a SWH range of from 1 to 20 m (Tapley et al. 1979a; Townsend 1980). The estimation of surface wind speed, from the GEOS-3 altimeter data, gave a precision of 2.6 m/sec for winds in the range 1 to 21 m/sec (Brown 1979).

The accuracy estimates, from both the GEOS-3 and early SEASAT-1 results, suggest that the altimeter data has reached a level of precision that makes possible its use for quantitative oceanographic investigations. Western boundary currents and eddy features should be discernable with the altimeter resolution at the 30 cm level. If the measurement accuracy is at the 10 cm level, measurements of global tides and the variation in position and strength of the strong western boundary currents becomes possible. However, as mentioned in Chapter 2, it is essential that independent determinations of the geoid at the 10 cm level are obtained for these analyses to be viable. Since there exists, at the present time, no independent measurement of the geoid comparable in accuracy to the satellite measurements, except perhaps in the North Atlantic area, only variable oceanic features will be measureable on a global basis in the near future.

If the measurement accuracy was at the 1-5 cm level, monitoring of the weaker ocean currents, such as the Equatorial currents would be possible. These altimeter measurements, when combined with conventional in-situ data describing the density field of the ocean, will allow calculations of the changes in mass transport of major ocean currents. This information will improve global calculations of the transport of heat and momentum by the oceans. However, this exciting prospect must await the prerequisite gravity field improvement to levels of 1-5 cm in the desired wavelengths.

3.2.2. Microwave Scatterometer.

Microwave scatterometers have been shown to be sensitive to ocean surface winds in previous aircraft test programs and the Skylab S-193 experiment (Grantham et al. 1975). The details of the scatterometer system outlined below relate to the design characteristics and performance requirements of the SEASAT-1 scatterometer.

3.2.2.1. Scatterometer Design.

The SEASAT scatterometer system is a microwave radar designed primarily to provide global measurements of the ocean surface wind vectors, but the sensor also provides measurements of ocean surface roughness. The physical basis for this system is the Bragg scattering of microwaves from the ocean surface in the capillary wave spectrum. The strength of the returned backscatter (σ_0) is proportional to the capillary wave amplitude, which in turn is proportional to the wind speed near the ocean surface. At the operating frequency of about 14.6 GHz, the return radar signals are most sensitive to ocean waves with wavelengths of 2-5 cm. Since the radar backscatter is anisotropic, wind direction can be derived from scatterometer measurements at different azimuths.

The sensor design incorporates four dual polarized antennas which produce a star-like pattern of illumination on the Earth. With both forward and aft-looking antennas on either side of the spacecraft, two independent radar measurements at the same location can be obtained. The antenna beams are oriented 45° relative to the sub-satellite groundtrack giving observations separated by 90° in azimuth. The location of the ocean surface area corresponding to a given processed return pulse is determined by timing (the antennas are pulsed sequentially) and doppler measurements. Twelve doppler filters are used to electronically subdivide the antenna footprint into resolution cells approximately 50 km x 50 km. The spatial extent of the footprint is from 200 to 950 km, on each side of the sub-satellite track, for incidence angles of between 25° to 65° .

A radio path attenuation correction for the atmospheric conditions of liquid water and water vapour must be made to the backscatter measurement. These can be made using standard meteorological atmospheric estimates or using the microwave radiometer data (see sub-section 3.2.3).

In addition, backscatter σ_0 values over a 140 km footprint under the satellite nadir point are measured providing surface wind speed and surface roughness measurements. The range in wind speed over which the scatterometer can provide wind vector measurements in the desired accuracy limit is from 4 to 28 m/sec.

3.2.2.2. Scatterometer Measurements.

Wind speed is determined from the σ_0 values taken by the two antennas located on either side of the spacecraft, separated in azimuth by 90° . Having obtained wind speed values, individual forward and aft antenna data can be used to derive wind direction values. Precision requirements for the scatterometer were ± 2 m/sec for wind speed and wind direction to $\pm 20^\circ$ (Grantham et al. 1976). These requirements appear to have been satisfied as indicated by preliminary analyses of the SEASAT-1 scatterometer data (Linwood Jones et al. 1979).

3.2.3. Microwave Radiometer.

A microwave radiometer is a passive sensor which measures all incident electromagnetic radiation in selected regions of interest on a nearly all-weather basis. Such measurements at different frequencies can be used to provide data on temperature and salinity (about 2-6 GHz), wind speeds (1-5 GHz from foam covered seas, 19 GHz from foam and surface roughness), sea ice (around 35 GHz) and atmospheric water vapour (around 21 GHz). The potential of using a radiometer system for the measurement of ocean surface temperature was indicated in Apel (1976). Initial microwave radiometer systems were tested onboard aircraft (Blume et al. 1978) and onboard the NIMBUS-5 and -6 satellites. An evaluation of applications of microwave radiometry to oceanography is given by Wilheit (1978) and Thrane (1978). Estimates of accuracy from these studies indicated that radiometric techniques, under favourable conditions, could measure ocean surface temperature to about 1°C , salinities to 1‰ and wind speeds to 3 m/sec. The latest radiometer system is the Scanning Multichannel Microwave Radiometer (SMMR) which was carried onboard SEASAT-1. This system is described below.

3.2.3.1. Radiometer Design.

A detailed description of the SEASAT SMMR design characteristics is given by Gloersen & Barath (1976). The SMMR is a ten-channel instrument delivering orthogonally polarised antenna temperature data at five microwave wavelengths, namely 4.55 cm, 2.81 cm, 1.67 cm, 1.43 cm and 0.81 cm corresponding to frequencies of 6.6, 10.69, 18.0, 21.0 and 37 GHz respectively. The sensor scans, for a period of about 4 secs, to

the right side of the satellite groundtrack at an incidence angle of 50° to the ocean surface. Swath width of the SMMR footprint is about 600 km with the smallest spatial resolution cell being 28 km x 18 km at the 0.8 cm wavelength (Njoku et al. 1978).

The radiation measured from the Earth's surface is the result of a complex function of the temperature, roughness and physical composition of the surface as well as the absorption, emission and scattering properties of the atmosphere. Temperature and salinity of the ocean effect the emission through their effect on the dielectric properties of sea water. The wind speed effects the emission in an indirect way through wind generated roughness and foam (Ross & Cardone 1974). However, the differing spectral properties of the various constituents makes it possible to separate the contributions to the observed emissivity, or so-called brightness temperature, by measurements at the above stated frequencies. Conversion of the raw radiometric readings to microwave brightness temperatures involves correcting for actual antenna patterns, including side lobe effects, as well as separating out the horizontal and vertical polarization components of each of the ten channels of radiometric data. These techniques have been well developed on earlier NIMBUS satellites (see Staelin et al. 1975).

3.2.3.2. Radiometer Measurements.

The SMMR sensor provides a basis for obtaining important oceanic parameters on a nearly all-weather basis. A limitation of the system described above is that the spatial resolution is somewhat coarse for some detailed oceanographic applications. However, the microwave radiometer can provide information on:-

- (i) ocean surface temperature and salinity,
- (ii) surface wind speeds,
- (iii) atmospheric content of water vapour and liquid water (clouds and rain), and
- (iv) sea ice boundaries and concentrations.

Target accuracies for (i) and (ii) are $1-2^\circ\text{C}$ for temperature and 2 m/sec for wind speeds in the range of 7 to 30 m/sec. Preliminary results of the SEASAT SMMR provide initial estimates of the quality of the measurements (Njoku et al. 1978; Lipes et al. 1979). Under varying meteorological conditions over open ocean areas, ocean surface

temperatures exhibited standard deviations of $\pm 1.5^{\circ}\text{C}$ and standard deviations for wind speed values were ± 3 m/sec when compared to surface truth data. These accuracies will improve with the sophistication of the present data processing algorithms used to convert the raw radiometric data to geophysical units.

3.2.4. Synthetic Aperature Radar (SAR).

The SAR is an active microwave radar made up basically of a pulsed transmitter, an antenna and a phase-coherent receiver. The sensor is designed to observe deep ocean waves, coastal wave patterns, polar ice and landforms. Preliminary studies of radar imaging of ocean surface features have been made by Brown et al. (1976). The SAR carried onboard SEASAT was the first sensor of this type to be used for oceanographic studies, the sensor having no space heritage beyond developmental work for Apollo 17. Details are given below of the design and measurement characteristics of the SEASAT SAR which was basically an experimental sensor for the mission.

3.2.4.1. SAR Design.

Complete descriptions of the design criteria and implementation of the SAR can be found in Thompson & Ladermann (1976) and Eaton & Munster (1977). Basically, the L-band radar (frequency 1274.8 MHz, wavelength 23.5 cm) transmits pulses of 33.8 μsec duration at the surface of the Earth via an antenna with a $1^{\circ} \times 6^{\circ}$ fan beam. The antenna is pointed 20° off nadir to the right side of the spacecraft illuminating a 100 km swath centred about 300 km from the satellite nadir point. The SAR has a 25m x 25m resolution over this swath. Radar reflections from the surface are collected by the antenna, then amplified and translated to S-Band telemetry frequency for transmission to a ground receiving station. This is required since the data rate of 20×10^6 bits/sec prohibits onboard recording. A typical pass of the SAR will produce a 100 x 4000 km image of the ocean surface.

The information sources required by the SAR are complicated. They include radar cross-section phase and phase rate, range and range rate for each resolution cell of the ocean surface. The SAR can function through clouds, nominal rain and day and night making it an "all-weather" sensor. However, because of the right-scanning antenna,

the SEASAT SAR scans from 75°N to 69°S latitudes giving a marginally different spatial coverage to the other sensors.

3.2.4.2. SAR Measurements.

The SAR senses surface effects of the ocean that are related to surface roughness. The surface roughness is, in turn, related to many different types of physical effects such as local wind, surface tension, and surface currents. The types of ocean phenomena that may be resolved by the SAR include:-

- (i) ocean swells and currents,
- (ii) surface wind changes,
- (iii) internal wave patterns, and
- (iv) sea ice conditions.

An evaluation of some uncontrolled SEASAT SAR data (Gonzalez et al. 1979) showed that ocean waves could be matched to within $\pm 15\%$ in wavelength and about $\pm 25^\circ$ in wave direction when compared to surface and aircraft measurements. This sensor is still very much in a developmental stage but could become the most important active microwave sensor with improved data processing capabilities.

3.2.5. Visible and IR Radiometer (VIRR).

3.2.5.1. VIRR Design.

The VIRR is again a passive device measuring the incoming radiation in two regions of the electromagnetic spectrum. The visible energy is detected at wavelengths of approximately 0.55 to 0.75 μm while the IR energy is detected by operating in the water vapour window (10.5 to 12.5 μm).

Detection of ocean currents in the visible wavelengths depends on the change of ocean colour and the change of sea state associated with the boundary as monitored by the observed radiance at the spacecraft sensor. In the 10.5 to 12.5 μm region of the electromagnetic spectrum, the ocean surface acts very nearly as a blackbody with emissivities greater than 0.99. Thermal radiation leaving the Earth's surface is modified by atmospheric absorption and emission. One consequence of atmospheric transmission, which restricts the full potential of VIRR

sensing is that ocean surface thermal gradients are decreased at satellite altitudes. At the wavelengths specified above the radiation cannot penetrate the clouds, therefore the VIRR is also restricted to cloud free times for useful oceanographic results.

In 1972, a very high resolution radiometer was introduced in the polar-orbiting satellites operated by the National Oceanic and Atmospheric Administration (NOAA). With the improved spatial resolution (about 1 km) and temperature sensitivity (about 1-3°C), ocean surface temperature fronts associated with current systems could be detected, e.g. Stumpf & Rao 1975; Legeckis 1977, 1979. The VIRR became the most established remote sensing instrument used by the oceanographic community even though the temperature measuring range (-90°C to +60°C) is too insensitive for some ocean dynamic applications.

Another source of remote sensed temperature data became available in 1974 with the launching of a Geostationary Operational Environmental Satellite (GOES). Although the spatial resolution from these geostationary satellites is coarser (about 8 km) than the NOAA polar satellites, useful analyses of oceanic features are still possible (e.g., Legeckis 1975; Maul et al. 1978).

In 1978, the NOAA satellite system was replaced by the next generation of NOAA polar orbiters, called Television Infrared Operational Satellite (TIROS) series. This system has the capacity for global spatial resolution of about 4 km and regional resolution of about 1 km. Data from TIROS-N are currently used to monitor the boundaries and eddies in the Gulf Stream region on a regular basis (see NOAA/NWS 1979).

The VIRR carried onboard SEASAT was originally built for the improved TIROS series. Hence, with the lower altitude of SEASAT and data rate limitations, the images generated by its VIRR are degraded by a factor of 2 in the IR region (10.5 to 12.5 μm) and by 4 in the visible region (0.49 to 0.94 μm) with respect to the full capability of the instrument (McClain & Marks 1979). Temperature sensitivity in the IR channel is accurate to 1.5°C and the footprint covers an area of about 2000 x 2000 km at the Earth's surface.

3.2.5.2. VIRR Measurements.

The principal measurement capabilities of a VIRR system are:-

- (i) to provide images of visual reflection and thermal IR

- emission from the ocean, coastal and atmospheric features;
- (ii) to provide derived quantitative measurements of ocean surface temperature and cloud-top height and type.

The VIRR scanners have been used to survey ocean fronts on a worldwide basis (Legeckis 1978). Usually the visible images are used to find cloud-free areas of the ocean, and the IR images are used to detect the ocean surface temperature fronts. When visible images are not available, it is possible to distinguish ocean surface temperature fronts from cloud pattern recognition and by the relative spatial stationarity of the fronts over periods of several days.

A number of features may restrict the usefulness of the VIRR images for playing a synoptic role in ocean dynamic studies:-

- (i) seasonal variability of the oceans related to changes in solar insolation and air/sea interaction. This means that during the summer months, nearly isothermal surface layers obscure the ocean temperature gradients which are known to exist at depth from hydrographic data. This ocean surface layer mixing is dominant between latitudes $\pm 35^\circ$.
- (ii) cloud cover obscures the ocean surface since IR radiation is absorbed by water vapour.
- (iii) atmospheric attenuation of the IR radiation through the atmosphere. The ocean temperature can appear to be 1° - 10°C lower at the satellite IR sensor than at the ocean surface. However, the relative distribution of ocean temperatures is preserved.

The planned performance level for the VIRR onboard SEASAT was for ocean surface temperatures to $\pm 2^\circ\text{C}$ over a resolution cell of 5 km. Preliminary analysis of SEASAT VIRR data (McClain & Marks 1979) shows that the instrument is adequate for the identification of cloud, land and water features. Ocean surface temperatures in cloud-free regions indicated standard deviations of $\pm 1.7^\circ\text{C}$ when compared to surface measurements.

3.3. Oceanographic Instruments.

A number of techniques have been developed over the last ten years which enable oceanographers to make measurements over spatial and time scales that cannot be reproduced using conventional ship surveys. The most important of these new technology systems is the use of thermal

IR imagery from the NOAA Environmental satellites or from the Synchronous Meteorological Satellite (SMS), or its operational equivalent, the GOES satellite. The IR imagery gives information on ocean features such as current boundary movements, detection of closed eddy features and upwelling/downwelling in coastal areas. The VIRR sensor has been discussed previously in sub-section 3.2.5 and will not be dealt with further.

The other sensors employed by oceanographers to provide "quasi-synoptic" data are:-

(i) Airborne radiation thermometer (ART): ART's, operating at bandwidths of 9.5 to 11 μm , can sense thermal differences as small as 0.1°C at the air/sea interface and have an absolute system accuracy of $\pm 0.2^\circ\text{C}$ taking into account atmospheric radiance corrections (Saunders 1970). This sensor provides virtually continuous information on ocean surface temperature along the flight path and can give sufficient information over regional extents for detailed analyses of current systems (Cheney 1977). However, the expense of carrying out these surveys restricts the use to special studies.

(ii) Free drifting buoys: The buoys are released from aircraft or cruise vessels and provide measurements of ocean surface and sub-surface temperatures, wind speed estimates, and current and eddy movements. The buoys are tracked by satellite, usually the NIMBUS series, and fixes are computed from the Doppler-shifted radio signal received by the satellite. Generally, two good fixes for the position of the buoy are obtained per day with positional accuracies of $\pm 1-2$ km. Several studies using these sensors have been reported by Kirwan et al. (1976), Richardson et al. (1977), Cresswell & Grieg (1979), Cresswell & Golding (1979), Cheney et al. (1980) and Richardson (1980). There are, however, several possible biases that may occur in the buoy data when used in highly variable, strong currents as indicated by Kirwan et al. (1975) and Cresswell & Garrett (1980). Problems occur in relating Eulerian and Lagrangian measurements in a complicated non-stationary field. Drifting buoys are cheaper than ocean mooring stations but the difficulty of maintaining a sufficient data density in all areas argues against their use for regular forecasting purposes.

(iii) Neutrally buoyant floats: These floats, placed at various depths from the ocean surface, are tracked acoustically from shore-based stations using SOFAR (Sound Fixing and Ranging) hydrophones (Rossby & Webb 1970, 1971). The floats record temperature ($\pm 0.05^\circ\text{C}$ rms), pressure

(± 5 dbar rms) and vertical current (to within 5%). They are designed to operate at depths of 1500 m and have a life span of about 1 year. Details of the float design are found in Rossby et al. (1975). Oceanographic results have indicated the float's usefulness for tracking eddies (Cheney et al. 1976) and monitoring current movements (Freeland et al. 1975).

(iv) Airborne Expendable Bathythermograph (AXBT): These instruments are deployed from aircraft and provide temperature profiles to depths of approximately 350 m. Sessions et al. (1976) describe the AXBT design characteristics and have shown them to give ocean temperatures to within $\pm 0.5^\circ\text{C}$. The AXBT probe takes only about 4 minutes to reach the 350 m depth restricting data coverage to small spatial and time scales compared to the satellite sensors described in section 3.2 .

The instruments briefly outlined give basic information on ocean surface and sub-surface temperature distributions, wind vector estimates, and current and eddy movements on reasonably synoptic scales over regional extents. The logistics and expense of using the above instruments for ocean dynamic forecasting is prohibitive.

A recent proposal for monitoring the mesoscale fluctuations in ocean areas over large scales has been given by Munk & Wunsch (1979). The technique, called ocean acoustic tomography, uses the measurements from acoustic transmissions to infer changes in the speed of sound through the ocean and then, by inference, the density structure of the ocean.

However, at the present time, the only realistic attempt at this problem can be made using satellite remote sensors with the advantage of using the oceanographic instruments for groundtruth studies.

3.4. Application of Satellite Data for Oceanographic Studies

The dynamic topography of the ocean surface is a relatively good indicator of the circulation of the surface layer of the ocean, as shown by numerous investigators (Reid 1961; Wyrcki 1975; Lisitzin 1974). Traditional oceanographic measurements have, however, only provided oceanographers with a smoothed representation of the ocean circulation due mainly to the non-synoptic nature of the measurements and also because of the assumptions of stationarity and geostrophy of ocean currents.

The use of satellite sensors to synoptically monitor the surface

layer of the ocean promises to provide data on sufficient time and spatial scales to quantify the classical picture of the world's oceans and provide information on its variability. However there are certain aspects that need to be addressed to ascertain the complete usefulness of the remote sensed data for studying ocean dynamics. Most importantly, consideration should be given to whether the time and spatial scales of certain oceanographic phenomenon can be recovered with the given satellite data coverage. The resolution in wavelength and magnitude of the satellite sensor will also restrict the oceanic features that may be studied. These details are discussed in the following sub-sections in terms of the primary remote sensed data used for analysis in this thesis, i.e. the GEOS-3 altimetry data, since this remote sensing instrument has the potential to provide the most quantitative information about the ocean and its circulation.

3.4.1. Oceanography Time-Space Scales.

The circulation of the world's ocean is a complex hydrodynamic system which varies both spatially and temporally over a large range of time and space scales. Preliminary global pictures of the ocean current variability were obtained by analysing surface drift currents in terms of their mean and eddy kinetic energies (Wyrтки et al. 1976) and further discussed by Düing (1978).

Regional studies, predominantly in the North Atlantic, have used hydrographic data (Bernstein & White 1974; Dantzler 1976a, Freeland & Gould 1976; Schmitz 1976, 1978; Luyten 1977) and geostationary satellite observations (Maul et al. 1978) to give information on the ocean time-space spectrum. These studies show that the maximum values of kinetic energy of the mean flow are found in western boundary current areas and minimum values are found in the interior of ocean gyres. Accumulating evidence suggests that the high eddy energies are associated with mesoscale, mid-oceanic eddies, which are fluctuating current cells extending throughout the water column (MODE Group 1978).

It appears that the mesoscale eddies play a dominant role in the dynamics of the ocean circulation, in a manner analogous to the mid-latitude atmospheric dynamics (Stommel 1965), i.e. the mesoscale eddies are the "weather" systems of the ocean. During the past decade, physical oceanographers have directed considerable effort to exploring and modelling mid-ocean eddies since their role in the general

circulation has emerged as a central problem in ocean circulation dynamics.

Progress in understanding the qualitative nature of the ocean variability and specifically the oceanic mesoscale eddy field has been made with the well-known mid-ocean dynamics experiment (MODE) and subsequent experiments such as POLYMODE and NORPAX. Some pertinent results from these studies may be found in references such as Richman et al. (1977), Wilson and Dugan (1977), Barnett et al. (1977), MODE Group (1978), and Schmitz and Owens (1980). General conclusions from these analyses indicate that superimposed on the mean circulation scale is an energetic time-space continuum that shows a remarkably complex spatial inhomogeneity with no clear distinction between particular scales.

Monin et al. (1977) have given a general classification of seven ranges for the time-space scale of ocean variability: (1) small scale phenomena, (2) mesoscale phenomena, (3) synoptic variability, (4) seasonal variations, (5) year-to-year variability, (6) secular variability and (7) century-to-century variability. Their Figure 1-4-1 gives a broad picture of the space-time spectrum of ocean temperature variations, showing times scales from 10^0 to 10^{12} secs and spatial variations of 10^0 to 10^{10} cm.

As mentioned in the next sub-section, the GEOS-3 altimeter has a wavelength resolution of about 30-50 km thereby limiting ocean dynamic investigations to those of planetary scale phenomena such as ocean eddies, western boundary currents, tides and equatorial currents. The satellite time-space scale distribution is further discussed in the next sub-section.

It has been shown that the length scales of planetary motions of the ocean should not be smaller than the Rossby radius of deformation R_0 , where (Pond & Pickard 1978, p.166)

$$R_0 = (g h \Delta\rho/\rho)^{1/2} / f \quad (3.1)$$

where g is the acceleration due to gravity,

$\Delta\rho/\rho$ is the relative vertical change in density,

h is the vertical distance over which this change occurs, and

f is the Coriolis parameter.

The time scale is given by the above length scale divided by the Rossby wave velocity, or

$$T_o = 2\pi R_m / (g h \Delta\rho/\rho)^{1/2} \quad (3.2)$$

where R_m is the mean radius of the Earth.

Using typical values in the global ocean for $(\Delta\rho/\rho)$ (see Monin et al. 1977, Chapter 2 and Section 5.2) and taking the depth (h) of the ocean as 4 km, then, at mid-latitudes, R_o is about 80 km and T_o is about 60 days. These figures give the relevant space and time scales for mesoscale eddies.

From the quoted references in this sub-section, a crude working time-space spectrum for three particular phenomena of interest has been derived. The estimates are set out below in Table 3.2 and illustrated in Figure 3.4 .

Table 3.2.

Guestimates of Time-Space Scales

Phenomena	Period (days)	Spatial (km)	Magnitude (cm)
Ocean Eddies*	20-400	10-300	20-80
Western boundary currents	10-40	200-700	50-200
Tides	< 1	500-10,000	10-100

*Includes mesoscale eddies (see MODE Group (1978) Section 1 for definition) and eddies associated with western boundary currents.

3.4.2. Satellite Time-Space Scales.

The orbital parameters of inclination and altitude set the spatial and time sampling scales of the satellite. The two-day groundtrack coverage for the GEOS-3 satellite is shown in Figure 3.3, where it can be seen that possible data acquisition is restricted between $\pm 65^\circ$ in latitude. GEOS-3 has an orbital period of 101.79 minutes which results in the groundtrack, on successive days, being offset by about 600 km at

the equator. Thus, an $n^\circ \times n^\circ$ grid is generated approximately every 25/n days. This satellite sampling rate is shown in Figure 3.4 together with the oceanographic time-space scales estimated in the previous sub-section. The estimated SEASAT-1 sampling rate is also indicated in Figure 3.4 .

It should be noted however that the satellite sampling rates shown in this figure are optimal, ie. it is assumed that the altimeter continuously samples the ocean surface over the time scale. This is definitely not the real situation as GEOS-3 did not have the onboard storage facilities to continuously measure to the ocean surface and thus, sampling distributions are irregular (see Mather et al. 1978b, Figures 4 to 7) .

It is obvious from Figure 3.4 that features above the satellite sampling rate line may be recovered. This means that for GEOS-3, a certain percentage of the ocean eddy and western boundary current spectra can be recovered but the major portion of the tides cannot be discriminated with the GEOS-3 time-space coverage. However since the periods of the tidal phenomena are known from astronomical considerations, it is possible to extract tidal information even with inadequate sampling periods.

Another point that needs to be noted in relation to Figure 3.4 is that it is also implied that the oceanic features are stationary. This generalisation can be accepted for western boundary currents and tidal variations over extended periods, but not for ocean eddies. Thus, the movement of the eddies has to be taken into account in matching up the time-space scales. As a rough approximation, the assumption is made that the ocean eddies move at rates of 5 km/day in a westward direction, orthogonal to the direction of the satellite groundtrack. Taking the eddy diameter to be 200 km, the ocean eddy will be sampled once every 23 days (at the equator) rather than about every 13 days as indicated in Figure 3.4.

The altimeter onboard GEOS-3 is capable of distinguishing ocean features above the 20-30 cm level which is adequate to resolve the phenomena listed in Table 3.2. However, the minimum meaningful wavelength sensed by the altimeter is about 30-50 km. This figure has been obtained from spectral analyses of overlapping pass residuals (see Chapter 6) and corroborated by the altimetric spectral estimates of Brammer (1979). Wunsch & Gaposchkin (1980) have indicated minimum meaningful wavelengths of about 25 km for the SEASAT-1 data. Therefore,

there is no significant information below this critical wavelength and this wavelength is indicated in Figure 3.4 as a dashed line. Thus, there is a reduction in the ocean eddy spectrum that may be recovered.

Following the development set out above, it is apparent that certain ocean dynamic results may be gained by using the GEOS-3 satellite altimeter data. The SEASAT-1 satellite will provide even more ocean dynamic information as indicated in Figure 3.4. The geodetic techniques used to extract ocean dynamic parameters of interest are set out in Chapters 6 and 7. The next Chapter sets out the regional ocean areas to be studied in detail using the proposed geodetic techniques.

GEOS-3 Two Day Groundtrack

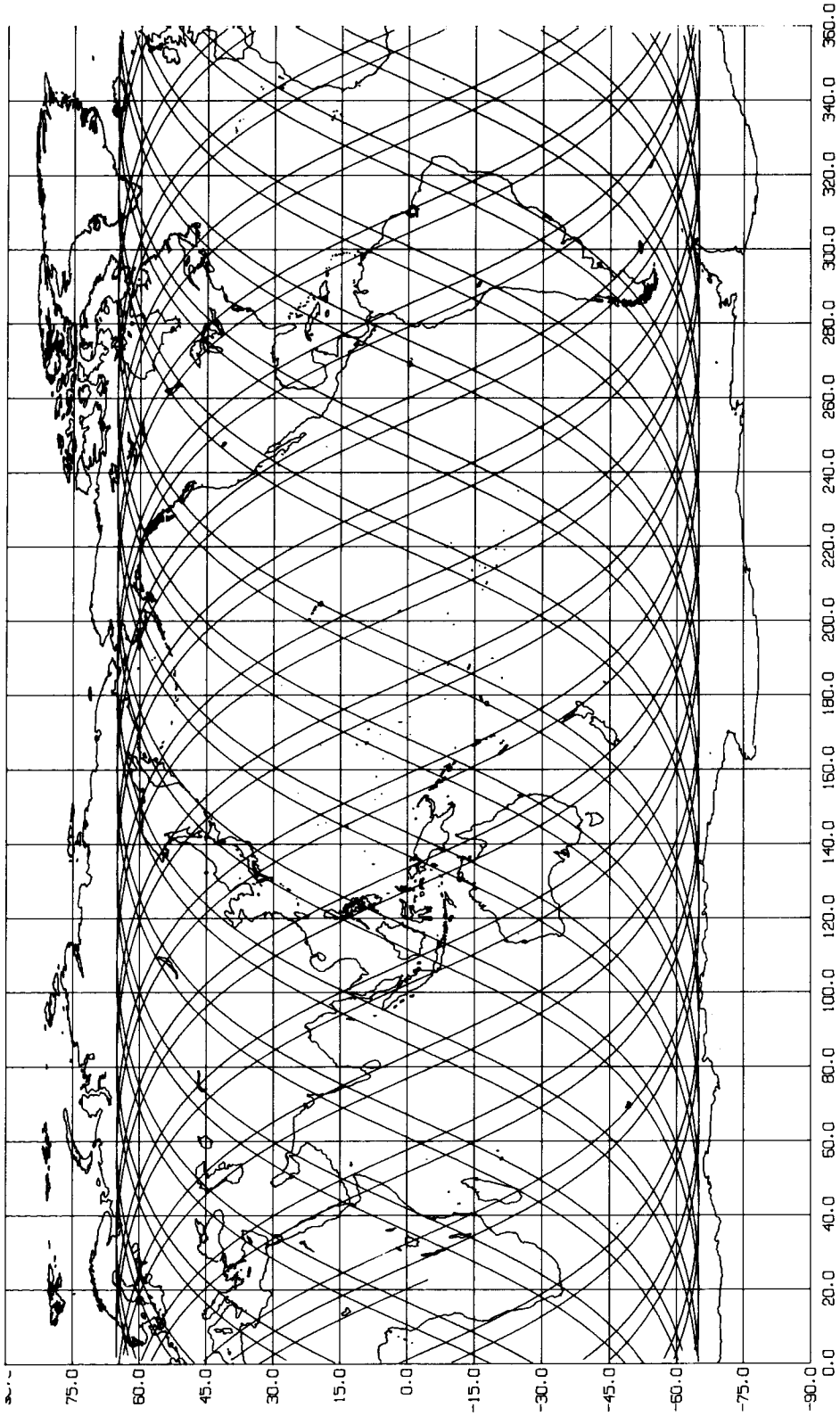


Figure 3.3.

Time/Space Scales

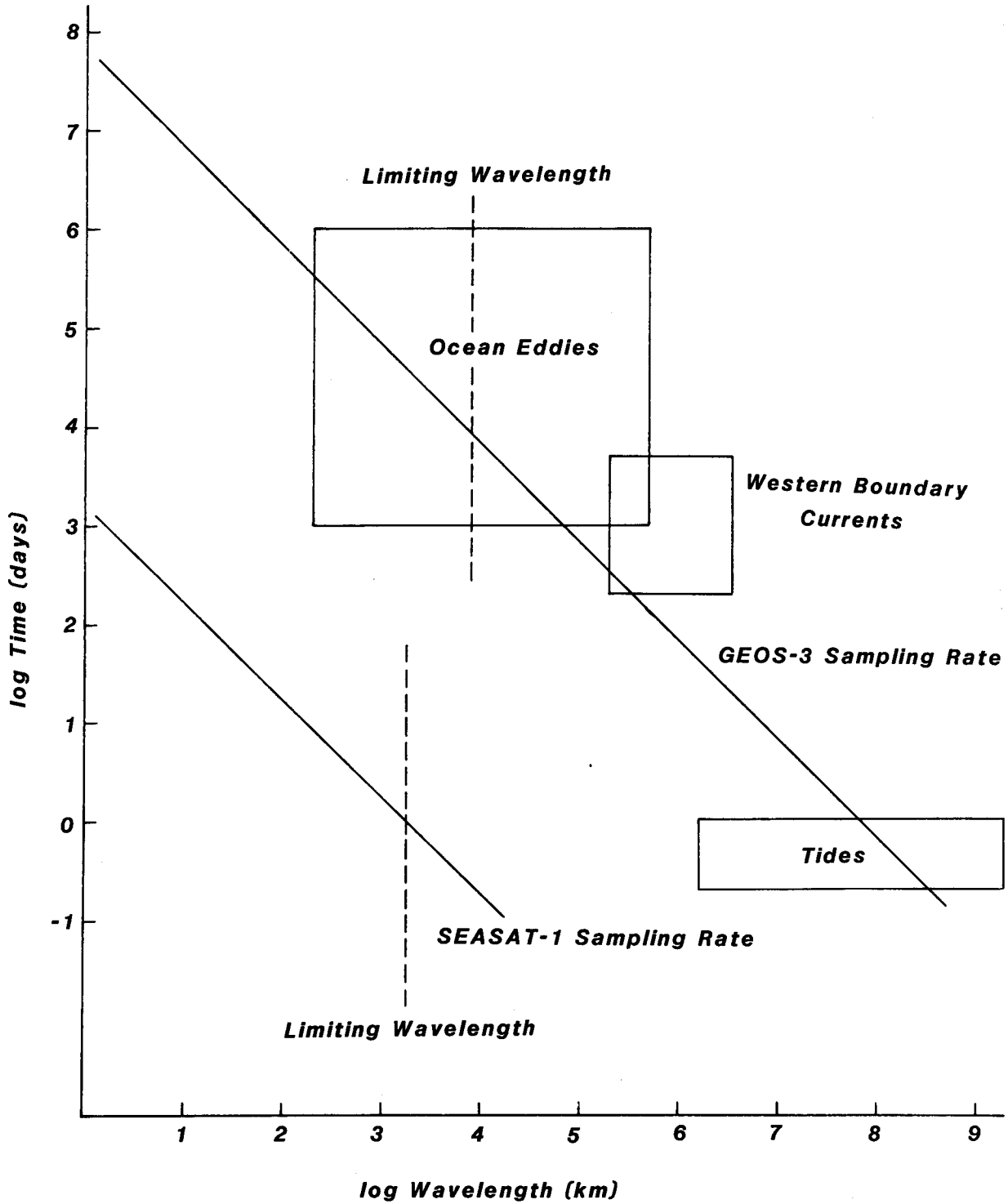


Figure 3.4

4. VARIABILITY OF THE OCEANS.

4.1. Basic Hydrodynamics.

4.1.1. Introduction.

A continuing research need in physical oceanography is the development of techniques to monitor the movement of strong western boundary current systems such as the Gulf Stream and associated eddy features. At present, the oceanographic community has adopted satellite remote sensing using IR radiometers to aid in synoptic monitoring of these phenomena. Of equal importance is the description of the large-scale mean movement of the ocean. The general circulation of the world's oceans have been studied in great detail but no adequate technique has been found to satisfactorily resolve the flow. The basic deficiency occurs since, as mentioned in Section 3.4, superimposed upon the mean circulation is a temporally varying field of widely different scales obscuring the mean flow signature.

As a new source of information available for quantifying ocean circulation dynamics, the dynamic ocean surface relative to a particular equipotential surface (geoid) can be studied using satellite radar altimeter data. The difference between the two surfaces provides an estimate of the dynamic SST (ζ_S). This data source has a number of advantages over traditional oceanographic methods used to describe flow fields, such as the dynamic height method (see Sverdrup et al. 1942; Fomin 1964). Firstly, the satellite data provides rapid global coverage of the ocean surface, e.g., for GEOS-3, a $1^\circ \times 1^\circ$ grid on the Earth's surface is sampled in 25 days (see Figure 3.4). The determination of ζ_S using geodetic techniques also enables the general circulation of the oceans to be determined absolutely in space, thus obviating the need for the arbitrary choice in selecting a level of no motion required for the dynamic height method. The requirements for obtaining an absolute velocity field from oceanographic measurements has been discussed recently by Stommel & Schott (1977), Schott & Stommel (1978), Schott & Zantopp (1979), Stengel (1979) and Wunsch (1978), the latter reference giving a rigorous generalised inverse approach for solving the ill-conditioned problem. Wunsch's technique has the potential to

incorporate altimetry data in the solution procedure for the circulation (see Wunsch & Gaposchkin 1980). However, only the use of altimeter data is considered in the following development for obtaining information on the ocean movement with the oceanographic data used as surface groundtruth - see Chapter 6.

4.1.2. Geostrophic Flow.

It is generally concluded that, to a first approximation, the major surface currents in the oceans are in geostrophic balance and their surface pressure gradients can be inferred from the sea surface slopes relative to an equipotential surface. It is thus required to set out the basic hydrodynamic equations at the air/sea interface and consider the approximations involved in the assumption of geostrophy.

As mentioned in sub-section 2.4.4, the equations of motion can be established in a local topographic Cartesian coordinate system for any circulation studies over regional extents. The x_i Cartesian coordinate system is defined such that the x_1x_2 plane defines the local horizon at a point $P(\phi, \lambda, h)$, the x_1 axis being oriented east and the x_2 axis north, while the x_3 axis coincides with the outward vertical at P . To the order of the flattening, ϕ and λ are the latitude and longitude on a spherical model of the Earth and h is the elevation of P above the reference surface.

The Navier-Stokes equations for a rotating homogeneous fluid can be expressed in vector notation as (Stern 1975, p.80)

$$\partial \tilde{X} / \partial t + (\tilde{X} \cdot \nabla) \tilde{X} + 2\Omega \times \tilde{X} = -\nabla p / \rho + g + \nu \nabla^2 \tilde{X} \quad (4.1)$$

where \tilde{X} is the total velocity vector having components $(\dot{x}_1, \dot{x}_2, \dot{x}_3)$,

Ω is the rotation vector of the Earth $(0, \Omega \cos \phi, \Omega \sin \phi)$,

g is the gravitational acceleration,

p is the pressure field defined in terms of surface stresses,

ρ is the density of the environment,

ν is the kinematic viscosity, and

∇^2 is the Laplacian operator defined in equation 2.13 .

Rewriting equation 4.1 in Cartesian component form and expanding in terms of a Laplacian description,

$$\begin{aligned}
\ddot{x}_1 + 2\Omega (\dot{x}_3 \cos\phi - \dot{x}_2 \sin\phi) &= -\frac{1}{\rho_w} \frac{\partial p}{\partial x_1} + F_1 \\
\ddot{x}_2 + 2\Omega (\dot{x}_1 \sin\phi) &= -\frac{1}{\rho_w} \frac{\partial p}{\partial x_2} + F_2 \\
\ddot{x}_3 - 2\Omega (\dot{x}_1 \cos\phi) &= -\frac{1}{\rho_w} \frac{\partial p}{\partial x_3} - g + F_3
\end{aligned} \tag{4.2}$$

where \ddot{x}_i and \dot{x}_i are the accelerations and velocities in the x_i coordinate system defined above and F_i are the components of the frictional forces ($=\nu \nabla^2 \ddot{X}$). The density of the environment is ρ_w , the density of sea water.

The velocities and accelerations in equation 4.2 refer to a system of reference in Earth space and the equations are applicable at any depth in the ocean layer. The effect of winds at the air/sea interface, apart from that implicit in the horizontal pressure gradient, are included in the terms F_i when applying these equations at the surface. With the values of \dot{x}_1 and \dot{x}_2 being of the order 3×10^2 cm/sec, and \dot{x}_3 being only about 3×10^{-2} cm/sec as well as noting that \ddot{x}_3 can be considered negligible in contexts other than short period wave motions, equation 4.2 can be further simplified.

Under the above conditions, the third equation in 4.2 reduces to the basic hydrostatic relation for steady, uniform flow

$$\partial p / \partial x_3 = -g \rho_w + \{10^{-4} (\partial p / \partial x_3)\} \text{ if } F_3=0 \tag{4.3}$$

The first two equations in 4.2 can be transformed by using the relation for the horizontal pressure gradient (Fomin 1964, p.163),

$$\partial p / \partial x_\alpha = g \rho_w \frac{\partial \zeta_s}{\partial x_\alpha} + \frac{\partial p_a}{\partial x_\alpha} + g \int \frac{\partial \rho}{\partial x_\alpha} dx_3, \quad \alpha=1,2 \tag{4.4}$$

giving a form of the equations of motion in the local horizon as

$$\ddot{x}_1 - f \dot{x}_2 = -g \partial \zeta_s / \partial x_1 - (1/\rho_w) (\partial p_a / \partial x_1) + F_1 \tag{4.5}$$

$$\ddot{x}_2 + f \dot{x}_1 = -g \partial \zeta_s / \partial x_2 - (1/\rho_w) (\partial p_a / \partial x_2) + F_2$$

where p_a is the atmospheric pressure at the air/sea interface, and f is the Coriolis parameter defined as $f=2\Omega \sin\phi$. These equations are

correct to the order of the Earth's flattening and the horizontal gradients of the dynamic SST can be considered equivalent to the terms $\partial\zeta_s/\partial x_\alpha$ in equation 4.5 as they represent vertical displacements at the air/sea interface due to non-gravitational considerations. Non-gravitational forces arise as a consequence of inhomogeneities in the strata on either side of the air/sea interface, such as wind stress at the surface of measurement.

Under the assumptions of a non-accelerated system (i.e., $\ddot{x}_\alpha = 0$) and the absence of frictional forces and atmospheric pressure gradients, the geostrophic components of the surface current in equation 4.5 can be written in terms of a (ϕ, λ) coordinate system as,

$$\begin{aligned}\dot{x}_1 &= \frac{-g}{f} \frac{\partial\zeta_s}{\partial x_2} = \frac{-g}{f} \frac{1}{R} \frac{\partial\zeta_s}{\partial\phi} \\ \dot{x}_2 &= \frac{g}{f} \frac{\partial\zeta_s}{\partial x_1} = \frac{g}{f} \frac{1}{R \cos\phi} \frac{\partial\zeta_s}{\partial\lambda}\end{aligned}\tag{4.6}$$

where R is the ellipsoidal radius. Equation 4.6 gives the basic geostrophic equations in which the horizontal SST gradients are balanced by the Coriolis forces. The equations assume that the dynamic SST gradients are the dominant factors driving the surface currents. These assumptions are discussed further in the next sub-section.

The variations in g need to be taken into account when applying the relations of equation 4.6 in regions with fast flowing currents if it is desired to achieve a precision of ± 10 cm/sec in the determination of \dot{x}_α . For this reason, the value of g has been computed using the Chebychev approximation for the computation of normal gravity (IAG 1971) when evaluating the geostrophic current components.

4.1.3. Non-Linear Terms in the Equations of Motion.

Assuming a non-accelerated system in equation 4.5, the basic horizontal equations of motion are given by

$$\begin{aligned}-f \dot{x}_2 &= -g (\partial\zeta_s/\partial x_1) - (1/\rho_w) (\partial p_a/\partial x_1) + F_1 \\ f \dot{x}_1 &= -g (\partial\zeta_s/\partial x_2) - (1/\rho_w) (\partial p_a/\partial x_2) + F_2\end{aligned}\tag{4.7}$$

It is desirable to know under what conditions the above equations can be generalised to the geostrophic equations in the form of equation 4.6 and

confirm the basic assumption that the dynamic SST gradients are the dominant forces driving the general ocean circulation.

Equation 4.7 shows a balance of forces between the frictional, Coriolis and pressure gradient components. The frictional forces give rise to a velocity shear in the ocean, where according to Newton's Law of Friction the friction stress τ is given by

$$\tau_{\alpha} = \rho_w v (\partial \bar{x}_{\alpha} / \partial x_3) \quad (4.8)$$

where all quantities have been previously defined. Of fundamental importance is the vertical velocity shear and from the expression for F_{α} , it can be seen that in terms of the friction stress or wind stress the friction force per unit mass is

$$F_{\alpha} = (1/\rho_w) (\partial \tau_{\alpha} / \partial x_3) \quad (4.9)$$

Considering the case of pure drift currents, an empirical relation is used to relate the wind stress τ in terms of a given wind speed W at the ocean surface as (Neumann 1968, p.179),

$$\tau = C W^2 \rho_a \quad (\text{dynes/cm}) \quad (4.10)$$

where C is the drag or resistance coefficient whose value is approximately 1.3×10^{-3} (Busch 1977), but varies as a function of wind speed (Amorocho & DeVries 1980),

W is the wind speed in cm/sec, and

ρ_a is the density of the atmosphere.

In terms of the horizontal components τ_{α} and W_{α} in the x_{α} directions,

$$\tau_{\alpha} = C W_{\alpha} \rho_a (W_1^2 + W_2^2)^{1/2} \quad (4.11)$$

Thus, the frictional forces F_{α} can be approximated by the expression

$$F_{\alpha} = \tau_{\alpha} / (\rho_w H) \quad (4.12)$$

where H is the depth of the mixed layer, which varies roughly from 25 to 200 m (Pickard 1963). This approximation assumes a linear rate of

change of τ with depth and is thus conservative. Equation 4.11 could probably be scaled by a factor of 2-4 since the surface wind stress will be more effective in the uppermost portion of the mixed layer (see Kundu 1980, Figure 10).

Using the above expressions for the frictional force, and values for ρ_w (=1.025 - Monin et al. 1977, p.36) and H (=100 m), estimates for the frictional forces, atmospheric pressure gradients and SST gradients were calculated for different values of surface current at latitude 35°, this latitude corresponding approximately to the mean latitude of the Gulf Stream and East Australian Current areas to be studied. The results are summarized in Table 4.1.

Noting the fact that major frontal variations will cause atmospheric pressure variations of the order 30×10^2 Pa and wind speeds of the order 36 m/s correspond to gale force winds with SWH's in excess of 20 m (Barrick 1972, Table 12.1), it is seen from Table 4.1 that the dominant driving forces in the oceans are the SST slopes. Thus, the basic geostrophic equations (4.6) used are considered adequate for use in the altimeter analyses described in sub-section 6.4.5 .

The next two sections summarize from the oceanographic literature the expected ocean variability in selected areas of the ocean where it is considered that the altimetry data could detect ocean dynamic signatures of interest. The regional areas selected were an area off the east coast of Australia where the dynamics of the East Australian Current should be seen in the altimeter signal and a region covering the western North Atlantic in the vicinity of the Gulf Stream. Results using the altimeter data are given in Sections 6.3 and 6.4.

4.2. The East Australian Current Area.

The literature describing the East Australian Current (EAC) region has not been widely published and compared to the Gulf Stream region little is known about the dynamics involved. Thus, a fairly detailed summary of the available literature has been given, specifically looking at the signatures of the EAC and the eddy features for possible altimeter application.

4.2.1. Introduction.

The traditional picture of the East Australian Current (EAC)

Table 4.1 Equations of Motion at the Ocean Surface.

Type of Current	x_α cm/s	$\partial \zeta_s / \partial x_\alpha$ cm per 10^2 km	$\partial p_a / \partial x_\alpha$ 10^2 Pa per 10^2 km	W_α m/s ²
Fast	100	86	86	74
Medium	10	9	9	24
Slow	1	1	1	7

system was gained from mariners who were long accustomed to experiencing strong, irregular, southerly currents with speeds of up to 200 cm/sec near the edge of the continental shelf off the New South Wales coast. These currents were known as the Southerly or EAC and were depicted on marine charts by cartographers as a series of arrows running from the Queensland coast around Fraser Island (latitude 25°S) down to beyond the Bass Strait (latitude 45°S). Even today in current atlases or charts of world ocean currents (e.g. Neumann 1968, Figure 25), the EAC is denoted as a relatively strong, narrow western boundary current close to the edge of the continental shelf between latitudes 27°S and 37°S. The current is present at all times of the year but is strongest between December and April. However, the atlases give no clear indication of the structure of the current at any particular time.

The information presented in current atlases is commonly constructed by collecting all available ship's drift data (Wyrtki 1960) and averaging according to the time of year and geographic areas. An analysis of this type emphasizes the large circulation systems persistent over many years, and does not give an indication of the temporal and spatial changes of the current system.

In reality, the EAC system changes rapidly in both space and time and the sections that follow trace some of the development of knowledge about the EAC system and its associated eddy features. The evolution of the oceanographic techniques used in understanding the ocean dynamics involved is also presented. It is only in the last few years that physical oceanographers have put forward a satisfactory explanation of the dynamics of the EAC system and the formation of the warm, anticyclonic eddies. The research institutions involved in data collection and analysis are the Commonwealth Scientific and Research Organisation's (CSIRO) Division of Fisheries and Oceanography, the Royal Australian Navy Research Laboratory (RANRL) and the Defence Research Centre, Salisbury (DRCS).

4.2.2. The EAC - to 1960.

In this period, traditional physical oceanographic techniques were employed onboard research vessels. Data collection was confined to sporadic surveys over some chosen area or finer detail surveys in localised areas and thus the details of the frequency spectrum of the

current system that could be studied were limited. Mechanical devices such as the Nansen sampling bottle and the bathythermograph (BT) were primarily used (and are still widely used) to take ocean water samples that are analysed for salinity, oxygen and nutrients.

Information about the ocean dynamics was gained by utilising two well-known techniques, water mass analysis and the dynamic height method. With the former method, it is possible to plot different bodies of water (density surfaces σ_0) in three dimensions and to determine their sources or origins and the changes in their distribution as a result of mixing (e.g. Rochford 1968; Newell 1966). Information from water mass analysis indicates ocean surface and sub-surface paths followed by the water bodies, but gives no indication of the speed of the water particles. Temperature and salinity measurements are used in the dynamic method to calculate densities, giving a dynamic height difference or pressure gradient between the two measurement stations. The density structure at different depths makes it possible to calculate the surface ocean currents and currents below the surface.

B.V. Hamon of CSIRO was among the first physical oceanographers to use the dynamic method to study the EAC system. From the early cruises of limited extent between 1954 and 1959 (Hamon 1961), a U-shaped current was revealed, initially running southward near the continental shelf, frequently leaving the coast near the latitude of Sydney (34°S) and then flowing east. The current was seen then to swing north or north-east still as a narrow, swift current. The volume transport in the northward and southward sections across the current was approximately the same, suggesting a northerly counter current further offshore from the southward EAC. However, there were occasions when the current was noted to run nearly due east and then pass to the south of Lord Howe Island (31.5°S , 159°E).

Hamon (1961) reported the existence of large anticyclonic eddies (anticlockwise rotation in the southern hemisphere) almost 250 km in diameter that seemed to move slowly southward from about 35°S . The currents around the eddies were observed to be 120-150 cm/sec which was comparable with the speed associated with the U-shaped EAC (Hamon 1962a). Wyrcki (1962) confirmed the existence of the U-shaped current and showed that the current crossed the Tasman Sea and passed to the north of New Zealand. His analysis was based on dynamic topography maps produced in the south west Pacific, referred to a 1750 decibar reference surface. Wyrcki suggested that eddies split off from the main current

and drifted south down the coast and this was confirmed from his observations by the existence of an anticyclonic eddy found as far south as Tasmania. However, Wyrтки drew a note of caution on his interpretations because of the wide station spacing, which meant that only isolated stations were present to define the current and/or eddy structures.

In locations covering various portions of the eastern coast of Australia between latitudes 25°S and 45°S, Hamon (1965) produced 8 maps of dynamic topography. These maps showed mainly south-directed baroclinic waves north of about 30°S to 33°S and some closer circular eddies south of about 34°S. The reference level, that is the surface at which horizontal motion is assumed to be zero, was chosen as 1300 decibars, differing from Wyrтки's (1962) level of no motion. Surface currents were measured with a towed geomagnetic electrokinetograph (GEK) cable and showed general agreement with the geostrophic surface currents derived from the dynamic height method. The main core of the EAC system (defined by velocities greater than 50 cm/sec and in terms of the 15°C isotherm at 240 m depth) was found to be between 40 and 80 km wide with an overall width estimated at 150 km. As expected, the horizontal shear associated with the western body current system was usually greater on the right hand side of the current, looking downstream, than on the left hand side, with typical values of approximately 9×10^{-5} /sec. Hamon noted that the surface temperature was quite a good indicator of the U-shaped EAC but generally lacked definition for eddy features in the area as the temperature gradients across the eddies at the surface were small and sometimes in the opposite direction to the gradients below the surface. The change in surface temperature on crossing the main EAC or counter current was between 1.5°C and 3.5°C but less than 1°C in crossing an eddy (Hamon 1965). The thermal gradients present in the EAC are quite different to those found in the Gulf Stream region where the temperature differences found in crossing the Gulf Stream are commonly of the order of 12°C. The volume transports of the EAC, countercurrent and eddies, above the 1300 decibar level, were found by Hamon to be in the range $12-43 \times 10^6 \text{ m}^3/\text{sec}$ which was about one half that of the Gulf Stream transports, and not consistent with expected values if the EAC is considered a western boundary current for the whole south Pacific ocean. From the available data, Hamon concluded that it seemed probable that the EAC was wind-driven, as are the western boundary currents in the northern hemisphere, but the exact details of the dynamics were unclear.

Hamon (1970) set out the major differences between other western boundary currents and the EAC system as : (1) the absence of a well developed surface temperature structure across the current and particularly in the eddies, (2) an apparent frequent formation of anticyclonic eddies at a particular locality (about 34°S), (3) a small net transport associated with the EAC system, and (4) the absence of a large area of relatively motionless warm water on the seaward side of the current.

By contrast to the other western boundary current systems, the flow patterns in the EAC are quite complex and variable, so much so that it is often difficult to decide whether a single, continuous current exists.

Ship surveys were speeded up by combining time-saving BT casts with the arduous hydrology station observations using a relationship derived by Hamon (1968b). He found that a reliable correlation existed between the dynamic height and the temperature at the 240 m level, with a regression equation for combined summer and winter cruises being given by

$$D = 8.85 C + 50.2 \quad (4.13)$$

where D is the dynamic height anomaly, 0/1300 decibars (in dynamic cm), and

C is the measured temperature at 240 m (in °C).

The BT casts from these cruises showed that the winter time eddies had isothermal layers from the surface down to more than 200 m.

Boland & Hamon (1970) produced another series of dynamic topography maps for the years 1965-1968 based on data from eight cruises. Results using inductive salinometers (Brown & Hamon 1961) and neutrally buoyant pinger floats (Swallow 1955) indicated that the 1300 decibar level of no motion used in previous calculations was too shallow and that the reference level may be at least as deep as 2300 m. Below 3000 m, the observed currents were in the range 2-7 cm/sec and showed no clear evidence of being coherent with surface currents.

The question arises: Does the change in level of no motion affect the surface expression of the EAC system? Boland and Hamon suggested that for a change in reference level, there is an equivalent addition of a small current at all depths when computing geostrophic currents. This has little effect on the computed surface current but may have a large

effect on the integrated volume transport.

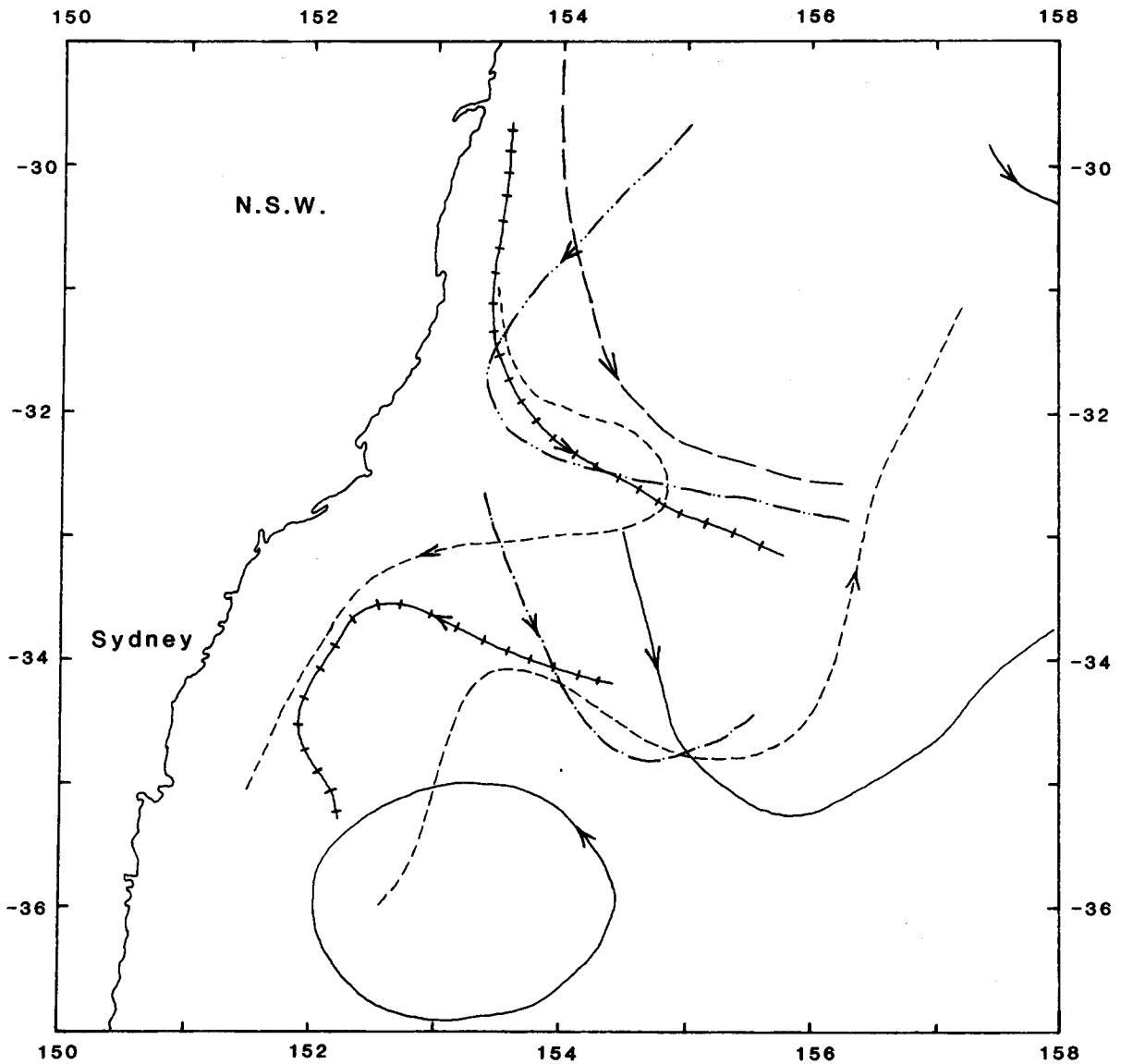
Hamon (1965) noted that the 190 dyn.cm contour of the surface dynamic topography almost always existed near the core of a region of strong current. Using this as a guide, Figure 4.1 is a composite picture, in the EAC area, for cruises between March 1965 and September 1967 of Boland & Hamon (1970), indicating the variability of the EAC axis. The figure shows the complex and variable nature of the EAC circulation pattern and at the time suggested that the existence of an EAC, in the sense of a continuous flow from the Coral Sea to around latitude 35°S, at any given time, seemed doubtful. The question of whether the EAC was topographically controlled, which is the case if the current extends to the ocean floor (Warren 1963) also remained unsettled. The figure also indicates the meandering movement of the EAC axis towards the east at around 32° - 34°S, and the presence of anticyclonic eddies south of these latitudes (an anticyclonic eddy was located on the first cruise, centred at 36°S, 153°E).

It is probably pertinent at this stage to have a clear idea of the "average" picture of the EAC and its variability, in both position and surface relief over time. This type of picture will give a better indication of the possible information that may be recovered using the satellite altimetry measurements and whether the expected fluctuations in the EAC system can be resolved above the noise level of the altimeter data. The question then to be answered is, whether the adjustment procedures set out in Section 6.2 are adequate for detecting the ocean phenomena of interest. For these reasons, an average surface dynamic height anomaly map, relative to 1300 decibars, was prepared in the form of 1°x 1° means and is illustrated in Figure 4.2. It was compiled from the dynamic height maps of Hamon (1965), Boland & Hamon (1970) and Lawrence (1979) and shows general agreement with Wyrтки's (1962) map. Figure 4.2 is also corroborated by the block mean values of dynamic height, over a 5°x 7° area, given by Pearce (personal communication, 1979). Both Figures 4.2 and 4.3 include only those 1°x 1° block values for which greater than 25% representation is available, using the 18 dynamic height maps available in the references given above.

The rms variability of dynamic heights in the same area is illustrated in Figure 4.3. It shows that the areas of largest variation are associated with the meandering of the EAC axis and its movement towards New Zealand, and the regions in which anticyclonic eddies are formed and drift southwards. The range of variation in dynamic height

Pattern of the EAC - 190 dyn.cm contours

Figure 4.1

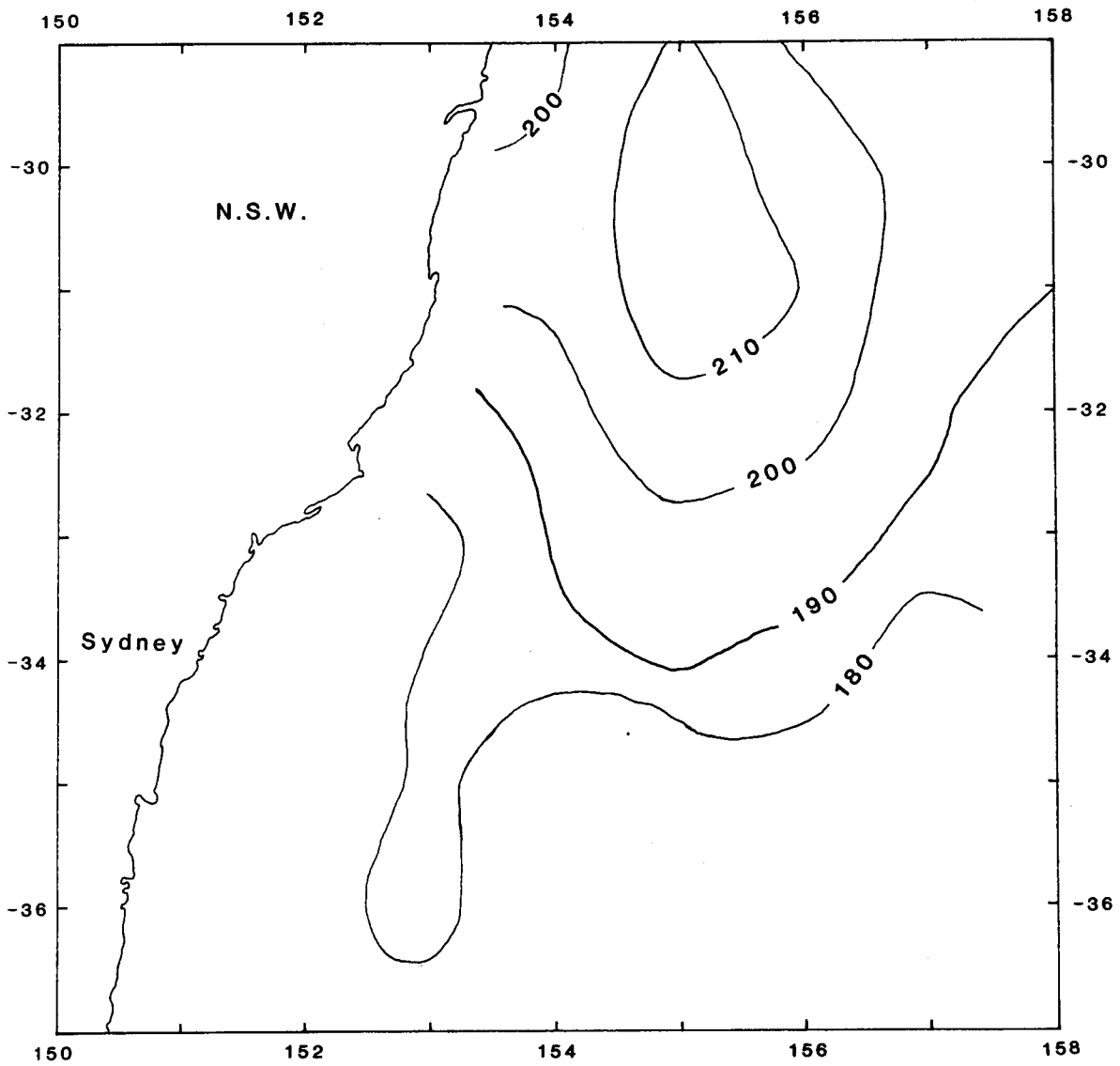


Cruise Dates

8-22 Mar 1965	———	27 Feb-7 Mar 1967	- · - · -
12-25 Jul 1965	- - - - -	29 Mar-18 Apr 1967	- · - · -
15-28 Nov 1965	+ + + + +	14 Aug-9 Sep 1967	— · — · —

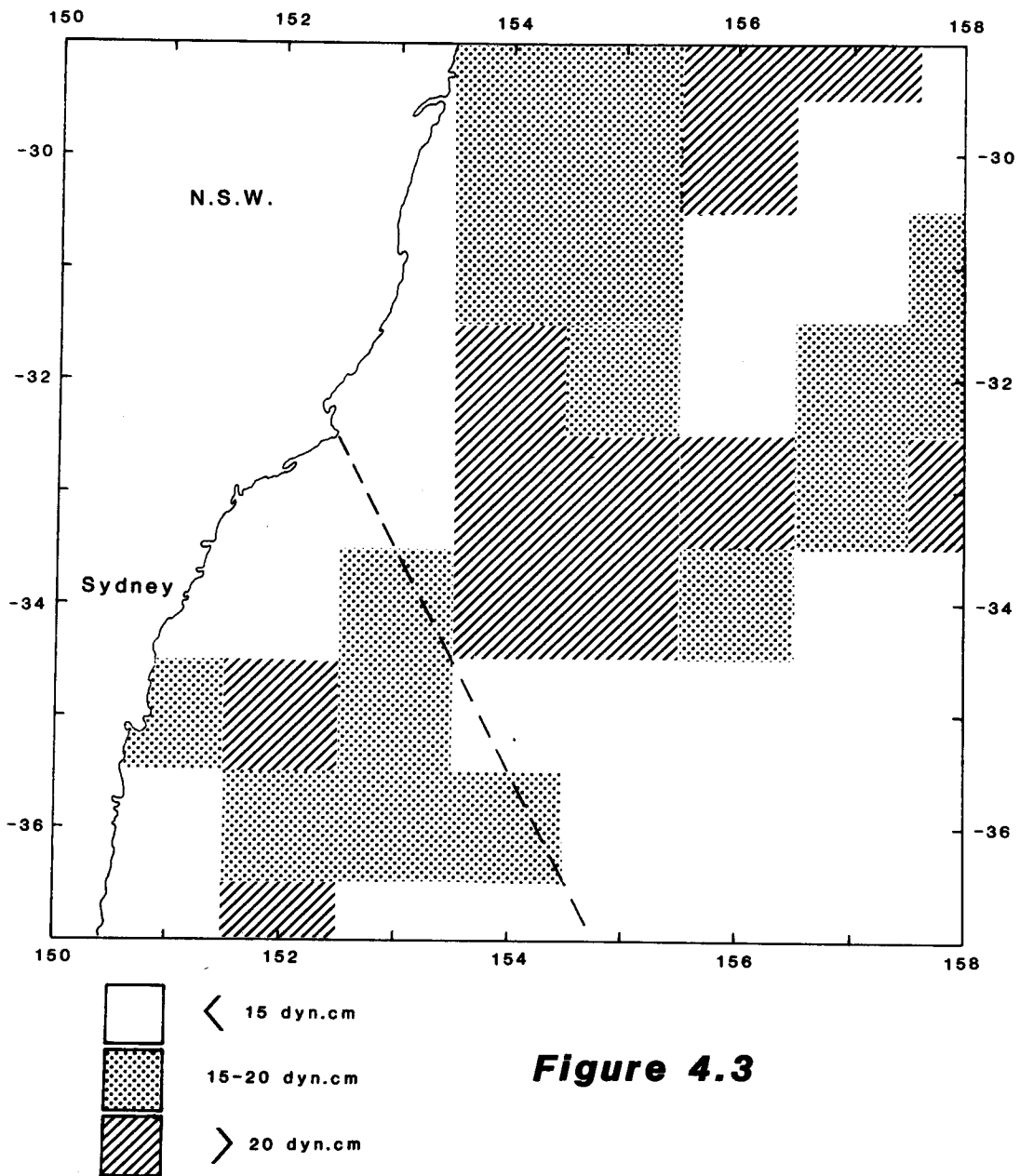
Average Surface Dynamic Height Anomaly (1960-1979)

(0/1300 m)



Contour Interval: 10 dyn.cm

Figure 4.2

Variation of EAC Dynamic Heights as a Function of Position(rms residual \pm dyn.cm)**Figure 4.3**

over the area is 17 cm. The dotted line represents an "imaginary" boundary as suggested by Godfrey et al. (1980b), in which the behaviour of the EAC system is qualitatively different on either side of this line. It can be generally concluded from this figure that the turning or inflexion point of meanders in the EAC lies to the north of the dotted line and that in the area shown to the south of this line, anticyclonic eddies are most commonly found in regions centred on 152°E and extending approximately 50 km either side of this longitude.

As an alternative technique, dynamic height changes (inferred from tide gauge records at suitable oceanic islands such as Lord Howe Island) could be thought of as actual changes in "mean sea level". The essentially continuous nature of tide gauge records makes them ideal for studying the time variations in dynamic height, and thus of the associated circulation patterns. Hamon (1962b, 1968a, 1969) found an anomalous peak in the adjusted MSL spectra from tide gauges at Sydney, Coff's Harbour and Lord Howe Island in the frequency range corresponding to periods from 20-50 days and irregular slow fluctuations in sea level of the order of 10 cm. These results were thought to be associated with moving circulation patterns; the drift rates for eddies of 200-250 km diameter, implied from the periods above, would be 5-10 km/day. The coherence between the Coff's Harbour and Lord Howe Island MSL spectra was low, especially at the longer periods. This was believed to be due to the movement of the axis of the EAC relative to the island (Hamon & Stacey 1960) but was later shown by Robinson (1964) to be explained by continental shelf waves.

Hynd (1969) tracked a "pool of warm water" or anticyclonic eddy with an airborne radiation thermometer (ART) for a month during the summer of 1968 and the analysis showed a drift rate for the eddy of 5.5 km/day. The eddy was about 50-70 km in diameter and was surrounded by marked temperature fronts, a sometimes distinguishing feature of the presence of an eddy (C.S. Nilsson, personal communication, 1979). These results seemed to corroborate earlier findings by Hamon and others.

In looking at the relation between MSL and geodetic levelling at tide gauge stations around the Australian coastline, Hamon & Greig (1972) showed that the net fall in dynamic height, amounting on average to about 55 cm from the Coral Sea to the southern end of the EAC is a permanent feature of the EAC system. This is partly seen from the quasi-stationary topography shown in Figure 4.2 - over the area shown in this figure there is a net fall of about 30 cm. Further details of

comparisons between geodetic levelling and MSL at tide gauges is discussed in relation to the slope in the sea surface along the east Australian coastline in Coleman et al. (1979).

4.2.3. Merchant Ship Records.

Hamon et al. (1975) collected ship's drift data along the New South Wales coast from 38 ships over a period of 2 years (916 passages). The resulting longshore currents were calculated for southward passages at the shelf edge (about 19 km offshore) and for northbound passages (about 6.5 km offshore). A clear correlation was found to exist between the shelf edge and the nearshore currents with the former leading the latter by 7-10 days. The southward drift of the averaged current patterns was of the order 9 km/day and this finding was of considerable interest as the drift had not shown up in a previous study (Hamon & Kerr 1968), due basically to an insufficient data coverage. Both studies showed the shelf edge current to have a periodicity in the range 50-170 days. Seasonal variations in the EAC were also found, being generally stronger in summer (mid-November to mid-April) than in winter, with the difference most marked in the northern sections of the coast. Mean currents in both summer and winter decreased with an increase in latitude from about 30°S.

Garrett (1979), in a subsequent analysis of the ship's drift data, suggested that these surface longshore currents, with fluctuations of the order 100 days, were due to topographic Rossby waves generated when eddies and meanders in the EAC encounter the continental slope.

From July, 1969, an expendable bathythermograph (XBT) system was operated for several years along an east-west section across the Tasman Sea at 33.5°S (Boland 1973; Boland 1979). Confirmation was obtained for earlier findings (Reed et al. 1968) of a strong, south-going current near the coast and an equally strong, north-going return flow further offshore. However, the single profile does not allow eddies to be distinguished from meanders of the EAC. The strong current regions were found to move longitudinally at speeds of 10 km/day and the currents displayed a transitory nature in that they would appear and disappear with a new influx of current appearing on average every 73 days. Thus, strong current patches appeared and disappeared within 40 day intervals. Assuming that the southerly baroclinic waves matured into circular

eddies at the approximate location of latitude 34°S , then the eddy formation time from the appearance of the EAC system on Boland's section to the disappearance of the two arms of the current ring from the section is equated to 40 days (Nilsson et al. 1977).

4.2.4. The EAC - to 1980.

Using the dynamic topography maps produced by Hamon (1965) and Boland & Hamon (1970), Hamon & Cresswell (1972) deduced a dominant length scale (distance between eddies) of approximately 500 km using structure function analysis. Combining this figure with the time scale estimate of 73 days (Boland 1973), this implies a southward drift rate of the eddies of around 7 km/day, which agrees with previous estimates.

Following the previous large scale coverage surveys of the EAC system, more attention was devoted by RANRL and DRCS to designing detailed fine mesh surveys for particular studies of the evolution/formation processes of the EAC eddies. The primary instrument used in the cruises was the XBT, with surface temperature and salinity measurements coming from a continuously recording thermosalinograph.

Andrews & Scully-Power (1976) gave details of an intense anticyclonic, warm core, winter eddy that had been surveyed off the coast near Sydney in September 1974. The eddy had a diameter of 250 km with a surface dynamic relief of 70 dyn.cm., the largest relief noted to date. A mixed layer depth extending to over 300 m in the main core of the eddy was also observed. Surface current speeds in the eddy ranged from 60 - 178 cm/sec. The temperature structure indicated that the current increased radially from zero at the eddy centre to a maximum velocity at half of the eddy radius. A peculiarity of the eddy surveyed was its anomalously high temperature gradient ($2^{\circ}\text{-}3^{\circ}\text{C}$), from the eddy core to the water beyond the core of the current, compared to that previously found by other investigators. Andrews & Scully-Power (1976), noting the axially symmetric structure of the winter eddy proposed a basic physical model for EAC eddies, assuming the eddy to be an inertio-gravity wave. Another interesting feature of their study, related to the dynamics of eddy formation, was the entrainment and complete encapsulation of Coral Sea water by the deeper shell of 16.75°C water. In some respects, this process of entrainment is similar to the cold-core current ring formation in the Gulf Stream region. Godfrey (1973b) had shown that Coral Sea surface water is uplifted over the

colder surface water to the south and the resulting water body is carried south with the near-coastal EAC system. This seems to provide a somewhat tentative explanation for the formation of an eddy and for the observations of Andrews and Scully-Power.

From a number of winter cruises in the Coral Sea area, Scully-Power (1973) postulated that the EAC was a series of southward meandering anticyclonic eddies near the edge of the continental shelf which originate near 15°S in summer and about 20°S in winter. This idea was rejected by Nilsson et al. (1977) for a number of reasons, primarily because of the observation of in-situ eddy formation noted from their cruise data and the lack of anticyclonic eddies found north of 34°S.

Detailed surveys were made around latitude 35°S between September 1974 and October 1976 confirming the existence of between 3 and 5 separate anticyclonic eddies (Nilsson et al. 1977). Their observations between late February and May 1975 showed that the same eddy had been identified on 4 separate occasions at approximately the same locality, implying that eddies can "stall" for at least seven weeks. A key feature of this eddy was a subsurface of warm, isothermal water that apparently formed within a 10 day period between cruises. This was attributed to convergence in the upper layers of the ocean and some net downwelling. Nilsson et al. (1977) concluded that, unlike the Gulf Stream area where a Stream meander pinches off to form an eddy, the process of EAC eddy formation had contributed to the separation of a segment of the EAC from the coast and that this process is associated with the bottom topography of the region. Over the 2 month period during which the eddy was tracked, it drifted westward at a rate of about 1 km/day.

The term "wintertime" eddy was loosely phrased for an eddy which had a mixed core open to the surface and intervening eddies from December-May were called "summertime" eddies because they had a mixed core overlain by a separate surface mixed layer, i.e. a process of in-situ eddy formation rather than advection of a fully formed eddy from the north. It was also noted from the work of Nilsson et al. that the temperatures at a depth of 400 m, rather than 240 m as used by Hamon (1968b), correlated better with the surface dynamic topography across the eddies. Temperature gradients between the eddy center and the EAC "tongue" boundary were of the order 2°C per 110 km. The tongue boundary marks a region of relatively high surface currents and, as pointed out by Andrews & Scully-Power (1976), is associated with surface

temperature fronts where the horizontal temperature gradients are large. There was no observational evidence to suggest that, after eddy formation, the EAC, as a well-defined stream, moved northward and/or eastward away from the eddy.

Synoptic evidence for the offshore movement of the EAC can be gained by use of satellite thermal IR images. Legeckis (1978) discusses results for the EAC area, using IR data from the polar orbiting, NOAA-5 satellite, taken during the period September 1976 to January 1978. Figure 4.4 (taken from Legeckis 1978, Figure 13) shows the EAC area on October 14 1977. The warmer surface water, seen as the darker tones of grey in the image, denotes the EAC axis. The axis appears to swing towards the east about 400 km offshore at latitude 32°S, and the main core of the EAC is of the order 40-60 km wide (Legeckis 1978). A narrow strip of cooler, shelf water (about 20 km wide), seen near the deflection point of the current, corroborates the findings of Godfrey et al. (1980b). This inshore, cooler water seems to be a common phenomena and may be linked to the eddy formation mechanism. On a particular IR image, Legeckis found evidence of 4 anticyclonic eddies between latitudes 54°-58° S, and longitudes 140°-150° E. The eddies were elliptical in shape, with diameters of the order 300 km. The observed sea surface temperature fronts associated with the eddies were of the order 2°C per 2 km.

Scully-Power & Twitchell (1975) used IR sensors in correlating observed nocturnal cloud patterns with the existence of an anticyclonic eddy. Earlier, Malkus (1957) reported that cumulus clouds were associated with warm spots on the ocean surface, the sea surface temperatures being measured by an IR radiometer. Evidence that cloud formation can sometimes be used to locate sea surface temperature fronts has also been reported in Legeckis (1977).

Making various assumptions about turbulent fluctuations at the air/sea interface and in the atmospheric mixed layer, Scully-Power and Twitchell showed that it was possible for the large warm eddy, surveyed by cruise and aircraft observations, to produce the nocturnal cloud patterns seen on the IR images. They did not, however, give any firm suggestion for using this correlation as a technique for tracking eddies or distinguishing the EAC boundary.

The first satellite-tracked, drifting buoy was released in the Tasman Sea in late 1972 and was reported by Cresswell (1973). The buoy, a PVC/fiberglass spar, carried an EOLE satellite transponder for

VHRR IR image of the EAC Area

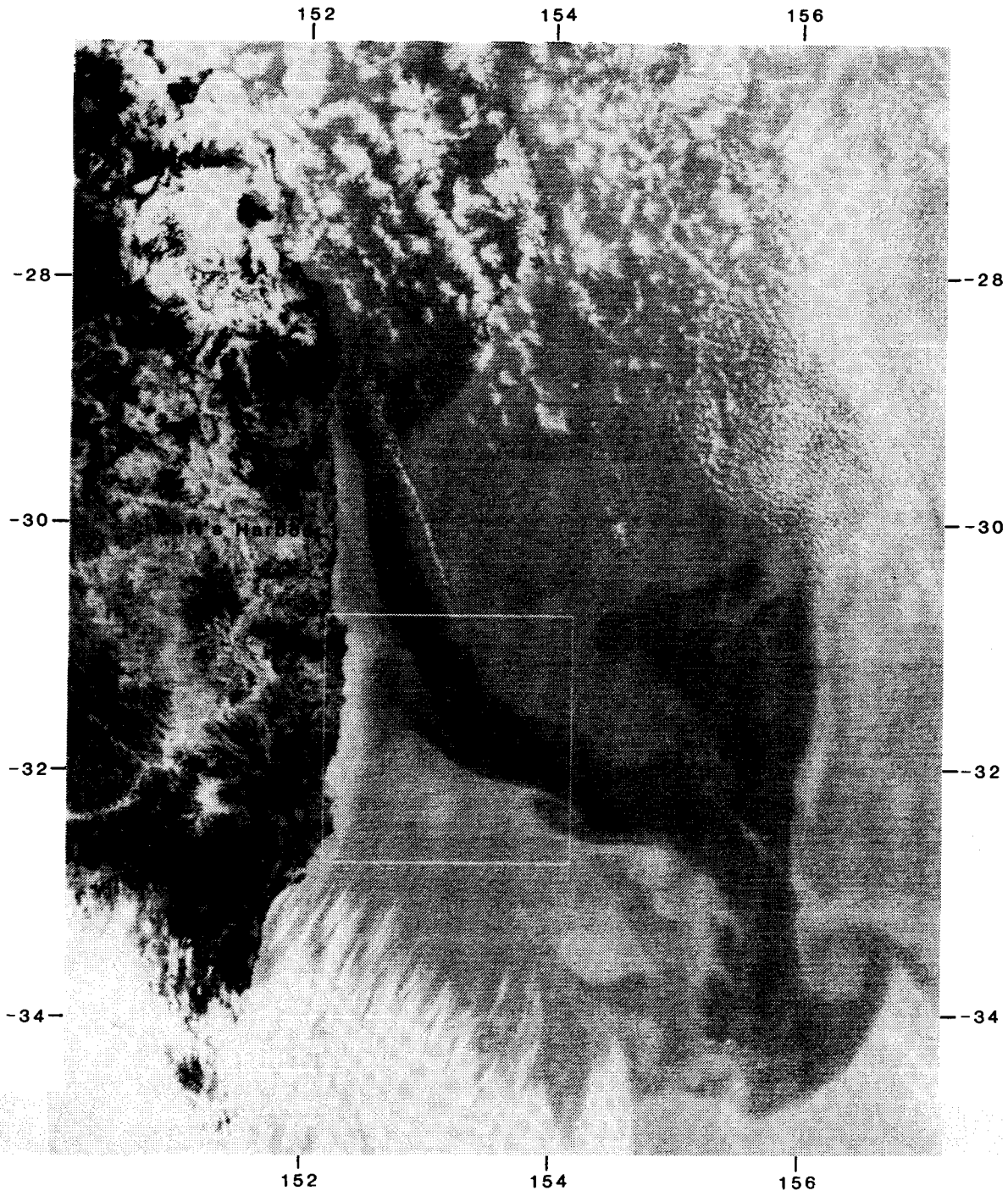


Figure 4.4

position fixing and thermistors to measure sea surface, air and transponder temperatures but its lifetime was only one month.

A second buoy was released on 30th April 1973 and operated for 11 months in the Tasman Sea (Cresswell 1976). The track of the buoy was compared to sea surface temperature records of merchant ships and it was found that the temperatures increased to the left hand side of the buoy track. For the southern hemisphere, these temperature highs correlate with increased dynamic heights. The large scale motions of the buoy tracked in the Tasman Sea agreed quite well with Wyrтки's generalised current pattern derived from ship observations (Wyrтки 1960). Problems arise with interpretation of buoy data since the buoy is locked into the mixed layer which responds primarily to the wind. Beneath the mixed layer is a sub-surface layer independent of wind and hence as pointed out by Cresswell (1976), the buoy's motion will depend on the relative magnitudes and directions of both wind-driven and sub-surface currents.

An interesting feature noted by XBT drops from merchant ship cruises between Sydney and New Zealand, taken during the period of the buoy's life, showed that the south-going core of the EAC was strong and situated at 153°E on 1 March. In 15 days the current strengthened and moved 50 km westward but after another 15 day period no strong current was evident anywhere along the section. This observation shows similarities with Hamon's (1965) findings about the variability of the EAC system.

In 1975, with the launching of the NASA weather satellite NIMBUS-6, a new series of 12 spar buoys was constructed by CSIRO for surface current measurement studies. A new torpedo buoy (described in detail in Cresswell et al. 1978) was first released into the Tasman Sea in November 1976. A total of 13 buoys (spar and torpedo) were released between November 1976 and December 1977 with a fairly high success rate of operation (77%). Both types of buoy had parachute sea anchors tethered 20 m beneath them. With a satellite fly-over time of approximately 15 minutes, the positions of the buoys, calculated from the changing frequencies of their transmissions relative to the satellite, were obtained with positional accuracies of ± 5 km. As many as 6 fixes have been obtained in 24 hours, but a more usual number is 1-2 good fixes per day.

Data reports detailing the progress of the released buoys can be found in Cresswell & Wood (1977), Cresswell et al. (1978), Cresswell & Golding (1979) and Cresswell & Greig (1979). To June 1978, from the

total of 16 buoys in the Tasman Sea, seven were functioning well, another four were giving sporadic returns and five had failed. The synoptic information that may be gained with regard to the EAC and the eddies, can be seen in the composite buoy track information depicted in Figure 4.5. The diagram, taken from Cresswell & Golding (1979), indicates the immense complexity confronting oceanographers in trying to piece together the overall dynamics of this boundary current. Drifting buoys, however, can play a major role in providing detailed synoptic data for small scale area dynamic studies when judiciously released in areas of known activity, preferably complemented with cruise data. A number of the buoys were released into eddies following XBT surveys from research vessels and provided new information on the dynamics of eddy formation in the EAC system.

One such documented study is on the evolution and formation of eddy "B" which was tracked by numerous research vessels and 12 buoys between late February 1977 until June 1978. Preliminary reports on eddy "B" are given in Cresswell (1979) and Cresswell & Nilsson (1979) and a detailed analysis of the dynamical evolution of the eddy is given in Nilsson & Cresswell (1980). Eddy "B" is indicated by the numerous loops east of Eden at 37°S , 152°E in Figure 4.5, and it was this information from the buoys that enabled the eddy to be unambiguously identified for the period March through to November 1977.

Eddy "B" formed from the pinching off of a tongue of warm northern water and a detailed close-up of its formation, using buoy and cruise data from Cresswell & Nilsson (1979), is given in Figure 4.6. The figure shows the detailed tracks of two drifting buoys, indicated by the heavy full lines, with the adjacent numbers being the day number of the year indicating the buoy's geographic position at that particular time. The northern buoy was trapped by a meander of the EAC and as this meander bifurcated from the main EAC current, the buoy moved in circular loops indicating the formation of a closed eddy (between day numbers 074 to 088). Eddy "B" was again identified on a subsequent cruise (26-30 May 1977) and the buoy tracks (day numbers 143 to 152) show the fully formed eddy to be drifting slowly southwards. The southern buoy positions show the buoy being trapped in a large, anticyclonic eddy and then being spun away and drifting towards the east. The letters A and B indicate the approximate centre of an existing and newly forming anticyclonic eddy respectively, and the numbers relate to the 4 cruise dates shown to the right of the figure. The 190 dyn.cm contour is also given for the 4

Buoy Tracks - 1977
(from Cresswell & Golding, 1979)

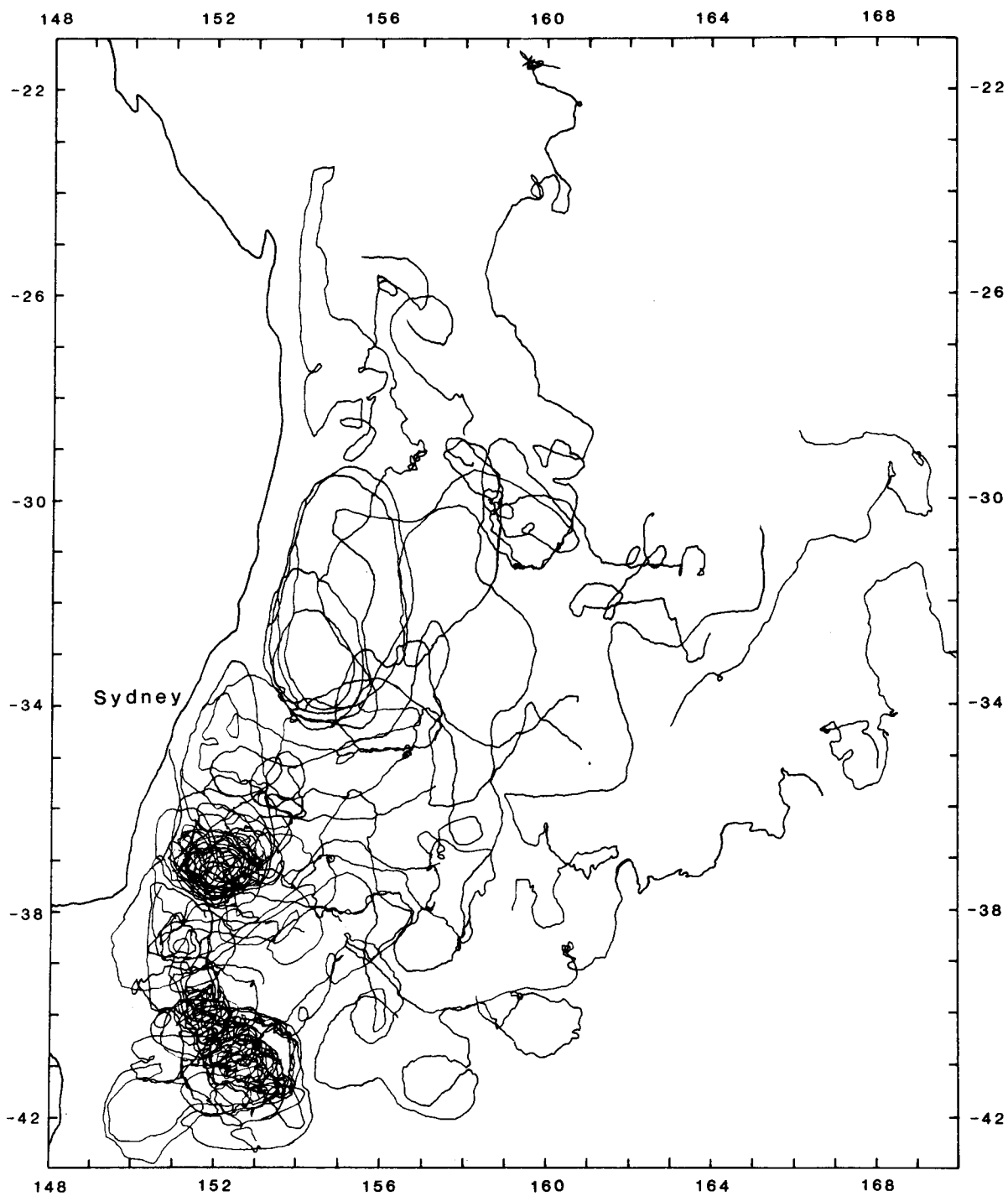


Figure 4.5

FORMATION OF AN ANTICYCLONIC EDDY

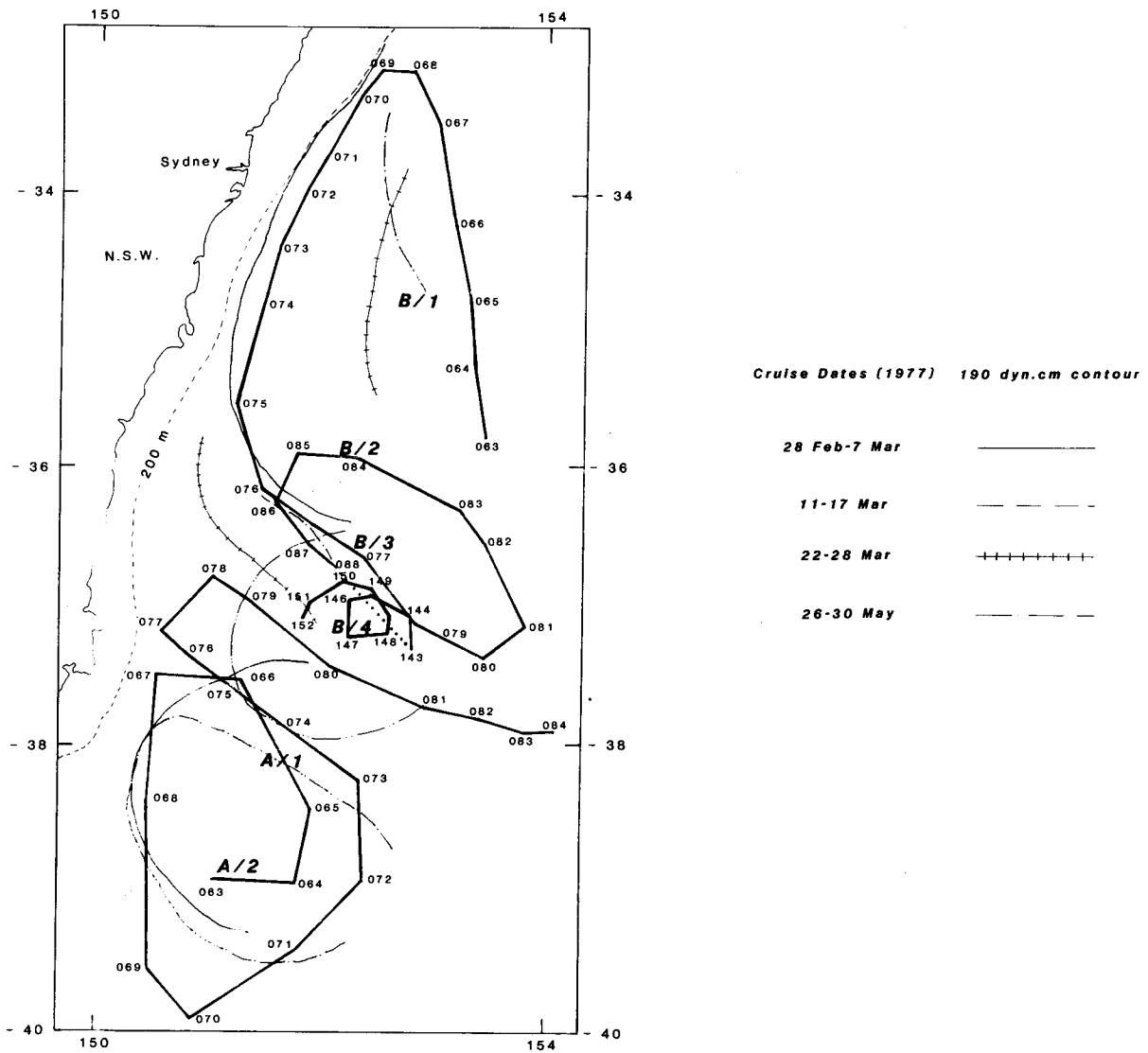


Figure 4.6

cruise dates, giving a rough indication of the position of the EAC axis or the extent of the eddy feature.

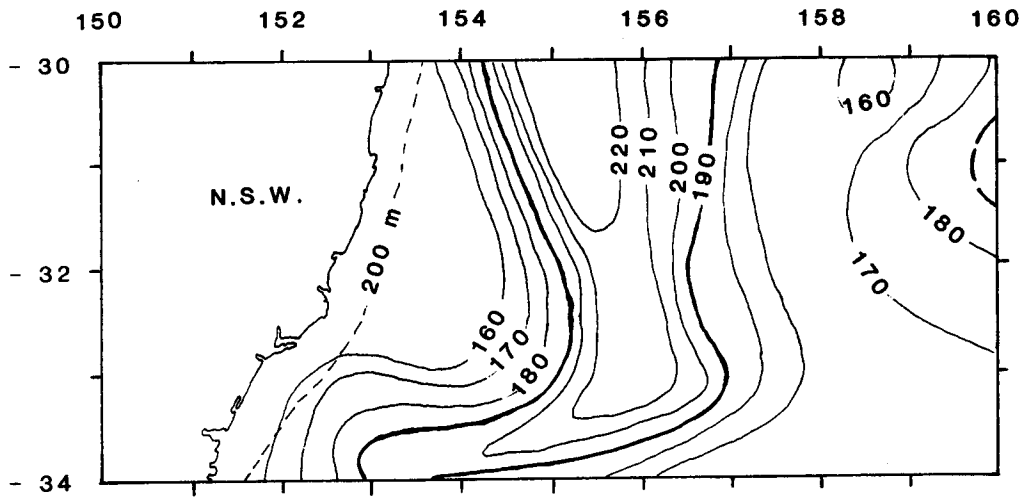
Eddy "B" trapped individual buoys for as long as 5 months and was found to have a lifetime exceeding one year. Cooling of the upper layers of the eddy during winter resulted in the progressive deepening of its isothermal mixing layer down to 350 m. Summer heating at the surface isolated the deepest part of this isothermal layer such that the layer became a signature of the eddy, i.e. summer "capping" as reasoned by Nilsson et al. (1977).

Pairs of buoys indicated that an annulus of the eddy rotated stiffly with periods of 7-10 days but that near the centre of the eddy the rotation period could be shorter (Nilsson & Cresswell 1980). Similar behaviour was seen in an Indian Ocean eddy (Cresswell 1977). At times the eddy moved in an anticlockwise arc, but it generally remained within 50 km of 37°S, 152°E. Eddy drift rates indicated by the buoys were observed to be up to 20 km/day but were usually of magnitudes 2-10 km/day.

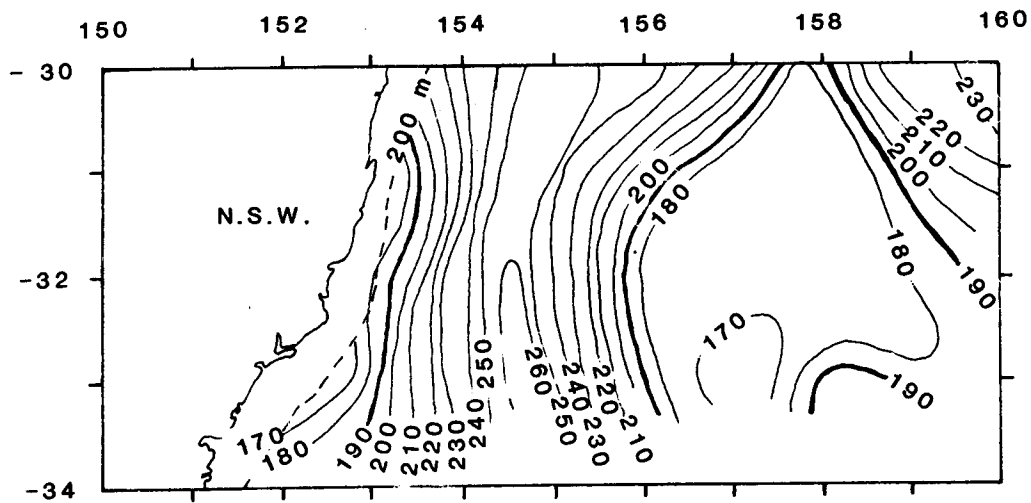
Recently several aircraft surveys of the Tasman Sea have been completed using airborne expendable bathythermographs (AXBT). A distinct advantage available using this data is the considerable area that may be surveyed in a relatively short period of time compared to conventional cruise techniques. From a knowledge of the temperature-salinity relationship for the area, the water density with depth may be calculated and hence a dynamic height map produced. The Tasman Front, the boundary between the warm Coral Sea water and the cooler Tasman Sea water was investigated by Andrews et al. (1979) using the AXBT data and cruise data. The Front as a coherent water mass, in one instance, was followed to the north of New Zealand. This pattern was evident on Wyrski's (1962) map but until that time had not been confirmed by direct evidence apart from observations to the northwest of New Zealand (Stanton 1976). The existence of the EAC and the Tasman Front as well as the considerable variation in time of the geographic position of the EAC axis is evident in Figure 4.7a & b taken from data available in Lawrence (1979). Figure 4.7b shows the large gradients (40 cm per 100 km) associated with the Tasman Front, which is seen to extend out to 160°E in the figure.

Recent studies by Godfrey et al. (1980a) suggest that colder, northward-flowing undercurrents move along the bottom of the continental shelf and slope areas with predicted speeds of 60 - 100 cm/sec. They

EAC and the Tasman Front



**A. Dynamic Height Anomaly (0/1300 m) Date: 13.12.1978
(in dyn. cm)**



**B. Dynamic Height Anomaly (0/1300 m) Date: 8.2.1979
(in dyn. cm)**

Figure 4.7

suggested that the entrainment of this cold water into the main EAC system may be a major source of frictional loss, comparable to the losses due to the shelf bottom topography. Utilising oceanographic data from the last two decades, Godfrey et al. (1980b) confirmed that the EAC behaves differently, at least qualitatively, on either side of a line extending south-southeast of Sugarloaf Point (32.5°S) - see Figure 4.3 . To the north of this imaginary axis, dynamic height contours are open and eddies are usually elongated in the north-south direction. Strong surface currents in this area are also marked by distinct surface temperature fronts. Smaller, relatively circular eddies seem to exist to the south of the line and the surface temperatures are not a reliable guide to dynamic height. As noted in Godfrey et al. (1980a), northward flowing, cooler currents on the continental shelf appear to be a common phenomena, suggesting entrainment with the EAC and a separation of flow near Sugarloaf Point. It has been proposed by Godfrey et al. (1980b) that this separation point may be topographically controlled due to the bend in the coastline at Sugarloaf Point.

4.2.5. Theoretical Studies of the Dynamics of the EAC.

Considerable value was derived from the theoretical studies and computer modelling of the EAC system by Godfrey & Robinson (1971) and Godfrey (1973a, 1973b). These studies focused observational attention on key dynamic features of the EAC system. Earlier cruise studies had revealed no obvious relationship between features of the local bottom topography and the patterns of dynamic topography which varied markedly within a time interval of a month or so.

The work of Godfrey & Robinson (1971) studied the hypothesis that the path of the EAC is determined by an approximate vorticity conservation equation appropriate to a thin, free current. A number of directly comparable studies had previously been attempted by Warren (1963) and Robinson & Niiler (1967) in connection with the Gulf Stream. According to the hypothesis above, the EAC may be regarded as a narrow filament of rapidly flowing water that moves steadily and without friction through a region of geostrophic flow. The success of the theory in reproducing some of the observed features of the current suggested that topographic effects are probably important in the dynamics of the EAC system. The modelled current, with an assumed velocity structure consistent with observational data, travelled about

1000 km southward along the east Australian coast before forming a loop around 35°S . However, some paths followed by the modelled current were unrealistic. The radii of curvature of the loops (70-110 km) agreed favourably with the radii of the eddies observed in the region. Godfrey and Robinson point out that despite their model being quantitatively invalid due to neglect of the longshore pressure gradient, the study showed the importance of bottom topography with respect to eddy generation.

Godfrey (1973a, 1973b) compared the EAC system with the numerical ocean model of Bryan & Cox (1968a, 1968b) pertaining to western boundary flow. The EAC was considered as a series of fluctuating, poleward, directed anticyclonic eddies. Dynamic height maps produced from Godfrey's model and from previous cruise data by Hamon (1965) generally showed:

(i) a net fall in dynamic height, from north to south, both close to the shore and out at sea,

(ii) a strong southward current near the shore and counter-current offshore,

(iii) a tendency for the current and counter-current to break up into anti-cyclonic eddies.

The dominant wavelength or distance between eddy centers derived from the model was 900 km compared to Hamon & Cresswell's (1972) figure of 400-600 km. Mass transport analysis in the model area roughly agreed with synoptic measurements taken over the same area (Scully-Power 1973; CSIRO Aust. 1962), in which subsurface inflow near Brisbane (30°S) appears to be a permanent feature of the EAC system. Godfrey showed that most of the time-averaged transport out of the EAC area occurs towards the east at around 35°S and that the remaining mass is transported southwards. In conclusion, Godfrey pointed out that for a more realistic model to be constructed, a proper understanding of how momentum is dissipated is required. It was also unlikely that a satisfactory understanding of the origin of seasonal variations in the current could be reached until increased knowledge of the frictional mechanisms was gained.

A drawback of theoretical studies in the EAC region at the time was that little was known about the evolution of EAC eddies from observational data so in comparing qualitatively the real and model systems, conclusions were difficult to draw as to the relevance of certain distinguishing model features.

4.2.6. Summary.

It is only in the last 3 years that the dynamics of the EAC have been determined with some degree of certainty. No longer is the EAC thought of as a southerly flowing steady current, originating in the Coral Sea and flowing to areas below Tasmania. The EAC flows south, just off the continental shelf adjacent to the coast between latitudes 20°S - 35°S and then the current separates from the shelf and travels in a meandering path across the Tasman Sea to the north of New Zealand. The current flows along the juncture of the warmer Coral Sea water and the cooler Tasman Sea water forming the Tasman Front. Due to the nature of hydrodynamic flow, the current moves in a meandering pattern. The major periodicity in the meanders is of the order 300 km and the point of separation of the current from the continental shelf is not constant in time but is located in the general area of 30°-34°S, especially near Sugarloaf Point (32.5°S), as noted by Godfrey et al. (1980b). Current speeds associated with the main axis of the current are in the range 100-200 cm/sec. Changes in surface temperature and dynamic height in crossing the main EAC are generally about 2°-4°C and 50 - 100 cm respectively.

The process of anticyclonic eddy formation is still not fully understood but much progress has been made in recent years. Satellite tracked buoys have confirmed the existence of between 3 to 5 anticyclonic eddies per year that drift slowly southward off the eastern NSW coast near the edge of the continental shelf. Drift rates of the eddies are generally between 2 - 10 km/day but at times have been observed to be as high as 20 km/day. The dynamics of anticyclonic eddy formation can simplistically be described as follows:- a sharp temperature front separates the warmer (about 24°C) southward flowing water, found offshore from the colder water (about 21°C) over the continental shelf. The colder shelf water often moves north (Godfrey et al. 1980b) and as the spill of warmer water is pinched off by the colder water, flow of the current to the south is broken and the warmer water is left resting on a layer of colder water and enclosed on the sides. This eddy feature moves away from the main front and drifts southward.

The dynamic relief of a typical warm core, anticyclonic eddy is about 50 - 100 cm and the eddies have diameters of the order 200 - 300 km. Temperature contrasts between the warmer, inner core and the surrounding colder water are in the range 1°-2° C but have been observed

to be up to 4°C. There is also a distinct, characteristic subsurface lens of mixed water associated with summertime eddies (December to May) whereas wintertime eddies have the mixed core open to the surface. The isothermal mixed layer depths vary between 150-350 m depending on the season and age of the eddy. EAC eddies have been noted to "stall" at around 35°S for periods of up to 50 days and generally remain in the same area for relatively long periods of time, as evidenced by the satellite buoy tracks.

It is considered that the altimetry data will be able to contribute to information about the anticyclonic eddies (e.g., the number of eddies present per year, their trajectories, overall shape and size, etc) and the presence and variability of the EAC and the Tasman Front. This type of data will greatly help to confirm and/or update the present understanding about the EAC described above.

4.3. The Gulf Stream Area.

4.3.1. Introduction.

It is not the intention here to give a detailed description of the Gulf Stream system since the literature relating to the dynamics of this area is considerable. An appropriate reference that describes the Gulf Stream dynamics in detail is Stommel (1965). In view of the analyses in Chapter 3, it would be of benefit however to have an idea of the temporal variability in this region and a general understanding of the dynamics of the eddy features, their formation, trajectories or paths in the ocean as the use of the altimeter data should be able to provide valuable information in studying these phenomena.

4.3.2. Variability of the Gulf Stream.

The Gulf Stream is a well defined dynamic boundary or front in the western North Atlantic between the slope water confined on the continental shelf areas and the Sargasso Sea. It is a continuous band of warm water about 100-150 km wide stretching from the Florida coast (26°N), past Cape Hatteras to a position of approximately 45°N, 310°E south of the Grand Banks of Newfoundland. The thermal front associated with the Gulf Stream is quite pronounced, being about 5°C in 20 km or

less. The strength of this temperature front varies considerably with season having a surface temperature differential of about 10°C in March and about 2°C in August. When crossing the Gulf Stream from west to east, one typically encounters an increase in temperature, salinity, and perhaps sea state, the water colour shifts from green to deep blue, and there is a rise in sea level of about 100 cm over 100 km due to steric effects, there is also a fairly sudden increase in horizontal velocity with maximum surface velocities of the order 300 cm/sec.

One of the most interesting features of the Gulf Stream is the horizontal wavelike perturbations or meanders that develop in its path when the Stream departs from the continental shelf near Cape Hatteras (35°N), leading to an ultimate loss of identity of the Stream as a coherent flow. Frequently these meanders become sufficiently large to pinch off from the main current and form eddies. Gulf Stream eddies play a vital role in transferring water, momentum, energy, etc northward across the Gulf Stream into the slope water regions and southward into the Sargasso Sea. Moreover, understanding eddy dynamics is a prerequisite for both valid modelling of large scale exchanges of momentum and energy, nutrients, etc and for realistic coupled ocean-atmospheric models necessary for climate modelling (Robinson & Baker 1979, Kraus 1977).

The oceanographic community has known about the existence of eddies for about 40 years (Iselin 1936) but detailed knowledge of their formation, distribution or paths in the ocean have been largely unknown until recent years, due to the lack of suitable long term tracking techniques. In the Gulf Stream area, the eddies or "rings" found can be generally classified into three categories:

- (i) Cold core (Cyclonic) eddies,
- (ii) Warm core (Anticyclonic) eddies, and
- (iii) Eastern eddies.

These classifications are described below. A comparison of eddy structures in the Sargasso Sea has been given in Cheney (1975), Hagan et al. (1978) and Robinson et al. (1979).

4.3.2.1. Cold core eddies.

During the past decade several cold water masses of slope water origin were found and tracked on the Sargasso Sea side of the Gulf Stream. Intensive surveys of these transient features have been made

and several time series and single hydrographic sections have been gathered in order to understand their physical structure. Until about 1970, all references to these ocean dynamic features used the term "eddy" but Fuglister (1972) suggested the term "ring" be used, since three distinct water types with a circular configuration were involved. Colder, less saline slope water is completely enclosed by a separated segment of the Gulf Stream (the "ring"), and these two volumes are surrounded by Sargasso Sea water. Thus, the term "ring" will be used in these sub-sections to distinguish between the frequent terminology related to mid-ocean mesoscale eddies (MODE Group 1978). During their lifetime, many rings qualify as mid-ocean mesoscale phenomena but unlike the mid-ocean eddies, rings are discernable through their water mass properties and their life cycle is more or less known.

Gulf Stream rings are the most energetic of ocean eddies in the North Atlantic and are known to play an important role in the general circulation of the area. Historically, observations of these rings have been reported by numerous investigators including Iselin (1936, 1940), Fuglister (1947), Iselin & Fuglister (1948), Fuglister & Worthington (1951), Fuglister (1963) and Barrett (1963). Observational data for these studies relied primarily on repeated ship cruises, and later, ART measurements.

The formation of all rings from the meanders of the Gulf Stream is basically similar in all cases and has been well documented in the literature (Fuglister & Worthington, 1951; Hansen 1970; Parker 1971; Cheney & Richardson 1976). The following sequence of events, from Parker (1971), explains in a simplified way the process of ring formation. When a meander of the Gulf Stream reaches sufficient amplitude, usually about 300-400 km in diameter, the direction of Gulf Stream flow altered from a generally eastward to a southward direction. Fresher, colder slope water (about 12°C, 33‰) is drawn south with the meander and as the meander deepens to the south, the northwest segment of the meander has a tendency to move gradually eastwards. Thus, the northern end of the meander is closed off as this segment merges with the eastern side of the Gulf Stream loop. This effectively cuts off a pocket, or ring, and the Stream resumes its easterly flow. A body of colder, less saline slope water is left south of the Gulf Stream, completely surrounded by a ring of warm Gulf Stream water (about 21°C, 36‰), whose velocity is essentially that of the main Gulf Stream system. When separation is complete, the ring and the cold core rotate

in an anticlockwise direction (in the northern hemisphere) in the surrounding Sargasso Sea water and do not appear to receive any further energy from the Gulf Stream. Rings have been observed to form over periods of approximately 4-5 weeks (Doblar & Cheney 1977).

Cyclonic surface circulation of the ring is of the order 100-200 cm/sec (Richardson et al. 1973). Each cyclonic ring is a unique mesoscale structure and is expected to exhibit distinct physical, chemical and biological differences from other rings. The primary dynamic elements associated with rings are the pressure gradients, Coriolis forces and frictional forces which combine in the upper layers to produce a convergence towards their interior. Evidence has been found for interior mixing and detrainment through the mid-thermocline (Vastano & Hagan 1977). The flow in rings is such that ring evolution will take place slowly provided that external interactions do not occur, such as collision with other rings or coalescing with the Gulf Stream (Richardson 1980).

The physical character of the cold core of a cyclonic ring resembles a dome, rising up about 500-600 m through the main thermocline. This dome, with a cyclonic rotation imparted to it during the entrainment process, may extend down to at least 3000 m. The size and shape of these rings can be determined from cruise temperature data, or remotely sensed data such as IR imagery or altimeter data. However, these latter two data sources can only give an indication of the surface character of the rings. Temperature differences at the surface between the ring centre and the surrounding Sargasso Sea are generally about 4-8°C but can be as low as 2°C during the summer months or as the ring core decays and there is increased mixing with the surrounding warmer water. Typical cold core ring diameters, defined by the conventional standard of the intersection of the 15°C isotherm and 500 m depth, are between 50-200 km depending on the age of the ring, with surface diameters for the rings being of the order 200-400 km (Cheney & Richardson 1976, Richardson et al. 1978). However, diameters of rings may vary considerably since they are a function of the magnitude of the initial meander, the width of the enclosed pocket and the width of the main Stream at the time of encirclement.

Generally rings are elliptical or circular in shape. Shape determination using XBT sections can be affected by the ring translation rate during the cruise observation period. Oceanographers suggest that despite the fact that the ring may drift several kilometers during a

survey, the error in determining the ring characteristics is small compared to the overall dimensions of the ring. In recent years, the use of satellite IR imagery has greatly aided oceanographers in defining the locations and shapes of Gulf Stream rings (Richardson et al. 1973; Stumpf et al. 1973; Vukovich 1976) and even enabled the planning of oceanographic field measurement programs (Vukovich & Crissman 1978).

A survey of Gulf Stream rings in the period March to May 1975 by Richardson et al. (1978) showed that the character of the cold core rings east of about 300°E appeared to be different from those of rings to the west of this limit. The western rings appeared nearly round, having steep gradients in the isotherms. The eastern rings have been classified as "big babies" by McCartney (1975) and will be discussed separately below.

Observations indicate that a high proportion of rings are formed between longitudes $290\text{--}300^{\circ}\text{E}$ with some 5 to 8 cyclonic rings being formed per year (Newton 1961; Fuglister 1972; Barrett 1971). At any one time about 8 to 14 rings have been located south of the Gulf Stream and west of 310°E (Richardson et al. 1977; Lai & Richardson 1977; Richardson et al. 1978). Few cyclonic rings have been found south of 30°N except in the extreme western regions near Florida.

The translation rates of the rings are highly irregular varying between 1-8 km/day (Lai & Richardson 1977). Ring trajectories have been noticed by Richardson (1980) to be of two types. Firstly, the movement of rings that are south of the Gulf Stream and away from its influences show general movement in a westward direction, but the movement may sometimes be northwest or southwest. The motion described here is the average mean motion and rings will exhibit considerable variation from this mean over periods of up to several months. The process causing rings to move generally westwards has not been determined. Mathematical models suggest a westward movement due to the meridional variation in the Coriolis effect (Warren 1967). It has also been suggested that the rings are advected by the mean ocean flow (Lai & Richardson 1977) associated with the general recirculation in the Atlantic. The second type of ring trajectory is directed in a downstream direction parallel with the Gulf Stream. This occurs when a cyclonic ring is attached to or interacting with the Gulf Stream.

Typical surface reliefs of cyclonic rings are between 30 to 80 cm (Cheney & Richardson 1976), being a depression of the ocean surface. Expected lifetimes of the cyclonic rings are of the order of 3 to 5

years based on the rates of decay of available potential energy of the rings (Barrett 1971) but again this figure varies greatly depending on whether the rings interact with the Gulf Stream (Watts & Olson 1978; Richardson 1980) or move onto the continental shelf areas (Cheney & Richardson 1976).

4.3.2.2. Warm core eddies.

Anticyclonic or warm core rings entrain warmer, more saline water from the Sargasso Sea into the colder, fresher slope water on the shelf areas north of the Gulf Stream. These rings appear to form in a similar manner as the cold core rings described above. The first observations of the formation of an anticyclonic ring were by Saunders (1971) and Gotthardt (1973). Typical dimensions of anticyclonic rings are about 200 x 100 km at the surface and about 120 x 60 km at 200 m depth measured by the 15° isotherm. Thus, warm rings are smaller in size compared to the cold rings. Downwarping of the isotherms and isopycnal surfaces of warm rings has been evident down to depths of 1800 m (Fornshell 1977).

Lai & Richardson (1977) and Richardson et al. (1978) indicated the formation of about 3 to 5 warm rings per year with approximately 3 rings existing at a single time. The rings were usually formed from between 500 to 1000 km downstream from Cape Hatteras and generally moved westwards towards Cape Hatteras with average speeds of between 3-7 km/day (Lai & Richardson 1977). There is little variation from this mean movement as the rings are confined by the continental slope to the north. Consequently, the warm rings are usually recaptured by the Gulf Stream close to the continental shelf near Cape Hatteras.

Observations of warm rings using both satellite and oceanographic data have been made by Gotthardt & Potocsky (1974), Apel & Apel (1976) and Halliwell & Mooers (1979). The latter study confirmed the existence of some 4 warm rings over a 2 year period with a mean southwest propagation speed of about 5 km/day.

Dynamic relief of the warm rings shows typical elevations of the ocean surface of between 20-60 cm. Expected lifetimes of these rings are about 1 year (Perchal 1975). However, warm rings exhibit considerable variation from the pattern described above as occasionally the warm rings are recaptured shortly after formation by Gulf Stream meanders or may even split into 2 smaller eddies (Gotthardt & Potocsky

1974). Warm rings have also been observed to form after a cold core ring has coalesced with the Gulf Stream (Cheney et al. 1976).

4.3.2.3. Eastern eddies.

Lai & Richardson (1977) identified 11 rings in the Sargasso Sea region east of 300°E from XBT data collected between 1970-1976. This region had previously been thought to be devoid of rings (Parker 1971). Early evidence for the existence of rings in this eastern region came from McCartney (1975) who used the term "big babies" to differentiate these rings from those cyclonic rings found further westward. The eastern rings have cold cores with slightly different characteristics than the parent slope water but they have larger diameters than the cold rings - typical diameters are about 200 km at 500 m using the 15°C isotherm.

Observations by McCartney et al. (1977) suggest that the eastern rings may form at the eastern end of the Sargasso Sea gyre, near 320°E and drift westwards with average speeds of 2-5 km/day. The lifetime of one of the observed rings was estimated at 11 months. The surface depression of an eastern ring, implied by the temperature profile of McCartney et al. (1977, Figure 11), is about 50 cm. Details about the eastern rings and where and how they form are very preliminary. The use of satellite altimetry data may provide the necessary observations to postulate quantitative details about these rings.

5. GRAVITY FIELD IMPROVEMENTS VIA THE BOUNDARY VALUE PROBLEM

5.1. Introduction.

5.1.1. Background.

The geodetic literature setting out mathematical formulations of the GBVP is quite substantial. Some selected references on the subject are Molodenskii et al. (1962), Bjerhammer (1962), Moritz (1966, 1969) and Krarup (1969). But the first comprehensive study of a direct solution of the BVP to satisfy the requirements for obtaining a precision of ± 10 cm, adequate for oceanographic studies, is due to Mather (1973a, 1973b). An alternate development for the computation of geoidal undulations accurate to 10 cm was given by Moritz (1974) taking into account corrections for the Earth's ellipticity, topography and atmosphere. However, the solution procedure adopted in this Chapter follows the principles developed in Mather (1973a).

In the investigations by Mather (1974a; 1974b; 1975b) it was recognised that any determination of quasi-stationary SST - the deviations of MSL from a level surface of the Earth's gravity field over the duration of a satellite mission - would have to contend with the following factors if a meaningful solution were to be obtained from satellite altimetry data:

- (i) The data available for the task is surface gravity information, on land and in continental shelf areas, and satellite altimetry data in oceanic regions. No complete global coverage is likely to exist in either data set. In the Australian region, the precision of oceanic gravity data is at least an order of magnitude worse than that of land gravity data. Individual marine gravity measurements can be made with accuracies of the order of 1 mGal, but the present global marine gravity data has standard errors in the range 5 to 10 mGal (Watts 1978). It has been shown that existing surface gravity data banks are only adequate for SST determinations with a precision of ± 30 cm (Mather et al. 1976).

- (ii) All data at (i) is referred to the ocean surface, either instantaneous or MSL, and not the geoid.
- (iii) Eventually, a precision of ± 10 cm or its equivalent would have to be achieved in all measurements for wavelengths equivalent to those sought in the determination of SST.
- (iv) Determinations have to contend with the presence of systematic errors of long wavelength in all data.
- (v) Local MSL approximates the geoid to no better than $\pm 1-2$ m .

The requirements to be met by surface gravity data in solutions for a ± 10 cm ocean geoid have already been assessed (Mather 1975b, p.80). These requirements may be summarized as

- (i) Global gravity standardisation networks should have a desirable station spacing of 1000 km in continental areas. Measurements of gravity should aim for a resolution of 0.1 mGal and be free of significant correlation of errors between adjacent values.
- (ii) Geopotential values of land gravity stations in a network should be derived from levelling data such that correlated errors are held below 0.15 kGal m, but individual connections may have uncorrelated errors at the 1-2 kGalm level.
- (iii) A gravity station spacing of approximately 10 km in non-mountainous areas should be used such that the error of representation is ± 3 mGal for such a sampling.
- (iv) Values of normal gravity (γ) should be computed using geocentric coordinates.
- (v) The contribution of long wavelength systematic errors in gravity anomalies due to (i) and (ii) should be kept below the ± 50 μ Gal level.

The current global gravity standardisation network (IGSN 71) is estimated to have a resolution at the 0.2 mGal level (Morelli et al. 1971). This is inadequate for SST determinations and it is questionable whether the gravity data banks currently available reflect even the resolution of this network. A gravity data bank for Australia, (AUSGAD 76) adequate for determinations of SST at the ± 30 cm level, was prepared by Mather et al. (1976, and subsequently updated by Rizos

(1980) with the inclusion of additional marine gravity data. However, a precision of 30 μ Gal in the gravity anomaly data is needed to satisfy the goal ± 10 cm resolution in SST studies. This precision is at present unattainable by field measurements where errors of 1-2 orders of magnitude greater than this figure occur in the individual observations.

The elevation of the instantaneous sea surface as deduced from satellite altimetry is affected by the following error sources:

- a) Errors in the tracking data and the satellite altimeter measurements.
- b) Effects of errors in the gravity field model used in the orbit analysis in the case where dynamic techniques are used in orbit determination (see Gaposchkin (1978) and Smith (1979) for reviews of the current status of dynamic satellite techniques).
- c) Effect of orbital distortion produced by holding erroneous tracking station coordinates fixed in orbit analysis.

The errors at b) and c) are functions of position while those at a) are more likely to be functions of time, especially if the radar altimeter and tracking equipment are regularly calibrated. As the SSH above a specified reference ellipsoid (ζ) is the average taken over a basic element of surface area, the errors at a) are more likely to have the characteristics of random errors as a function of position. Those at b) and c) are expected to give rise to systematic error patterns in the global distribution of ζ . The nature of the errors at b) can be seen in Rapp (1975, Figure 1) where the southern ocean areas are dominated by long wavelength errors of the order 2×10^3 km.

5.1.2. Fundamental Relations.

Any solution procedure seeking the definition of SST should have the capacity to achieve an unambiguous result with a resolution of ± 10 cm in the presence of the above mentioned errors. It was in this context that a technique was outlined (Mather 1975b, p.74) for the definition of quasi-stationary SST. The method was based on a solution of the GBVP taking factors b) and c) into account.

The basic solution could be defined via the following relations. The height anomaly (ζ') in relation to the "higher" reference system (see Section 2.2) is defined by (Mather 1974b, p.100),

$$\zeta' = N_s + N_{ns} \quad (5.1)$$

where the Stokesian term N_s and the non-Stokesian contribution N_{ns} are given by

$$N_s = \frac{1}{\gamma} [(W_o - U_o) - \bar{R} M\{\Delta g_c\} + 2M\{\delta W\} - \delta W] + \frac{\bar{R}}{4\pi\gamma} \iint f(\psi) \Delta g_c d\sigma - \frac{1}{2\pi\gamma} \iint f(\psi) \delta W d\sigma + O\{f N_s\} \quad (5.2)$$

and

$$N_{ns} = \sum_{\alpha=1}^2 \left(\frac{V}{\gamma} + \frac{1}{2\pi\gamma} \iint \frac{R^2}{r} \left(\frac{\partial T''}{\partial x_\alpha} \tan\beta_\alpha + T'' \left(\frac{x_\alpha \tan\beta_\alpha}{r^2} - \frac{1}{2R} [\phi - 3[c_\Delta - 3\frac{dR}{R}]] \right) - \delta\Delta g'' + \Delta g'' \left(c_\Delta + \frac{3}{2} \frac{dR}{R} \right) + O\{f^2 \Delta g\} \right) d\sigma \right) \quad (5.3)$$

where the following terms are defined :

- $c_R = f(1/3 - \sin^2\phi_c) + h/R + o\{f^2\}$. Subscript p refers to values at the point of computation
 $c_r = ((R_p - R)/r_o)^2 + c_R + c_R + o\{f^2\}$; c_r is the value on the Brillouin sphere P
 $c_\Delta = (1 + 2 dR/R)/(1 + c_r)^{1/2} - 1$
 $c = f + m - 3f \sin^2\phi_c$ (see equation 2.51)
 $dR = \bar{R} - R$
 $d\sigma =$ Element of solid angle
 $f =$ flattening of meridian Earth ellipse
 $f(\psi) =$ Stokes' function $= \sum_{n=2}^{\infty} \frac{2n+1}{n-1} P_{no}(\cos\psi)$
 $M\{X\} =$ global mean value of X
 $m =$ Ratio of centrifugal force (Ω) to normal gravity at the equator (γ_e) of an equipotential ellipsoid; $m = a\Omega^2/\gamma_e$
 $R =$ distance from the centre of mass of the solid Earth & oceans. Subscript p refers to the point of computation.
 $\bar{R} =$ Radius of the Brillouin sphere
 $r =$ distance of an element of surface area on the Earth from the point of computation, P.
 $\bar{r} = 2\bar{R} \sin \frac{1}{2}\psi$
 $r_o = 2R \sin \frac{1}{2}\psi + o\{fr_o\}$
 $U_o =$ potential of the equipotential ellipsoidal reference

- system on the surface of the ellipsoid of reference .
- V = potential of the atmosphere
- W_0 = potential of the geoid (unknown)
- x_α = two dimensional Cartesian coordinate system in the horizontal plane at the point of computation P, with the x_1 axis oriented north and x_2 axis east.
- β = ground slope; β_1 and β_2 are components in the meridian and prime vertical directions respectively
- γ = normal gravity on the "higher" reference model
- Δg = gravity anomaly at the surface of the Earth
- $\delta \Delta g''$ = change in $\Delta g''$ between the Earth's surface and the Brillouin sphere (see Mather 1975b, p.71)
- δW = Geopotential between the sea surface/levelling datum and the geoid
- Φ = $2R(R \cos \delta - R_p \cos (\psi + \delta))/r^2 - 1$
- δ = $f \sin 2\phi_c \cos A_z + o\{f^2\}$
- A_z = azimuth of the point of computation P from $d\sigma$
- ψ = Angle between geocentric radii to the element of surface area $d\sigma$ and the point of computation P.
- ϕ_c = geocentric latitude
- λ = longitude
- T' = disturbing potential of the solid Earth and oceans with relation to an ellipsoidal reference model
- T'' = disturbing potential of the solid Earth and oceans on the "higher" reference system.

The Stokesian term in equation 5.1 is defined on the smallest geocentric sphere enclosing the Earth and its topography but not its atmosphere (the Brillouin sphere). This permits the inter-conversion between surface and spherical harmonic representations on the Brillouin sphere, of functions related to the disturbing potential T'' of the solid Earth and oceans on the "higher" reference system. Equation 5.2 makes allowance for the fact that

- a) at sea, surface gravity is measured at the ocean surface and not the geoid and/or ,
- b) on land, the gravity anomaly is constructed from normal gravity values which are computed using geopotential differences from a datum level surface which is not necessarily the geoid.

The following equations define the basic quantities. The

disturbing potential of the solid Earth and oceans on the "higher" reference system, T'' , is given by (equation 2.46)

$$T'' = (W_o - U_o) + \delta W - V + \gamma \zeta' + O\{10^{-3} T''\} \quad (5.4)$$

at the Earth's surface where ζ' is the height anomaly on the "higher" reference system. This is a generalisation of Brun's formula (H & M 1967, p.85) for the basic harmonic quantity at the surface of measurement. T_c is the part of T'' which can be evaluated prior to computations, possibly in an iterative procedure, on the Brillouin sphere. T_c is given by (Mather 1975b, p.75)

$$T_c = \gamma \zeta' + dR \frac{\partial T''}{\partial h} - V + O\left\{\frac{1}{2}(dR)^2 \frac{\partial^2 T''}{\partial h^2}\right\} \quad (5.5)$$

The pseudo gravity anomaly $\Delta g''$ is exactly related to T'' and is therefore harmonic in the space exterior to and down to the surface of measurement. $\Delta g''$ is given by (Mather 1975b, p.73),

$$\Delta g'' = -\frac{\partial T''}{\partial h} - \frac{2T''}{R} = \Delta g + \delta g_a - \delta \gamma + \frac{2T''}{R} c_\phi - \frac{1}{2} g \zeta_d^2 - \frac{2}{R}(W_o - U_o) - \frac{2\delta W}{R} + O\{10^{-8} g\} \quad (5.6)$$

the second relation holding at the surface of measurement, where δg_a is the atmospheric effect on the gravity anomaly observed at the Earth's surface and ζ_d is the deflection of the vertical, positive if the outward vertical is north/east of the spherop normal. Δg_c is the estimate of $\Delta g''$ on the Brillouin sphere which can be computed in advance of numerical evaluations and is given by (Mather 1975b, p.75),

$$\Delta g_c = \Delta g + \delta g_a + \frac{2T''}{R} c_\phi - \frac{1}{2} g \zeta_d^2 + \delta \Delta g'' + O\{10^{-8} g\} \quad (5.7)$$

where $\delta \Delta g''$ is the change in $\Delta g''$ between the surface of measurement and the Brillouin sphere and, to the first order, is (Mather 1975b, p.71),

$$\delta \Delta g'' = -\gamma \left(\sum_{\alpha=1}^2 \frac{\partial \xi_\alpha}{\partial x_\alpha} - (\xi_1 \tan \phi) / R - 2\zeta' / R^2 + O\{f(\partial \Delta g'' / \partial h)\} \right) dR + O\{dR^2 (\partial^2 \Delta g / \partial h^2)\} \quad (5.8)$$

where $\partial \xi_\alpha / \partial x_\alpha$ are the horizontal gradients of the components of the deflection of the vertical. For a variation in $\partial \xi_\alpha / \partial x_\alpha$ of 1-10 arcsec per 100 km, the magnitude of $\delta \Delta g''$ varies from 1-10 mGal (Mather 1974b, p.99). As in the case of equation 5.5, equation 5.7 has to be evaluated

iteratively in relation to equations 5.1, 5.2 and 5.3. In oceanic regions, the height of the ocean surface (ζ') above the "higher" reference surface is related to the ocean geoid height N by

$$\zeta' = N - \delta W/\gamma - \zeta_t \quad (5.9)$$

where δW is the difference in potential between the ocean surface and the geoid (see equation 2.44) but if δW is not considered, errors of ± 0.3 mGal per ± 1 m of SST will occur in gravity anomaly data banks (Rizos 1980, p.165). ζ_t is the height of the ocean tide defined in equation 7.31.

In an earlier development (Mather 1975b, p.78), it was suggested that an alternate form of the Stokesian term

$$N_s = \frac{1}{\gamma} [M\{T_c\} + M\{\delta W\}] + \frac{1}{4\pi\gamma} \iint M(\psi) T_c \, d\sigma + \frac{1}{4\pi\gamma} \iint M(\psi) \delta W \, d\sigma \quad (5.10)$$

where

$$M(\psi) = \sum_{n=2}^{\infty} (2n+1) P_{no}(\cos\psi) = -(1+3 \cos \psi) \quad \text{if } \psi \neq 0 \quad (5.11)$$

be used to filter out the errors in ζ' obtained as input from

- (a) satellite altimetry in ocean areas; and
- (b) evaluations of equations 5.1, 5.2 and 5.3 in continental areas.

The technique required setting up observation equations in oceanic areas of the form

$$\zeta'_{oi} + e_{Ni} = \frac{1}{\gamma} M\{T_c\} - \frac{1}{\gamma} \delta W_i + \sum_j A_{ij} \delta W_j + K_i \quad (5.12)$$

on defining the geoid as the surface for which $M\{\delta W\} = 0$, where

$$A_{ij} = \frac{1}{4\pi\gamma} \iint_{\sigma_j} M(\psi_{ij}) \, d\sigma_j \quad (5.13)$$

and

$$K_i = \frac{1}{4\pi\gamma} \iint M(\psi_i) T_c \, d\sigma + N_{ci} \quad (5.14)$$

would be solved for δW in the form of a surface harmonic series

$$\delta W = \sum_{n=1}^{\infty} \delta W_n = \sum_{n=1}^{\infty} \sum_{m=0}^n \sum_{\alpha=1}^2 \delta W_{\alpha nm} S_{\alpha nm} \quad (5.15)$$

where $S_{\alpha nm}$ are surface spherical harmonics given by equation 2.32 .

$$S_{1nm} = P_{nm}(\sin\phi) \cos m\lambda \quad (5.16)$$

$$S_{2nm} = P_{nm}(\sin\phi) \sin m\lambda$$

In equation 5.12, the height anomaly on the "higher" reference system ζ' is related to the quantity deduced from satellite altimetry (ζ'_0) in ocean areas by the relation

$$\zeta' = \zeta'_0 + e_N \quad (5.17)$$

where e_N is the observational error. The quadratures evaluation of the surface integral in equation 5.14 using the closed form for $M(\psi)$ in equation 5.11 results in a value which tends to zero due to the non-existence of this form when $\psi = 0$. On using the orthogonal properties of surface harmonics, it can be shown that

$$K'_i = K_i - N_{ci} = \frac{1}{4\pi\gamma} \iint M(\psi_i) (T_c - T_{ci}) d\sigma + \frac{T_{ci}}{4\pi\gamma} \iint M(\psi_i) d\sigma = \frac{1}{4\pi\gamma} \iint M(\psi_i) (T_c - T_{ci}) d\sigma \quad (5.18)$$

Equation 5.18 could be evaluated using $M(\psi)$ in its closed form given in equation 5.11. On using equation 5.17 in equation 5.18,

$$K'_i = \frac{1}{4\pi\gamma} \iint M(\psi_i) (T_{co} - T_{coi}) d\sigma + \frac{1}{4\pi} \iint M(\psi_i) (e_N - e_{Ni}) d\sigma \quad (5.19)$$

where

$$T_{co} = \gamma\zeta'_0 - V + dR \frac{\partial T''}{\partial h} \quad (5.20)$$

If e_N is expressed as a series of surface spherical harmonics of the form

$$e_N = \sum_{n=0}^{\infty} e_{Nn} \quad (5.21)$$

then, on using the orthogonal properties of surface harmonics and

equation 5.11, it follows that

$$\frac{1}{4\pi} \iint M(\psi_i) (e_N - e_{Ni}) d\sigma = e_{Ni} - e_{No} - e_{Nli} \quad (5.22)$$

the subscript i referring to evaluation at the i -th point. e_{No} and e_{Nli} define the zero and first degree terms of equation 5.21. In this case, equation 5.12 reduces to

$$\zeta'_{oi} + e_{Nli} = \frac{1}{\gamma} [M\{T_{co}\} - \delta W_{li}] + \frac{1}{4\pi\gamma} \iint M(\psi_i) (T_{co} - T_{coi}) d\sigma + N_{ci} \quad (5.23)$$

with contributions of first degree occurring as a result of terms not involved in surface integrations on the Brillouin sphere. Such harmonics are specifically excluded from surface integrals in maintaining coordinate systems (Mather 1974b, p.97).

Thus, the solution proposed in Mather (1975b) is only sensitive to effects of first degree in the input values (ζ'_o) of ζ . Therefore, the integral at 5.10 is unable to differentiate between the SST and any observational errors in the satellite altimetry. Consequently, one of these quantities should be significantly smaller than the other before a definitive determination is possible. It will be shown, in sub-section 5.2.3, that this limitation in one form or another occurs in all possible expressions relating the SST, satellite altimetry and/or surface gravity data in terms of formulations of the GBVP which are valid at the surface of the Earth.

It therefore becomes necessary to explore other avenues for separating the signal of the SST from error sources of equivalent wavelength in the data.

5.2. Relations Between the Gravity Anomaly, Height Anomaly and SST.

5.2.1. A Basic Relation.

A scalar which satisfies Laplace's equation exterior to and down to the surface of measurement is the disturbing potential due to the solid Earth and oceans (T''), given on the surface of measurement by equation 5.5. T'' can be expressed by the relation (see H & M 1967, equation 1-87b)

$$T'' = \frac{GM_e}{R} \sum_{n=0}^{\infty} \left(\frac{a}{R}\right)^n T''_n \quad n \neq 1 \quad (5.24)$$

where the surface spherical harmonic T''_n is given by

$$T''_n = \sum_{m=0}^n \sum_{\alpha=1}^2 dC_{\alpha nm} S_{\alpha nm} \quad (5.25)$$

$dC_{\alpha nm}$ are the spherical harmonic coefficients of degree n and order m in the spherical harmonic representation of T''_n . They are defined by the expression

$$dC_{\alpha nm} = C_{\alpha nm} - C'_{\alpha nm} - \left(\frac{R}{a}\right)^n V_{\alpha nm} \quad (5.26)$$

where $C_{\alpha nm}$ are the "true" spherical harmonic coefficients of the Earth's geopotential, $C'_{\alpha nm}$ are estimates of the spherical harmonic coefficients of the geopotential $C_{\alpha nm}$ to some maximum degree n' , as obtained from satellite orbit analysis and $V_{\alpha nm}$ are the spherical harmonic coefficients of a representation of the atmospheric potential for all points exterior to the geocentric sphere (radius R_a) enclosing the Earth's atmosphere. If the coefficients $C'_{\alpha nm}$ are free of error, $dC_{\alpha nm}$ contains only terms relating to the atmospheric potential. Hence T'' contains only the short wavelength components of the geopotential, corresponding to degrees higher than n' in the representation of the spheropotential ΔU_s (Equation 2.31), and all wavelengths in the atmospheric potential. In practice, the satellite determined gravity field model coefficients $C'_{\alpha nm}$ are incorporated into the "higher" reference model (see Section 2.2) and,

$$dC_{\alpha nm} = \left(\frac{R}{a}\right)^n V_{\alpha nm} + 0\{+0.1 \text{ kGal m}\} \quad \text{for } n \leq n' \quad (5.27)$$

The other quantities defined in equation 5.24 are the mass of the solid Earth and oceans M_e , G the gravitational constant, R the distance from the centre of mass of the solid Earth and oceans and the equatorial radius of the Earth, a . The exclusion of the first degree term in Equation 5.24 has the effect of placing the centre of the reference ellipsoid at the centre of mass of the solid Earth and oceans.

Let the value of T'' on the Brillouin sphere (\bar{T}'') be given by

$$\bar{T}'' = \frac{GM_e}{R} \sum_{n=0}^{\infty} \left(\frac{a}{R}\right)^n \bar{T}''_n = \frac{GM_e}{R} \sum_{n=0}^{\infty} \left(\frac{a}{R}\right)^n \sum_{m=0}^n \sum_{\alpha=1}^2 dC_{\alpha nm} S_{\alpha nm}, \quad n \neq 1 \quad (5.28)$$

Define \bar{N}'' , using Brun's formula (H & M 1967, equation 2-144),

$$\bar{N}'' = \frac{\bar{T}''}{\gamma} = \sum_{n=0}^{\infty} \bar{N}''_n, \quad n \neq 1 \quad (5.29)$$

where

$$\bar{N}''_n = \frac{1}{\gamma} \bar{T}''_n \quad (5.30)$$

γ is adequately represented by the mean value of normal gravity on the Brillouin sphere as the "higher" reference model is being used. The pseudo gravity anomaly $\Delta g''$ is also harmonic in the space exterior to and on the surface of measurement, as can be seen from equation 5.6, taking the value $\Delta \bar{g}''$ on the Brillouin sphere. Consequently, $\Delta \bar{g}''$ can be expressed in terms of a spherical harmonic representation, as

$$\begin{aligned} \Delta \bar{g}'' &= GM_e / \bar{R}^2 \sum_{n=0}^{\infty} (n-1) (a/\bar{R})^n \bar{T}''_n, \quad n \neq 1 \\ &= \gamma \left(\sum_{n=0}^{\infty} (n-1) \bar{N}''_n \right) / \bar{R}, \quad n \neq 1 \end{aligned} \quad (5.31)$$

on using equation 5.30.

Equation 5.31 can be written as

$$\Delta \bar{g}'' + \gamma \bar{N}'' / \bar{R} = \gamma \left(\sum_{n=2}^{\infty} n \bar{N}''_n \right) / \bar{R} \quad (5.32)$$

The use of the orthogonal properties of surface spherical harmonics on the Brillouin sphere gives

$$\Delta \bar{g}'' + \gamma \bar{N}'' / \bar{R} = \frac{\gamma}{4\pi \bar{R}} \sum_{n=2}^{\infty} (2n+1) n \iint P_{no}(\cos\psi) \bar{N}'' d\sigma = \frac{\gamma}{4\pi \bar{R}} \iint M_1(\psi) \bar{N}'' d\sigma \quad (5.33)$$

where

$$M_1(\psi) = \lim_{R_p \rightarrow \bar{R}} \left(\sum_{n=2}^{\infty} (2n+1)n \left(\frac{\bar{R}}{R_p}\right)^n P_{no}(\cos\psi) \right) \quad (5.34)$$

R_p being the geocentric distance to the computation point upward continued to the Brillouin sphere. On using the zonal harmonic representation for the distance r between this point and the element of surface area $d\sigma$ on this sphere, given by (H & M 1967, equation 1-81)

$$\frac{1}{r} = \frac{1}{R_p} \sum_{n=0}^{\infty} \left(\frac{\bar{R}}{R_p}\right)^n P_{no}(\cos\psi)$$

it follows that

$$M_1(\psi) = \lim_{R_p \rightarrow \bar{R}} \left(2 \sum_{n=2}^{\infty} n(n+1) \left(\frac{\bar{R}}{R_p}\right)^n P_{no}(\cos\psi) - \sum_{n=2}^{\infty} n \left(\frac{\bar{R}}{R_p}\right)^n P_{no}(\cos\psi) \right)$$

$$\text{As } R_p \rightarrow \bar{R}, \quad r \rightarrow 2\bar{R} \sin \frac{1}{2}\psi$$

$$M_1(\psi) = \sum_{n=2}^{\infty} (2n+1)n P_{no}(\cos\psi) = -\frac{1}{4} \cos^3 \psi / 2 - 3 \cos \psi, \quad \text{if } \psi \neq 0 \quad (5.35)$$

The quantity \bar{T}'' (and hence \bar{N}'') has an unambiguous definition in the context of a rigorous solution of the GBVP (e.g., Mather 1974b, p.97) on the Brillouin sphere, as does $\Delta\bar{g}''$, being defined by equations 5.4 and 5.6. Thus combination with equation 5.29 gives

$$\bar{N}'' = \frac{1}{\gamma} ((W_o - U_o) + \delta W - V + dR (\partial T'' / \partial h)) + \zeta' + O\{\bar{fN}''\} \quad (5.36)$$

$$\text{if } \frac{1}{\gamma} (dR)^2 \frac{\partial^2 T''}{\partial h^2} = O\{\bar{fN}''\}$$

with a precision which is adequate for the determination of SST.

For the same reasons which required the re-formulation of the surface integral in equation 5.14 to that in equation 5.18, the instability at $\psi = 0$ is overcome by writing equation 5.33 as

$$\Delta\bar{g}'' + \gamma\bar{N}''/\bar{R} = \frac{\gamma}{4\pi\bar{R}} \iint M_1(\psi) (\bar{N}'' - \bar{N}_p'') d\sigma \quad (5.37)$$

since

$$\frac{\gamma\bar{N}''}{4\pi\bar{R}} \sum_{n=2}^{\infty} (2n+1)n \iint P_{no}(\cos\psi) d\sigma = 0 \quad (5.38)$$

Equation 5.37 is similar to the inverse relation to Stokes' problem propounded by Molodenskii et al. (1962, p.50). It affords an alternative method for expressing the fundamental relationship between the two types of measured quantities:

- a) gravity anomalies defined as the difference between observed gravity measured at the physical surface, and normal gravity on the reference surface (i.e., Δg for the telluroid or $\Delta g'$ for the "higher" reference surface T1 (Mather 1974b, Figure 1);
- b) heights of the physical surface above the reference surface (ζ in the case of the telluroid and ζ' in the case of T1).

5.2.2. Computational Possibilities.

The basic data which are likely to be available for attempts at the definition of the stationary SST by geodetic means are the following:

- a) Gravity field models consistent with tracking station positions and the determination of orbits of altimeter equipped spacecraft,
- b) Estimates of ζ' for oceanic areas consistent with the orbits determined at a), and
- c) Values of Δg_c primarily on land and in continental shelf areas as deduced from measurements of surface gravity and geodetic elevations established with respect to a local MSL datum.

It is preferable to express $\Delta \bar{g}''$ and \bar{N}'' , which include the unknown quantities $(W_o - U_o)$ and δW , in terms of the following relations :

$$\Delta \bar{g}'' = \Delta g_c - 2(W_o - U_o)/\bar{R} - 2\delta W/\bar{R} \quad (5.39)$$

where Δg_c has the advantage that it can be numerically evaluated from the input data, as expressed in equation 5.7, and

$$\bar{N}'' = N_c'' + \frac{1}{\gamma} ((W_o - U_o) + \delta W) \quad (5.40)$$

The use of equations 5.4, 5.5 and 5.29 along with equation 5.40 gives

$$N_c'' = T_c/\gamma = \zeta' - \frac{1}{\gamma} (V-dR \frac{\partial T''}{\partial h}) \quad (5.41)$$

Equation 5.37 can be rewritten in terms of the computable quantities Δg_c and N_c'' . On using equations 5.39 and 5.40,

$$\Delta g_c + (\gamma N_c'' - (W_o - U_o) - \delta W) / \bar{R} = \frac{\gamma}{4\pi\bar{R}} \iint M_1(\psi) (N_c'' - N_{cp}'') d\sigma + \frac{1}{4\pi\bar{R}} \iint M_1(\psi) (\delta W - \delta W_p) d\sigma \quad (5.42)$$

the subscript p is used to denote values at the point of computation where such meaning is not obvious. On the assumption that it is desired to determine, in the first instance, a long wave model for the stationary SST, together with discrete corrections δW_j to the n finite geodetic levelling datums which are currently used, it is essential to look at the probable error patterns in both Δg_c and N_c'' with wavelengths equivalent to those sought in the SST. The successful separation of the latter from such errors can only be achieved if the structure of the errors in the observational data have substantially different patterns on global analysis when using equation 5.42.

If Δg_{co} and N_{co}'' are the values of Δg_c and N_c'' deduced from observations, it follows from equation 5.36 that in the absence of serious errors in the evaluation of V and $\partial T'' / \partial h$,

$$N_c'' = N_{co}'' + e_N \quad (5.43)$$

where e_N is given by equations 5.17 and 5.21. The errors in the observed values of Δg_c can be represented by :

$$\Delta g_c = \Delta g_{co} + e_g \quad (5.44)$$

where the observational error can be expressed as :

$$e_g = \sum_{n=0}^{\infty} e_{g_n} \quad (5.45)$$

As the two basic data types derive from different measuring techniques, no relation can be assumed to exist between e_g and e_N . Equation 5.32 can be re-written in terms of the observations and errors as

$$\Delta g_{co} + \frac{\gamma N_{co}''}{\bar{R}} - ((W_o - U_o) + \delta W_p) / \bar{R} - \frac{1}{4\pi\bar{R}} \iint M_1(\psi) (\delta W - \delta W_p) d\sigma + e_g + \gamma e_N / \bar{R} - \frac{\gamma}{4\pi\bar{R}} \iint M_1(\psi) (e_N - e_{Np}) d\sigma = \frac{\gamma}{4\pi\bar{R}} \iint M_1(\psi) (N_{co}'' - N_{cop}'') d\sigma \quad (5.46)$$

Thus

$$\Delta g_{CO} + \gamma N''_{CO} / \bar{R} + v = \frac{\gamma}{4\pi\bar{R}} \iint M_1(\psi) (N''_{CO} - N''_{COP}) d\sigma \quad (5.47)$$

where the use of equation 5.15, 5.21 and 5.35 gives the form of v , on ignoring harmonics of degree one, as

$$v = e_g - (W_o - U_o) / \bar{R} - \frac{\gamma}{\bar{R}} \left(\sum_{n=0}^{\infty} (n-1) e_{N_n} \right) - \frac{1}{\bar{R}} \left(\sum_{n=2}^{\infty} (n+1) \delta W_n \right) \quad (5.48)$$

It can be seen from a study of equation 5.48 that there is only one circumstance in which the SST will be unambiguously determined from equation 5.47 - i.e., when the magnitudes of e_{N_n} and e_{g_n} are at least a factor of 10 smaller than that of δW_n for all n in the desired spectrum of the SST. If the input data are considered to be a near-global coverage of N''_{CO} and values of Δg_{CO} , as described at paragraph 5.2.2 c) above, and assuming that the Earth is effectively sampled at a sufficient number of discrete points to enable the various error signatures to be filtered through terms of the desired wavelength, then three distinct cases are possible in circumstances where equation 5.47 can be applied

- i) The magnitudes of e_{g_n} and $\gamma(n-1)e_{N_n} / \bar{R}$ are significantly larger (presently at least by a factor of 3 or 4) than that of $(n+1)\delta W_n / \bar{R}$.
- ii) The magnitudes of e_{g_n} and $\gamma(n-1)e_{N_n} / \bar{R}$ are of the same order as that of $(n+1)\delta W_n / \bar{R}$.
- iii) The magnitudes of the error terms are about an order of magnitude smaller than the SST.

It is expected that the chronological sequence of events will follow the order given above. The gravity field models presently available can be improved by the use of equation 5.47 to a level equivalent to the magnitude of the SST if e_{g_n} could be successfully controlled with a precision equivalent to that of IGSN 71 (Morelli et al. 1971). The main problem in using equation 5.47 is the difficulty of determining N''_{CO} in land areas. Fortunately, the magnitude of $M_1(\psi)$ diminishes rapidly with increasing ψ (see Section 5.3), offering the hope that the equation is numerically tenable.

In any event, equation 5.47 cannot be applied in case ii) above.

Its relation to alternate procedures is discussed in sub-section 5.2.4 . It is shown that all solutions of the GBVP are incapable of surmounting this obstacle solely from surface observations because no data taken at the surface of the Earth are free from the influence of SST. Possible alternatives for circumventing the problem are outlined in Section 5.5.

A possible iterative solution procedure is outlined in the next sub-section using various formulations of the GBVP as posed in either equations 5.1 to 5.3 or in equation 5.33 .

5.2.3. Possibilities for Model Improvement using Iterative Procedures.

It should be noted that equations 5.32 and 5.47 are equivalent and as such equation 5.47 can be written as

$$\Delta g_{co} + \gamma N_{co}'' / \bar{R} + v = \frac{\gamma}{R} \left(\sum_{n=2}^{\infty} n N_{con}'' \right) = \frac{\gamma}{4\pi R} \iint M_1(\psi) (N_{co}'' - N_{cop}'') d\sigma \quad (5.49)$$

where v is defined by equation 5.48 and N_{con}'' is the surface harmonic of degree n in the representation of the global distribution of N_{co}'' . Such a set of harmonics will be obtained from satellite altimetry data in oceanic regions together with equivalent values on land using some appropriate method, noting that N_{co}'' is related to N_c'' by equation 5.43.

It would be possible to determine the long wavelength features of the SST (to degree n') if the magnitudes of e_{Nn} (equation 5.21) and e_{gn} (equation 5.45), as represented by harmonics in the range $n < n'$, were held to below ± 10 cm or ± 30 μ Gal in this range of wavelengths. While the problems of achieving the former are investigated in Section 5.4, the latter has to be achieved, in the foreseeable future, in the absence of a global coverage of Δg_c . It still remains to be seen whether it is possible to determine e_N or materially improve N_c'' given as input, a global data set N_{co}'' (see equation 5.43).

On using equation 5.47, the quantity

$$E\{\Delta g_c\} = \Delta g_{co} + v = \frac{\gamma}{4\pi R} \iint M_1(\psi) (N_{co}'' - N_{cop}'') d\sigma - \gamma N_{co}'' / \bar{R} \quad (5.50)$$

can be defined where $E\{X\}$ represents the numerically computed value of X from the input observational data. It can be shown, using equation 5.48, that

$$E\{\Delta g_c\} = \Delta g_c - \frac{1}{R} (\gamma \sum_{n=0}^{\infty} (n-1)e_{N_n} + (W_o - U_o) + \sum_{n=2}^{\infty} (n+1)\delta W_n) \quad (5.51)$$

From equations 5.1 to 5.3,

$$\begin{aligned} \zeta' = N_{ns} + (W_o - U_o)/\gamma - \bar{R} M\{\Delta g_c\}/\gamma + 2M\{\delta W\}/\gamma - \delta W/\gamma - \frac{1}{2\pi\gamma} \iint f(\psi)\delta W d\sigma \\ + \frac{\bar{R}}{4\pi\gamma} \iint f(\psi)\Delta g_c d\sigma \end{aligned} \quad (5.52)$$

The terms of zero degree in equation 5.52, $(W_o - U_o)$, $\bar{R}M\{\Delta g_c\}$ and $2M\{\delta W\}$, contain information on the scale of the system.

The effect of the term $(W_o - U_o)$ can only be reliably separated from that of $\bar{R}M\{\Delta g_c\}$ in solutions of the GBVP if a global representation is available for the gravity anomaly, as sampled at the surface of the Earth. The term $(W_o - U_o)$ can be estimated independently of any BVP formulation using satellite altimetry as was done in Mather et al. (1978) where a value for W_o of 626382.76 ± 0.4 kGal m, consistent with a value of $GM = 398600.47 \text{ km}^3 \text{ sec}^{-2}$ and equatorial radius $a = 6378140$ m, was obtained. It should be noted however that the adoption of a specific definition for the geoid influences the value of this zero degree term. The quantity $M\{\Delta g_c\}$ can also be estimated using techniques described in H & M (1967, Section 2-20). However, such "classical" techniques are unsuited for high precision marine geoid studies.

The term $M\{\delta W\}$ is equal to zero if the BVP definition for the geoid is adopted (see sub-section 2.4.2). Any other conceptual definition of the geoid based on oceanic and/or tide gauge data will not necessarily result in $M\{\delta W\} = 0$ in solutions of the GBVP.

In practice, the quantity available is ζ'_c (instead of ζ'), thus on using the computable quantity $E\{\Delta g_c\}$ (equation 5.50) in lieu of Δg_c in equation 5.52, ζ'_c is given by

$$\zeta'_c = N_{ns} - \frac{\bar{R}}{\gamma} M\{E\{\Delta g_c\}\} + \frac{\bar{R}}{4\pi\gamma} \iint f(\psi) E\{\Delta g_c\} d\sigma \quad (5.53)$$

On using the quantity $E\{\Delta g_c\}$ in the implicit form given in equation 5.51, equation 5.53 can be written as

$$\zeta'_c = \zeta' - e_N + (e_{N1} + \delta W_1/\gamma) \quad (5.54)$$

As T'' has no first degree harmonic, the term within the brackets in equation 5.54 is zero. The result embodied in equation 5.54 indicates that no additional information is obtained by firstly computing estimates of Δg_c from the data set N''_{co} and then attempting to compute ζ' using equation 5.52. This result shows that equations 5.42 and 5.52 are consistent with one another and define alternative but not mutually exclusive relationships between height anomalies, gravity anomalies and SST. It is also obvious that no relationship between quantities observed at the surface of the Earth will unambiguously define the SST in the presence of errors in the observational data whose magnitude exceeds that of the SST itself for equivalent wavelengths. Further, there is no advantage, apart from that of convenience in relation to the nature of the input data, for the use of either one or other (or both) integrals at 5.42 and 5.52 in determining SST. The only information uncontaminated by the SST is the satellite determined gravity field model.

The height anomaly ζ' on the "higher" reference system can be defined by the equation

$$\zeta' = \zeta'_c + \delta\zeta + \delta e_N \quad (5.55)$$

where ζ'_c is defined by equation 5.53, $\delta\zeta$ is the improvement in ζ' produced by incorporating the available surface gravity data and δe_N is the residual error. Let $\delta\Delta g$ be given by

$$\delta\Delta g = \Delta g_{co} - E\{\Delta g_c\} \quad (5.56)$$

where $E\{\Delta g_c\}$ is computed from satellite altimetry using equation 5.50 (without concern about the problem of representation in continental and polar regions) and Δg_{co} is obtained from observed gravity and applies to the Brillouin sphere, given by equation 5.7. From equation 5.51,

$$\Delta g_c = E\{\Delta g_c\} + \frac{1}{R} ((W_o - U_o) + \gamma \sum_{n=0}^{\infty} (n-1)e_{N_n} + \sum_{n=2}^{\infty} (n+1)\delta W_n) = \Delta g_{co} + e_g \quad (5.57)$$

the first equality holds if the values of $E\{\Delta g_c\}$ are computed using equation 5.50, whilst the second applies at points where observed gravity is available. The resulting error (e'_g) in the composite data set so formed is given by

$$e'_g = \begin{cases} \Delta g_c - \Delta g_{co} (=e_g) & \text{if surface gravity available} \\ \Delta g_c - E\{\Delta g_c\} & \text{if surface gravity not available} \\ & \text{and altimetry data are used instead} \end{cases} \quad (5.58)$$

From equation 5.49 and 5.55, it follows that the improvement $\delta\zeta$ produced by the introduction of additional surface gravity anomalies Δg_{co} , can be defined by the relation

$$\delta\zeta = -\bar{R} M\{\delta\Delta g\}/\gamma + \frac{\bar{R}}{4\pi\gamma} \iint f(\psi) \delta\Delta g \, d\sigma \quad (5.59)$$

Further, from equations 5.56 and 5.57, it follows that non zero values of $\delta\Delta g$ are given by

$$\delta\Delta g = \frac{1}{R} ((W_o - U_o) + \gamma \sum_{n=0}^{\infty} (n-1)e_{N_n} + \sum_{n=2}^{\infty} (n+1)\delta W_n) - e_g \quad (5.60)$$

If it is assumed that a global surface gravity data set is available, the incorporation of equation 5.60 in 5.59, together with the use of the orthogonal properties of surface harmonics on the Brillouin sphere, gives

$$\delta\zeta = \bar{R} e_{g_o}/\gamma + e_N - e_{N1} - (W_o - U_o)/\gamma + \frac{1}{\gamma} \sum_{n=2}^{\infty} \frac{n+1}{n-1} \delta W_n - \frac{\bar{R}}{4\pi\gamma} \iint f(\psi) e_g \, d\sigma \quad (5.61)$$

where the effect of the first degree harmonic in δW causes $\delta\zeta$ to be defined in relation to a reference figure whose centre is displaced with respect to the geocentre. However, the existence of the term e_{N1} in equation 5.61 is likely to result in terms of first degree having no effect of significance on the results.

While $\delta\zeta$ can be numerically evaluated from equation 5.59, it can be seen from equation 5.57 that the non-equivalence of e_g and e'_g in the second equation at 5.58 causes numerical evaluations, in practice, to deviate from the relationship set out in equation 5.61. In areas where no surface gravity is available, the use of equation 5.59 is not consistent with the definition of $\delta\Delta g$ in equation 5.56 as equation 5.58 implies that $\delta\Delta g$ is zero in such areas. However, equation 5.61 would be valid if values of Δg_{co} were predicted from the available surface gravity data to provide a representation through terms of wavelength equivalent to those sought in the SST. In this case, the use of

equation 5.45 in equation 5.61 gives

$$\delta\zeta = e_N + \bar{R}(e_{g_0} - \sum_{n=2}^{\infty} \frac{1}{n-1} e_{g_n})/\gamma + \frac{1}{\gamma} \sum_{n=2}^{\infty} \frac{n+1}{n-1} \delta W_n - (W_o - U_o)/\gamma \quad (5.62)$$

where the terms of first degree have been excluded. Once again, it is seen that the limitations described in the discussion following equation 5.54 apply. No unique solution of the SST is possible unless e_N and e_g are significantly smaller than δW .

It is apparent that no combination of data collected from satellite altimetry and surface gravity can provide a definition of SST unless both data types have global distributions such that error patterns with wavelengths equivalent to those sought in the SST have cumulative magnitudes less than ± 10 cm (or ± 30 μ Gal).

It is not possible to assume that gravity information maintained in data banks at the present time can meet these criteria. It has been observed that particular gravity field models based on satellite data alone (e.g., the odd-numbered Goddard Earth Models - GEM) fit satellite orbits better than those which include surface gravity data (e.g., the even-numbered GEM models) as illustrated in Lerch et al. (1974, p.61). It is suspected that this may be due, at least in part, to errors in the gravity data banks over wavelengths which are effective at satellite altitudes and also due to the adopted combination solution procedures. This problem is not as apparent in the Smithsonian gravity field models (Gaposchkin & Lambeck 1971, Gaposchkin 1974, 1980).

The first internationally accepted global gravity standardization network (IGSN 71) was finalized in 1971. It is not uncommon for all gravity data on a single datum to require corrections of up to $\pm 3-4$ mGal before they are consistent with the unified system afforded by IGSN 71. However, the precision of IGSN 71 does not exceed ± 0.2 mGal through wavelengths of the order of 4000 km (Morelli et al. 1971). The doubts about the quality of oceanic gravity data are even greater. In the Australian region, the quality of the marine gravity data are assessed as ± 3 mGal with long wavelength errors of the order 1000 km (B.C. Barlow, private communication, 1977). Furthermore, the oceanic coverage is generally sparse and irregular.

5.2.4. Discussion.

The three basic equations relating observed quantities at the

Earth's surface to SST described in the earlier sub-sections are the following:

$$T'' = (W_o - U_o) + \delta W + \delta \zeta' - V$$

$$\Delta g_c + \gamma N_c'' / \bar{R} - (W_o - U_o) / \bar{R} - \sum_{n=2}^{\infty} (n+1) \delta W_n / \bar{R} = \frac{\gamma}{4\pi \bar{R}} \iint M_1(\psi) (N_c'' - N_{cp}'') d\sigma$$

$$T'' = \gamma N_{ns} + 2(W_o - U_o) - \bar{R} M\{\Delta g_c\} + 2M\{\delta W\} - \sum_{n=2}^{\infty} \frac{2}{n-1} \delta W_n + \frac{\bar{R}}{4\pi} \iint f(\psi) \Delta g_c d\sigma - V$$

where N_c'' is related to T'' by equations 5.29 and 5.40, Δg_c is given by equation 5.7 and δW_n by equation 5.15.

It has been shown in sub-section 5.2.3 that cycling the same input information through the above equations cannot improve the solution stability in the context of SST determinations over and above that achievable by using any one of the above three equations if quadrature errors are excluded from consideration. This confirms the intuitive appreciation that all surface integrals inter-relating harmonic quantities under conditions where orthogonality relations prevail without approximation, are equivalent. The choice of one integral over another is merely a matter of convenience, being a function of the nature of the input data.

The three likely computational possibilities, described in sub-section 5.2.2, are as follows :

- a) e_N and $\bar{R}e_g/\gamma$ are significantly larger than $\delta W/\gamma$ for the wavelengths under consideration, as appears to be the case at the present time, or
- b) All quantities mentioned at a) are of approximately the same order of magnitude, or
- c) The term $\delta W/\gamma$ is significantly larger than e_N and $\bar{R}e_g/\gamma$. This situation is unlikely in the next few years in the case of the wavelengths under consideration as it would imply that the long wavelength errors in the altimeter and gravity data and gravity field models are at the ± 10 cm level.

The irregular distribution of the available surface gravity data in conjunction with the questionable precision of gravity measurements

at sea and the absence of a global coverage of altimeter-derived height anomalies makes the latter two equations relatively unattractive when attempting a determination of the SST.

Equation 5.42 has the apparent advantage that the function $M_1(\psi)$ rapidly decreases with increase of ψ (see Figure 5.1). Over 80% of the signal comes from the contributions in the range $0^\circ < \psi < 5^\circ$ (see Table 5.1). However about a quarter of the signal is lost due to the finite nature of the altimeter footprint. Such a loss is mostly expected through short wavelength contributions, estimated at less than 10 km. The precision of the resulting determination of Δg_c are highly correlated with the orbit determination, as any radial errors directly influence SST determinations. The use of equation 5.42 in oceanic regions close to the coast is limited to those areas where reliable values of N_c'' can be computed in adjacent land areas. ζ' could be determined in these areas using dynamic satellite techniques but it would be uneconomic to create this data set. However, with the foreseeable use of systems such as the GPS (Larden and Bender, 1980) and radio interferometric positioning techniques (Niell et al. 1980; Silverberg 1978) the use of this approach could be worthwhile. The nature of the kernel function $M_1(\psi)$ is assessed in the next Section together with a recommendation for a practical sub-division for quadratures evaluation of equation 5.47 .

The surface integral at equation 5.52 is the well-known Stokes' integral which converges even more slowly than the kernel function $M_1(\psi)$. Its use, in practice, is not favoured due to the absence of a global field of Δg_c . Both equations 5.42 and 5.52 have to be evaluated from global stationary fields of ζ' or $\Delta g'$. It is therefore assumed that the effect of the ocean tides has been removed from the data prior to use in numerical evaluations. Equation 5.4 can be applied to the instantaneous value of ζ' , corrected for the tides as set out in equation 5.9. In view of the equivalence of equations 5.4, 5.42 and 5.52, it is more convenient to work with equation 5.4 in the case of non-global data sets of $\Delta g'$ and ζ' . The use of equation 5.4 under appropriately controlled conditions appears to provide a more promising basis for improving both the gravity field model using satellite altimetry as well as for determining the long wave features of the quasi-stationary SST. This is discussed further in Section 5.4 .

Variations of the Inverse Operator $M_1(\psi)$ with ψ

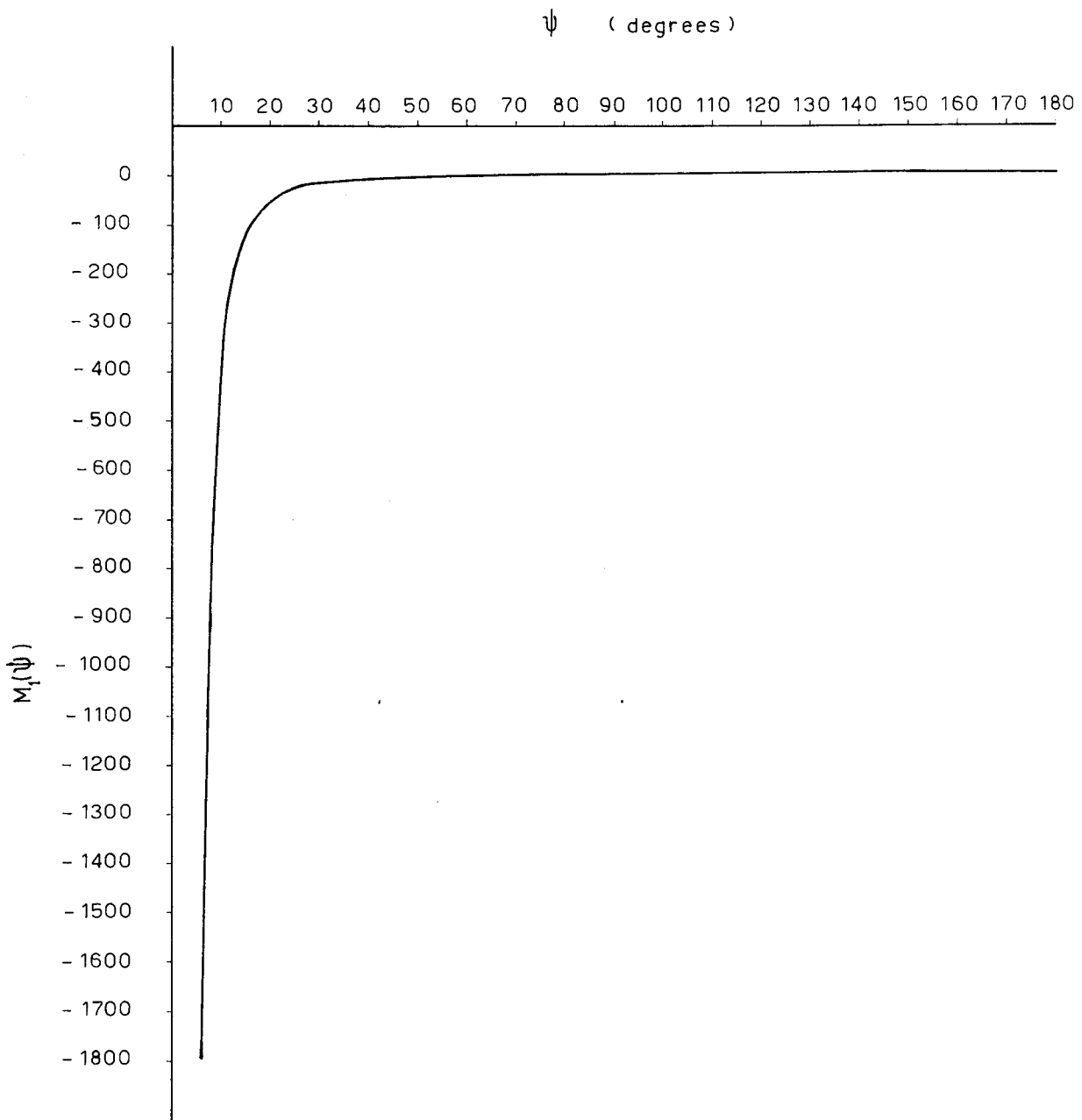


Figure 5.1

5.3. The Function $M_1(\psi)$ and its Characteristics on Surface Integration.

5.3.1. Surface Sub-Divisions.

The nature of the function $M_1(\psi)$, defined by equation 5.35, is such that the contribution of different elements of area to the quadratures evaluation of the surface integral in equation 5.47 is a nonlinear function of ψ rather than one of surface area. An assessment of the rate of fade of the signal on surface integration by quadratures can be obtained in the following manner.

If m_N is the unsigned magnitude of $(N_c'' - N_{cp}'')$, it can be assessed on the basis of experience with satellite altimetry data that

$$m_N = \begin{cases} 0\{\psi^\circ\} & \text{for } \psi < 10^\circ \\ 0\{10\} & \text{for } \psi \geq 10^\circ \end{cases} \quad (5.63)$$

In addition

$$d\sigma = \sin\psi \, d\psi \, d\alpha$$

where α is the azimuth. The contribution $C(\psi)$ of an annulus of surface area, with width $d\psi^\circ$ at an angular distance ψ from the point at which $(\Delta g_c + \gamma N_c''/\bar{R})$ is being computed, is estimated as

$$C(\psi) = 0\{K m_N M_1(\psi) \sin\psi \, d\psi^\circ\} \quad (5.64)$$

where

$$K = \frac{\gamma}{4\pi\bar{R}} \times \frac{\pi}{180} \times 2\pi \quad \text{m Gal m}^{-1} \quad (5.65)$$

It is necessary to establish the optimum ring thickness ($d\psi$) as a function of ψ for the quadratures evaluation of equation 5.47. Let squares of size $m^\circ \times m^\circ$ be small enough to permit evaluation of the contribution of a ring of thickness $d\psi^\circ$ which is ψ° away from the point of computation, so that the resulting error introduced in the quadratures procedure is acceptably small. It is sought to replace a set of N such sub-divisions by a larger $n^\circ \times n^\circ$ sub-division where $M_1(\psi)$ for each of the smaller sub-divisions is now represented by the value

$M_1(\psi)$ for the larger square centre. In addition, the individual values $(N''_c - N''_{cp}) (= \delta N)$ are replaced by their mean value $\delta \bar{N}$ for the larger square. The contribution C for the total area is given by an expression of the form

$$C = K_d \sum_{i=1}^N (\bar{M}_2(\psi) + \Delta M_{2i}) (\delta \bar{N} + \Delta \delta N_i) \quad (5.66)$$

where $M_2(\psi) = M_1(\psi) \sin \psi = \bar{M}_2(\psi) + \Delta M_2$ and $\delta N = \delta \bar{N} + \Delta \delta N$,

$\bar{M}_2(\psi)$ having the same significance in relation to $M_2(\psi)$ as $\bar{M}_1(\psi)$ has to $M_1(\psi)$, and K_d is the appropriate constant. It follows that

$$C = N K_d \bar{M}_2(\psi) \delta \bar{N} + K_d \bar{M}_2(\psi) \sum_{i=1}^N \Delta \delta N_i + K_d \delta \bar{N} \sum_{i=1}^N \Delta M_{2i} + K_d \sum_{i=1}^N \Delta M_{2i} \Delta \delta N_i \quad (5.67)$$

The first term on the right of equation 5.67 would be equivalent to the contribution obtained when the larger $n^\circ \times n^\circ$ area was represented by the mean value $\delta \bar{N}$ at its centre if $\bar{M}_2(\psi)$ were the value of $M_2(\psi)$ at the centre of the larger square. This could be expected only if the variations of $M_2(\psi)$ within the larger area were symmetrical with respect to the centre. The second and third terms are zero by definition, leaving the fourth term as the only non-zero contribution to C. This final term will tend to zero if there is no correlation between the variations in δN and $M_2(\psi)$ from the values adopted for the representation of the $n^\circ \times n^\circ$ square. On the assumption that $\Delta \delta N$ varies smoothly over the $n^\circ \times n^\circ$ region, it could be inferred that the criterion which needs to be satisfied in SST determinations using a "higher" reference model, is (Mather 1973a, p.63)

$$\frac{1}{2} (d\psi)^2 \frac{\partial^2 M_2(\psi)}{\partial \psi^2} \dagger 0\{10^{-3}\}$$

where $d\psi$ is the radian equivalent of n° . Column 5 in Table 5.2 sets out the resulting error $e_{\Delta g}$, given by

$$e_{\Delta g} = \frac{\gamma}{4\pi R} \left[\frac{1}{2} (d\psi)^2 \frac{\partial^2 M_2(\psi)}{\partial \psi^2} \right] (N''_c - N''_{cp}) d\sigma \quad (5.69)$$

as a consequence of the term at equation 5.68, for acceptable values of $d\psi$ from equation 5.70.

Another criterion of interest is the definition of the width ($d\psi$) of annuli, as a function of ψ , which make the same contribution C_g to $(\Delta g_c + \gamma N_c''/\bar{R})$ for a specific value (\bar{V}) of $(N_c'' - N_{cp}'')$. From equations 5.64 and 5.65, it follows that

$$C_g = (\gamma M_2(\psi) \bar{V} d\psi(\psi))/2\bar{R}$$

or

$$d\psi(\psi) = (2\bar{R} C_g)/(\gamma M_2(\psi) \bar{V}) \quad (5.70)$$

where the magnitude of \bar{V} can be expressed by a relation of the form given at equation 5.63. Table 5.1 sets out information on values of $d\psi$ as a function of ψ such that the contribution C_g is 1 mGal for \bar{V} defined by equation 5.63. The fifth column in Table 5.1 gives a measure of the strength of signal on the basis of the unsigned contribution of each zone to the final result.

Two conclusions can be drawn from this table:

- i) More than two-thirds of the signal comes from the areas in the range ψ less than 1° .
- ii) As the altimeter footprints are unlikely to have diameters less than 2 km (0.02°), it follows that more than a quarter of the signal cannot be recovered merely as a consequence of the nature of the input data.

These results are also corroborated by the figures given in Table 5.3. It would be more realistic to assume that satellite altimetry data are unlikely to resolve $(N_c'' - N_{cp}'')$ with wavelengths shorter than 10 km (or 0.1°). Consequently, annuli smaller than 0.1° in width cannot be represented by true observational data.

Table 5.2 gives values of $C(\psi)$ on the basis of a minimum ring width of 0.1° or for rings which make a contribution of 1 mGal to $(\Delta g_c + \gamma N_c''/\bar{R})$, whenever the contribution is less than 1 mGal for $d\psi = 0.1^\circ$.

On the basis of the results given in Table 5.2, it would appear that the pattern of annuli that could be used in the quadratures evaluation of the inverse of Stokes' integral is as follows :

T A B L E 5.1.
Width ($d\psi$) of Annuli Making One mGal Contributions to $(\Delta g_c + \gamma_N^{N1}/R)$ as a Function of ψ
(Equation 5.69)

Column 1	2	3	4	5
Range of ψ ($^\circ$)	Range of V ($= m_N$) (m) (Equation 5.63)	Range of $d\psi$ ($^\circ$)	Number of Rings	Strength of Signal % Cumulative %
$\psi < 0.0016$	$V < 0.0016$	$d\psi < 0.0018$	5	5.4
$0.0016 < \psi < 0.01$	$0.0016 < V < 0.01$	$0.0018 < d\psi < 0.0011$	16	17.4
$0.01 < \psi < 0.1$	$0.01 < V < 0.1$	$0.0011 < d\psi < 0.0107$	20	21.7
$0.1 < \psi < 1.0$	$0.1 < V < 1.0$	$0.0107 < d\psi < 0.1173$	21	22.8
$1.0 < \psi < 5.0$	$1.0 < V < 5.0$	$0.1173 < d\psi < 0.5768$	14	15.3
$5.0 < \psi < 180$	$5.0 < V < 10.0$	$0.5768 < d\psi < 84.6555$	16	17.4

Table 5.2Factors Affecting the Quadratures Evaluation of $(\Delta g_c + \gamma N_c^2/R)$ i) Annular Sub-Divisions as a Function of ψ for Contributions $C(\psi)$ [Columns 3 & 4]
for a data resolution of 0.1° ($C(\psi) \dagger 1 \text{ mGal}$)

ii) Estimates of Quadratures Errors [Column 5]

Column 1	2	3	4	5
ψ ($^\circ$)	V (=m _N) (m) Equation 5.63	d ψ ($^\circ$) Equation 5.70	C(ψ) (mGal)	e _{Δg} (mGal) Equation 5.69
0.05	0.05	0.10	17.6	4.22
0.15	0.15	0.10	5.9	0.156
0.25	0.25	0.10	3.5	0.034
0.35	0.35	0.10	2.5	0.012
0.45	0.45	0.10	1.9	0.006
0.55	0.55	0.10	1.6	0.003
0.65	0.65	0.10	1.3	0.002
0.75	0.75	0.10	1.2	0.001
0.85	0.85	0.10	1.0	0.000(9)
0.95	0.95	0.11	1.0	0.000(7)
1.07	1.07	0.12	1.0	0.000(7)
1.20	1.20	0.14	1.0	0.000(7)
1.34	1.34	0.15	1.0	0.000(6)
1.50	1.50	0.17	1.0	0.000(7)
1.68	1.68	0.19	1.0	0.000(7)
1.88	1.88	0.21	1.0	0.000(7)
2.11	2.11	0.24	1.0	0.000(7)
2.36	2.36	0.27	1.0	0.000(7)
2.65	2.65	0.30	1.0	0.000(7)
2.96	2.96	0.34	1.0	0.000(7)
3.32	3.32	0.38	1.0	0.000(7)
3.72	3.72	0.42	1.0	0.000(7)
4.17	4.17	0.47	1.0	0.000(7)
4.67	4.67	0.53	1.0	0.000(7)
5.23	5.23	0.59	1.0	0.000(7)
5.86	5.86	0.66	1.0	0.000(7)
6.56	6.56	0.74	1.0	0.000(7)
7.35	7.35	0.83	1.0	0.000(7)
8.24	8.24	0.93	1.0	0.000(7)
9.22	9.22	1.04	1.0	0.000(7)
10.35	10.0	1.21	1.0	0.000(7)
11.73	10.0	1.55	1.0	0.000(8)
13.52	10.0	2.05	1.0	0.001(0)
15.96	10.0	2.82	1.0	0.001(4)
19.41	10.0	4.08	1.0	0.001(8)
24.58	10.0	6.27	1.0	0.002(4)
32.76	10.0	10.10	1.0	0.002(9)
46.11	10.0	16.60	1.0	0.003(0)
74.41	10.0	40.02	1.0	0.003(7)
126.69	10.0	64.56	1.0	0.006(7)

Range of ψ	Width of Annulus ($d\psi$)	Data Source
$\psi < 0.25^\circ$	0.01°	Interpolated from Observation
$0.25^\circ < \psi < 0.5^\circ$	0.05°	Interpolated from Observation
$0.5^\circ < \psi < 3^\circ$	0.1°	Altimetry Data
$3^\circ < \psi < 5^\circ$	0.5°	Area Means from Altimetry
$5^\circ < \psi < 20^\circ$	1°	Area Means from Altimetry
$\psi > 20^\circ$	5°	From Composite Data Set

Values for $C(\psi)$ on the basis of this ring structure are given in Table 5.3. Also tabulated are estimates of the accumulation of $C(\psi)$ in the evaluation of equation 5.47 using the following three models as the basis for error accumulation of $C(\psi)$:

Model 1

$$S = o\{\Delta g_c + \gamma N_c''/\bar{R}\} = \sum C(\psi)$$

Model 2

$$S = o\{\Delta g_c + \gamma N_c''/\bar{R}\} = (\sum C(\psi)_{\psi < 10^\circ}) + (\sum C(\psi)^2)_{\psi \geq 10^\circ}^{1/2} \quad (5.71)$$

Model 3

$$S = o\{\Delta g_c + \gamma N_c''/\bar{R}\} = (\sum C(\psi)^2)^{1/2}$$

Model 1 indicates that the strength of signal S is subject to systematic error patterns while Model 3 assumes that the contributions are accidental in nature. Model 2 is a combination of both error types for a varying ψ of 10° .

For the accumulation of signal strength, Models 1 and 2 give plausible values for $o\{\Delta g_c + \gamma N_c''/\bar{R}\}$ of approximately 70 mGal while Model 3 gives a value of around 13 mGal indicating that the assumption of no correlation between values of m_N for each ring, when ψ is small, is unrealistic.

All models indicate that approximately 40% of the signal should be recovered by considering only contributions from regions where $\psi >$

T A B L E 5.3.
Strength of Signal in Computations of $(\Delta g_c + \gamma H^3/R)$ Using Equation 5.47

ψ (°)	$d\psi$ (°)	m_N (m)	$C(\psi)$ (mGal)	Cumulative Strength of Signals for Models in Equation 5.71					
				Model 1		Model 2		Model 3	
				mGal	%	mGal	%	mGal	%
0.01	0.01	0.01	8.8	76.5	100	68.7	100	12.9	100
0.02	0.01	0.02	4.4	67.7	88	59.9	87	9.5	73
0.03	0.01	0.03	2.9	63.3	83	55.5	81	8.4	65
0.04	0.01	0.04	2.2	60.4	79	52.6	76	7.9	61
0.05	0.01	0.05	1.8	58.2	76	50.4	73	7.6	59
0.06	0.01	0.06	1.5	56.4	74	48.6	71	7.4	57
0.07	0.01	0.07	1.2	55.0	72	47.1	69	7.2	56
0.08	0.01	0.08	1.1	53.7	70	45.9	67	7.1	55
0.09	0.01	0.09	1.0	52.6	69	44.8	65	7.0	54
0.10 < ψ < 0.22	0.01	0.10 < m < 0.22	0.9 > C > 0.4	51.6 > S > 44.4	67 > S > 58	43.8 > S > 36.6	64 > S > 53	7.0 > S > 6.6	54 > S > 51
0.25 < ψ < 0.45	0.05	0.25 < m < 0.45	1.8 > C > 1.0	44.0 > S > 38.5	57 > S > 50	36.2 > S > 30.6	53 > S > 45	6.6 > S > 6.0	51 > S > 46
0.50 < ψ < 2.70	0.10	0.50 < m < 2.70	1.8 > C > 0.3	37.5 > S > 21.9	49 > S > 29	29.7 > S > 14.1	43 > S > 20	5.9 > S > 4.5	46 > S > 35
3.0 < ψ < 4.5	0.5	3.0 < m < 4.5	1.5 > C > 1.0	21.6 > S > 17.7	28 > S > 23	13.8 > S > 9.9	20 > S > 14	4.5 > S > 3.9	35 > S > 30
5.0 < ψ < 17	1.0	5.0 < m < 10	1.8 > C > 0.3	16.8 > S > 6.2	22 > S > 8	8.9 > S > 1.8	13 > S > 3	3.8 > S > 1.8	29 > S > 14
20 < ψ < 175	5.0	10	1.2 > C > 0	5.9 > S > 0	8 > S > 0	1.7 > S > 0	2 > S > 0	1.7 > S > 0	13 > S > 0

1°. Such contributions are likely to come from the longer wavelength components in the global distribution of $(\Delta g_c + \gamma N_c''/\bar{R})$. The strength of signal increases to about 50% when contributions due to areas in the range $0.2^\circ < \psi < 1^\circ$ are also considered. This is likely to occur through terms of intermediate wavelength (10 to 100 km).

5.3.2. Error Accumulation Patterns.

A study of Tables 5.2 and 5.3 indicates that the precision with which the quantity $(\Delta g_c + \gamma N_c''/\bar{R})$ is recovered is considerably influenced by that of $(N_c'' - N_{cp}'')$. As interest centres primarily on the recovery of long wavelength features, the question is how do the errors of equivalent wavelength in $(N_c'' - N_{cp}'')$ influence the result through contributions from areas where $\psi < 10^\circ$. In the case of input from satellite altimetry, the data are in the form of profiles which, in the absence of reliable models for ocean tides, will contain a tidal signal. This tidal signature will probably have a random effect on area mean values of $(N_c'' - N_{cp}'')$ for an entire mission, though there will be a tendency for the errors in sequential area means to be correlated. This will not be considered in the present development as it has been previously assumed that the altimetry data have been corrected for tidal effects.

The satellites launched for oceanographic studies during EODAP have approximately 800 km altitudes with 1-2 degree beam widths. Consequently, each value of N_c'' is likely to be an average over a finite footprint estimated at less than 10 km, depending on the reflectivity of the instantaneous ocean surface. The nature of the data collected in any given area during a particular satellite mission, will consist of profiles taken along two sets of nearly orthogonal groundtracks. The pattern of errors (e_N) in values of N_c'' used in the quadratures evaluation of the inverse of Stokes' integral is therefore likely to have both random (e_{Nr}) and systematic (e_{Ns}) components. While the structure of the former can largely be described by a bounded magnitude, the latter can only be estimated if a plausible structure is assumed for its variation over the inner zone region described above.

One such model for $(e_N - e_{Np})$ without the benefit of any empirical evidence is assessed as

$$(e_N - e_{Np}) = 0\{+(K_1 + K_2 \psi^\circ)m\} \quad \text{for } 0.2^\circ < \psi < 5^\circ$$

where

$$K_1 = \begin{matrix} 0.3 & 1 & \text{for Doppler orbits} \\ 0.2 & K_2 = 0.1 & \text{for laser ranging} \end{matrix} \quad (5.72)$$

Let the annulus ψ° from the point of computation be represented by m° equal area sub-divisions. The number of sub-divisions (n_ψ) in such an annulus is given by (Mather 1973a, p.67),

$$n_\psi = (360 \sin \psi) / m$$

The accumulation of accidental error (δe_{ga}) in quadratures evaluation for such a ring is given by

$$\begin{aligned} \delta e_{ga} &= \pm 0\{K_a M_1(\psi) \sin \psi \Delta e_{Na} (m \times \frac{360}{n_\psi}) \sqrt{n_\psi}\} \\ &= \pm 0\{K_b M_1(\psi) \sin^{1/2} \psi \Delta e_{Na} m^{3/2}\} \end{aligned} \quad (5.73)$$

where Δe_{Na} is the accidental error component in $(e_N - e_{Np})$,

$$K_a = \frac{\gamma}{4\pi R} \times \frac{\pi}{180} \quad K_b = \frac{K_a}{\sqrt{360}} \quad (5.74)$$

On the other hand, if there is a systematic error e_{Ns} in $(e_N - e_{Np})$ which is constant for the annulus, as could occur in the case of annuli when ψ is small, the resulting error accumulation per annulus (δe_{gs}) is better expressed as,

$$\delta e_{gs} = \pm 0\{K_c M_1(\psi) \sin \psi \Delta e_{Ns} m\} \quad (5.75)$$

where

$$K_c = \frac{\gamma}{4\pi R} \times \frac{\pi}{180} \times 2\pi$$

Table 5.4 sets out values of δe_{ga} and δe_{gs} for ring thicknesses suggested in sub-section 5.2.1 in the range $0.05^\circ < \psi < 10^\circ$ to illustrate the magnitudes of the error accumulations involved for $e_{Na} =$

$e_{Ns} = \pm 10$ cm. In view of the disturbingly large magnitudes of δe_{gs} , it is important to take a closer look at the cumulative effects of the systematic error component Δe_{Ns} on quadratures evaluation over an inner cap, given a plausible error structure of the form at equation 5.72.

The expression below is based on the first few terms of a Taylor series

$$\Delta e_{Ns}(d) = K_1 + \sum_i K_{i+1} \frac{d^i}{i!} \quad (5.76)$$

where d is the distance along the satellite altimetry profile from the location at which $e_{Ns} = K_1$. It should be sufficient to limit the expression to only the first few terms. The data for the area around the computation point P , are collected along a series of parallel tracks making an angle i with the prime vertical direction (Figure 5.2). e_{Ns} is obviously zero in the case of the groundtrack that passes through the point of computation P . It is convenient to define the values $K_1(d')$, $K_2(d')$ etc. for any groundtrack which is displaced by a distance d' from that passing through the point of computation P , by the relations

$$K_1(d') = K_{10} + K_{11} d' + K_{12} \frac{(d')^2}{2} + K_{13} \frac{(d')^3}{6} + \dots \quad (5.77)$$

or more generally

$$K_i(d') = K_{i0} + \sum_j K_{ij} \frac{(d')^j}{j!} \quad (5.78)$$

The error $\Delta e_{Ns}(\psi, \alpha)$ at the element (ψ, α) , in relation to the point of computation P , can be defined as a function of the parameters K_{ij} which describe the regional systematic error model through equations 5.76 and 5.78. It can be seen from Figure 5.2 that

$$d' = \psi \sin \theta \quad \& \quad d = \psi \cos \theta \quad (5.79)$$

where

$$\theta = \psi + i - \frac{1}{2} \pi \quad (5.80)$$

Thus, using equations 5.78 and 5.79 in equation 5.76,

T A B L E 5.4.

Linear Zone Error Accumulation Patterns in the Quadratures Evaluation of $(\Delta g_c + \gamma N_c^u/R)$

Range of ψ (deg)	No. of Rings	δe_{ga} (μGal) (Eqn. 5.73)†		δe_{gs} (μGal) (Eqn. 5.75)†		δe_{gs} (μGal) (Eqn. 5.84)			
		Mean Value	Range	Cumul. Signal	Mean Value	Range	Cumul. Signal	Mean Value	Cumulative Signal
0.05 < ψ < 0.25	18	0.34	1.74 > δe_{ga} > 0.04	7.79	864	3517 > δe_{gs} > 182	19 464	3.96	4 253 2 844
0.25 < ψ < 0.5	5	0.18	0.35 > δe_{ga} > 0.08	1.64	408	703 > δe_{gs} > 217	3 911	19.78	4 182 2 773
0.5 < ψ < 3.0	23	0.03	0.17 > δe_{ga} > 0.00	0.73	71	352 > δe_{gs} > 12	1 869	39.57	4 083 2 674
3.0 < ψ < 5.0	4	0.01	0.02 > δe_{ga} > 0.01	0.10	34	49 > δe_{gs} > 22	245	197.89	3 173 1 764
5.0 < ψ < 10.0	6	0.01	0.02 > δe_{ga} > 0.00	0.05	19	35 > δe_{gs} > 9	111	396.89	2 381 972

† $\Delta e_{Ns} = \dagger \Delta e_{Na} = 10$ cm

* See Equation 5.71, Model 1

** See Equation 5.71, Model 2

$$\Delta e_{Ns}(\psi, \alpha) = \sum_i \sum_j K_{(i+1)j} \frac{\psi^{i+j}}{i! j!} \cos^i \theta \sin^j \theta \quad (5.81)$$

On using equation 5.80 in equation 5.79 and using the result in equation 5.81,

$$\Delta e_{Ns}(\psi, \alpha) = \sum_i \sum_j (-1)^j K_{(i+1)j} \frac{\psi^{i+j}}{i! j!} \sin^i(\alpha+i) \cos^j(\alpha+i) \quad (5.82)$$

the series in equations 5.81 and 5.82 being summed from zero.

The systematic error δe_{gs} due to errors Δe_{Ns} in $(N''_c - N''_{cp})$ in the computation for an annulus of thickness $d\psi$ at a distance ψ from the point of computation can be written as :

$$\delta e_{gs} = \int_0^{2\pi} K_c M_1(\psi) \sin\psi \Delta e_{Ns}(\psi, \alpha) d\alpha d\psi \quad (5.83)$$

where K_c is given by equation 5.75 and $\Delta e_{Ns}(\psi, \alpha)$ by equation 5.82. If attention is confined to $\psi < 5^\circ$, $\Delta e_{Ns}(\psi, \alpha)$ can be assumed to be a rapidly convergent power series in ψ . For $(i+j) \neq 2$, the only non-zero contributions arise when $(i=0; j=0)$, $(i=2; j=0)$ and $(i=0; j=2)$. Integration of equation 5.83 gives

$$\delta e_{gs} = \frac{\gamma}{8\bar{R}} M_2(\psi) d\psi \psi^2 [K_{12} + K_{30}] (1 + O\{\psi^2\}) \quad (5.84)$$

as $K_{10} = 0$ by definition and $K_c = \gamma/(4\pi\bar{R})$.

Assuming that Δe_{Ns} should attain a value of 1 m when $\psi = 1^\circ$ and 6 m when $\psi = 10^\circ$, it was estimated that both K_{12} and $K_{30} = O\{-8.9 \times 10^{-4}\}$.

The results in the last column of Table 5.4 give results obtained by the use of equation 5.84 using this particular model for the accumulation of systematic error along parallel profiles of satellite altimetry. It is obvious that the most damaging source of error in computations of $(\Delta g_c + \gamma N''_c/\bar{R})$ are those in the representation of $(N''_c - N''_{cp})$ which have characteristics represented by K_{12} and K_{30} in equation 5.78. Such errors must be contained at magnitudes of at least an order smaller than that referred to above for successful evaluation of equation 5.47 by quadratures.

5.3.3. Discussion.

It is obvious that a large percentage of the signal of the

function $(\Delta g_c + \gamma N_c''/\bar{R})$ cannot be recovered on the basis of the input data $(N_c'' - N_{cp}'')$ being obtained from satellite altimetry. The 50% of the signal which is likely to be recovered, is probably influenced by factors giving rise to the long wave characteristics of the Earth's gravity field. The magnitude of the signal from the inner zones is very large as shown in Table 5.3.

Consequently, the effect of systematic error through the near zones could become quite significant. The nature of equation 5.84, however, illustrates that such errors do not degrade the results of a quadratures computation if their variations as a function of position are symmetrical about the point of computation. Systematic errors in values of N_c'' deduced from data collected over a wide span of time (e.g., the duration of an altimeter-satellite mission) are likely to be due to gravity model errors contaminating orbit determination. If the resulting errors in N_c'' were to vary smoothly over the area with half wavelengths in excess of 1000 km, there would appear to be no reason to believe that long wave features in $(\Delta g_c + \gamma N_c''/\bar{R})$ cannot be recovered using this technique.

As less than one quarter of the signal comes from regions beyond 5° from the computation point (see Table 5.4), the computational procedure could be considerably improved by using truncation functions for the evaluation of outer zone effects. The necessary formulae are established in sub-section 5.3.4.

5.3.4. Truncation Function Representation of Distant Zone Effects.

On using the form for the SST given in equation 5.48, it is possible to rewrite equation 5.42 as

$$\Delta g_c + \gamma N_c''/\bar{R} - \frac{1}{R} ((W_o - U_o) + \sum_{n=2}^{\infty} (n+1) \delta W_n) = c_{in} + c_{out} \quad (5.85)$$

where

$$c_{in} = \frac{\gamma}{4\pi R} \iint_{\psi < \psi_0} M_1(\psi) (N_c'' - N_{cp}'') d\sigma \quad (5.86)$$

$$c_{out} = \frac{\gamma}{4\pi R} \iint_{\psi \geq \psi_0} M_1(\psi) (N_c'' - N_{cp}'') d\sigma$$

Let

$$\Phi(\psi_0) = \begin{cases} M_1(\psi) & \psi_0 \leq \psi \leq \pi \\ 0 & \psi < \psi_0 \end{cases} = \frac{1}{2} \sum_{n=0}^{\infty} (2n+1) H_n(\psi_0) P_{no}(\cos\psi) \quad (5.87)$$

where $H_n(\psi_0)$ are the truncation functions given by

$$\begin{aligned} H_n(\psi_0) &= \int_{-1}^1 \Phi(\psi_0) P_{no}(\cos\psi) d(\cos\psi) \\ &= \int_{-1}^{\cos\psi_0} M_1(\psi) P_{no}(\cos\psi) d(\cos\psi) \end{aligned} \quad (5.88)$$

As $M_1(\psi)$ is given by equation 5.35

$$\begin{aligned} c_{out} &= \frac{\gamma}{4\pi R} \sum_{n=2}^{\infty} \frac{2n+1}{2} H_n(\psi_0) \sum_{i=0}^{\infty} \iint N_{ci}'' P_{no}(\cos\psi) d\sigma \\ &= \frac{\gamma}{2R} \sum_{n=2}^{\infty} H_n(\psi_0) N_{cn}'' \end{aligned} \quad (5.89)$$

as

$$\frac{N_{cp}''}{4\pi R} \sum_{n=2}^{\infty} H_n(\psi_0) \frac{2n+1}{2} \iint P_{no}(\cos\psi) d\sigma = 0$$

N_{cn}'' in equation 5.89 is the n -th degree surface spherical harmonic in the global representation of N_c'' . This is related to the quantity \bar{N}'' by equation 5.40 which satisfies Laplace's equation in the space exterior to the surface of measurement.

On combining equations 5.85, 5.86 and 5.89

$$\begin{aligned} \Delta g_c + \gamma N_c'' / R - \frac{1}{R} ((W_o - U_o) + \sum_{n=2}^{\infty} (n+1) \delta W_n) &= \frac{\gamma}{2R} \sum_{n=2}^{\infty} H_n(\psi_0) N_{cn}'' \\ &+ \frac{\gamma}{4\pi R} \iint_{\psi < \psi_0} M_1(\psi) (N_c'' - N_{cp}'') d\sigma \end{aligned} \quad (5.90)$$

As it would appear that spherical harmonic representations of the gravity anomaly field to degree and order 20 contain only about 30% of the total signal (e.g., Lerch et al. 1974, p.51), it follows from Table 5.3 that ψ_0 in equation 5.90 can be as low as 5° . Consequently, the use of a set of annular rings for the area in the range ψ less than 5° , together with evaluation of the effect of the rest of the globe using

equation 5.89, provides an effective method for the numerical computation of $(\Delta g_c + \gamma N_c''/\bar{R})$ and hence Δg_c through contributions of long wavelength provided the harmonic coefficients N_{cn}'' can be defined to sufficient accuracy.

5.3.5. Conclusions.

Despite the apparent instability of the kernel function of the inverse of Stokes' integral as $\psi \rightarrow 0$, the nature of $M_1(\psi)$ offers hope that equation 5.47 can be used to recover the quantity $(\Delta g_c + \gamma N_c''/\bar{R})$ with wavelengths of interest in SST studies using satellite altimetry data as input.

The design of an appropriate set of annular sub-divisions for the quadratures evaluation of this integral, using the premise of a fixed contribution from each annulus, fails as ψ approaches zero, as the sampling interval is significantly smaller than that at which data are collected during measurement.

A system of annuli more suitable for practical use was obtained by restricting the contribution of each annulus to 1 mGal provided the width of the annulus did not fall below the sampling interval of the satellite altimetry (estimated as 0.1° at the present time).

As low degree harmonics up to (20,20) appear to account for about 30% of the total signal in the case of gravity anomalies, and as the results of Table 5.4 indicate that regions beyond 5° of the computation point contribute less than 30% to the magnitude of $(\Delta g_c + \gamma N_c''/\bar{R})$ in equation 5.90, considerable economy in computation could be obtained by using truncation functions to evaluate outer zone effects beyond 5° of the computation point. The main problem in practical computations is the reliable estimation of the harmonic coefficients N_{cn}'' in equation 5.90 from data confined to oceanic areas and subject to considerable systematic error.

The nature of the inverse of Stokes' integral and that of the input data from satellite altimetry precludes the possibility of recovering point gravity anomalies in view of the doubts about the precision with which the contributions of regions within 0.1° of the point of computation can be estimated. These regions are estimated to contribute approximately 30% of the signal in quadratures computations. For more details, refer to Table 5.3. It is however, assessed that the contributions to $(\Delta g_c + \gamma N_c''/\bar{R})$ through wavelengths of interest in SST

determinations are likely to be recovered using the presently available satellite altimetry data.

A recommended pattern of sub-divisions which should recover about 60% of the signal in computations of $(\Delta g_c + \gamma N_c''/\bar{R})$, including the contributions of longer wavelength sought for in determinations of the SST is the following:

Range of ψ	Input Data	Thickness of Annuli	No. of Annuli
$\psi > 5^\circ$	Harmonic Coefficients		(Truncation Functions)
$3^\circ < \psi < 5^\circ$	$\frac{1}{2}^\circ$ Area Means	0.5°	4
$0.5^\circ < \psi < 3^\circ$	0.1° Area Means	0.1°	25
$0.25^\circ < \psi < 0.5^\circ$	0.1° Area Means	0.05°	5
$0.1^\circ < \psi < 0.25^\circ$	0.1° Area Means	0.01°	15

Successful numerical evaluations could be seriously inhibited by the occurrence of excessive error in the input data but fortunately, the most critical effects occur when ψ is small. For such ranges of ψ , the error Δe_N in $(N_c'' - N_{cp}'')$ is relatively small, being governed by functions of the type given in equation 5.72. Even on allowing for a more general form for Δe_N as given in equation 5.82, significant degradation of the result occurs only when the distribution of error in the vicinity of the computation point is significantly asymmetrical about the latter with long wavelengths.

5.4. Criteria for Determining SST with Minimum Reliance on Gravity Data.

5.4.1. Preamble.

There appears to be a tendency for some gravity field models based on solutions which include surface gravity information in the definition of low degree harmonics, to result in inferior representations at orbital altitudes (e.g., Lerch et al. 1974, p.61). One possible cause is due to systematic errors of long wavelength in the irregularly spaced surface gravity data, as discussed in the last paragraph of sub-section 5.2.3.

It is also of interest to investigate whether there is any

correlation between errors in the gravity field model and the distribution of tracking stations on the surface of the Earth. One means of obtaining some information on this matter at the present time is to compare a purely satellite solution for the gravity field (e.g., GEM 7) with equivalent area means reliably computed from surface gravity data, and study the discrepancies as a function of distance from the nearest tracking station. Table 5.5 presents the results in the case of the Goddard Earth Models GEM 7 and GEM 8. Comparisons were made between the harmonic models and ten degree equal area gravity means compiled from a $1^\circ \times 1^\circ$ data set (R.H. Rapp, private communication, 1977). The comparisons were restricted to those ten degree means which were based on at least a 30% representation in the square. Such a procedure excluded the more dubious area means from surface gravity representation. These comparisons were studied as a function of distance (d in Table 5.5) from the nearest tracking station whose station position was considered to have been established with an error estimate of less than ± 6 m in the internal statistics of the solution (e.g., Lerch et al. 1974, p.69).

While the residuals for $d > 4000$ km are not meaningful in view of the limited sample, it would appear that a correlation does exist between errors in the gravity field model and the distance from the nearest tracking station in the range $d < 3000$ km. As might be expected, there is a marginal improvement in the fit to surface gravity when using GEM 8. The rms values for comparisons in the range $3000 < d < 4000$ are smaller than those in the range $1000 < d < 3000$. It is not certain whether this is due to a distorting effect produced in harmonics of intermediate wavelength ($n > 5$) in an attempt to fit observations taken at the tracking stations.

The error e_N defined in equations 5.17 and 5.21 probably has three constituent sources of error, given by

$$e_N = e_{Na} + e_{Ng} + e_{Nt} \quad (5.91)$$

where e_{Na} is the error due to instrumental errors in the tracking equipment and the radar altimeter,
 e_{Ng} is the error in the orbit determination due to errors in the gravity field model used in the orbit analysis
 e_{Nt} is the error in orbit determination due to errors in the tracking station coordinates which are held fixed in the

T A B L E 5.5.

Discrepancies Between Satellite Determined Gravity Models and Surface Gravity Anomalies
(10° area means) as a Function of Distance from the Nearest Tracking Station

Distance from Nearest Tracking Station d (km)	GEM 7		GEM 8	
	RMS Discrepancy (\pm mGal)	Sample Size	RMS Discrepancy (\pm mGal)	Sample Size
$0 < d \leq 100$	6.0	4	5.1	4
$100 < d \leq 500$	10.3	19	10.0	19
$500 < d \leq 1000$	9.7	37	8.8	37
$1000 < d \leq 2000$	11.7	83	10.2	83
$2000 < d \leq 3000$	13.1	54	12.1	54
$3000 < d \leq 4000$	9.6	18	9.9	18
$4000 < d \leq 5000$	10.9	5	11.1	5
$5000 < d$	-	1	-	1

orbit determination.

As e_N is the average value from tracking data collected during an extended period of time, and if the instrumentation is regularly calibrated, e_{Na} is likely to be an error source of comparatively short wavelength and therefore of secondary consideration in the context of the goals of this development. It is debatable whether e_{Ng} can be separated from e_{Nt} . The next section establishes the relation between errors $dC_{\alpha nm}$ in the coefficients defining the gravity field model used in the orbit analysis, and e_{Ng} . It should be noted that these coefficients $dC_{\alpha nm}$ comprise the long wave terms in T'' when the "higher" reference model is used.

5.4.2. The Effect of Gravity Field Model Errors on e_N .

The geopotential W can be related to the value W_c computed by the use of the set of coefficients $C'_{\alpha nm}$ and the value $(GM)_{e_o}$ adopted for the product of the gravitational constant and the mass of the solid Earth and oceans, by the relations

$$W = W_c + e_{T'} = \frac{(GM)_{e_o}}{R} + (T'_o + V) + \delta T + e_{T'}, \quad (5.92)$$

where δT is the difference in potential between equivalent spherical and equipotential ellipsoidal models of the Earth, and $e_{T'}$ is related to e_{Ng} by

$$e_{T'} = \gamma e_{Ng} \{1 + O\{f\}\} \quad (5.93)$$

The disturbing potential T' of the solid Earth and oceans in relation to the equipotential ellipsoidal reference model, satisfies Laplace's equation in the space exterior to the Earth's bounding surface and down to the surface of measurement. T' can be fully represented in this space by the relation

$$T' = T'_o + e_{T'}, \quad (5.94)$$

T'_o and $e_{T'}$ being given by

$$T'_o = \frac{(GM)_{e_o}}{R} \sum_{n=2}^{\infty} \left(\frac{a}{R}\right)^n \sum_{m=0}^n \sum_{\alpha=1}^2 C'_{\alpha nm} S_{\alpha nm} \quad (5.95)$$

and

$$e_{T'} = \frac{(GM_{e_o})}{R} \sum_{n=2}^{\infty} \left(\frac{a}{R}\right)^n \sum_{m=0}^n \sum_{\alpha=1}^2 dC_{\alpha nm} S_{\alpha nm} + \frac{e_{GM}}{R} \quad (5.96)$$

where $C'_{\alpha nm}$ are the coefficients of the gravity field model used in the orbit determination, $S_{\alpha nm}$ being defined in equation 5.16, e_{GM} is the error in the value adopted for GM_e , (R, ϕ, λ) defining a geocentric system of spherical coordinates in Earth space, the first degree harmonic being excluded on initialization of coordinate systems.

On following the practice of adopting the gravity field model used in orbital analysis as the "higher" reference model, along with the Earth parameters (GM_{e_o}) , a and δT , it can be seen that

$$T'' = T' - T'_O = e_{T'}, \quad (5.97)$$

which is defined by equation 5.4 at the surface of the Earth. Also, T'' satisfies Laplace's equation at both orbital elevations and down to the surface of measurement. Estimates of the height anomaly ζ' at the ocean surface from satellite altimetry (ζ'_O) are related to e_N by equation 5.17 while associated values on the Brillouin sphere are given by equations 5.20, 5.40, 5.41 and 5.43. On combining these relations with equation 5.15 at the Brillouin sphere,

$$\begin{aligned} \bar{T}'' &= \frac{(GM_{e_o})}{R} \sum_{n=0}^{\infty} \left(\frac{a}{R}\right)^n \sum_{m=0}^n \sum_{\alpha=1}^2 dC_{\alpha nm} S_{\alpha nm}, \quad n \neq 1 \\ &= (W_O - U_O) + \gamma \sum_{n=0}^{\infty} \sum_{m=0}^n \sum_{\alpha=1}^2 (\bar{\zeta}_{\alpha nm} + e_{N\alpha nm}) S_{\alpha nm} \\ &+ \sum_{n=1}^{\infty} \sum_{m=0}^n \sum_{\alpha=1}^2 \delta W_{\alpha nm} S_{\alpha nm} - \sum_{n=0}^{\infty} \sum_{m=0}^n \sum_{\alpha=1}^2 V_{\alpha nm} S_{\alpha nm} \end{aligned} \quad (5.98)$$

where $V_{\alpha nm}$ are the coefficients in the representation of the atmospheric potential at the surface of the Earth, $e_{N\alpha nm}$ are those defining the harmonics in equation 5.21, and

$$\begin{aligned} \gamma \sum_{n=0}^{\infty} \sum_{m=0}^n \sum_{\alpha=1}^2 (\bar{\zeta}_{\alpha nm} + e_{N\alpha nm}) S_{\alpha nm} &= \gamma(\zeta'_O + e_N) + dR \frac{\partial T''}{\partial h} \\ &= \gamma \zeta' + dR \frac{\partial T''}{\partial h} \end{aligned} \quad (5.99)$$

The following relations hold

For $n = 0$

$$dC_{100} = \frac{e_{GM}}{(GM_e)_o} = \frac{\bar{R}}{(GM_e)_o} [(W_o - U_o) + \gamma \zeta'_{100} - V_{100}] + \frac{\bar{R}}{(GM_e)_o} \gamma e_{N100} \quad (5.100)$$

For $n = 1$

$$\gamma \bar{\zeta}_{\alpha 1 m} + \delta W_{\alpha 1 m} + \gamma e_{N\alpha 1 m} = 0 \quad (5.101)$$

For $n > 1$

$$dC_{\alpha n m} = \frac{\bar{R}}{(GM_e)_o} \left(\frac{\bar{R}}{a}\right)^n [\gamma \bar{\zeta}_{\alpha n m} + \delta W_{\alpha n m} - V_{\alpha n m}] + \frac{\bar{R}}{(GM_e)_o} \left(\frac{\bar{R}}{a}\right)^n \gamma e_{N\alpha n m} \quad (5.102)$$

Equations 5.101 and 5.102 can be solved for the long wave features of the SST only if $dC_{\alpha n m}$ and $e_{N\alpha n m}$ are significantly smaller than $\delta W_{\alpha n m}$. In other circumstances, it would be helpful if a relationship, if any, between $dC_{\alpha n m}$ and $e_{N\alpha n m}$ were established. Some provisional ideas on the subject are given in the next sub-section.

5.4.3. Relationship between errors $dC_{\alpha n m}$ and $e_{N\alpha n m}$.

This development attempts to examine whether any relationship can be defined between the errors $dC_{\alpha n m}$ in the model used to represent the gravity field in satellite-altimeter orbit analysis, and those ($e_{N\alpha n m}$) defining e_N in equations 5.43 and 5.123. The input gravity field model for the orbit determination is obtained from equation 5.92 as

$$W_c = \frac{(GM_e)_o}{R} + T'_o + V + \delta T \quad (5.103)$$

The dominant variations in e_N , as a function of time, are caused by the radial component (e_R) of the positional error of the altimeter-equipped spacecraft. Let the position of the altimeter-equipped spacecraft at epoch ($\tau=t$) be described by the set of geocentric Cartesian coordinates $X_i(t)$ in Earth space. Let the equivalent geocentric distance computed from these coordinates be $R_o(t)$, given by

$$R_o(t) = \left(\sum_{i=1}^3 (X_i(t))^2 \right)^{1/2} \quad (5.104)$$

The other geocentric coordinates are given by

$$\lambda(t) = \tan^{-1}(X_2(t)/X_1(t)) ; \quad \phi(t) = \tan^{-1}(X_3(t)\cos \lambda(t)/X_1(t)) \quad (5.105)$$

If e_R is the error in R_o , which is unlikely to exceed ± 10 m at the present time,

$$e_R(t) = \left(\sum_{n=0}^{\infty} \sum_{m=0}^n \sum_{\alpha=1}^2 \frac{\partial W}{\partial C_{\alpha nm}} dC_{\alpha nm} + \frac{\partial W}{\partial R} e_{R_o} \right) / \frac{\partial W}{\partial R} \quad (5.106)$$

all partial derivatives being evaluated in terms of the values for (R, ϕ, λ) at time $(\tau=t)$. The effects of errors introduced in the radial direction by those in the computed values of ϕ and λ are not accounted for in equation 5.106 as they are assessed as being significantly smaller. Also,

$$\frac{\partial W}{\partial R} e_{R_o} = - \frac{(GM)_{e_o}}{R_o^2} \sum_{n=0}^{\infty} (n+1) \left(\frac{a}{R_o} \right)^n \sum_{m=0}^n \sum_{\alpha=1}^2 C'_{\alpha nm} S_{\alpha nm} e_{R_o} ; \quad n \neq 1 \quad (5.107)$$

Thus equation 5.106 can be written as

$$e_R(t) = \frac{1}{F(R)} \left\{ \frac{(GM)_{e_o}}{R_o(t)^2} \sum_{n=0}^{\infty} \left(\frac{a}{R_o(t)} \right)^n \sum_{m=0}^n \sum_{\alpha=1}^2 S_{\alpha nm}(t) \right. \quad (5.108)$$

$$\left. \cdot (dC_{\alpha nm} - (n+1) C'_{\alpha nm} [e_{R_o}(t)/R_o(t)]) \right\}, \quad n \neq 1$$

where

$$F(R) = - \frac{(GM)_{e_o}}{R_o^2(t)} \sum_{n=0}^{\infty} \left(\frac{a}{R_o(t)} \right)^n (n+1) \sum_{m=0}^n \sum_{\alpha=1}^2 C'_{\alpha nm} S_{\alpha nm}, \quad n \neq 1 \quad (5.109)$$

In equations 5.108 and 5.109, $C'_{100} = 1$, $C'_{120} = o\{10^{-3}\}$ and $C'_{\alpha nm} = o\{10^{-5}/n^2\}$ for all other α , n and m . As $e_R(t) = o\{\pm 10 \text{ m}\}$, $F(R)$ can be expressed as

$$F(R) = - \frac{(GM)_{e_o}}{R_o^2(t)} \{1 + o\{f\}\} \quad (5.110)$$

For this same reason, only the harmonics C'_{100} and C'_{120} will have any influence through the second set of terms on the right in equation

5.109 at altimeter-satellite altitudes.

The effect of station coordinate errors e_{Nt} on e_N in equation 5.91 is only of significance if erroneous values of tracking station coordinates are held fixed when solving for the orbit of altimeter equipped spacecraft. On the other hand, if tracking station coordinates are allowed to float when solving for the orbit and/or gravity field model, it could be interpreted that e_{Nt} need not be considered as a separate entity in the definition of e_N as the characteristics of e_{Nt} would be variable with time and therefore behave as high frequency errors similar to e_{Na} in sub-section 5.4.1 in the context of a satellite altimeter mission.

However, if the tracking station positions were held fixed during the analysis of the orbits for an entire mission, e_{Nt} would have the form

$$e_{Nt} = \sum_{n=0}^{n_m} \sum_{m=0}^n \sum_{\alpha=1}^2 e_{Nt\alpha nm} S_{\alpha nm} \quad (5.111)$$

where n_m is a function of the spacing of tracking stations on the surface of the Earth. On using equations 5.108 and 5.111 in equation 5.91 and treating e_{Na} as random and negligible in the present context,

$$e_N = \frac{(GM_e)_o}{F(R)R_o} \left(\sum_{n=0}^{\infty} \left(\frac{a}{R_o(t)} \right)^n \sum_{m=0}^n \sum_{\alpha=1}^2 dC_{\alpha nm} S_{\alpha nm} \right. \\ \left. - \left(1 + 3 \left(\frac{a}{R_o(t)} \right)^2 C'_{120} S_{120} \right) e_{R_o} / R_o(t) \right) + \sum_{n=0}^{n_m} \sum_{m=0}^n \sum_{\alpha=1}^2 e_{Nt\alpha nm} S_{\alpha nm}, \quad n \neq 1 \quad (5.112)$$

The use of equation 5.112 in equations 5.100 and 5.102 gives

For $n = 0$

$$dC_{100} \left(1 - \frac{\gamma}{F(R)} \frac{\bar{R}}{R_o} \right) = \frac{\bar{R}}{(GM_e)_o} \left((W_o - U_o) + \gamma \bar{z}'_{100} - V_{100} \right) + \frac{\gamma \bar{R}}{(GM_e)_o} e_{Nt100} \\ - \frac{\gamma}{F(R)} \frac{\bar{R}}{R_o} [e_{R_o} / R_o] \quad (5.113)$$

For $n = 1$

No change in equation 5.101 as $dC_{\alpha 1m} = 0$ by definition, except to replace $e_{N\alpha 1m}$ by $e_{Nt\alpha 1m}$.

For $n = 2$ and $m = 0$

$$dC_{120} \left(1 - \frac{\gamma}{F(R)} \left(\frac{\bar{R}}{R_o}\right)^3\right) = \frac{\bar{R}}{(GM_e)_o} \left(\frac{\bar{R}}{R_o}\right)^2 (\gamma \bar{\zeta}'_{120} + \delta W_{120} - V_{120})$$

$$+ \frac{\gamma \bar{R}}{(GM_e)_o} \left(\frac{\bar{R}}{R_o}\right)^2 e_{Nt120} - \frac{3\gamma}{F(R)} \left(\frac{\bar{R}}{R_o}\right)^3 C'_{120} [e_{R_o}/R_o]$$
(5.114)

For all other n

$$dC_{\alpha nm} \left(1 - \frac{\gamma}{F(R)} \left(\frac{\bar{R}}{R_o}\right)^{n+1}\right) = \frac{\bar{R}}{(GM_e)_o} \left(\frac{\bar{R}}{R_o}\right)^n (\gamma \bar{\zeta}'_{\alpha nm} + \delta W_{\alpha nm} - V_{\alpha nm})$$

$$+ \frac{\gamma \bar{R}}{(GM_e)_o} \left(\frac{\bar{R}}{R_o}\right)^n e_{Nt\alpha nm}$$
(5.115)

5.4.4. Discussion.

The following observations can be made from the material set out in Sections 5.2 and 5.4.

- i) Any orbital errors which are functions of position and independent of time for the duration of a satellite altimeter mission cannot be distinguished from quasi-stationary SST by the use of equation 5.102 . Possible alternative forms for $e_{N\alpha nm}$ are given in equations 5.113 to 5.115. Errors of this type would have to be held to below ± 10 cm for a successful determination of long wave features of the SST, in the equivalent frequency range.
- ii) It would be advantageous to minimize the effect of orbit distortion due to errors in tracking station coordinates held fixed during orbit integration for satellite altimetry.
- iii) An analysis of equation 5.102 indicates that it can be used in two distinct circumstances:
 - a) If $dC_{\alpha nm}$ are significantly larger than equivalent harmonic coefficients $\delta W_{\alpha nm}$ and $e_{N\alpha nm}$, then $dC_{\alpha nm}$ can be improved until their magnitude is substantially the same as the latter quantities. This is tantamount to gravity field model improvement using satellite altimetry data .
 - b) If both $dC_{\alpha nm}$ and $e_{N\alpha nm}$ are both significantly smaller than $\delta W_{\alpha nm}$, then equation 5.102 can be used to determine the wavelengths in the SST equivalent to those in the gravity field model which are known without error at the 10 cm level.
- iv) Equation 5.102 would be useful in practice only if

reliable values of $\bar{\zeta}_{\alpha nm}$ could be computed for wavelengths sought at iii(a) and iii(b) above. In fact, observational data are likely to be available for oceanic areas only (approximately 70% global representation). This data alone cannot give estimates of $\bar{\zeta}_{\alpha nm}$ as ζ'_0 is not zero in non-oceanic areas. For further consideration of this problem, see Section 5.5 .

- v) In the light of the observation at iii(a) above, it can be seen that satellite altimetry data can play no role in the improvement of gravity field models to precisions below the magnitude of the SST.
- vi) The problems involved in unifying all the geodetic levelling datums in relation to the global datum level surface (geoid) have not been considered so far. For a discussion, see Section 5.5.
- vii) It follows from the development in Sections 5.2 and 5.4 that no geodetic determinations of the long wave features of the SST can be achieved in the absence of a gravity field model consistent with the orbit determination of the altimeter-equipped spacecraft using a ± 10 cm global tracking network. The resolution of the gravity field model should be such as to provide an error free representation of wavelengths of the Earth's gravity field equivalent to those sought in the SST. A corollary is that wavelengths in the SST shorter than those in the representation of the Earth's gravity field which have an effect on satellite orbits at the 10 cm level, cannot be determined by geodetic means unless there is a global coverage of sufficiently precise gravity anomaly data (see Section 6.1).

5.5. The Unification of Geodetic Levelling Networks.

5.5.1. Description of the Problem.

An important adjunct to the determination of quasi-stationary SST is the unification of geodetic levelling datums in relation to a global

datum level surface - the geoid. The object of such a unification of levelling datums is to define normal displacements, as determined incrementally by the combination of geodetic levelling and astro-geodetic levelling, in absolute global terms with reference to the geoid instead of a regional MSL datum. It can be argued that such a definition could be provided in purely geometrical terms by relating such level datums to three dimensional positional systems. However, the operations of geodetic levelling have practical utility by virtue of their direct relation to level surfaces of the Earth's gravity field.

It is therefore of importance to continue to relate the results of geodetic levelling to functions of the geopotential and hence reference all regional levelling datums to a unique level surface - the geoid.

In the following development, let each of the n MSL datums in use at the present time, be displaced in relation to the geoid by a difference in geopotential δW_j ($j=1,n$). Obviously, the numerical values of the δW_j 's are dependent on the definition adopted for the geoid (see sub-section 2.4.2) .

The level surface adopted as the geoid is required for the following purposes:

- i) The definition of SST.
- ii) The unification of geodetic levelling datums.
- iii) The definition of relations in physical geodesy.

One means for defining the geoid is the adoption of the level surface which satisfies the relation

$$M\{\delta W\} = \delta W_0 = 0 \quad (5.116)$$

in the context of equations 5.2 and 5.15.

Different level surfaces will be adopted as the geoid depending on whether δW is chosen as zero over continents (i.e., SST is considered to exist only in oceanic areas) or whether $\delta W = \delta W_j$ in continental areas, the δW_j chosen for a particular area depending on the levelling datum to which the elevation of the area is referred. The former definition will have a direct appeal to oceanographers. The latter definition is more attuned to the needs of physical geodesy which has to cope with the handling of data from both satellite altimetry and gravimetry.

5.5.2. Determination of δW_j for the Continental Levelling Datums.

It is unlikely that a unified global datum level surface can be directly obtained at the ± 10 cm level from satellite altimetry data alone due to the probable influence of abnormal coastal effects on the observational data. If a global representation of surface gravity were available, T'' could be related at the surface of measurement to gravity anomalies by the combination of equations 5.4 and 5.52

$$T'' = \gamma N_{ns} - V + 2(W_o - U_o) - RM\{\Delta g_c\} + 2M\{\delta W\} - \sum_{n=2}^{\infty} \frac{2}{n-1} \delta W_n + \frac{\bar{R}}{4\pi} \iint f(\psi) \Delta g_c d\sigma \quad (5.117)$$

In this equation, δW_n is the n -th degree surface harmonic in the global representation of δW , with the δW for any $d\sigma$ on land being the value δW_j for the appropriate levelling datum to which the height used in the computation of Δg_c was referred.

A quantity similar to that defined in equation 5.53 which can be numerically evaluated from such a surface gravity coverage is ζ'_ℓ , given by

$$\zeta'_\ell = N_{ns} - \bar{R} M\{\Delta g_c\} / \gamma + \frac{\bar{R}}{4\pi\gamma} \iint f(\psi) \Delta g_c d\sigma \quad (5.118)$$

The following relation is obtained on the combination of equations 5.117 and 5.118 at the surface of measurement:

$$T'' = 2(W_o - U_o) - \sum_{n=2}^{\infty} \frac{2}{n-1} \delta W_n + \gamma \zeta'_\ell - V \quad (5.119)$$

on defining the geoid as the level surface such that $M\{\delta W\} = 0$ (the Oceanic definition). Note that ζ'_ℓ is not equal to ζ' . The relation between the two is obtained by combining equation 5.119 with equation 5.4, giving

$$\gamma(\zeta' - \zeta'_\ell) = (W_o - U_o) - \delta W_1 - \sum_{n=2}^{\infty} \frac{n+1}{n-1} \delta W_n \quad (5.120)$$

\bar{T}'' on the Brillouin sphere for land areas can be expressed as

$$\bar{T}'' = 2(W_o - U_o) - \sum_{n=2}^{\infty} \frac{2}{n-1} \delta W_n + \gamma \bar{\zeta}'_\ell - V \quad (5.121)$$

where

$$\bar{\zeta}'_l = \zeta'_l + \frac{dR}{\gamma} \frac{\partial T''}{\partial h} + O\left\{\frac{1}{2}(dR)^2 \frac{\partial^2 T''}{\partial h^2}\right\} = \sum_{n=0}^{\infty} \sum_{m=0}^n \sum_{\alpha=1}^2 \bar{\zeta}_{l\alpha nm} S_{\alpha nm} \quad (5.122)$$

It should be noted that equation 5.121 applies to both land and oceanic areas if a global coverage of gravity anomalies is available. This is unlikely to be the situation in the next few years. Data that are likely to be available in oceanic areas can be defined on the Brillouin sphere by the relation

$$\bar{T}'' = (W_o - U_o) + \delta W - V + \gamma(\zeta'_o + e_N) \quad (5.123)$$

on using equations 5.4 and 5.17, where

$$\bar{\zeta}'_o = \zeta'_o + \frac{dR}{\gamma} \frac{\partial T''}{\partial h} + O\left\{\frac{1}{2}(dR)^2 \frac{\partial^2 T''}{\partial h^2}\right\} = \sum_{n=0}^{\infty} \sum_{m=0}^n \sum_{\alpha=1}^2 \bar{\zeta}_{o\alpha nm} S_{\alpha nm} \quad (5.124)$$

ζ'_o being the value of ζ' obtained from satellite altimetry.

Equation 5.120 provides a mean of defining the long wave features of the SST in relation to a geoid defined by equation 5.116, such that each element of land area is represented by the δW_j for the elevation datum. A successful determination would require that the errors in the global gravity anomaly field through wavelengths equivalent to those sought in the SST were held to below $\pm 30 \mu\text{Gal}$ and the orbital errors in the satellite altimetry were held to $\pm 10 \text{ cm}$.

Equations 5.121 and 5.123 are equivalent to equation 5.115 in terms of the development above. However, the manner in which a global representation of the surface gravity anomaly field is processed would differ in each case. Both sets of equations provide definitions for the δW_j 's but in the form of harmonic models. It might be necessary to continue the harmonic analysis to terms of higher degree when determining the δW_j 's in addition to the representation in oceanic areas, than in the case when only the latter is being defined.

It is obvious that unification of the geodetic levelling datums in relation to a unique datum level surface (the geoid) cannot proceed without surface gravity information of adequate precision. It remains to be seen whether a practically useful unification of the levelling datums can be achieved in the foreseeable future to a precision equivalent to the resolution of first order geodetic levelling.

A technique for establishing a world vertical network, to a precision of the order of 0.2-0.3 kGal m, has been proposed by Colombo (1980a,1980b) using gravimetric, geodetic levelling and precise position fixing data. This technique geometrically fixes the positions of geodetic levelling datums in relation to the centre of mass of the Earth, or to a geocentric reference ellipsoid thereby overcoming the problem of having to define a specific level surface such as the geoid.

5.5.3. Practical Possibilities in the Foreseeable Future.

The gravity data available at the present time are largely confined to continental land masses and their environs. Data at sea are more sparsely distributed. It is possible to envisage all the land gravity data achieving the above stated accuracy standards (ie. $\pm 30 \mu\text{Gal}$) in representations with wavelengths equivalent to those sought in the SST, but with substantial high frequency noise. However, the same cannot be said for oceanic gravity data. It only requires, as a common occurrence, a non-linear drift of 0.1 mGal to be systematic over 1000 km to make the data inadequate for SST determinations. The irregular distribution of surface gravity precludes the use of equation 5.120 in the foreseeable future. Equation 5.7 defines the input data (Δg_c) for the evaluation of ζ'_λ using equation 5.118. The quantity related to the gravity anomaly Δg which is harmonic exterior to and on the surface of measurement (and therefore on the Brillouin sphere) is $\Delta g''$. This quantity takes the values $\overline{\Delta g''}$ on the Brillouin sphere which is obtained from equations 5.6 and 5.7 as

$$\overline{\Delta g''} = \Delta g_c - 2(W_o - U_o)/R - 2\delta W/R \quad (5.125)$$

On using the first equality in equation 5.6 and the definition of T'' in equation 5.27, along with equations 5.15 and 5.44, equation 5.125 can be written as

$$\begin{aligned} \overline{\Delta g''} &= \Delta g_{c0} + e_g - 2(W_o - U_o)/R - \frac{2}{R} \sum_{n=1}^{\infty} \sum_{m=0}^n \sum_{\alpha=1}^2 \delta W_{\alpha nm} S_{\alpha nm} \\ &= \frac{(GM_e)_o}{R^2} \sum_{n=0}^{\infty} (n-1) \left(\frac{a}{R}\right)^n \sum_{m=0}^n \sum_{\alpha=1}^2 dC_{\alpha nm} S_{\alpha nm}, \quad n \neq 1 \quad (\text{for all } \phi, \lambda) \end{aligned} \quad (5.126)$$

the first equality holding at points where observed surface gravity data are available. At locations where satellite altimetry data are

available, the use of equation 5.15, 5.17 and 5.27 in equation 5.123 on the Brillouin sphere, gives

$$\begin{aligned} \bar{T}'' &= \gamma(\bar{\zeta}'_0 + e_N) + (W_0 - U_0) + \sum_{n=1}^{\infty} \sum_{m=0}^n \sum_{\alpha=1}^2 \delta W_{\alpha nm} S_{\alpha nm} - V \\ &= \frac{(GM_{e_0})}{R} \sum_{n=0}^{\infty} \left(\frac{a}{R}\right)^n \sum_{m=0}^n \sum_{\alpha=1}^2 dC_{\alpha nm} S_{\alpha nm}, \quad n \neq 1 \quad (\text{for all } \phi, \lambda) \end{aligned} \quad (5.127)$$

$\bar{\zeta}'_0$ being defined by equation 5.124. Equations 5.126 and 5.127 provide a basis for the determination of SST under the same conditions as outlined in sub-section 5.4.3. This technique has the advantage of being able to handle the corrections δW_j for the n discrete levelling datums though with the same limitations as given in sub-section 5.5.2(iii). However, it does not introduce any instability into the harmonic analysis due to the lack of continuity in either of the data sets as observation equations are formed for all elements of surface area where data are available in either form.

The use of truncated surface harmonic formulations to represent the δW_j for discrete areas can be improved upon to obtain more definitive values for the set of δW_j 's in the following manner. Having obtained a set of coefficients $\delta W_{\alpha nm}$ for an acceptable number of degrees from equations 5.126 and 5.127, the latter can be used in equation 5.119 with the SST terms expressed in the form given in equation 5.52, on adopting the truncation function approach (Molodenskii et al. 1962, p.150) for distant zone effects.

The resulting form of equation 5.119 is

$$T'' = 2(W_0 - U_0) + \gamma \zeta'_\ell - V - \sum_{n=2}^{\infty} Q_n(\psi_0) \delta W_n - \frac{1}{2\pi} \iint_{\psi < \psi_0} f(\psi) \delta W \, d\sigma \quad (5.128)$$

This is equivalent to a set of observation equations (e.g., see equation 5.12) that can be solved for the improved values of δW_j , introduced as discrete quantities in the quadratures evaluation of the surface integral.

In conclusion, it must be emphasized that any success in obtaining a solution based on equations 5.126 to 5.128 is conditional upon the errors in the orbit determination and in the long wave characteristics of gravity anomalies being substantially smaller than the magnitude of the SST.

5.6. Conclusions.

The development in Section 5.2 indicates that relatively simple techniques are available for determining the long wave features in the quasi-stationary SST from a combination of satellite altimetry and gravity anomaly data provided the data are of adequate quality. If the determination were restricted to ocean areas, a solution for wavelengths in the SST equivalent to those in the gravity field affecting satellite orbits for altimeter missions (approximately 1000 km) could be obtained from satellite altimetry data alone if the gravity field model used in the orbit analysis is without error for the wavelengths of interest and the position of the altimeter-equipped spacecraft is known at the ± 10 cm level. In pragmatic terms, such a determination will be difficult to achieve in the absence of a minimum of twenty five evenly distributed 10 cm laser tracking systems and excluding weather limitations (Mather 1974b, p.103).

The first stage in any determination of the long wavelength characteristics of the SST is the development of a model for T'' , consistent with all the tracking data to 0.1 kGal m. It is also assessed that the surface gravity anomaly data available at present are unlikely to play the hoped for role of improving the definition of the gravity field model through all but the lowest degree harmonics (up to degree and order 20) because the precision required for 10° area means should approach ± 1 mGal on a global basis to produce a gravity model correct to ± 6 kGal cm. Model improvement to the level equivalent to the magnitude of quasi-stationary SST (estimated at 1-2 m) would require at least a three-fold improvement in the precision of 10° area means through wavelengths of interest.

It is possible to relate the observations from satellite altimetry in oceanic areas directly to SST and errors in the gravity field model, as set out in equation 5.102, if orbit determinations were performed using tracking data observed from a truly global network of observing stations on a regular basis, without imposing the undue distorting constraints of fixed tracking station positions. On the other hand, such a relation could be used to improve the gravity field model if its errors were larger than the magnitude of SST. Alternatively, if the gravity field model errors were acceptably small (approximately ± 0.1 kGal m) and the orbit determination satisfied the criteria given above, these equations could be used to determine SST in

oceanic areas.

An important corollary is that neither surface gravity information nor satellite altimetry data on their own can provide information on level surfaces to a precision below the magnitude of the SST because all measurements are made either at or in relation to the ocean surface and not the geoid. In any solution procedure, the incorporation of gravity field models used in orbit determinations is vital for the resolution of the SST.

The world's geodetic levelling datums are generally linked to local estimates of MSL. The unification of these datums in relation to a datum equipotential surface - the geoid - cannot be achieved with any degree of confidence unless surface gravity data were used in the determination. Any resolution of this problem in the future may have to be achieved with the limitation that reliable surface gravity anomaly data are confined to the land area and its environs (Mather et al. 1978c). The analysis of the basic equations shows that for this datum problem, a pre-requisite is an acceptable low degree harmonic model of the gravity field which is consistent with the altimeter-satellite orbit at the 0.1 m level. In addition, errors in the surface gravity data with wavelengths equivalent to or greater than the magnitude of the surface area covered by each of the level datums (usually, about 2% of the Earth's surface area) should be held to below 30 μ Gal. The principal sources of such errors are

- a) the global gravity standardization network which should aim at having a station placed every 1000 km square on each of the Earth's land areas; and
- b) systematic errors in the systems of elevations used to compute the gravity anomalies.

Equations 5.126 to 5.128 provide a basis for obtaining a solution when neither the satellite altimetry nor the gravity data have a global coverage.

6. SENSING SURFACE OCEAN DYNAMICS USING SATELLITE ALTIMETRY.

6.1. Recovering the Short Wavelength Components of the SST.

6.1.1. Introduction.

A considerable amount of satellite remote-sensed data are available for quantifying the surface dynamics of the oceans. Parameters of significance cannot be obtained from satellite altimetry without the utilization of appropriate geodetic techniques, calling for a precision which has not been previously achieved.

The methods of analyses required are dependent on the frequencies, both in space and time, sought in the ocean dynamic parameters. The evaluation of quasi-stationary parameters, as concluded in the previous chapter, are compounded by the fact that all the available data are related to the ocean surface and not the geoid to better than ± 2 m. It was also concluded in Section 5.6 that satellite altimetry data alone cannot provide parameters of use in quantifying ocean circulation features with wavelengths greater than \bar{l} where \bar{l} is the shortest wavelength in the Earth's geopotential which contributes to the orbital perturbations of near-Earth satellites above the noise level of the tracking data (about 1000 km) with the proviso that a global network of tracking stations is available. Thus, procedures are outlined in this chapter for circumventing these problems in relation to the short wavelength components of the SST, i.e. the quasi-stationary component ζ_{qs} and the time-varying component ζ_{ns} of equation 2.52.

6.1.2. Possibilities for Determining ζ_{qs} .

The requirements for recovering the quasi-stationary SST with wavelengths shorter than \bar{l} in the satellite determined gravity field model have been investigated in Mather (1978d, Section 7) and Mather & Coleman (1977). The discussion below summarizes the prerequisite conditions.

Assuming that the quasi-stationary component ζ_{ql} of the SST can be modelled by a low degree spherical harmonic series of the form

$$\zeta_{q\ell} = \sum_{n=0}^{n'} \sum_{m=0}^n \sum_{\alpha=1}^2 \zeta_{q\alpha nm} S_{\alpha nm} \quad (6.1)$$

where the maximum degree n' is defined by the limiting wavelength $\bar{\lambda}$,

$\zeta_{q\alpha nm}$ are the coefficients, and

$S_{\alpha nm}$ are the surface spherical harmonic functions of degree n and order m (see equation 2.32),

then using equation 2.52, equation 5.42 may be rewritten as

$$\begin{aligned} \Delta g_{cp} + \gamma N''_{cp} / \bar{R} - (W_o - U_o) / \bar{R} + \gamma \left(\sum_{n=1}^{n'} (n+1) \sum_{m=0}^n \sum_{\alpha=1}^2 \zeta_{q\alpha nm} S_{\alpha nm} \right) / \bar{R} \\ + \gamma \zeta_{q100} / \bar{R} - (\gamma / 4\pi \bar{R}) \iint M_1(\psi) (N''_c - N''_{cp}) d\sigma \\ = -\gamma \zeta_{qs} / \bar{R} - (1/4\pi \bar{R}) \iint M_1(\psi) (\zeta_{qs} - \zeta_{qsp}) d\sigma \quad (6.2) \end{aligned}$$

noting that $\zeta_{q\alpha nm} = \frac{1}{4\pi} \iint \zeta_{q\ell} S_{\alpha nm} d\sigma$. In equation 6.2, the values of N''_c can be obtained from equation 5.41 using values of ζ' deduced from satellite altimetry, while Δg_c is derived from gravity anomaly data using equation 5.7 (where the disturbing potential is assumed negligible in the first instance as T'' is about 10 kGal m on the "higher" reference system). The zero degree term $(W_o - U_o)$ is dependent on the adopted definition of the geoid (see sub-section 2.3.2) as is the zero degree term in the representation of $\zeta_{q\ell}$.

The right hand side of equation 6.2 contains the unknown terms ζ_{qs} . This equation has the advantage that the $M_1(\psi)$ function fades rapidly with increasing ψ with over 80% of the signal coming from contributions within 5° of the computation point (see Section 5.3). Reasonable estimates of ζ_{qs} would be obtained if the Δg_c and N''_c values were averaged over area means constructed to avoid aliasing effects due to the finite nature of the altimeter footprint.

But the limitations inherent in solutions for ζ_{qs} may be stated as:

(i) gravity anomalies have to be defined in oceanic regions to ± 30 μ Gal through wavelengths of interest for a meaningful determination of ζ_{qs} .

(ii) values of ζ' to ± 10 cm are required within 500 km of the coastline for establishing useful values of N''_c . This tedious position fixing effort is considered undesirable.

(iii) evaluations of ζ_{qs} are restricted to regional areas.

It is considered likely, at the present time, that values of Δg_c and N_c'' cannot be defined with sufficient precision to obtain realistic estimates of the short wavelength SST. This is especially true for the gravity data where there can be nearly an order of magnitude precision discrepancy between oceanic and land gravity data (Mather et al. 1976). Problems have also been encountered with analyses of the long wavelength terms in ζ_{ql} by Mather et al. (1978b). It was found in this latter study that the origin of the system of reference used in integrating the satellite orbits was displaced from the geocentre by about 1.5 m, implied by the first degree harmonic in ζ_{ql} , whereas the oceanographic estimates indicated that a maximum displacement of only 25 cm should occur. No reasons for the discrepancy can be given at the present time.

6.1.3. Time Variations in the Short Wavelength SST.

The small scale time variations in the SST can be described by the relation

$$\zeta_{ns} = \zeta'(t+dt) - \zeta'(t) \quad (6.3)$$

where dt represents the time difference between measurements, initially acquired at time t . Provided values of ζ' can be defined to ± 10 cm accuracies, the spectrum of ζ_{ns} could be analysed on both a global and regional basis.

The time varying constituents of the SST are expected to have frequencies ranging from a few days for transient phenomena to a year for seasonal variations with amplitudes varying from about 1-2 cm to around 1 m. Determinations of variations in the SST using equation 6.3 can be treated as being equivalent to those in the radial component of the sea surface position if the variations in the geoid over the same time period are considered invariant.

Two techniques have been used to study temporal variations in the SST. They are:

- (i) the method of overlapping passes, and
- (ii) the method of sea surface models.

Both techniques are usually restricted to regional areas for investigation and are described in subsequent sections of this chapter. The results of Chapter 3 (see Figure 3.4) indicate that temporal

features with wavelengths greater than about 50 km and amplitudes larger than about 30 cm should be seen in the GEOS-3 altimeter data. It should be pointed out, however, that the basic equations used in (i) and the solution procedure at (ii) can be used to extract information on the quasi-stationary SST provided a geoid of adequate quality is available. As mentioned in Chapter 5, the present geoid models are not adequate and this constitutes one of the major limiting factors in obtaining long wavelength information on the SST. Thus, the techniques (i) and (ii) are used predominantly to study only the temporal variations in the SST.

6.2. Geodetic Techniques for Studying Temporal Variations.

6.2.1. Overlapping Pass Analysis.

6.2.1.1. Basic Requirements.

The condition for a repeating groundtrack or overlapping pass may be determined by a relationship between the angular rotation rate of the Earth Ω , and the instantaneous rate of precession of the orbital node of the satellite, $\dot{\bar{\Omega}}$. This relation may be shown to be

$$\sum_{i=1}^N (\dot{\bar{\Omega}}_i t_i - \Omega_i t_i) = \delta\lambda \quad (6.4)$$

on suppressing multiples of 2π in the Ω term. The satellite completes the i -th revolution in time t_i and $\delta\lambda$ is the longitudinal difference of the equator crossing between the initial and N -th revolutions.

The requirements for an overlapping pass mean that $\delta\lambda$ is equal to zero. An estimate of the nodal rate may be found from the equation (Kaula 1966, p.39)

$$d\bar{\Omega}/dt = (3n_\alpha / 2(1-e^2)^2) (a_e/a)^2 \sqrt{5} \bar{C}'_{20} \cos i \quad (6.5)$$

where n_α is the angular velocity of the satellite ($= GM^{1/2} / a_e^{3/2}$),

e is the eccentricity of the orbital ellipse,

a_e is the semi-major axis of the orbital ellipse,

a is the equatorial radius of the reference ellipse,

i is the satellite inclination, and

\bar{C}'_{20} is the normalised zonal coefficient of degree 2 in the representation of the geopotential ($\approx -484.2 \times 10^{-6}$).

Using appropriate values of the quantities in equation 6.5 for the GEOS-3 satellite, the nodal rate is about 2.72 degrees/day. The angular velocity of the Earth has been previously defined in equation 2.2 and is about 360.986 degrees/day. The condition for $\delta\lambda = 0$ is nearly satisfied every 37.18 days or 526 revolutions. The discrepancy ($\delta\lambda$) from an exactly repeating groundtrack (at the equator) is illustrated in Figure 6.1 as a function of time, from the launch date of GEOS-3 in April, 1975 to about October, 1976.

6.2.1.2. Analysis Techniques.

Considering the situation of two overlapping passes where the j -th element of the i -th pass and the l -th element of the k -th pass have identical latitudes and longitudes (ϕ, λ) along each profile, then the following observation equation can be used to obtain information on the short wavelength spectrum of the SST,

$$\begin{aligned} \zeta_{ij} - \zeta_{kl} + (b_i - b_k) + c_i (t_{ij} - t_{il}) - c_k (t_{kl} - t_{kl}) \\ + (\zeta_{tij} - \zeta_{tkl}) = v_s \end{aligned} \quad (6.6)$$

where ζ_{ij} and ζ_{kl} are the observed SSH's on the i -th and k -th passes respectively (about ± 100 m), (b_i, b_k) and (c_i, c_k) are corrections for bias and tilt to the i -th and k -th passes (about ± 50 m and $\pm 1-2$ arcsec), $(\zeta_{tij}, \zeta_{tkl})$ are the tidal heights (about ± 1 m) at the location (ϕ, λ) at the times of measurement (t_{ij}, t_{kl}) , and (t_{il}, t_{kl}) are the times corresponding to the initial instant of data acquisition per pass.

The corrections for bias and tilt are used to remove any long wavelength orbital errors. It is obvious that the times and positions of each altimeter measurement on each pass will not match, so by using one pass as a reference, any other pass can be fitted to the reference pass by simple linear interpolation in latitude.

The non-tidal information of the SST will be contained in the residual of fit, v (about ± 2 m), in equation 6.6. However, solutions using this technique will contain no tidal information on wavelengths greater than twice the length of the altimeter pass nor for periods

OFFSET IN LONGITUDE FOR OVERLAPPING PASSES AS A FUNCTION OF TIME

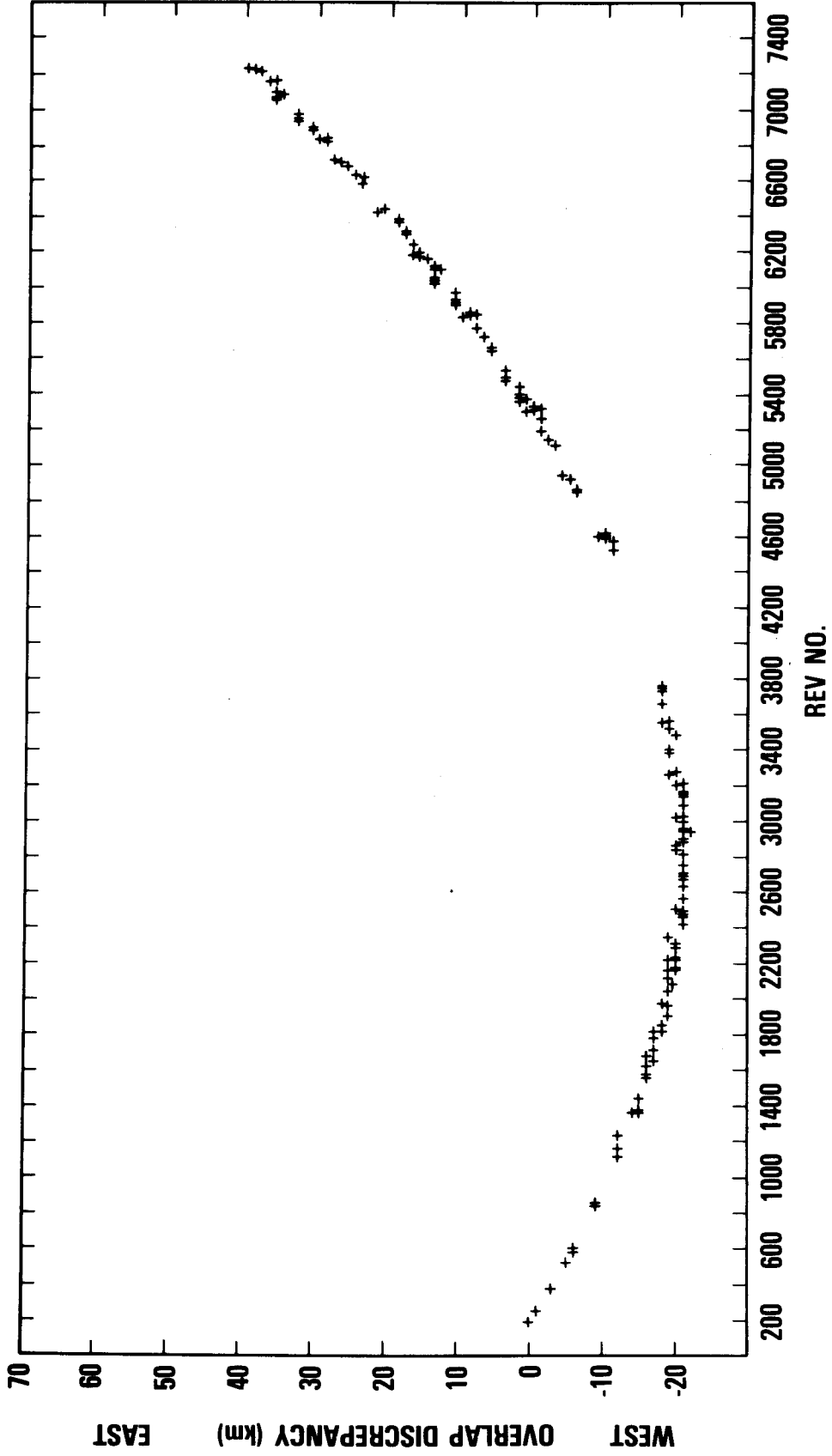


Figure 6.1

shorter than 37.18 days. An example of three overlapping passes in the Tasman and Coral Sea areas is illustrated in Figure 6.2 where passes 62 and 109 (Rev. nos. 826 and 2404) have been fitted to the reference pass 57 (Rev. no. 300) (see Figure 6.3 for location), as well as pass 62 referenced to the GEM 9 gravity field model.

It was found from the early analyses of GEOS-3 overlapping passes (Mather et. al.1977b, Mather and Coleman 1977) that the above technique of using equation 6.6 (called FIT1) had limitations when a large number of overlapping passes were to be compared and/or if the reference pass chosen exhibited high noise levels in the individual altimeter pass measurements.

A more representative comparison can be obtained if each overlapping pass is compared to the mean of all the overlapping passes considered in a set - i.e. a mean set of ζ 's are obtained as a reference with the positions and times of the first overlapping pass used for interpolation. This updated technique is denoted as FIT2 and is equivalent to using equation 6.6 with the mean profile replacing the k-th pass.

As evidenced in Figure 6.1, there is not an exact match in overlap as a function of time. The displacement in longitude $\delta\lambda$ can be used to apply a second order correction since in both techniques FIT1 and FIT2 it has been assumed that the geoid heights at the corresponding j-th and ℓ -th elements are equivalent. The correction term is of the form,

$$\Delta\zeta = N_{ij} - N_{k\ell} \quad (6.7)$$

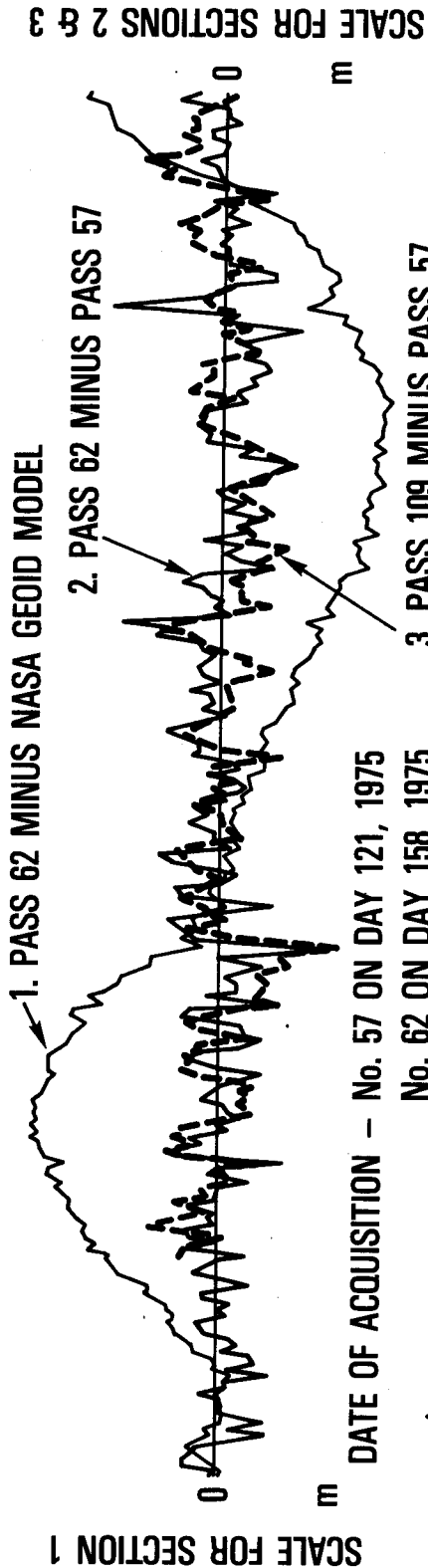
where N_{ij} and $N_{k\ell}$ are the geoid heights on the i-th and k-th passes. A further correction term was implemented to reduce non-oceanographic noise in the residuals. This correction is a consequence of the data acquisition and corrects for effects of the variable pass lengths fitted to the mean profile. These latter two corrections to equation 6.6 constitute the technique (FIT3) predominantly used in the analyses set out in the subsequent sections.

The residuals of fit (v) can now be analysed using band-pass filtering techniques to study the wavelengths of interest in the SST spectrum. The wavelengths of interest for ocean eddy detection are of the order 10-300 km (see Table 3.2). It is obvious that any short wavelength SST information greater than twice the length of the pass will be lost when using these techniques. For the GEOS-3 altimetry data

Overlapping Passes after Tilt & Bias Corrections

10 — BIAS CORRECTION BETWEEN NASA GEOID MODEL AND PASS 62 = -1.6m

—3



DATE OF ACQUISITION — No. 57 ON DAY 121, 1975
 No. 62 ON DAY 158, 1975
 No. 109 ON DAY 269, 1975

ϕ -26°4 -30°3
 λ 166°5 163°6

ELLIPSOID USED

a = 6,378,145m

f = 1/298,255

-47°7

147°3 —3

Figure 6.2

studied, this limiting wavelength is of the order 6000 km.

The internal consistency of the altimeter can be gauged by studying the root mean square (rms) discrepancy σ_m of fit of each overlapping pass, where

$$\sigma_m = \left(\frac{1}{n-1} \sum_{i=1}^n (v_{s_i})^2 \right)^{1/2} \quad (6.8)$$

The result of analyses of some 500 sets of overlapping passes in the Pacific and Atlantic areas indicates that the relative precision of the altimeter was of the order of $\pm 20-30$ cm. The disadvantage of using overlapping pass techniques is that there is a lack of a unique datum for intercomparisons between overlapping sets and also analyses are restricted in the both the space and time coverage obtained.

6.2.2. Regional Sea Surface Models from Satellite Altimetry.

6.2.2.1. Methodology.

Early studies of intensive mode GEOS-3 altimetry in the Tasman and Coral Seas off eastern Australia (Mather et al. 1977b, Mather 1977) indicated that passes of altimetry data provided to Principal Investigators were subject to orbital errors varying from ± 2 m to in excess of ± 10 m. Pairs of overlapping passes in this data bank were studied, including a pair where one of the passes was subject to a radial error in excess of 700 m. The relative discrepancy could be reduced to ± 61 cm of which 66% occurred with wavelengths equal to twice the length of the pass if the passes were fitted to each other (Mather and Coleman 1977, Tables 1 and 2, Row 1). The improved relative fit was obtained by applying a correction for tilt c and bias b per pass with lengths in excess of 1000 km. In less extreme cases, the rms discrepancy (σ_m) after allowing for tilt and bias, is significantly smaller.

The inspection of other pairs of overlapping passes showed that a basis existed for determining a regional model of the sea surface with a resolution of at least 1 m from the available altimetry data under the following assumptions:

- (i) Orbital errors greater than ± 1 m can be adequately modelled by corrections for bias and tilt.

- (ii) The sea surface was radially stationary during the period of data acquisition.

Maximum pass lengths were approximately 3500 km. The assumption at (i) would be questionable for such long groundtracks if the effect of gravity model errors with short wavelengths were to significantly affect the radial component of orbital position. However, computations appear to indicate that the contribution of this effect is likely to be less than ± 20 cm (C.A. Wagner, personal communication, 1977).

As the ocean tide amplitudes in deep oceans are not expected to greatly exceed 30 cm, a quasi-stationary differential model of the sea surface with a precision of $\pm \ell$ cm ($\ell > 30$) can be obtained by adopting one of the techniques described below if the following assumptions are valid:

- (a) Orbital errors with wavelengths greater than 7000 km contributed less than $\ell/3$ cm² to the error spectrum.
- (b) Time variations in SST were less than $\pm \ell\sqrt{3}$ cm.
- (c) Variations in the geoid height over the area adopted as a junction (cross-over) point were less than $\pm \ell\sqrt{3}$ cm.
- (d) The ocean tide amplitudes were either eliminated by modelling/averaging or, alternately, too small to affect the adjustment (e.g., only 30 cm when the precision sought is ± 50 cm).

A cross-over point or junction point is defined as the intersection point of the north-to-south (descending) pass with the south-to-north (ascending) pass.

Two techniques of adjustment suggest themselves with strong analogies to conventional geodetic levelling. Both techniques described below incorporate assumption (ii) above.

Technique 1 - The Invariant Junction Point Height Method

The basic assumptions in this method are the following:

(a) The junction or cross-over "point" of a north-to-south pass and a south-to-north pass was an invariant "point" in Earth space.

(b) The internal fidelity of a pass was not in question. The information required to obtain an absolute fix of a pass of SSH's provided by NASA was the determination of a bias b and a tilt represented by the grade c .

The assumption at (a) should introduce noise into the system conservatively estimated at no greater than ± 1.5 m due to the existence

of the unmodelled tidal signal as well as any mesoscale variations in the SST with periods less than the data acquisition period. Assumption (b) appears to be viable at the ± 1 m level in the case of the 4000 km passes which resulted when data processing were restricted to the 60° by 50° area in the Tasman and Coral Seas.

If the j -th pass required a bias correction of b_j and a grade correction of c_j , and if the i -th element recorded at time t_{ij} , coincided with the k -th junction "point" whose true SSH was ζ_k , the quasi-stationary component ζ_{ok} and the temporal variation $\Delta\zeta(t_{ij})$ at the k -th junction point were related to ζ_k and the altimeter sea surface measurement ζ_{ij} according to the relation

$$\zeta_k = \zeta_{ok} + \Delta\zeta(t_{ij}) = \zeta_{ij} + b_j + c_j(t_{ij} - t_{1j})/\Delta t_j \quad (6.9)$$

t_{1j} being the time at which the first element in the pass was recorded, and Δt_j the total duration of the j -th pass.

In view of the uncertainties associated with current ocean tide models, the entire network of passes was adjusted, in the first instance, using equations of the form

$$\zeta_k = \zeta_{ok} + v_k \quad (6.10)$$

instead of the first equality at equation 6.9, v_k being treated as a normally distributed quantity. Thus, if the i -th element of the j -th pass and the ℓ -th element of the m -th pass both provided estimates of ζ_k , it is possible to set up observation equations of the form

$$v_d = b_j - b_m + c_j(t_{ij} - t_{1j})/\Delta t_j - c_m(t_{\ell m} - t_{1m})/\Delta t_m + (\zeta_{ij} - \zeta_{\ell m}) \quad (6.11)$$

where v_d is the residual to be minimised, and the tidal signal has been assumed to be included in either v_d or ζ .

The resulting set of observation equations (6.11) can be solved by least squares techniques for the biases b_j and the grades c_j for all passes which traverse at least one junction point. The number of junction points must be greater than or equal to the number of coefficients for a solution, making a minimum requirement of 4 ascending and 4 descending passes.

Technique 2 - The Gradient Method

The basic assumptions made in this method are the following:

(a) The junction "point" of a north-to-south pass and a south-to-north pass was an invariant "point" in Earth space.

(b) The difference in SSH between adjacent junction points on a single pass was subject to only random errors. The internal fidelity of the pass is no longer assumed.

If ζ_{tj}, ζ_{tk} are the trial SSH's at the two adjacent junction points corresponding to the i -th and l -th points on the m -th pass, where the altimeter SSH's are ζ_{im}, ζ_{lm} , the resulting observation equation is

$$v_d = \Delta\zeta_j - \Delta\zeta_k + (\zeta_{tj} - \zeta_{tk}) + (\zeta_{im} - \zeta_{lm}) \quad (6.12)$$

where $\Delta\zeta_j$, $\Delta\zeta_k$ are the desired corrections to the trial SSH's ζ_{tj}, ζ_{tk} at the j -th and k -th points respectively. The trial SSH estimates ζ_{tj} and ζ_{tk} were usually derived from a satellite gravity field model, such as GEM 9 (Lerch et al. 1977).

Considering a tilt of 1 arcsec, this would introduce an error of 2.5 m over a 500 km distance between junction points. It follows that this method of adjustment would only be suitable if either the distance between junction points was less than 200 km or the tilts in passes were less than ± 1 arcsec. The resulting equations (6.12) give estimates of the heights ζ_k of the sea surface at each of the junction points.

Both Technique 1 and Technique 2 solutions can be used to determine:

(i) the height of the quasi-stationary sea surface at each junction point, and

(ii) the corrections for bias and tilt per pass needed to fit the satellite orbits to the resulting sea surface model. No bias and tilt corrections are obtained for passes which do not have a junction point.

However, using these techniques the resulting sea surface models are:

(i) insensitive to an absolute datum, being based on a set of observation equations (6.11 and 6.12) which are differential in nature, and

(ii) subject to random variations in Earth space orientation which are functions of the junction point positions over the area.

The internal statistics of both Technique 1 and Technique 2

solutions are represented by the junction point rms discrepancy given by

$$\sigma_{jp} = \left(\frac{1}{n-1} \sum_{i=1}^N (v_d)^2 \right)^{\frac{1}{2}} \quad (6.13)$$

where N is the number of observation equations generated (either 6.11 or 6.12). It is also possible to generate secondary parameters (i.e. values of ζ_k in the case of Technique 1 solutions or values of b_j , c_j in the case of Technique 2 solutions) and the resulting rms discrepancies are referred to as the solution rms (σ_s). The junction point rms will give an indication of the variability in the $p^\circ \times p^\circ$ squares while the solution rms estimates the quality of fit for the sea surface model.

Preliminary tests using the two solution procedures outlined above were carried out in the Tasman and Coral Seas (Mather et al. 1977b). It was found necessary in this study to alter the definition of a junction point to be that of a $p^\circ \times p^\circ$ square, in which the average SSH in the square was used in the observation equations at 6.11 and 6.12. The adoption of such a procedure introduces an additional source of noise into the resulting sea surface model due to the variation of the geoid height within the selected $p^\circ \times p^\circ$ square. This alteration was a consequence of a number of factors, being

- (i) the finite nature of the altimeter footprint,
- (ii) computer limitations for large numbers of junction points in the solution,
- (iii) some aliasing problems caused by high frequency noise at junction points, and
- (iv) for improvement in stability of solutions when bad pass geometry was present.

Tests showed that the junction point rms residuals obtained from the solutions varied as a function of junction point size (see Mather et al. 1977b, Table 3, Mather et al. 1978a, Table 3). In another series of tests, the square size was fixed, and the solution technique varied (see Mather et al. 1977b, Table 4, Mather 1977, Table 2).

The conclusions from these investigations were that Technique 2 solutions were subject to more distortion than the Technique 1 sea surface models. This is due to each pass in the Technique 2 solution being adjusted in sections between junction points and not as complete entities. Consequently, larger features in the sea surface, with wavelengths comparable with the spacing between junction points, tend to

be absorbed into the residuals as orbit errors. However, both techniques could provide a continuous sea surface model on a differential basis with noise levels of about ± 1 m if a well balanced set of altimetry passes were available. Refinements to these initial solution procedures are set out in paragraph 6.2.2.3 as a consequence of the availability of more altimetry data.

Regional sea surface model solutions contain no information on wavelengths greater than twice the dimension of the area studied nor on periods less than the time span of the data used in solution. It appears therefore that a basis exists for obtaining models of the sea surface with a precision equivalent to that underlying the assumption of stationarity of the sea surface, over extents of 6000 km². The correctness of such models in a global context depends on the precision with which harmonics of the gravity field with longer wavelengths are known.

It is important that the internal geometry of altimeter passes be maintained over the regional area in order that the geometry of intermediate features in the sea surface are not smoothed or lost by absorption into the system errors. The precision achievable from the techniques suggested is limited by the following factors:

- (i) Tidal uncertainties, not expected to exceed ± 30 cm.
- (ii) Mesoscale variations in the SST of up to 50 cm with decay times of 100 days.
- (iii) Size adopted for junction points - a limitation controlled by computer dependent factors.
- (iv) The extent of data coverage in the region.

The minimum practicable data acquisition period in the case of GEOS-3 is 25 days. Assuming that adequate data coverage and tidal models are available, it follows that a system of 50 km junction points should be adequate for obtaining a 30 cm model of the sea surface for the study of time varying features. The uncertainties in the resulting model can be expected to increase with the data acquisition period and decrease with the extent of coverage.

6.2.2.2. Refinement of Modelling Procedures.

It was found that a combination of both Technique 1 and Technique 2 solutions yielded the best estimates for the sea surface models. The solution procedure adopted is as follows:

(i) An average bias (BIAS1) is removed from the input altimeter SSH estimates ζ_{ij} according to the relation

$$\text{BIAS1} = \left(\sum_{i=1}^s \sum_{j=1}^t (\zeta_{ij} - N_{ij}) \right) / \left(\sum_{i=1}^s t_i \right) \quad (6.14)$$

where s is the total number of altimeter passes selected in the regional area,

t is the number of points in each altimeter pass, and

N_{ij} is the geoid height value corresponding to the ζ_{ij} estimate.

(ii) Using equation 6.12 and values of geoid height N (estimated either from geopotential models or from gravimetric geoid solutions such as the Marsh-Chang detailed geoid in the North Atlantic (Marsh & Chang 1978)), new junction point SSH values ζ_k are obtained.

(iii) A second bias per pass (BIAS2) is solved for by setting $c_j = 0$ in equation 6.9 and using the ζ_k values obtained in (ii).

(iv) The solution procedure solves for a final bias (BIAS3) and a tilt c_j along each altimeter pass. The final solution is then obtained as a bias b_j (=BIAS1+BIAS2+BIAS3) and a tilt c_j .

(v) The corrected b_j and c_j are used to generate a final set of ζ_k values.

(vi) Values of SSH ζ_k are block meaned over a specified $n^\circ \times m^\circ$ area (minimum block size is the junction point size).

(vii) Corrections are applied to the averaged ζ_k values for absolute datum.

The regional sea surface models are oriented in Earth space to an absolute datum by making a three parameter fit to a satellite gravity field model such as GEM 9. The orientation is achieved by using observation equations of the form

$$v_r = \zeta_k - \zeta_{\text{GEM9}} + a_0 + a_1(\phi - \phi_0) + a_2(\lambda - \lambda_0) \quad (6.15)$$

over the regional area where (ϕ_0, λ_0) are the coordinates of the centre-point of the area studied, and (ϕ, λ) the coordinates of the centres of the $n^\circ \times m^\circ$ areas used in (vi).

From previous monthly sea surface model solutions it was apparent that altimeter passes which traversed few junction points added little information to the sea surface model and in some instances, depending on the particular solution geometry, aliased the resulting models. For these reasons, altimeter passes were excluded from solution if the

passes contained less than a certain number of data points or contained less than 3 junction points along its length. Regional sea surface model solutions reported in Mather et al. (1980) used 10 data points (approximately 70 km) as a cutoff criterion while Coleman (1980), in a subsequent analysis, used 100 data points (approximately 700 km) as the limit.

The ocean tides have been considered as noise in the development outlined above. In an attempt to study the effect of this assumption, Mather et al. (1977b) and Mather et al. (1978a) obtained sea surface models for a time period with, in one instance, tidal effects removed from the altimeter data and in the other, using the raw altimeter values. It was found that the σ_{jp} and σ_s values remained unchanged but the average value of the heights at the junction points changed by 3 cm. This fact supports the contention that the tidal signals, being predominantly of long wavelength, are largely removed on applying tilt corrections (see sub-section 7.3.1).

Thus, the results reported in the next sections use the above techniques to obtain regional sea surface models which should have resolutions of the order $\pm 30-50$ cm.

6.2.3. Alternate Techniques.

Numerous studies by the group at Wallops Flight Center (WFC) (Leitao et al. 1977, 1978a, 1978b, 1979a, 1979b; Huang et al. 1978) have illustrated the remote sensing capabilities of the GEOS-3 altimeter data using both profile techniques, similar to those described in sub-section 6.2.1, and dynamic topographic models. The latter technique is documented in Allen & Martin (1977) and is based on minimum variance techniques to minimise the differences of the ascending and descending profiles at the intersection points. The basic observation equation used is (Allen & Martin 1977, p.5)

$$v = \sum_{i=1}^s \sum_{j=i+1}^s \delta_{ij} \left\{ \left(d_{ij} - \sum_{e=0}^{K-1} a_{ie} t_{ij}^e + \sum_{e=0}^{K-1} a_{je} t_{ji}^e \right)^2 w_{ij} \right\} \quad (6.16)$$

where s is the total number of altimeter passes,

K is the number of coefficients to be solved for in the solution,

δ_{ij} is defined as 0 if no intersection occurs and

1 if pass j intersects pass i,
 d_{ij} is the crossover discrepancy at the point of intersection,
 a_{ie}, a_{je} are the coefficients of a polynomial in time
 t_{ij}, t_{ji} along the i-th and j-th passes respectively, and
 w_{ij} is a weighting factor.

This solution procedure gives corrected SSH's at each intersection point whereas the solution described in sub-section 6.2.2 averages over $p^\circ \times p^\circ$ squares giving averaged SSH values if more than 1 crossover point occurs within the $p^\circ \times p^\circ$ square. However, Leitao et al. (1978b) found the need to average at "cluster points" when many profiles crossed each other within a small region. This basically has the same effect as using junction points but is a more labour intensive exercise for either manual or computer implementation.

"Absolute" datum is obtained in the WFC sea surface model solution by referencing the altimeter profiles to a geoid model with a bias correction and then removing any long wavelength errors (predominantly orbital) by the artificial requirement of tilting the profiles such that the profile best fits a straight line in open ocean areas. The selection of what defines "open ocean areas" requires an extensive manual effort of subdividing the region of interest into bands of longitude for both ascending and descending passes (see Leitao et al. 1979b). This effort is again required for studying other areas of interest. The procedure outlined in sub-section 6.2.3 is basically a "hands-off" operation and is capable of producing a mean sea surface model in any regional area using the complete 3.6 year GEOS-3 data set whereas this cannot be done using the WFC technique (Leitao et al. 1979b).

Estimation of mean sea surfaces using altimeter data has been accomplished by Marsh et al. (1978, 1979). The technique uses crossover differences in a least squares correction process to compute a bias and tilt per pass in order to remove long wavelength orbital errors. The solved biases and tilts can be used to calculate new crossover differences and the solution iterated until convergence. In order to fix the sea surface model in space relative to the centre of mass of the Earth, a number of laser reference orbits are selected and held fixed in the above solution. After the final iteration, the bias and tilt corrections are applied to the data of each pass, and corrected SSH's obtained. Sea surface models derived from these techniques have been used to derive oceanographic information in the western North Atlantic

(Cheney & Marsh 1980a).

Many other investigators (Rapp 1979; Kearsley 1977; Balmino et al. 1977, 1979; Brace 1978; Smith & Chappell 1977) have computed altimeter sea surface models (in most instances incorrectly referred to as geoids) using the techniques of removing long wavelength errors with low-degree polynomials and imposing crossover conditions at intersection points. All of the above techniques used to compute sea surface models are similar in approach with certain techniques having advantages in data management and computer requirements. The rms discrepancy at crossover points after adjustment is however consistent at the ± 50 cm level.

Direct comparisons between the technique proposed in sub-section 6.2.2 and the techniques mentioned here have not been made. However, visual verification of results can be made in the North Atlantic area comparing the results of Marsh et al. (1978, Figure 4) and Mather et al. (1980, Figure 3) in which similar altimeter data sets were used and both sea surfaces have been referenced to GEM 9.

6.3. East Australian Current Study.

6.3.1. GEOS-3 Altimetry Data.

Profiles of intensive mode GEOS-3 altimetry were selected in an area between latitudes 10°S and 40°S and longitudes 140°E and 180°E covering the period May, 1975 to July, 1976. The data set used in this analysis (AUST79) is based on orbits computed using the GEM 10 gravity field model (Lerch et al. 1977) and all available laser tracking data. The global altimetry data base (LAS79), of which AUST79 is a subset, updates the previous altimetry data set reported in Mather et al. (1978b), the latter data set referred to as the WALLOPS data set. Details of the LAS79 GEOS-3 altimetry data set are given in sub-section 7.3.2.

The AUST79 altimetry data set contains some 27,740 observation points in the area, made up of 72 north-to-south passes and 64 south-to-north passes. The time distribution of the data is extremely disproportionate with some 77% of the altimetry measurements in the period July 1 to October 31, 1975.

6.3.2. Overlapping Pass Analysis.

A number of preliminary studies of overlapping passes in the Tasman and Coral Sea areas have been reported in Mather et al. (1977b); Mather and Coleman (1977); Mather (1977) and Coleman & Mather (1978). These analyses used the WALLOPS data set. With the limited amount of overlapping data sets available in the AUST79 data set (only 14 pairs), the region of interest was extended to include all ocean areas around Australia. The total complement of overlapping pass sets in the extended area (see Figure 6.3) is 39, with 14 north-to-south sets and 25 south-to-north sets.

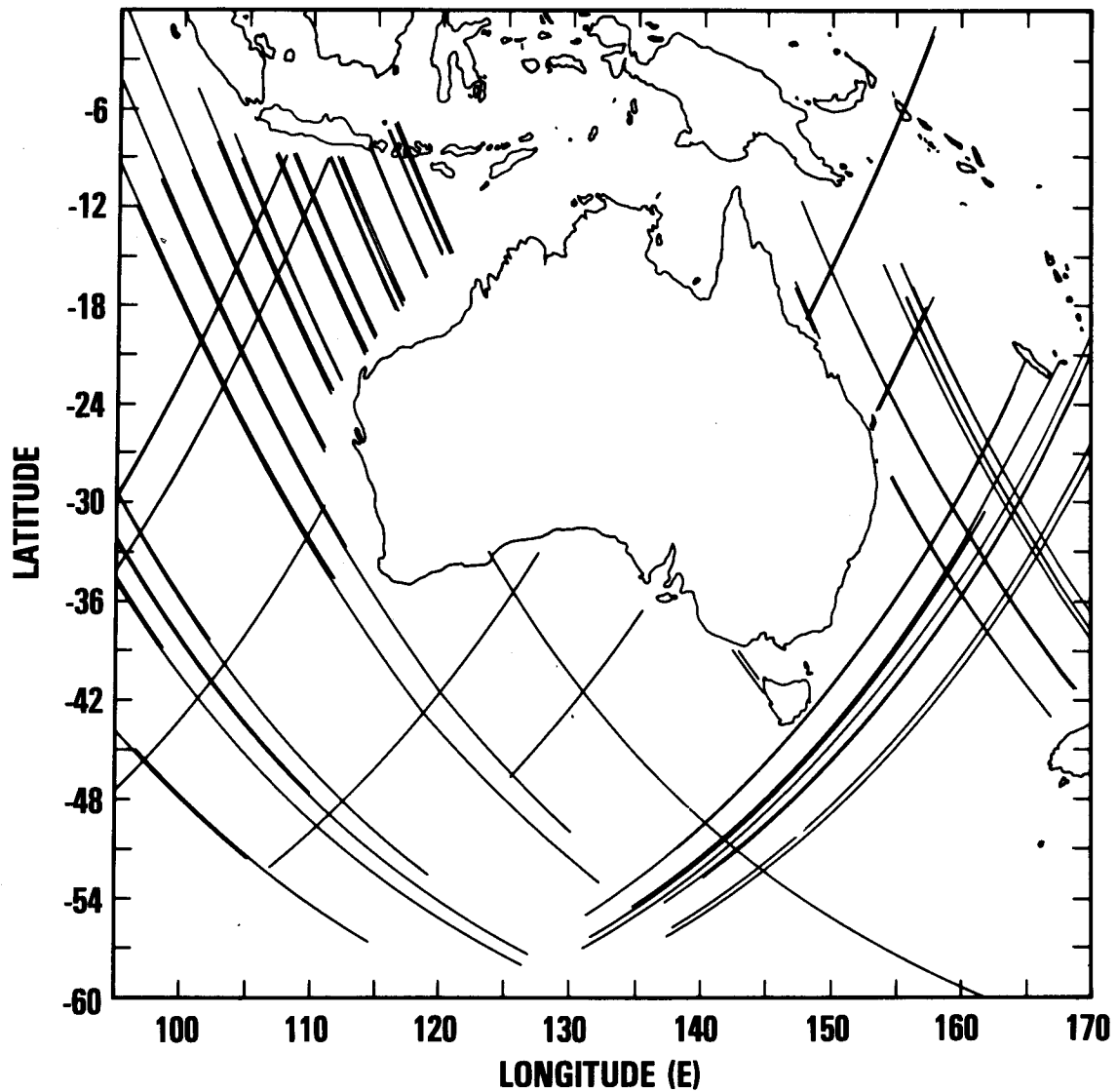
The details of analyses of the 39 sets of overlapping passes are given in Table 6.1 where the sets have been separated into ascending (SN) or descending (NS) sets. Two different types of analyses were performed, one using technique FIT1 and the other using FIT3 (see sub-section 6.2.1). The particulars for the passes such as pass length, start of overlap, bias, tilt, etc. refer to the solutions using technique FIT3. The rms residual of fit shown for FIT1 has been obtained using the first pass in the set as the reference pass.

A number of points of interest can be seen in Table 6.1. It is apparent that technique FIT3 reduces the rms fit of overlapping passes compared to the technique FIT1 of using one particular pass as the reference pass. The average σ_m for FIT3 is ± 21.4 cm and for FIT1 about ± 40.2 cm. In this case, the improvement is by a factor of approximately 2. It is also noted that the bias and tilt corrections for the NS set are, on the average, smaller than those for SN passes. This can be explained by the fact that the SN passes have to be integrated over the south Pacific Ocean using only the gravity field model as these passes will not be tracked for up to half a revolution. This will result in more variable quality orbits than the NS passes which are more consistently tracked (see Laser Tracking Station complement in Mather et al. 1978b, Figure 3, and also see GEOS-3 groundtrack in Figure 3.3, sub-section 3.2.2).

A plot of the discrepancies after bias and tilt corrections for Set No. 1, using FIT1, is shown in Figure 6.2. Notice the long wavelength errors, with wavelengths of about 2×10^3 km and amplitudes of 6 m, between the altimeter estimates of ζ and the geoid heights N computed from the GEM 9 gravity field model.

To study the dynamics of the EAC region, overlapping passes can be

DISTRIBUTION OF GEOS-3 ALTIMETRY PASSES IN THE CORAL AND TASMAN SEAS AND THE INDIAN OCEAN



TOTAL COMPLIMENT - 39 PAIRS WITH 14 NORTH SOUTH PASSES
25 SOUTH NORTH PASSES

Figure 6.3

Table 6.1 Statistics for Overlapping Pass Sets - Australia

Set No.	Rev. No.	Date		DIRN	Length (km)	Start of Overlap		No. of Pts	Bias (m)	Tilt (arc sec)	$\delta\lambda$ (km)	RMS Residual [†] (±cm)	
		YY	DDD			ϕ	λ					FIT1	FIT3
1	300	75	121	NS	3797	-26.30	166.64	380	-2.64	0.067	0		19.5
	826	75	158	NS	3797	-26.30	166.64	380	0.27	-0.001	-7	31.1	17.7
	2404	75	269	NS	3797	-26.30	166.64	380	2.37	-0.066	-20	38.8	22.7
2	627	75	144	NS	273	-23.44	167.80	24	-4.84	-0.06	0		16.3
	1679	75	218	NS	273	-23.44	167.80	24	4.84	0.062	-13	28.7	16.3
3	855	75	160	NS	1055	-18.05	157.41	92	-0.45	-0.012	0		24.8
	2433	75	271	NS	1055	-18.05	157.41	92	0.45	0.012	-13	50.1	24.8
4	1396	75	198	NS	280	-33.11	127.38	34	0.39	0.048	0		16.0
	1922	75	235	NS	280	-33.11	127.38	34	-0.39	-0.048	-5	26.2	16.0
5	1424	75	200	NS	1322	-36.65	135.46	151	-5.29	-0.118	0		14.4
	2476	75	275	NS	1322	-36.65	135.46	151	5.29	0.118	-7	28.5	14.4
6	1494	75	205	NS	4174	-26.64	170.37	531	0.27	-0.039	0		17.5
	3072	75	317	NS	4174	-26.64	170.37	531	0.45	0.022	-8	32.5	21.0
	4650	76	63	NS	4174	-26.64	170.37	531	-0.76	0.016	4	31.9	19.9
7	1679	75	218	NS	4842	-23.32	167.75	559	-1.02	0.025	0		18.3
	2205	75	255	NS	4842	-23.32	167.75	559	1.02	-0.025	-3	37.0	18.3
8	1710	75	220	NS	4767	-9.10	111.10	518	-1.92	0.195	0		17.3
	4866	76	78	NS	4767	-9.10	111.10	518	1.92	-0.195	9	33.8	17.3
9	1767	75	224	NS	5021	-9.06	107.70	577	-0.05	-0.046	0		17.1
	4923	76	82	NS	5021	-9.06	107.70	577	0.05	0.046	11	33.4	17.1
10	1809	75	227	NS	956	-38.43	104.44	99	1.05	-0.002	0		16.6
	4965	76	85	NS	956	-38.43	104.44	99	-1.05	0.002	12	31.7	16.6
11	1821	75	228	NS	4817	-21.80	172.80	617	-0.16	-0.024	0		17.9
	2347	75	265	NS	4817	-21.80	172.80	617	0.16	0.024	-2	35.3	17.9
12	2476	75	275	NS	3040	-1.59	157.60	282	0.29	0.025	0		41.2
	5106	76	95	NS	3040	-1.59	157.60	282	-0.29	-0.025	18	73.2	41.2
13	2859	75	302	NS	3450	-30.54	161.40	458	1.51	-0.102	0		25.7
	6015	76	160	NS	3450	-30.54	161.40	458	1.51	0.102	38	53.4	25.7
14	3115	75	320	NS	4146	-22.13	164.34	535	0.83	-0.007	0		18.5
	4693	76	66	NS	4146	-22.13	164.34	535	-0.83	0.007	12	37.3	18.5
15	351	75	124	SN	2277	-43.05	166.84	261	3.12	-0.024	0		25.0
	1929	75	236	SN	2277	-43.05	166.84	261	3.12	0.024	-14	53.3	25.0
16	351	75	124	SN	459	-19.59	148.78	38	1.88	0.200	0		23.0
	1929	75	236	SN	459	-19.59	148.78	38	-3.26	-0.294	-15	23.3	22.8
	2455	75	273	SN	438	-19.47	148.71	36	1.65	-0.193	-17	32.0	17.2
17	820	75	157	SN	3928	-41.22	168.38	408	-0.399	0.022	0		18.1
	1872	75	232	SN	3928	-41.22	168.38	408	0.399	-0.022	-11	35.8	18.1
18	834	75	158	SN	3472	-38.11	170.95	355	0.78	-0.009	0		20.8
	886	75	233	SN	3472	-38.11	170.95	355	-0.78	0.009	-11	42.7	20.8
19	1161	75	182	SN	2393	-32.11	165.32	255	23.71	-0.258	0		15.8
	2739	75	293	SN	2393	-32.11	165.32	255	-23.71	0.258	-10	32.3	15.8

Table 6.1 Statistics for Overlapping Pass Sets - Australia

Set No.	Rev. No.	Date		DIRN	Length (km)	Start of Overlap		No. of Pts	Bias (m)	Tilt (arc sec)	$\delta\lambda$ (km)	RMS Residual [†] (±cm)	
		YY	DDD			ϕ	λ					FIT1	FIT3
20	1745	75	223	SN	244	-40.67	143.78	25	-1.08	0.648	0		23.7
	6479	76	192	SN	198	-40.67	143.78	16	1.21	-0.929	50	60.6	22.4
21	1349	75	195	SN	2822	-51.62	105.13	344	-6.26	0.381	0		18.3
	5557	76	127	SN	2822	-51.62	105.13	344	6.26	-0.381	21	37.3	18.3
22	1390	75	198	SN	1539	-17.74	116.76	157	0.60	-0.016	0		29.9
	5598	76	130	SN	1539	-17.74	116.76	157	-0.60	0.016	23	59.6	29.9
23	1391	75	198	SN	690	-28.45	98.30	80	-0.14	-0.161	0		16.6
	5599	76	130	SN	690	-28.45	98.30	80	0.14	0.161	23	32.8	16.6
24	1404	75	199	SN	1423	-14.87	120.55	119	0.94	0.223	0		38.1
	5612	76	131	SN	1423	-14.87	120.55	109	-0.92	-0.229	23	72.7	38.6
25	1419	75	200	SN	3808	-32.71	112.36	380	-0.36	0.041	0		20.9
	5627	76	132	SN	3808	-32.71	112.36	380	0.36	-0.041	24	39.8	20.9
26	1433	75	201	SN	2664	-23.25	111.25	269	1.68	0.046	0		25.3
	5641	76	133	SN	2664	-23.25	111.25	266	-1.68	-0.046	24	49.2	25.3
27	1447	75	202	SN	2728	-53.76	147.06	314	-11.51	-0.048	0		21.0
	1973	75	239	SN	2728	-53.76	147.06	314	11.51	0.048	-3	39.0	21.0
28	1447	75	202	SN	1924	-19.92	114.64	194	-11.70	0.074	0		24.3
	5655	76	134	SN	1924	-19.92	114.64	187	11.71	-0.076	24	47.5	24.2
29	1488	75	205	SN	3585	-39.27	170.55	404	-30.36	0.708	0		28.4
	2014	75	242	SN	3585	-39.27	170.55	404	30.36	-0.708	-3	50.7	28.4
30	1575	75	211	SN	2073	-20.79	113.80	172	2.07	0.030	0		27.6
	5783	76	143	SN	2073	-20.79	113.80	160	-2.09	-0.026	29	57.9	27.0
31	1633	75	215	SN	1080	-38.79	98.23	125	3.16	0.024	0		19.2
	5841	76	147	SN	1080	-38.79	98.23	125	-3.16	-0.024	31	40.1	19.2
32	1660	75	217	SN	1323	-16.20	118.56	132	-0.90	-0.004	0		16.9
	4816	76	75	SN	1323	-16.20	118.56	132	0.90	0.004	11	34.2	16.9
33	1675	75	218	SN	3904	-35.29	111.64	379	0.20	0.046	0		23.1
	5357	76	113	SN	3904	-35.29	111.64	379	-0.20	-0.046	21	45.6	23.1
34	1689	75	218	SN	2948	-26.65	110.72	304	-2.72	0.070	0		20.8
	5371	76	114	SN	2948	-26.65	110.72	304	2.72	-0.070	21	41.0	20.8
35	1704	75	220	SN	4134	-47.65	109.74	449	1.38	0.010	0		20.6
	5386	76	115	SN	4134	-47.65	109.74	449	-1.38	-0.010	21	39.7	20.6
36	1717	75	221	SN	1634	-18.31	116.38	167	-0.73	0.100	0		22.2
	4873	76	79	SN	1634	-18.31	116.38	167	0.73	-0.100	12	43.9	22.2
37	1731	75	222	SN	1343	-14.88	119.85	117	0.84	0.019	0		17.6
	4887	76	80	SN	1343	-14.88	119.85	117	-0.84	-0.019	13	38.7	17.6
38	1775	75	225	SN	2607	-38.33	101.92	282	0.95	0.050	0		15.8
	5457	76	120	SN	2607	-38.33	101.92	282	-0.95	-0.050	23	31.5	15.8
39	1831	75	229	SN	2379	-22.39	112.04	241	-1.53	-0.034	0		20.3
	4987	76	87	SN	2379	-22.39	112.04	241	1.53	0.034	15	37.8	20.3

† σ_m (see Equation 6.8)

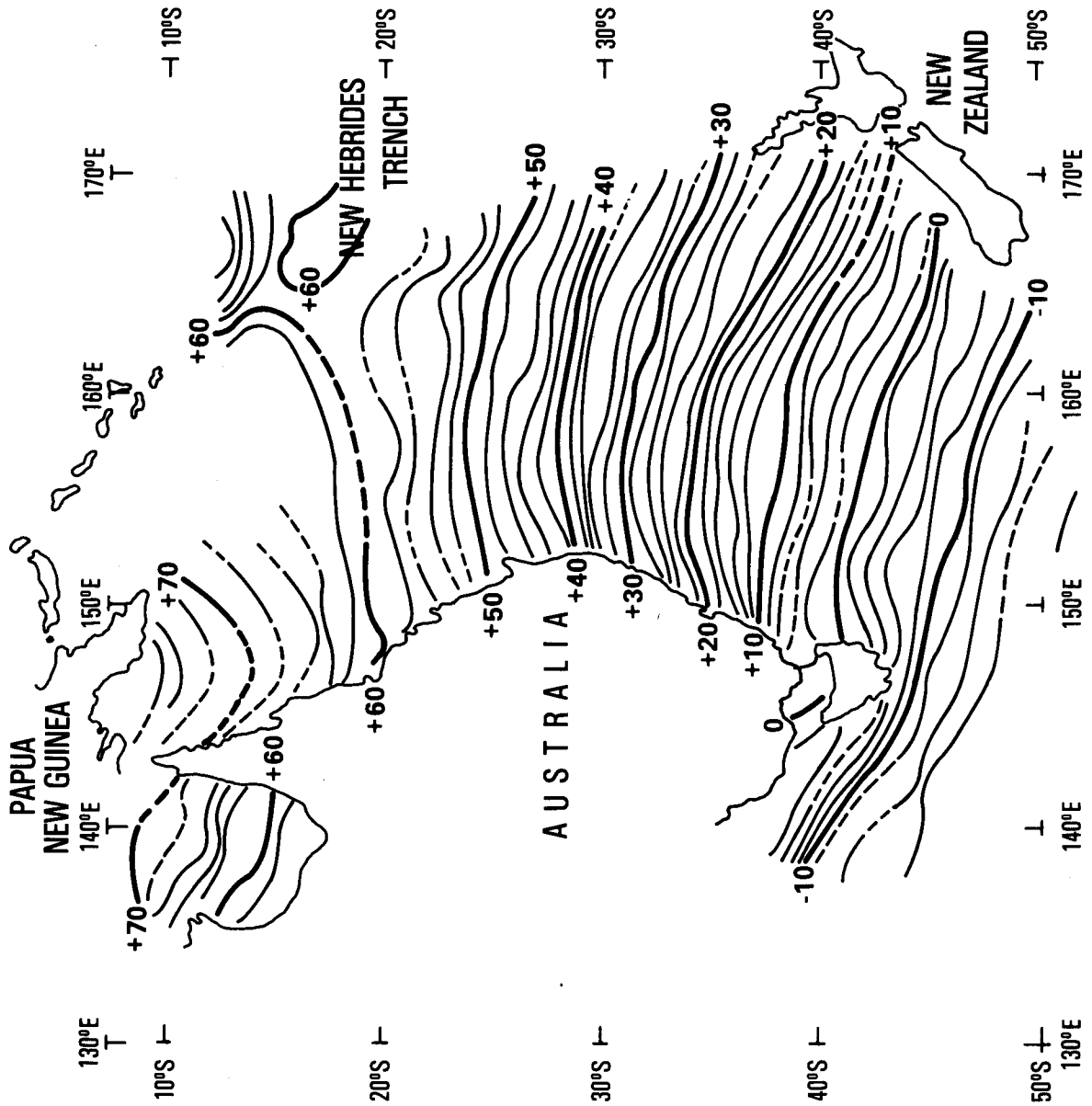
used to locate eddy features or the movement of the main current axis. The oceanographic cruise data available over the EAC region in the time period May 1975 to July 1976 is extremely limited being confined to 3 cruises of about 4 days duration per cruise (Nilsson et al. 1977, Table 1). The majority of the detailed cruise data in the EAC area covers the period from January 1977 to June 1978 (see sub-section 4.2.4). It is also obvious from Figure 6.3 that no overlapping pass sets traverse the EAC region thereby making analysis in this area impossible.

Another possibility would be to reference individual profiles to a detailed geoid, covering the ocean areas of interest, by applying bias and tilt corrections and studying the resulting estimates of ζ_s for oceanographic features. This again cannot be attempted in the Australian region since no detailed gravimetric geoid of sufficient precision or coverage in ocean areas is available. It remains to wait until the complete 3.6 year GEOS-3 altimetry data set becomes available before attempts at definitive oceanographic studies in the EAC can be made. These results are reported in Coleman (1981).

6.3.3. Regional Sea Surface Model Analysis.

Sea surface models were produced in the Australian area using the techniques outlined in sub-section 6.2.2 and results have been given in Mather et al. (1977b) and Mather (1977). These studies showed that systematic discrepancies occurred between a chosen geoid model and the sea surface model and were correlated with position in relation to the east Australian coast (Mather et al. 1977b, Figure 8).

Results, from Mather (1977), are indicated in Figure 6.4. The sea surface model was computed using the WALLOPS data for the period April to November 1975 and referenced to the GEM 7 geoid (Wagner et al. 1976) using $1^\circ \times 1^\circ$ squares as the junction point size. Figure 6.5 shows the discrepancies between the quasi-stationary sea surface model and the Marsh-Chang detailed gravimetric geoid (Marsh & Chang 1976). This figure reflects the absence of high frequency gravity information available in the gravimetric geoid, the largest discrepancies corresponding roughly to geophysical features of interest such as the New Hebrides Trench and Lord Howe Rise. These shorter wavelength anomalies, associated with crustal structure, can be used to infer the rheology of the ocean lithosphere using techniques outlined in Lambeck et al. (1981).



REFERENCE ELLIPSOID

a = 6,378,145m
f = 1/298.255

Figure 6.4

MODEL OF
QUASI-STATIONARY
SEA SURFACE

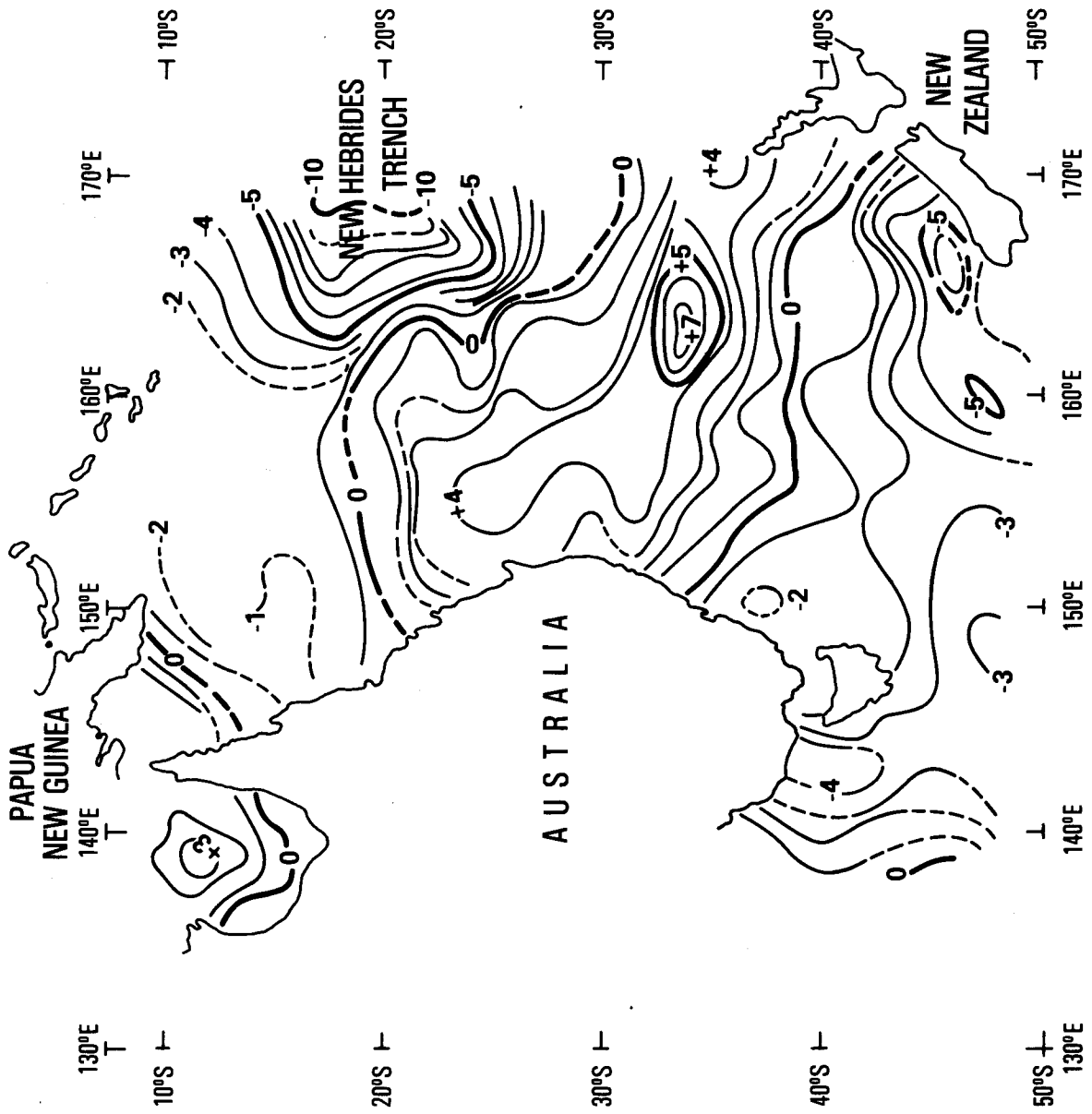
TASMAN & CORAL SEAS
SEP77

EPOCH - APRIL TO NOVEMBER 1975

NO. OF GEOS-3 ALTIMETRY
PASSES USED = 167

WAVELENGTHS >200 km

CONTOUR INTERVAL - 2m



**DISCREPANCIES BETWEEN
SEA SURFACE MODEL SEP77
AND MARSH GEM10 DETAILED
GRAVIMETRIC GEOID IN
TASMAN AND CORAL SEAS**

WAVELENGTHS > 200 km
CONTOUR INTERVAL — 1m

Figure 6.5

The regional sea surface model computed using the AUST79 data set may be found in Lambeck et al. (1980). The model displays similar features to that shown in Figure 6.4. There was, however, no attempt made to study temporal variations in the EAC area as each monthly altimetry distribution was totally inadequate to compute reliable monthly sea surface models. It was therefore decided to concentrate efforts on studying the Gulf Stream area where the distribution and density of GEOS-3 data, plus the improved regional tracking, would permit evaluation of the proposed techniques.

6.3.4. Correlation Studies.

In view of the inadequate data coverage in the EAC area for ocean dynamic investigations, an attempt was made to evaluate the response of the altimeter, as reflected in the ζ values, during different sea state and wind stress conditions and to examine if any correlation could be seen. Data on atmospheric and ocean conditions were obtained from the records at the Bureau of Meteorology and from ship's log information held at the Fisheries Department. The information is summarised in Table 6.2 where for the altimetry profiles investigated, corresponding weather conditions were available. Each profile was biased and tilted to the GEM 9 geoid and the residuals of fit were examined. However, these results give only some information on the ocean variability and it was impossible to infer any correlation. There were however two overlapping pass pairs (Revs 300,826 and Revs 1417,1943) that could be examined for some evidence of sea state correlation. The fitting of Rev 826 to Rev 300 is illustrated in Figure 6.2 and statistics of the rms fit are given in Table 6.1 (Set No. 1). The weather conditions for these two passes were much the same, being moderate to rough seas. The average σ_m value for the last column shown in Table 6.1 is about 20 cm. The statistics for Set No. 1 are of the same order as this average, whereas it would be expected to be higher for rougher seas. Revs 1417 and 1943 showed similar uncertainties. Details on the sea state could also be gained by studying the SWH and AGC values given for the altimeter passes (see sub-section 3.2.1) but these were not available at the time of analysis.

Table 6.2. Altimeter Performance.

Rev. No.	Date YY DDD	Weather Conditions	Ocean Surface Information	Start (ϕ, λ)	Stop (ϕ, λ)
201	75 114	Generally unsettled conditions changing from clear weather with light breezes to rain, strong breezes (~ 25 knots)	Swell $\sim 1.5-3$ m Wind Waves ~ 1 m	-36.8, 171.0	-53.1, 151.5
300	75 121	Weather easing from strong breeze (28 knots) to light (6 knots), clear	Swell $\sim 1.0-1.5$ m Wind Waves $\sim 0.5-1$ m	-27.6, 165.7	-51.5, 142.0
592	75 141	Gale force winds (37 knots) on day 139 easing to light breezes on day 142, weather clearing from showers to fine	Moderate seas, Wind waves $\sim 2.5 \rightarrow 0.5$ m Swell $\sim 1.5 \rightarrow 0.5$ m	-46.5, 162.6	-34.5, 150.9
826	75 158	Winds about 25 knots, intermittent showers	Swell $\sim 1 \rightarrow 5$ m Wind Waves $\sim 1.5 \rightarrow 2.5$ m Rough Seas	-24.9, 167.4	-46.4, 148.9
1189	75 184	Generally fine, light breeze (2-9 knots)	Swell ~ 4 m Rough seas	-45.9, 163.9	-33.8, 152.4
1189	75 184	Wind ~ 20 knots, some rain	Swell ~ 3 m Wind Waves $\sim 1-1.5$ m	-19.0, 161.6	-33.3, 151.8
1223	75 186	Fresh breeze ~ 21 knots, rain	Swell ~ 3 m Wind Waves ~ 2 m	-24.9, 168.7	-46.5, 150.0
1417	75 200	Fresh breeze $\sim 14-18$ knots Fine	Swell $\sim 1.5-2.5$ m Wind Waves ~ 1 m	-40.6, 169.9	-17.6, 153.0
1943	75 237	Gentle breeze $\sim 1-8$ knots, Fine	Swell $\sim 0.5-1.5$ m Wind Waves ~ 0.5 m	-40.8, 170.0	-17.0, 152.6

6.4. Gulf Stream Study.

6.4.1. GEOS-3 Altimetry Data.

The data set used for analyses in the Gulf Stream region has been described in paragraph 7.3.2.1. Some 21,676 observations are available in the SARG data set between latitudes 25°N and 37°N and longitudes 282°E and 294°E, with a total component of 183 passes. The data distribution in time was again irregular but with the increased density of data in this region the problem is not as severe as in the EAC area. In all some 9 monthly regional sea surface models were computed between May 1975 and May 1976.

6.4.2. Overlapping Pass Analyses.

Previous analyses of overlapping passes in the Sargasso Sea area by Mather et al. (1978a) used the WALLOPS altimetry data set. These initial results have been re-examined with the more precise SARG altimetry data set. Details of the 189 passes which make up the 32 overlapping sets shown in Figure 6.6 are given in Table 6.3. The region used for the regional sea surface model analysis is indicated by dashed lines in Figure 6.6.

Each set of overlapping passes consisted of from 5 to 9 overlapping passes and a pass was excluded from analysis if $\delta\lambda$ was greater than ± 40 km. The average rms discrepancy σ_m for the laser orbits was ± 29.5 cm, a slight improvement over the WALLOPS data set result of ± 33.1 cm (Mather et al. 1978a). The results in the Australian region are somewhat lower (± 21.4 cm), as expected, since this region is subject to less ocean variability than the Gulf Stream region. It can be seen then that the internal precision of the GEOS-3 altimetry, reflected in the values of σ_m , is between ± 20 -30 cm. The analysis of the values of σ_m in Table 6.3 as a function of length (Figure 6.7) shows some correlation with pass length to 4000 km. The data used in the construction of this figure has not been filtered in any way but the complexity of the Sargasso Sea test area makes it hard to draw simple conclusions.

An example of the information derived from the overlapping pass techniques is illustrated in Figure 6.8. The upper part of this figure

Sets of Overlapping Passes in the western North Atlantic

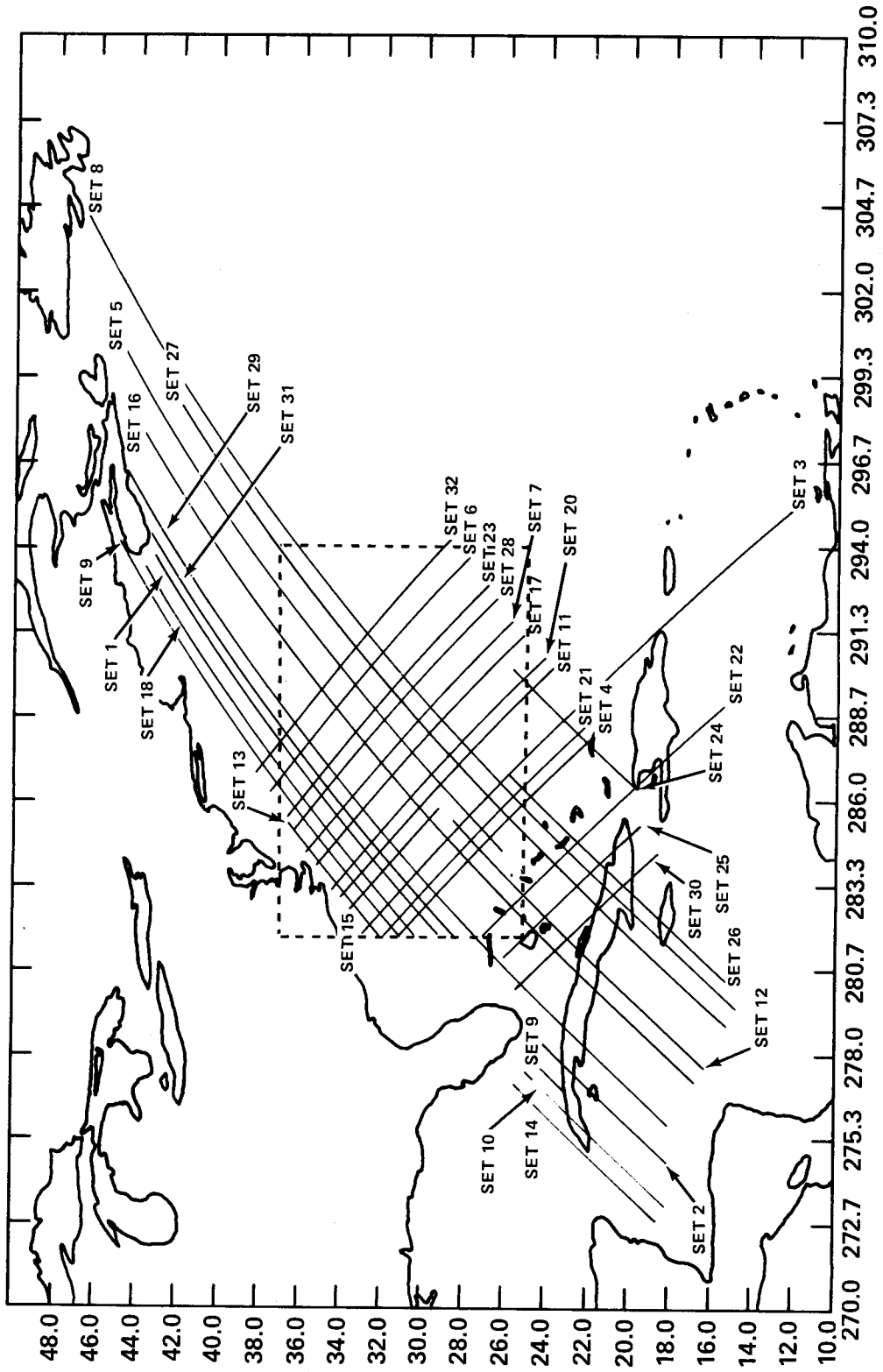


Figure 6.6

Table 6.3 (cont.) Statistics for Overlapping Pass Sets

Set No.	Rev No.	Date		DIRN	Length (km)	Start of Overlap		No. of Pts	Bias (m)	Tilt (arc sec)	$\delta\lambda \phi=0^\circ$ (km)	RMS Residual (+ cm)
		YY	DDD			ϕ	λ					
10	837	75	159	NS	1188	24.99	277.74	104	-0.00	0.148	0	21.5
	1363		196	NS	1188	24.99	277.74	104	-0.09	0.305	-5	24.3
	2941		307	NS	1188	24.99	277.74	104	-0.09	-0.343	-12	26.8
	6097	76	165	NS	1133	24.78	277.70	94	0.63	-0.224	22	43.1
	6623		203	NS	1134	24.67	277.53	92	-0.71	-0.088	33	34.8
	7149		240	NS	1034	24.24	277.25				45	
11	843	75	159	SN	1614	23.67	290.47	185	0.06	-0.695	0	22.7
	1369		196	SN	1545	24.10	290.19	178	-0.09	0.045	-6	19.2
	1895		233	SN	247	23.67	290.47	27	0.19	-0.006	-10	12.1
	2421		271	SN	1554	24.05	290.22	178	0.33	0.071	-12	21.8
	2947		308	SN	1614	23.67	290.47	185	-0.05	0.110	-13	22.9
	4525	76	54	SN	1614	23.67	290.47	185	-0.14	0.042	-2	22.4
	6103		166	SN	1563	23.99	290.26	180	0.28	0.137	23	25.9
	6629		203	SN	1571	23.94	290.29	175	-0.22	-0.045	34	19.6
12	851	75	160	NS	2091	28.58	285.66	185	0.03	-1.020	0	44.6
	1377		197	NS	1947	28.58	285.66	177	-0.06	0.456	-6	30.1
	1903		234	NS	2082	28.58	285.66	182	-0.59	-0.834	-10	39.8
	2429		271	NS	2072	28.58	285.66	180	-0.11	0.579	-12	33.5
	2955		308	NS	2082	28.58	285.66	180	-0.02	-0.063	-12	28.5
	3481		346	NS	2082	28.58	285.66	181	0.12	0.402	-11	40.7
	6111	76	166	NS	2091	28.58	285.66	185	-0.24	0.454	23	41.7
	6637		204	NS	2091	28.58	285.66	175	-0.05	0.241	34	45.4
	7163		241	NS	2014	28.63	285.69				46	
	30	2464	75	274	SN	1130	18.57	284.61	88	-0.14	0.182	0
3516			348	SN	213	18.67	284.61	22	0.04	0.186	2	27.4
3516			348	SN	532	22.09	282.45	59	-0.40	0.691	2	15.6
4568		76	57	SN	1130	18.57	284.61	88	0.22	-0.108	10	47.0
6146			169	SN	1066	18.95	284.38	80	-0.66	-0.129	36	55.4
7198			243	SN							59	
4	374	75	126	SN	1456	22.02	288.15	151	0.89	0.121	0	30.8
	2478		275	SN	1404	22.02	288.15	148	0.59	0.097	-18	26.0
	3004		312	SN	1404	22.02	288.15	148	0.35	0.056	-18	25.7
	6160	76	170	SN	1456	22.02	288.15	151	-0.87	-0.062	18	25.8
	6686		207	SN	1427	22.19	288.04	146	-1.38	-0.196	29	33.0
	7212		244	SN							41	
31	2486	75	275	NS	2392	43.51	294.81	238	-0.10	-0.062	0	21.9
	3012		312	NS	2346	43.51	294.81	234	-0.31	0.029	0	38.4
	4590	76	59	NS	2392	43.51	294.81	238	0.56	-0.084	11	22.7
	5116		96	NS	2384	43.46	294.76	237	0.43	-0.037	18	24.4
	5642		133	NS	2392	43.51	294.81	238	0.17	-0.076	27	25.8
	6694		208	NS							48	
			245	NS						60		

Table 6.3 (cont.) Statistics for Overlapping Pass Sets

Set No.	Rev No.	Date		DIRN	Length (km)	Start of Overlap		No. of Pts	Bias (m)	Tilt (arc sec)	$\delta\lambda$ $\phi=0^\circ$ (km)	RMS Residual (\pm cm)
		YY	DDD			ϕ	λ					
17	1440	75	301	SN	1558	25.14	291.50	161	-0.02	-0.571	0	21.9
	1966		238	SN	1558	25.14	291.50	161	-0.16	0.103	-4	18.1
	2492		276	SN	1558	25.14	291.50	161	-0.01	0.000	-6	14.8
	3018		313	SN	1535	25.19	291.47	158	0.27	0.145	-6	21.4
	4596	76	59	SN	1558	25.14	291.50	161	0.12	0.029	5	16.3
	6174		171	SN	1523	25.36	291.35	157	0.18	0.162	31	18.7
	6700		208	SN							42	
	7226		245	SN							54	
27	1974	75	239	NS	4481	41.96	298.71	429	-0.05	-0.284	0	29.8
	2500		276	NS	4471	41.96	298.71	428	0.15	0.288	-2	26.8
	3026		313	NS	4462	41.96	298.71	429	-0.34	-0.010	-2	25.1
	3552		351	NS	4471	41.96	298.71	429	-0.03	-0.023	0	27.1
	4604	76	60	NS	3036	41.96	298.71	324	0.35	-0.009	9	20.9
	6182		171	NS	4481	41.96	298.71	428	0.97	-0.085	35	34.6
	6708		209	NS							46	
	6708		209	NS							46	
	7234		246	NS							58	
32	2506	75	277	SN	1431	28.72	294.48	167	-0.05	0.302	0	21.4
	3558		351	SN	1423	28.72	294.48	166	0.32	-0.117	2	21.4
	4610	76	60	SN	1431	28.72	294.48	167	0.18	-0.158	11	14.5
	5136		98	SN	1423	28.78	294.44	167	0.54	-0.158	19	16.6
	5662		135	SN	1406	28.88	294.88	165	0.49	-0.143	27	19.1
	6188		172	SN	1366	29.15	294.18	160	0.67	-0.049	37	24.7
28	2037	75	243	SN	1526	26.35	292.70	172	-0.11	-0.445	0	22.2
	2563		281	SN	1526	26.35	292.70	172	0.19	-0.047	-2	15.5
	3089		318	SN	1526	26.35	292.70	172	0.38	-0.099	-2	19.0
	5193	76	102	SN	1480	26.41	292.67	167	0.55	-0.001	18	25.3
	5719		139	SN	1518	26.41	292.67	172	0.82	-0.039	26	21.7
	6245		176	SN	1501	26.52	292.60	170	0.41	0.034	36	19.6
29	1562	75	210	NS	2081	43.61	293.60	217	-0.05	-0.022	0	29.0
	3140		321	NS	2064	43.61	293.60	214	0.33	-0.055	-5	22.6
	3666		359	NS	2081	43.61	293.60	217	-0.17	-0.173	-2	28.8
	5770	76	142	NS	2042	43.37	293.34	213	0.17	0.171	24	25.9
	6822		217	NS	2049	43.46	293.44				45	
19	1562	75	210	NS	258	24.63	278.10	15	0.02	0.652	0	30.6
	3140		321	NS	258	24.63	278.10	15	-0.25	0.016	-5	23.7
	3666		359	NS	258	24.63	278.10	15	-0.14	-0.173	-2	21.9
	5770	76	142	NS	142	24.20	277.82	8	2.43	-12.041	24	14.2
	6822		217	NS	107	23.77	277.54				45	

Table 6.3 (cont.) Statistics for Overlapping Pass Sets

Set No.	Rev No.	Date		DIRN	Length (km)	Start of Overlap		No. of Pts	Bias (m)	Tilt (arc sec)	$\delta\lambda \phi=0^\circ$ (km)	RMS Residual
		YY	DDD			ϕ	λ					
20	1568	75	210	SN	1607	24.13	290.77	183	-0.16	-0.039	0	24.0
	2620		285	SN	1565	24.35	290.63	178	0.11	-0.115	-5	19.5
	3146		322	SN	1599	24.13	290.77	182	0.04	-0.100	-5	21.1
	5776	76	143	SN	1590	24.24	290.70	182	0.09	-0.165	24	23.1
	6302		180	SN	1590	24.24	290.70	179	0.07	-0.004	34	23.3
	6828		217	SN	1565	24.35	290.63				46	
	524	75	137	NS	2990	44.87	300.56	339	-0.21	-0.071	0	23.9
1576		211	NS	2967	44.73	300.40	335	-0.31	-0.061	-11	35.3	
2678		285	NS	121	26.84	285.16	15	-1.04	0.446	-16	8.7	
3154		322	NS	2983	44.83	300.51	337	-0.46	-0.060	-16	39.9	
5258	76	106	NS	2990	44.87	300.56	339	0.10	-0.031	4	23.4	
6310		181	NS	2967	44.73	300.40	336	0.89	0.101	23	29.6	
6836		218	NS	2975	44.78	300.45	336	1.32	-0.022	34	41.4	

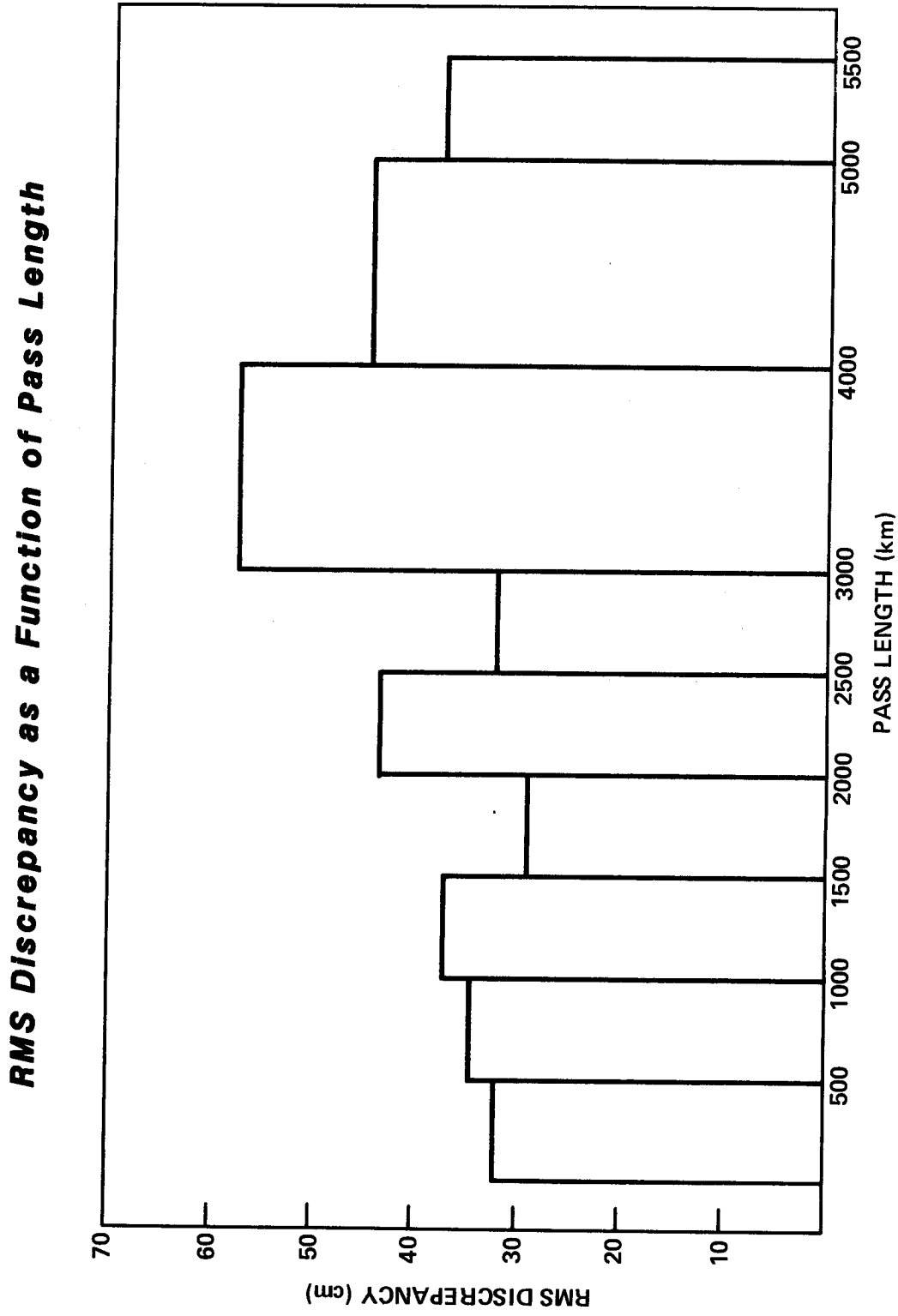


Figure 6.7

shows the 1 sec altimeter SSH data, plotted before bias and tilt corrections were applied, for the six overlapping passes of set 1 (see Figure 6.6 for location). Also shown is the Marsh-Chang gravimetric geoid (Marsh & Chang 1978) along the same profile. The lower block shows the residuals for revolution 2813 of set 1 after fitting by a bias and tilt to the mean sea surface for the set. The location along this profile of oceanographic features (anticyclonic and cyclonic eddies, Gulf Stream) is also illustrated, this information being obtained from the October 1975 issue of the publication Gulfstream (NOAA/NWS 1975).

The residuals of fit (v_s) to the mean surface for each overlapping pass contain information on variations in SSH with wavelengths between 2ℓ (ℓ = length of pass) and the Nyquist limit. Typical eddy features are expected to have half-wavelengths between 50 and 100 km, amplitudes up to 100 cm and decay periods of up to 800 days (Richardson et al. 1977). The data analysed in Table 6.3 indicate that the SSH variations with amplitudes greater than 30 cm can be recovered with confidence.

A spectral analysis of the residuals v_s from each overlapping pass gives information on variability and characteristics of periodic oscillations of the data. The harmonic coefficients determined (A_i, B_i , where i is the integral number of complete wavelengths in the length ℓ over which comparisons are made) can be given by the relations,

$$\begin{vmatrix} A_i \\ B_i \end{vmatrix} = \frac{2}{\ell} \int_0^{\ell} v_s \begin{vmatrix} \sin \\ \cos \end{vmatrix} \frac{2\pi s}{\ell} i ds \quad (6.17)$$

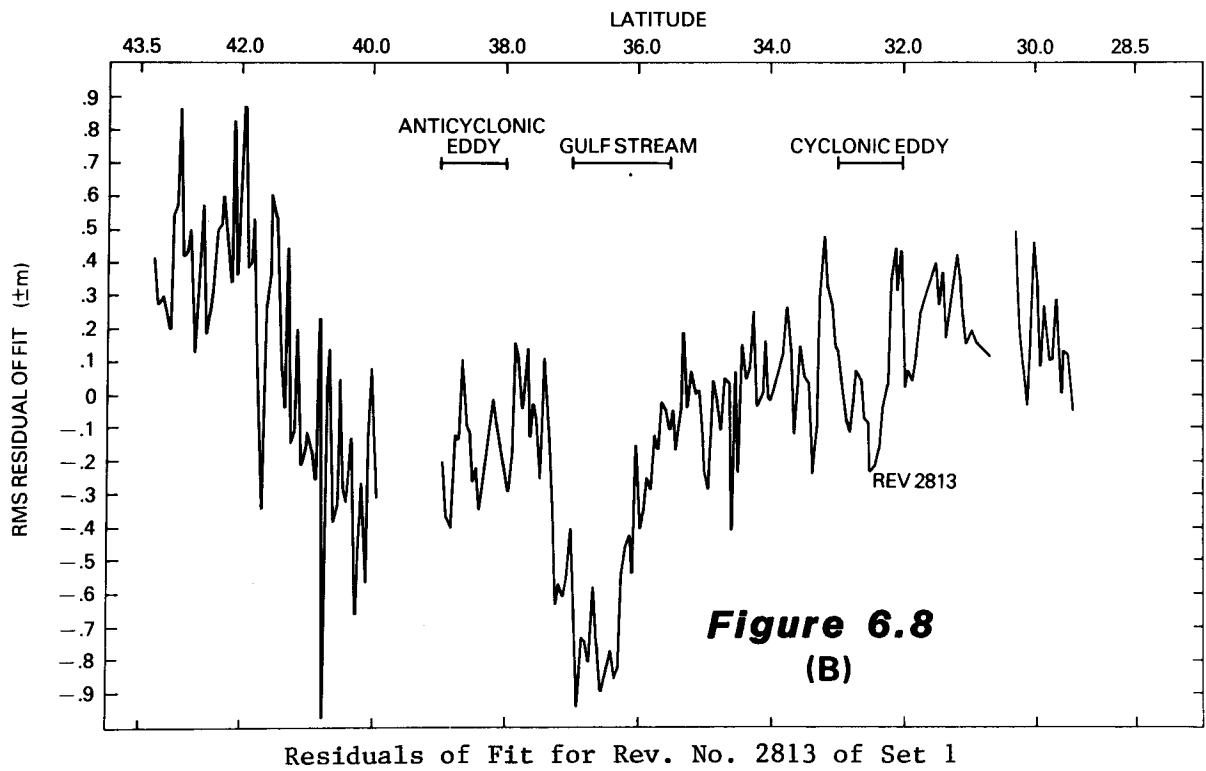
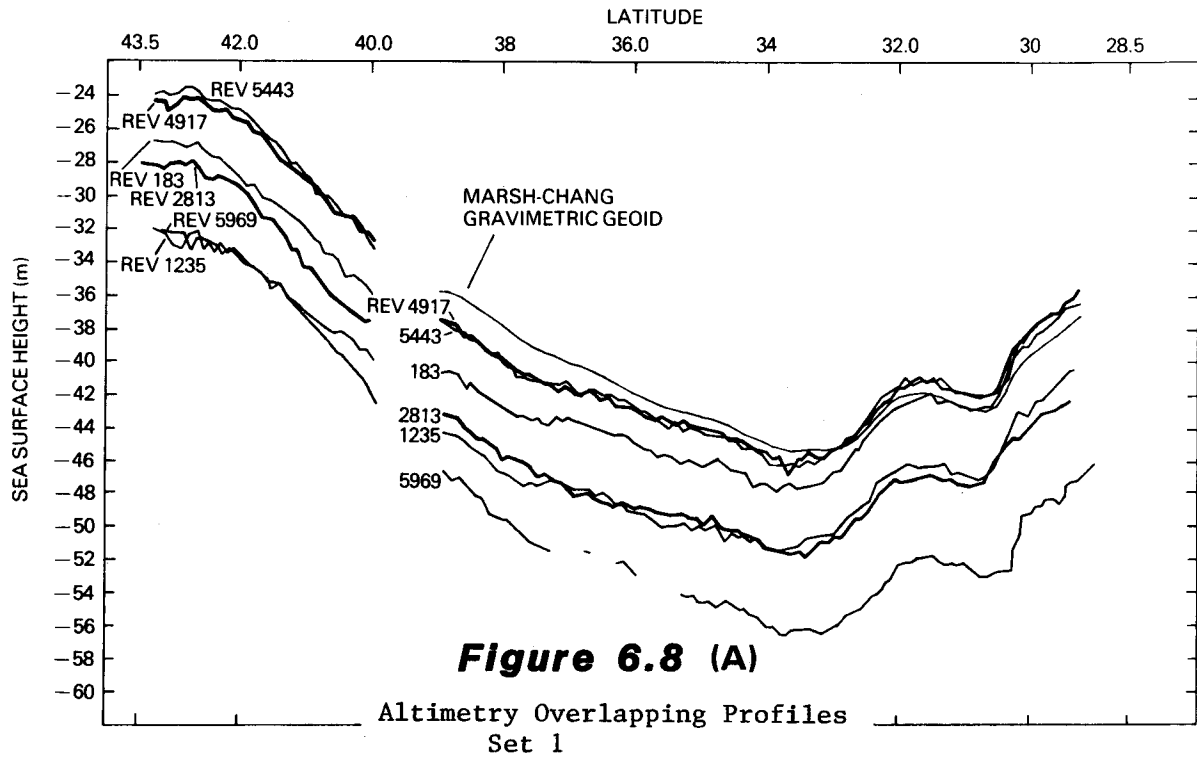
where ds is the sampling interval, the residual v_s defined by equation 6.6 being at a distance s from the commencement of comparisons.

The significance of the amplitudes (A_i, B_i) so obtained is assessed by comparison against a spectrum of white noise (Mather 1977, p.17). If the rms residual of comparison is σ_m , the percentage contribution per frequency (E) to the white noise spectrum is given by

$$E = \frac{100}{N} \quad (6.18)$$

where N is the number of frequencies between 1 and the Nyquist limit imposed largely by the altimeter footprint ($\ell/10$).

The percentage strength of signal 0 obtained from equation 6.17 is



defined by

$$O = \frac{A^2 + B^2}{2\sigma_m^2} \quad (6.19)$$

The results of the spectral analysis for all 32 sets of passes as an average per set is given in Table 6.4. Significant strengths of signal from the normalized power spectrum are obtained in several wavelength bands in excess of 150 km. The average square of the strength of signal for wavelengths between 150 and 5000 km is 784 cm^2 and, for comparison with oceanographic information, the variability for wavelengths between 50 and 1500 km is 535 cm^2 . These values are not unlike estimates quoted by oceanographers for structure functions of the dynamic SST. Dantzler (1976a, Fig.4a) gives values for the northwestern area of the North Atlantic ranging from 60 cm^2 at 80 km wavelengths to 300 cm^2 at 1200km wavelengths, but his values exclude the Gulf Stream variability. Hamon & Cresswell (1972) give values for the structure function off the east coast of Australia between 150 cm^2 at 25 km wavelengths and 750 cm^2 at 1200 km wavelengths.

The next stage in the processing of sets of overlapping passes is the analysis of the data for the tidal signal on a regional basis. This is attempted in Chapter 7. In the interim, attempts have been made to study correlations between remote sensed temperature data supported by XBT data and the variations in the SSH as a function of position and time.

The first step in this analysis was to apply a high-pass filter corresponding to wavelengths less than 100 km to profiles of v_s in the 32 sets of overlapping passes. The altimeter profiles which crossed an eddy (reported in NOAA/NWS 1975,1976; Lai & Richardson 1977) for the periods September-December 1975 and April 1976 were examined through the window obtained for equivalent features in the profiles. Some of the results of the overlapping pass analysis are given in Figures 6.9 and 6.10. The remaining results are given in Appendix A1.

The hatched and stippled areas in Figure 6.9 show the positions of cyclonic and anticyclonic eddies, respectively, in October 1975, as observed by ship or satellite IR data. The symbol H is used to designate anticyclonic eddies which should be associated with a SST high, while the symbol L is used to designate cyclonic eddies which are expected to be associated with a low in the SST. The second symbol is

Table 6.4
Spectral Analysis of 32 Sets of Overlapping Passes in the western North Atlantic

Set No. Range of W.L. (km)	1		2		3		4		5		6		7		8		9							
	N	E	O	S	N	E	O	S	N	E	O	S	N	E	O	S	N	E	O	S				
0	78	64.6	21.4	21	50.6	24.1	50	65.2	13.8	80	63.2	17.9	102	67.4	20.8	60	68.0	23.0	61	67.0	34.0	162	61.0	13.0
50	22	18.0	13.2	10	24.7	20.8	16	17.4	11.6	24	18.7	12.8	27	17.3	10.1	15	17.0	15.0	15	17.0	20.0	51	19.0	8.0
100	7	5.9	7.1	4	9.9	14.4	6	7.1	5.7	8	6.3	6.4	9	7.1	5.2	5	6.0	11.0	5	5.0	10.0	17	7.0	10.0
150	4	3.0	3.8	1	2.5	3.5	3	2.8	7.4	4	3.1	4.5	5	2.8	3.5	2	2.0	5.0	3	3.0	7.0	9	3.0	10.0
200	2	1.8	3.5	1	2.5	7.1	2	3.3	15.1	2	1.5	2.7	3	1.7	4.6	2	2.0	8.0	2	2.0	3.0	5	2.0	4.0
250	2	1.7	3.8	1	2.5	9.5	2	2.1	5.1	2	1.5	4.6	2	1.1	3.4	1	1.0	5.0	1	1.0	4.0	4	1.0	4.0
300	2	1.7	3.7	1	2.5	8.9	2	2.0	6.7	1	0.8	3.1	1	0.6	1.0	1	0.6	3.6	2	2.0	5.0	2	1.0	2.0
350	1	0.8	3.6	1	2.5	8.9	1	1.0	1.5	1	0.8	6.5	1	0.6	3.6	1	1.0	8.0	1	1.0	3.0	2	1.0	3.0
400	2	1.7	4.8	1	1.1	5.3	1	1.1	5.3	2	1.6	27.5	2	1.1	7.7	1	1.0	7.0	2	1.0	3.0	2	1.0	3.0
450	3	2.5	25.8	1	2.5	9.0	1	1.0	10.0	2	1.6	27.5	1	0.6	6.5	1	1.0	7.0	1	1.0	3.0	2	1.0	6.0
500	1	0.9	16.0	2	1.9	34.2	1	1.1	1.7	1	0.8	3.8	1	0.6	4.8	1	0.6	4.8	1	1.0	4.0	4	2.0	12.0
600	2	1.6	10.4	1	1.1	8.1	2	1.9	16.5	1	0.8	5.8	1	0.6	6.1	2	2.0	16.0	2	2.0	11.0	3	1.0	5.0
700	3	2.5	35.0	2	4.9	4.9	4	4.2	121.0	1	0.8	8.6	2	1.1	24.8	3	3.0	25.0	2	2.0	11.0	2	1.0	3.0
800	4	3.3	77.4	2	4.9	4.9	4	4.2	121.0	2	1.6	45.5	2	1.1	26.6	3	3.0	15.0	2	1.0	3.0	2	1.0	3.0
900									2	1.6	45.5	2	1.1	26.6	3	3.0	15.0	2	1.0	3.0	2	1.0	3.0	
1000									4	4.2	121.0	2	1.1	24.8	3	3.0	25.0	2	2.0	11.0	2	1.0	3.0	
1500									4	4.2	121.0	2	1.1	24.8	3	3.0	25.0	2	2.0	11.0	2	1.0	3.0	
2000									4	4.2	121.0	2	1.1	24.8	3	3.0	25.0	2	2.0	11.0	2	1.0	3.0	
2500									4	4.2	121.0	2	1.1	24.8	3	3.0	25.0	2	2.0	11.0	2	1.0	3.0	
3000									4	4.2	121.0	2	1.1	24.8	3	3.0	25.0	2	2.0	11.0	2	1.0	3.0	
3500									4	4.2	121.0	2	1.1	24.8	3	3.0	25.0	2	2.0	11.0	2	1.0	3.0	
4000									4	4.2	121.0	2	1.1	24.8	3	3.0	25.0	2	2.0	11.0	2	1.0	3.0	
4500									4	4.2	121.0	2	1.1	24.8	3	3.0	25.0	2	2.0	11.0	2	1.0	3.0	
5000									4	4.2	121.0	2	1.1	24.8	3	3.0	25.0	2	2.0	11.0	2	1.0	3.0	
>5000									4	4.2	121.0	2	1.1	24.8	3	3.0	25.0	2	2.0	11.0	2	1.0	3.0	

Table 6.4 (cont.)

Set No. Range of W.L. (km)	28			29			30			31			32			Mean						
	N	E	O/S	N	E	O/S	N	E	O/S	N	E	O/S	N	E	O/S	N	E	O/S	σ_E	σ_S	σ_E/σ_S	
0																						
50	55	64.9	23.2	103	62.0	7.0 ***	21	69.1	20.6	80	63.2	17.9	54	65.9	20.5	62	63.9	6.6	18.7	7.8	0.3	
100	15	17.6	17.1	34	19.0	5.0	9	24.6	21.8	24	18.7	12.8	14	17.2	10.0	19	19.4	1.6	13.4	5.1	0.7	
150	5	5.9	7.7	13	7.0	10.0 *	3	9.2	7.4	8	6.3	6.4	5	5.9	8.5 *	6	6.9	1.3	10.0	5.0	1.4	
200	3	43.0	6.4 *	6	3.0	3.0	2	4.9	11.7 **	4	3.1	4.5 *	2	2.6	4.2 *	3	3.5	0.7	8.4	4.0	2.4	
250	2	2.4	1.6	4	3.0	3.0	2	8.5	21.3 **	2	1.6	2.7 *	2	2.4	7.1 **	3	2.6	1.0	8.2	3.8	3.2	
300	2	2.4	3.2 *	3	1.0	5.0 ***	2	5.2	13.2 **	2	1.5	4.6 ***	2	2.5	18.7 ***	2	2.5	1.2	10.3	9.3	4.1	
350	1	1.2	6.0 ***	2	1.0	1.0	1	0.8	3.1 ***	1	0.8	3.1 ***	1	1.3	3.9 ***	2	2.1	1.0	8.9	6.0	4.2	
400	2	2.4	10.3 ***	2	1.0	2.0 **	2	4.7	19.2 ***	1	0.8	6.5 ***	1	1.2	5.6 ***	2	2.1	0.6	10.7	6.2	5.1	
450				1	0.5	1.0 **																
500	1	1.2	14.2 ***	1	0.5	2.0 ***				2	1.6	27.5 ***				2	1.8	0.5	12.5	6.8	6.9	
600	1	1.2	3.5 **	2	1.0	13.0 ***	2	5.2	29.4 ***	1	0.8	3.8 ***				4	4.5	0.7	25.5	6.7	5.7	
700				1	0.5	4.0 ***										1	1.3	0.6				
800	2	2.4	9.0 ***	2	1.0	17.0 ***				1	0.8	5.8 ***				4	3.2	0.5	20.5	5.1	6.4	
900				1	0.5	6.0 ***										4	4.1	0.5	33.8	9.0	8.2	
1000				3	2.0	14.0 ***	2	4.7	63.8 ***							4	2.5	0.2	25.0	4.1	10.0	
1500	1	1.2	47.4 ***							2	1.6	8.6 ***				4	3.9	0.6	28.7	7.2	7.4	
2000	2	2.3	30.9 ***										3	3.7	48.5 ***	16	15.7	0.5	144.0	8.0	9.2	
2500				1	0.5	24.0 ***				2	1.6	45.5 ***				13	12.9	0.1	172.8	9.5	13.4	
3000																13	9.0	0.1	219.5	13.8	24.4	
3500				1	1.0	25.0 ***										4	1.9	0	35.7	4.4	18.8	
4000																1	0.7	0	25.1	0	35.4	
4500				1	0.5	25.0 ***										1	0.5	0	2.7	0	5.0	
5000																3	1.3	0	84.2	18.2	64.8	
> 5000																5	2.1	0	23.2	1.2	11.0	
																2	0.8	0	31.4	8.7	39.2	

Correlation of IR Imagery with GEOS-3 Altimetry Profiles - October 1975

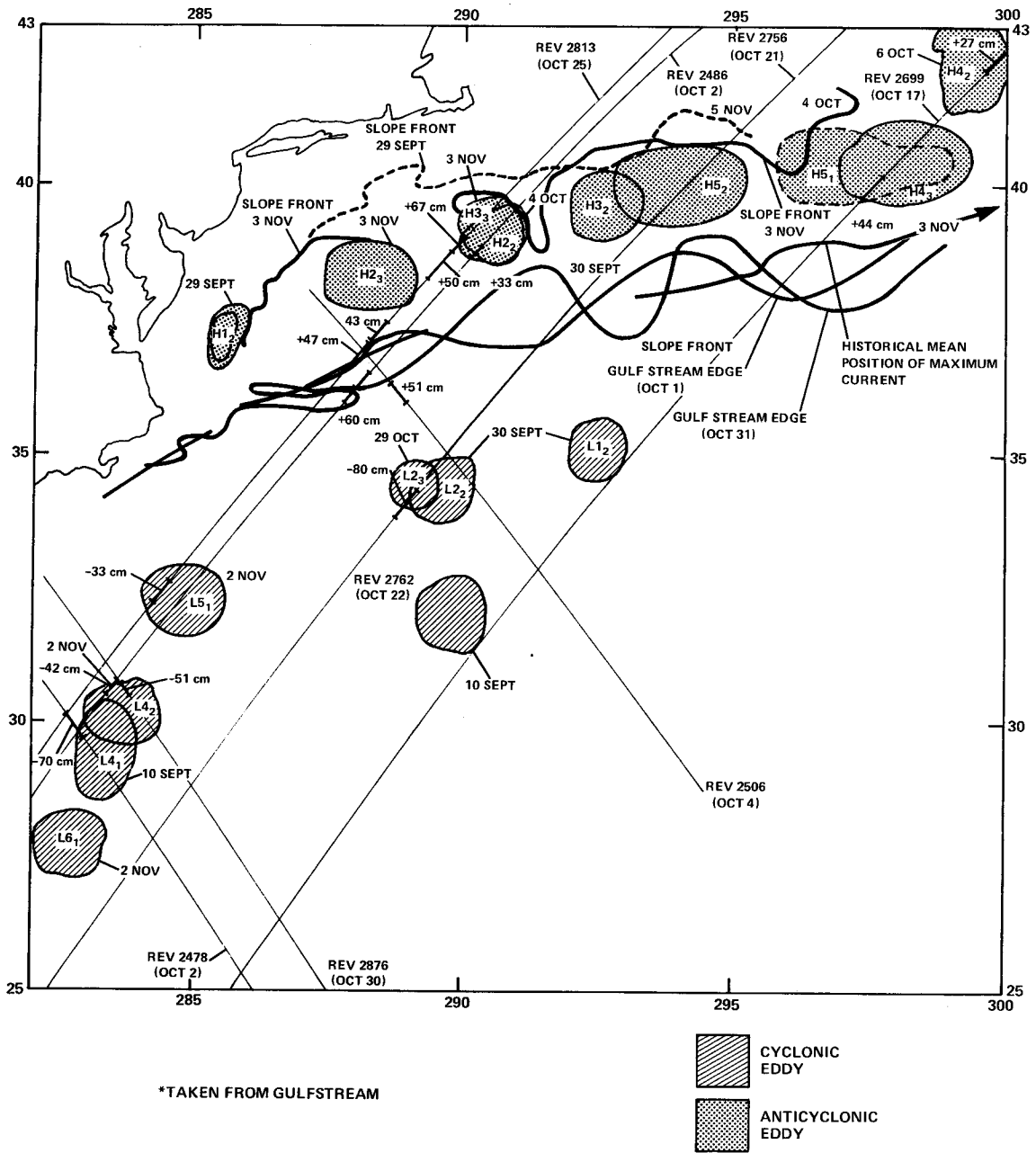


Figure 6.9

Correlation of IR Imagery with GEOS-3 Altimetry Profiles - April 1976

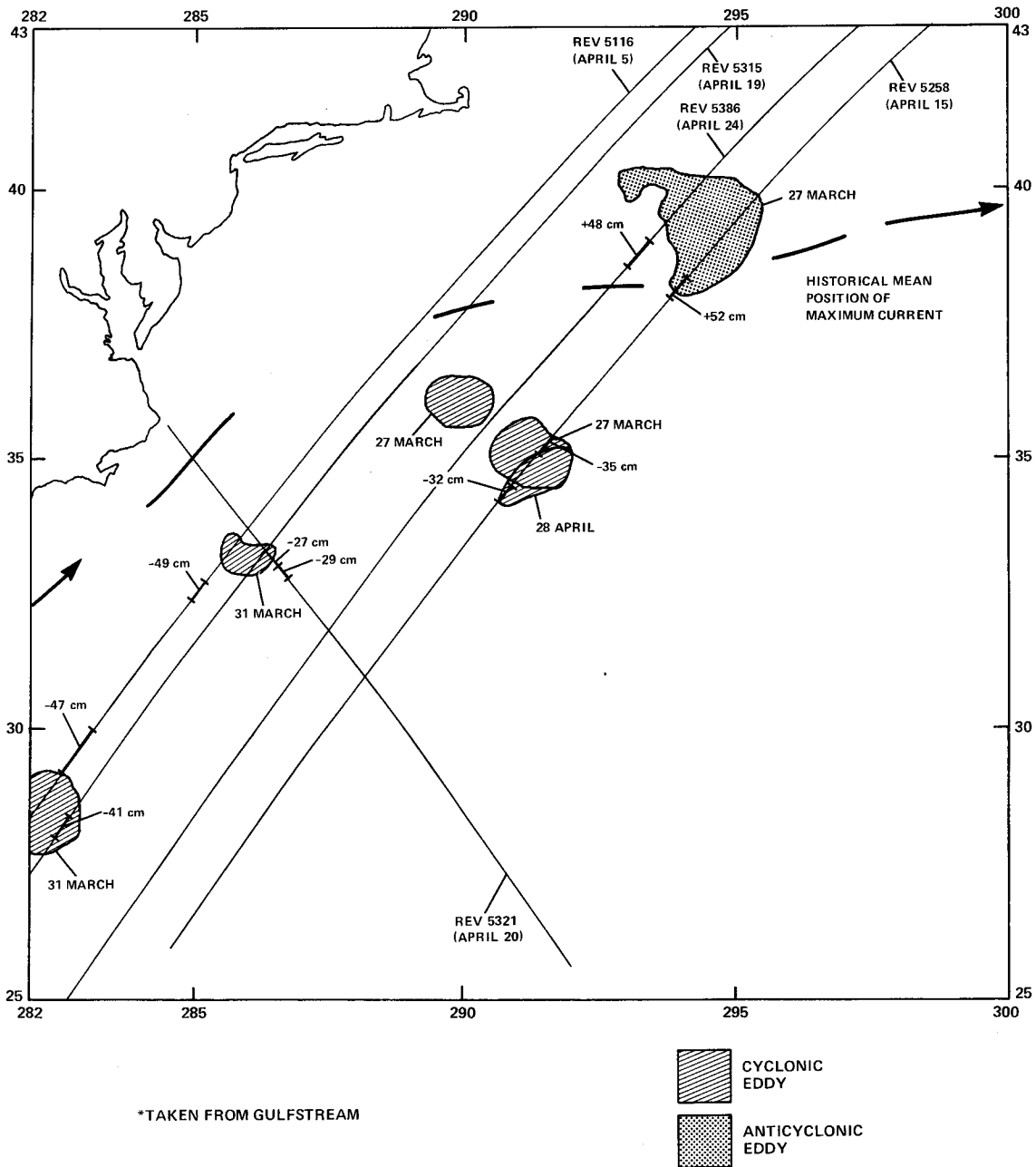
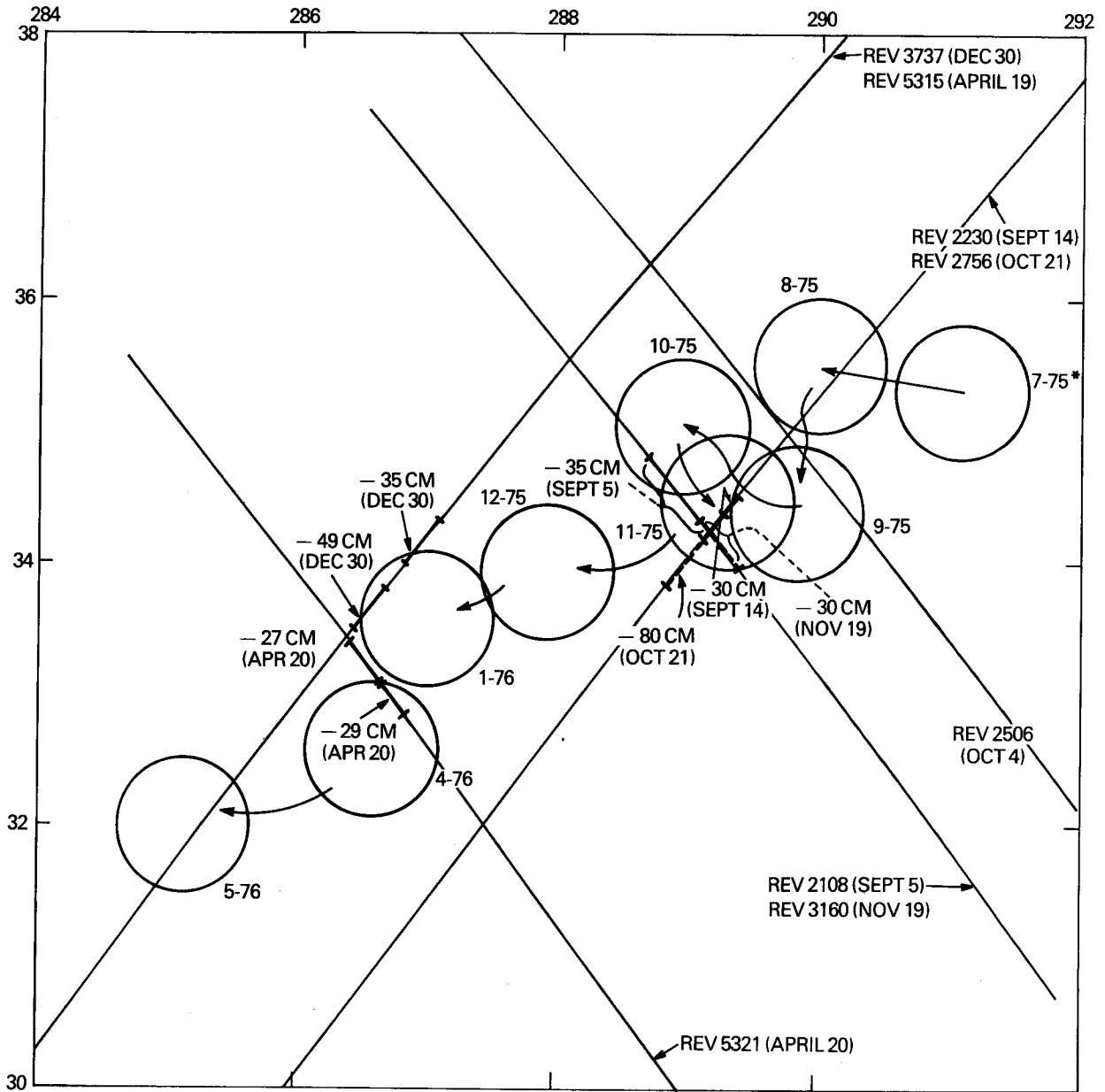


Figure 6.10

Tracking a Gulf Stream Ring



* MONTHLY EDDY POSITIONS FROM LAI AND RICHARDSON (1977)

Figure 6.11

an eddy identifying number, while the subscript refers to the i -th confirmation of the eddy. Those GEOS-3 groundtracks, from overlapping sets, that passed over the eddy features in the same month are shown. On each groundtrack, the positions and magnitudes of significant features from the window residuals have been indicated and these residuals show good correlation with the satellite (and/or ship) defined eddy feature. The results for April 1976 are shown in Figure 6.10 .

A sequence where one particular cyclonic eddy is crossed by different altimeter profiles over an 8-month period is illustrated in Figure 6.11. The monthly eddy locations have been taken from Lai and Richardson (1977). Note the reasonable consistency of the altimeter-defined SST low associated with the Gulf Stream ring over the period the eddy was identified and the slight decrease in SST low which could be associated with the ring decay (Cheney & Richardson 1976).

Another clear indication of the value of using overlapping passes to distinguish eddy movement is reported in Cheney & Marsh (1980b, Figure 11) where it is seen that a cold ring moves out underneath the satellite groundtrack over a period of 23 days.

A summary of results of the correlation between altimeter features and ocean eddies is given in sub-section 6.4.4.

6.4.3. Regional Sea Surface Model Analysis.

The SARG data set has been used to investigate temporal variations in regional monthly models of the sea surface between May 1975 and May 1976. The results presented here have been reported in Coleman (1980) and thus update previous analyses reported in Mather et al. (1978a, 1980). However, these latter results, based on the WALLOPS data, are useful for comparison of pass geometry and accuracy differences between the two solutions.

The area covered by the dense network of GEOS-3 altimetry is shown in Figure 6.12. The intensive mode GEOS-3 altimetry was processed on a monthly regional basis using the intersection of passes to provide a framework of control for adjustment of the sea surface model (see sub-section 6.2.2) . It was assessed that meaningful regional models of the sea surface could not be obtained unless the number of passes (n) approached 10 and the number of junction points was approximately $4n$. On this basis, it was decided to restrict the study of time variations on a regional basis to monthly analyses, covering the period July to

**Distribution of Altimeter Passes
in the Sargasso Sea Test Area**

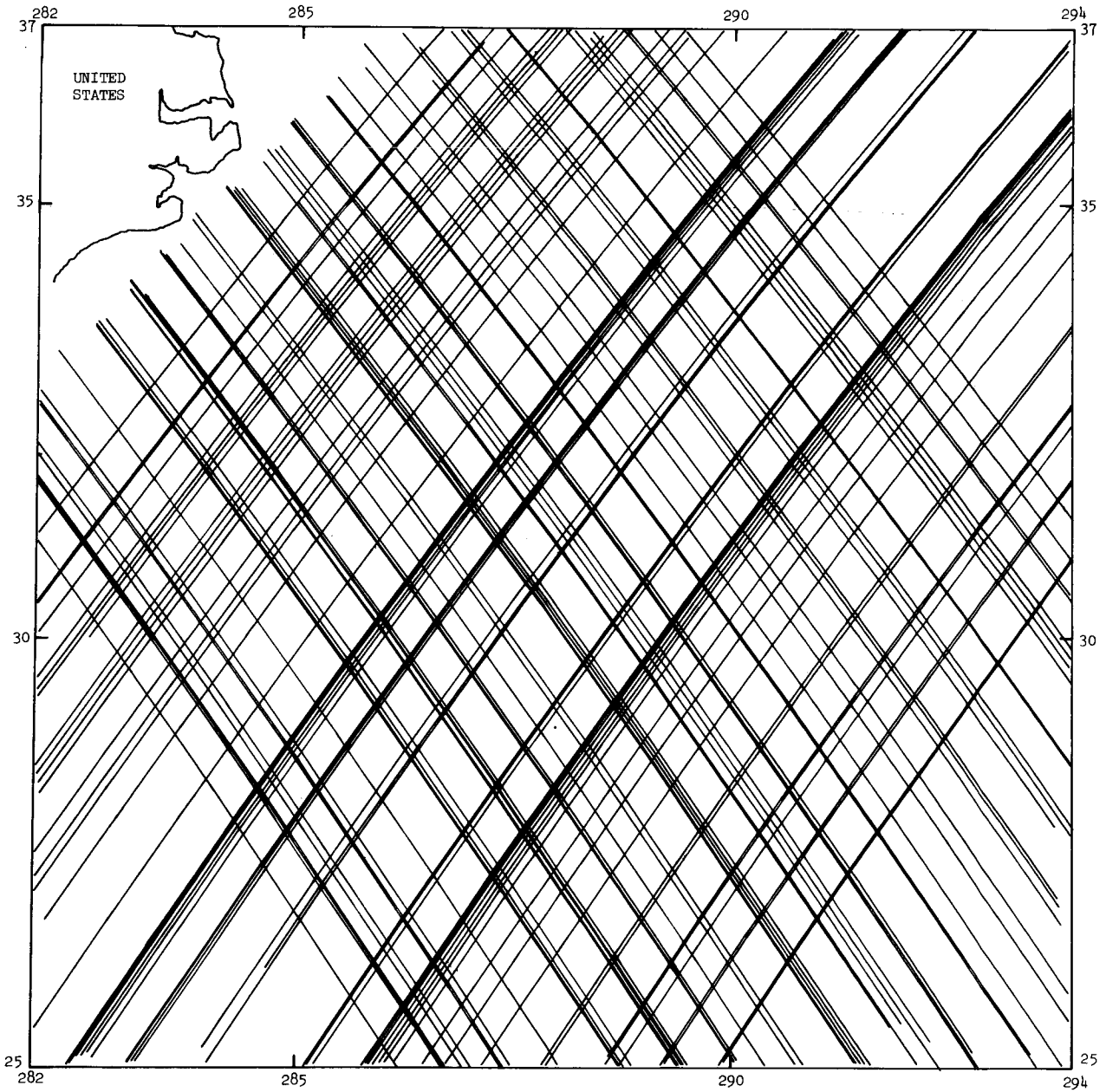


Figure 6.12

October 1975, and April and May 1976.

Table 6.5 provides a summary of the regional monthly solution statistics. The figures, for these laser derived solutions, show a factor of approximately two improvement when compared to the WALLOPS solutions reported in Mather et al. (1980). These latter results are shown in brackets in Table 6.5 alongside the laser results. Passes were excluded from the solution if they were less than 600 km in length or contained less than 3 junction points. This criterion was applied to avoid unwanted tilts in the sea surface model. The ocean tides were treated as noise in the computations, since the inclusion of the Hendershott (1972) tidal model for the area had a negligible effect on the heights of the sea surface and is, in fact, eliminated in the tilt corrections as pointed out in Mather et al. (1978a) and corroborated by studies of Douglas & Goad (1978).

Table 6.5.
Regional Monthly Solutions for the Shape
of the Sargasso Sea from GEOS-3 Altimetry.

$25^{\circ} < \phi < 37^{\circ} \text{ N}$ $282^{\circ} < \lambda < 294^{\circ} \text{ E}$
Basic Junction Point Size - $0.2^{\circ} \times 0.2^{\circ}$

Period	No. of Obsns.	No. of Passes	No. of Jn. Pts.	RMS (+cm)	
				Jnt.Pt. (σ)	Sol.
1 July 1975	1698 (2058)	10 (15)	38 (63)	16 (40)	28
2 August 1975	2431 (2836)	15 (23)	80 (97)	24 (50)	45
3 September 1975	2901 (3446)	18 (28)	115 (156)	15 (35)	27
4 October 1975	3617 (4225)	23 (35)	176 (243)	16 (29)	30
5 April 1976	1765 (2205)	11 (19)	47 (63)	23 (17)	48
6 May 1976	1579 (2092)	11 (16)	39 (70)	20 (19)	36

Excluding passes < 100 data points and 3 jn. pts.

The noise level of the GEOS-3 altimeter is assessed to be ± 20 cm on a relative basis. Being constrained by the finite footprint of the altimeter, computer limitations, and the desired resolution needed for detecting SSH variations, a $0.2^\circ \times 0.2^\circ$ square has been treated as a junction point in devising an objective system for regional sea surface modelling. Within each 0.2° junction point square the average SSH value was used in forming observation equations (see sub-section 6.2.2). It has been assessed that geoid variations within a 0.2° square should not materially mask features in the sea surface with amplitudes greater than ± 30 cm and wavelengths in excess of 40 km. Regional sea surface models using 0.2° squares should be adequate for the location of eddies in the Western Sargasso Sea which are expected to exhibit SSH variations in excess of ± 50 cm over extents larger than 100 km (e.g., Cheney & Richardson 1976).

An absolute datum to the six monthly models was obtained by making a three parameter fit of the monthly model to the geoid, where the geoid was deduced from the best available satellite gravity field model GEM 9 (Lerch et al. 1977) using equation 6.15. The corrections obtained are listed in Table 6.6. The variation in the overall tilt between different sea surface models is less than 10 cm per 100 km giving credence to the internal stability of each monthly solution.

From the six monthly solutions the rms SSH variation within a 0.2° square was obtained and is illustrated in Figure 6.13 as a function of position. This figure should provide an overall picture of the geostrophic variability over the region and as such can be compared to eddy kinetic energy maps such as Wyrтки et al. (1976), Dantzler (1976a, 1976b). It is expected to see a relatively low variability in the Sargasso Sea and a strong energy distribution along the path of the Gulf Stream. It is evident in Figure 6.13 that this is somewhat true, taking into account the weak determinations in the sea surface models (thus high variability) at the peripheries of the region being studied. The large anomalous variability centred at about 32°N , 286°E has been found to be due to suspect data in a north-to-south pass not eliminated in the preprocessing. In addition, this figure should also be correlated with eddy flow patterns, as for example indicated in the EAC region in Figure 4.3 derived from dynamic height measurements.

The pooled estimate of the sample rms discrepancy of the SSH's occurring in the same 0.2° (20 km) square between the different monthly solutions is ± 30 cm. Despite this fact, the disagreement with the best

Table 6.6.
 Three Parameter Transformations of Regional Sea Surface
 Models to the GEM9 Datum. (GEM9 to (30,30)).

Solution Description	Meridional Tilt (+ N) cm per 10 km	Prime Vertical Tilt (+ E) cm per 10 km	Radial Correction (m)	Area of Block For Transformation (%)
July 1975	-5.0	+3.5	0.94	39
August 1975	-5.5	+5.0	1.70	74
September 1975	-6.0	+4.5	1.70	76
October 1975	-5.5	+4.0	1.46	74
April 1976	-6.0	+4.5	1.53	64
May 1976	-5.5	+4.5	1.48	52

available geoid in the area (Marsh & Chang 1978) is considerable, the discrepancies being correlated with distance from the east coast of North America, as illustrated in Figure 6.14. This is probably due to the decreasing density of gravity data of adequate quality as a function of position in computations of the gravimetric geoid. Similar tilts were observed if a more recent gravity field model, GEM 10B (Lerch et al. 1978a) was used in the solutions.

Plots of the regional sea surface models listed in Table 6.5 are given in Figures 6.15 to 6.20. The contours shown in Figures 6.15 to 6.20 are estimated heights of the average sea surface for the month relative to the mean SSH model for the epoch (May 1975 to May 1976) and do not reflect the quasi-stationary SST in the region. The depth contour indicated is the 2000 m bathymetry line. The six plots are based on the 0.2° data averaged at 0.5° intervals but are enhanced by the 0.2° monthly model data in the vicinity of confirmed eddy locations. However, the contours shown in Figures 6.15 to 6.20 are reliable only in the vicinity of the plotted groundtracks. The precision of contours is significantly worse than $\pm\sigma_{jp}$ in Table 6.5 at locations more than 50 km away from a groundtrack, and these contours should be treated as suspect with errors being as large as ± 60 cm. Despite the improvement provided by the laser orbits, a number of monthly solutions suffered from an inadequate number of passes for correlation studies to be reliably attempted.

However, the six monthly solutions so obtained were examined against the locations of eddies derived from satellite remote sensing and ship cruise data, as described in the next section. For comparison purposes, the regional monthly sea surface models computed using the WALLOPS data and partly reported in Mather et al. (1980) have been given in Appendix A2.

6.4.4. Correlations with Surface Ocean Data.

6.4.4.1. Introduction.

The Sargasso Sea is one of the best surveyed oceans of the world for surface temperature fields. The motion of the major eddies and the location of both the edge of the slope water and the Gulf Stream are monitored on a monthly basis and a monthly record is published by the

**Variation of Monthly Sea Surface Heights as
a Function of Position (rms residual \pm cm)**

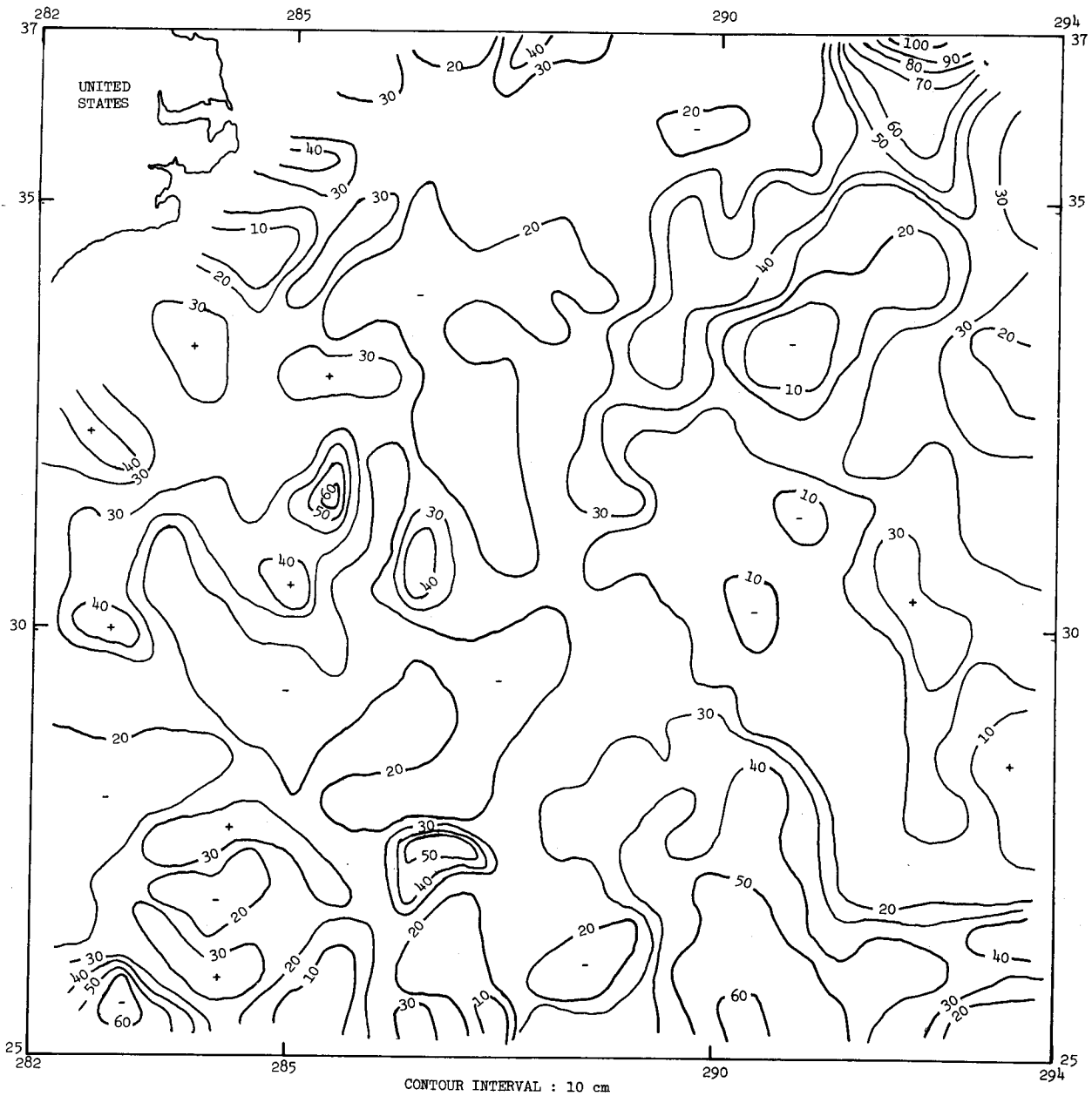


Figure 6.13

Discrepancies Between Average Sea Surface Heights (Oriented on GEM9) and Marsh-Chang 5 Minute Gravimetric Geoid (Contour Interval: 1 m)

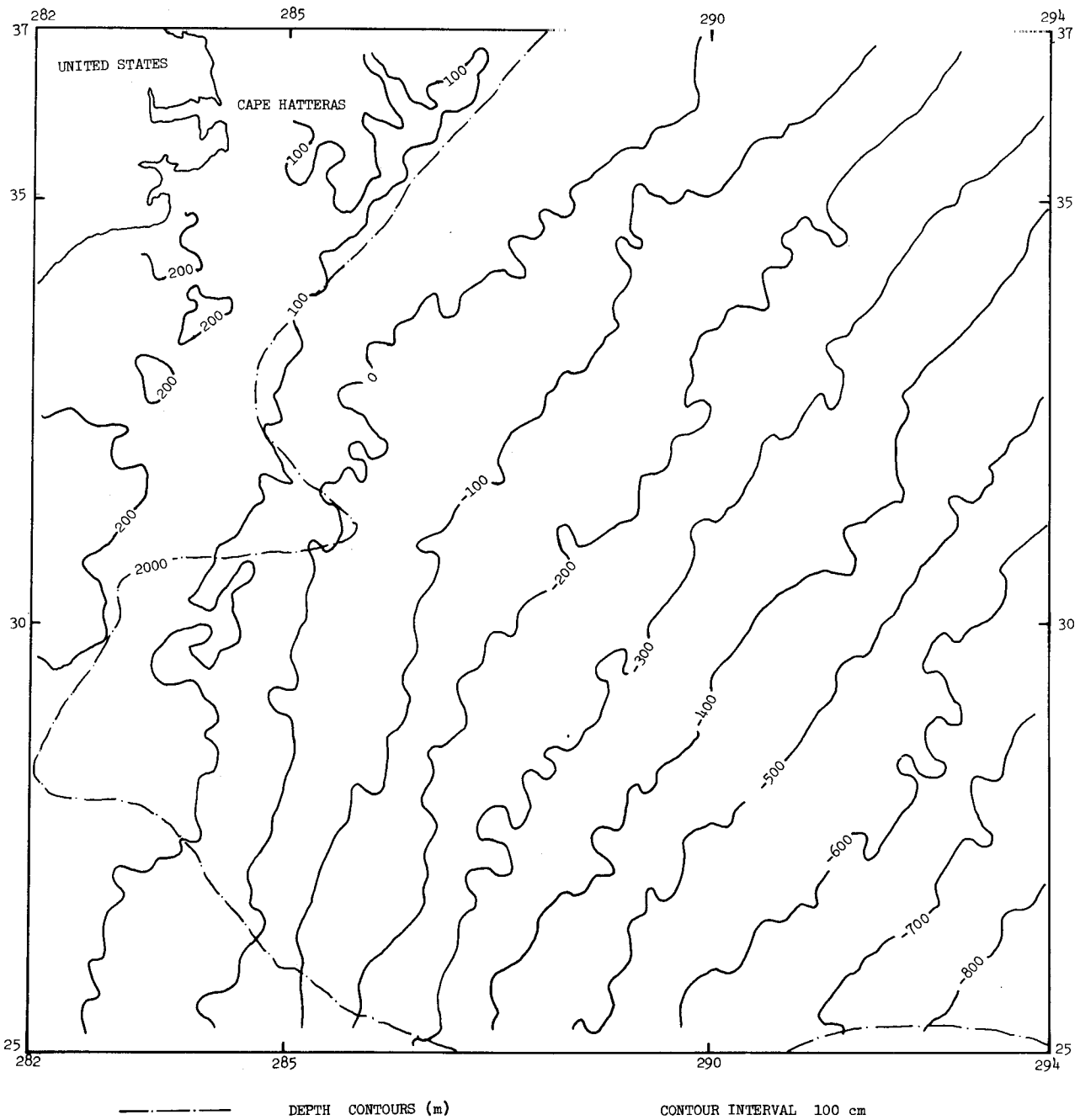


Figure 6.14

Dynamic SSH Variations - July 1975

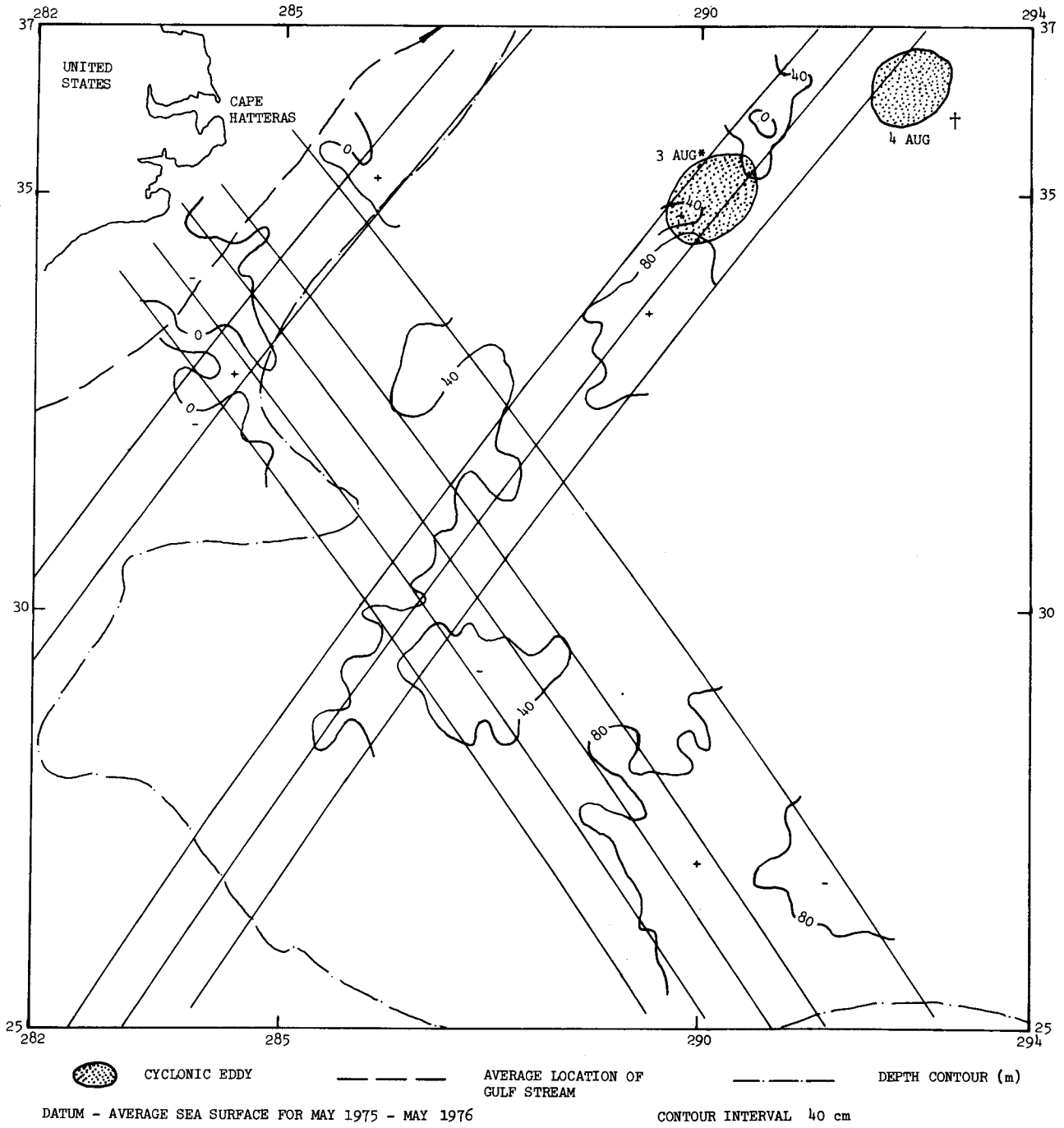
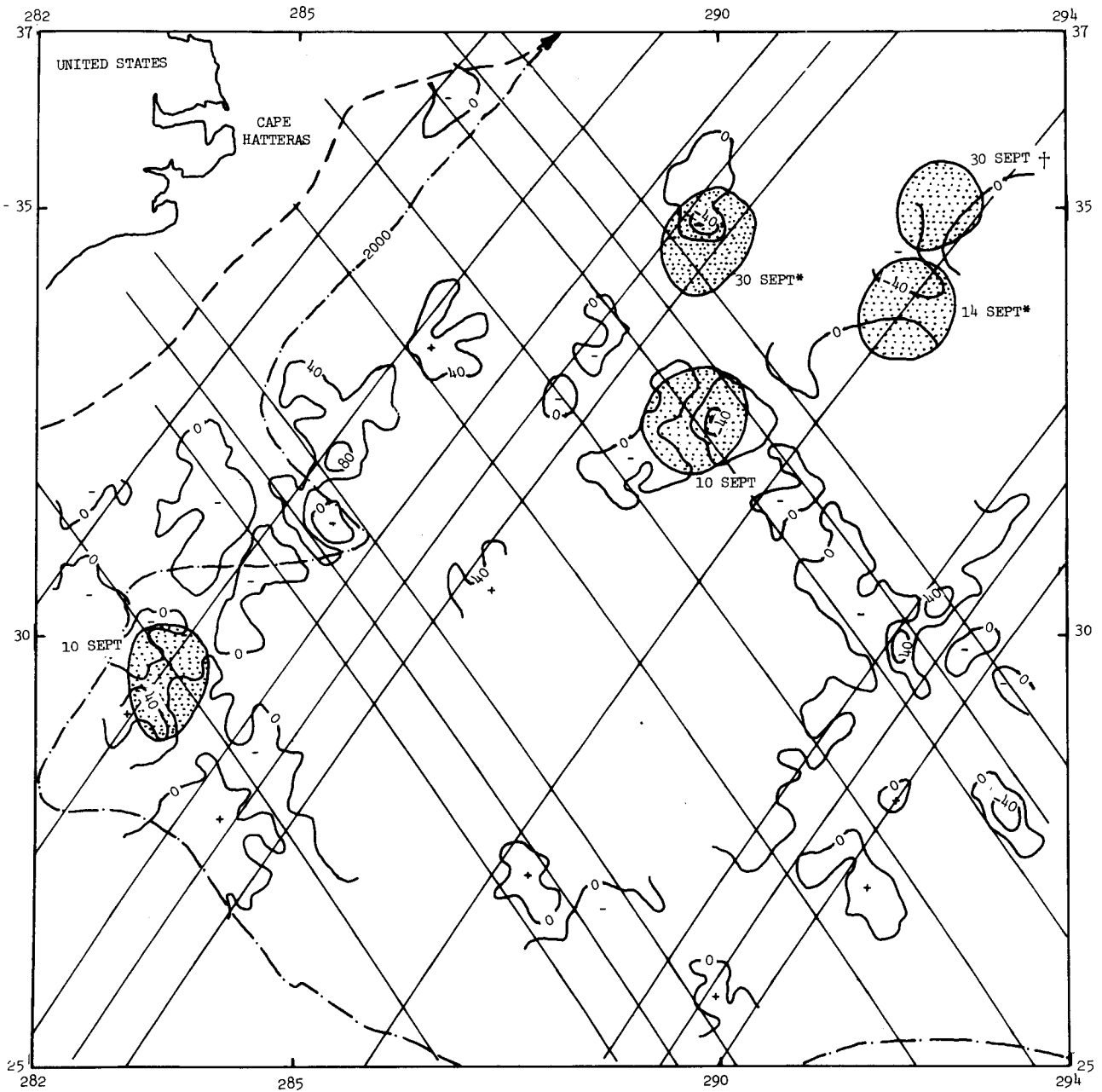



Figure 6.15

Dynamic SSH Variations - September 1975



 CYCLONIC EDDY - - - - AVERAGE LOCATION OF GULF STREAM - · - · - DEPTH CONTOUR (m)

DATUM - AVERAGE SEA SURFACE FOR MAY 1975 - MAY 1976 CONTOUR INTERVAL 40 CM

Figure 6.17

Dynamic SSH Variations - October 1975

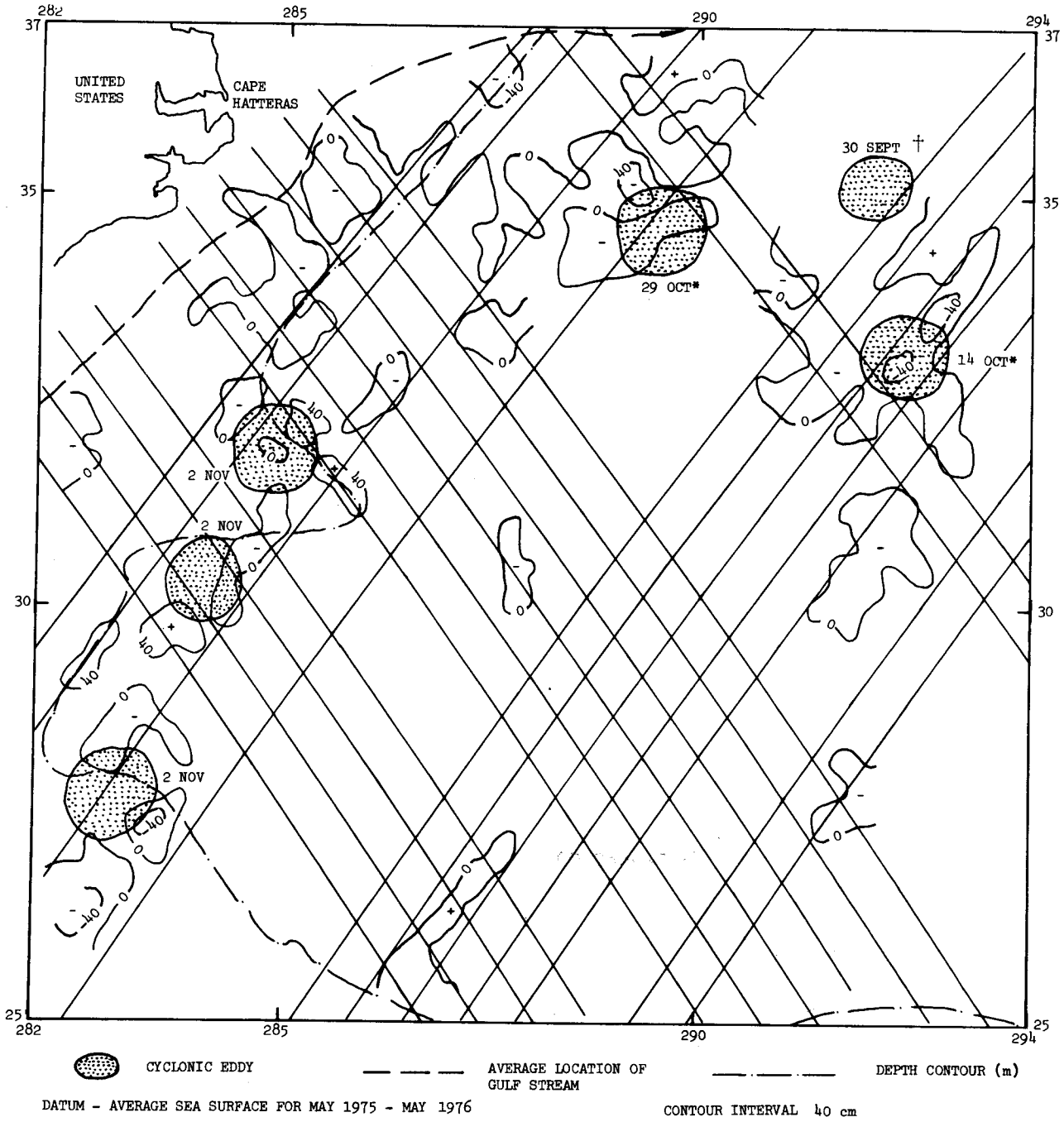


Figure 6.18

Dynamic SSH Variations - April 1976

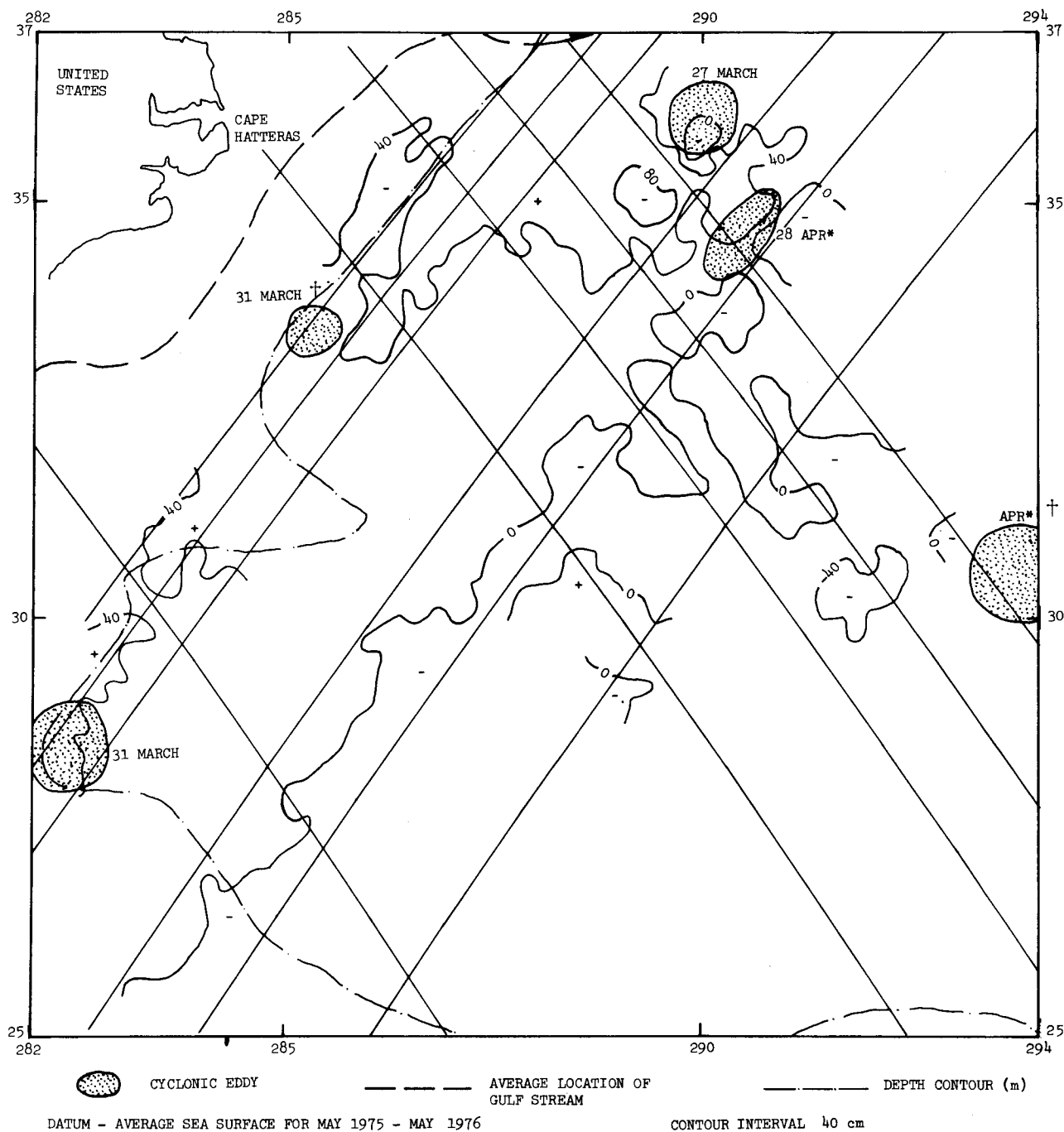


Figure 6.19

Dynamic SSH Variations - May 1976

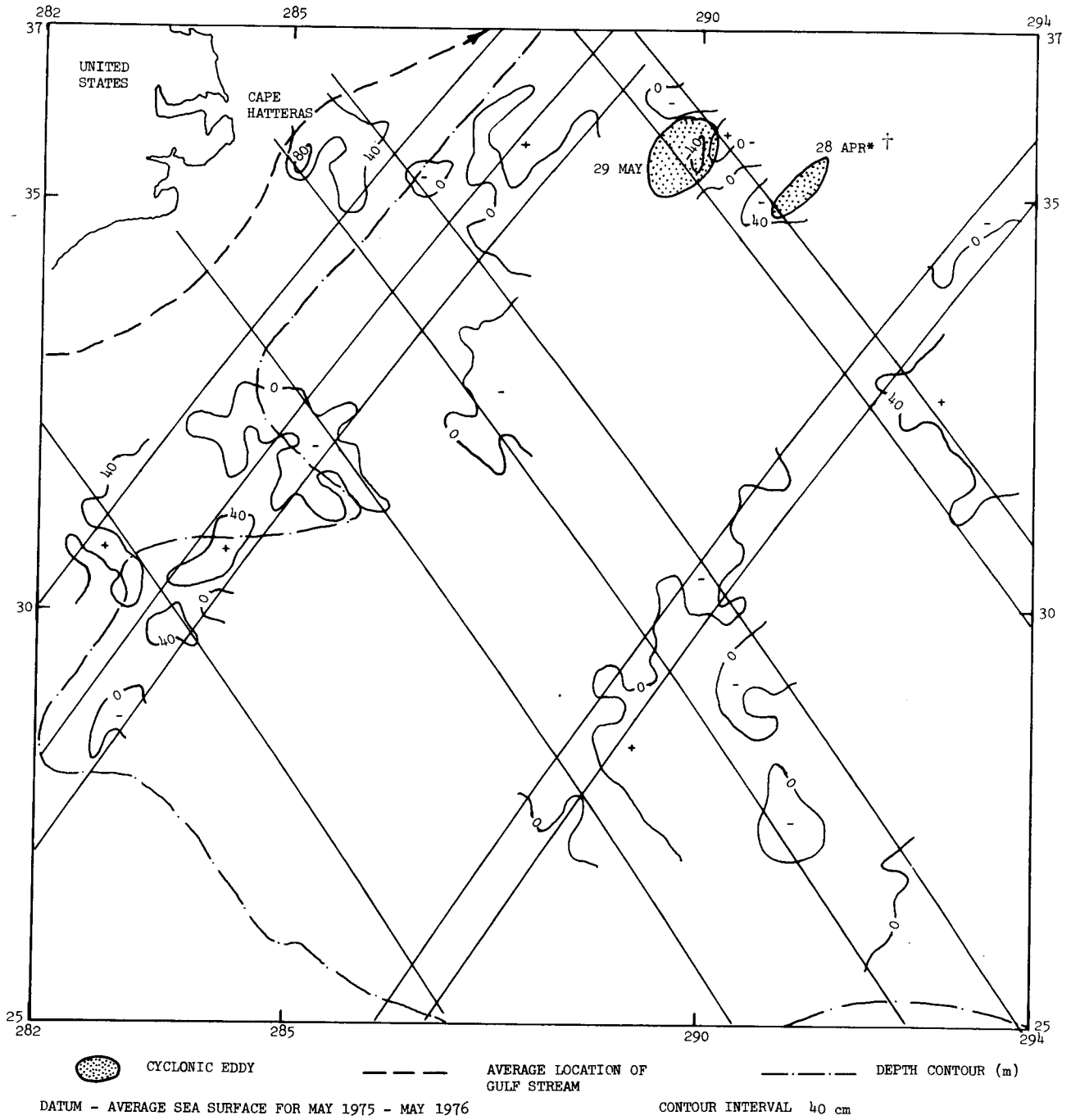


Figure 6.20

U.S. National Weather Service (NOAA/NWS 1975,1976). The Gulf Stream has been defined as a narrow band of high velocity water flowing along a boundary between the warm, highly saline water in the Sargasso Sea and the colder, fresher slope water to the shoreward side (Stommel 1965), with the Stream being in geostrophic balance with the pronounced pressure gradient between the two water masses.

Gulf Stream rings formed from large, 200- to 300-km diameter, meanders are an important part of the Gulf Stream system (Fuglister 1972, 1977; Parker 1971; Barrett 1971), and are an example of an oceanic phenomena in which there are large variations in temperature and salinity and therefore of dynamic SST. Cyclonic rings that migrate through the Sargasso Sea create depressions, while anticyclonic rings north of the Stream appear as sea surface highs, these rings have been observed to move at irregular rates ranging from 1-8 km/day (Lai & Richardson 1977).

To assess the significance of the results illustrated in Figures 6.15 to 6.20, it is appropriate to assess the likely magnitudes of features such as the eddies based on oceanographic considerations. Assuming the existence of a layer of no motion at great depth H (approximately 2000 m) in the region at which isobaric and level surfaces coincide, the constant pressure P at depth ($h=H$) is given by,

$$P = \left(\int_H^0 g \rho_w dz \right)_{\text{ocean}} + \left(\int_0^h g \rho_a dz \right)_{\text{atmosphere}} = \text{Constant} \quad (6.20)$$

where g is the observed gravity, ρ_w the density of sea water and ρ_a the atmospheric density at the element of height dz for a given location, the integration being along the local vertical. The variations in ρ_w , ρ_a cause anomalies dh in the height of the standard column of water above the level of no motion. These can be related to the temperature anomalies dT and salinity anomalies dS at the pressure increment dp corresponding to dz , in terms of the relation

$$dh = \left(\int_{p_0}^P \frac{\partial \alpha}{\partial T} dT dp + \int_{p_0}^P \frac{\partial \alpha}{\partial S} dS dp - \frac{1}{\rho_w} dp_a \right) / g + O\{f dh\} \quad (6.21)$$

where α is the specific volume of sea water and dp_a the atmospheric pressure anomaly from the standard atmospheric model at the air/sea interface where the pressure is p_0 .

The density of sea water ρ_w varies from 1.022 in the surface

layers of the equatorial oceans to about 1.028 in deep oceans (Monin et al. 1977, p.36).

Equation 6.21 can be simplified by assuming $\partial\alpha/\partial S=0$ and ignoring atmospheric pressure variations dp_a , giving

$$dh = \frac{1}{g} \int_p^{p_0} \frac{\partial\alpha}{\partial T} dT dp \quad (6.22)$$

Assuming a standard salinity of 35‰ and using estimates of $\partial\alpha/\partial T$ from Mameyev (1975, Figure 14), this equation provides a simplified, even simplistic estimate of the SST anomaly which can be expected from a typical Gulf Stream eddy. For example, the cyclonic eddy reported by Cheney and Richardson (1976, p.145) is equivalent to changes in SST of between -34 cm and -80 cm, assuming a level of no motion at 1000 m depth. Temperature anomalies which average 1°C over 2000 m are equivalent to a SST anomaly of approximately 13 cm.

However, surface temperature measurements do not appear to be representative of the entire oceans especially if representative of an eddy-type structure (Cheney & Richardson 1976). In the case of such structures, temperatures from the deeper layers have a greater influence on local SST maxima and minima than an estimate of the surface temperature which could be deceptively near normal. Consequently, correlations between surface temperature measurements and local maxima and minima in the shape of the sea surface should not be expected in all cases.

6.4.4.2. Overlapping Pass Correlations.

For the five months studied, a total of 37 comparisons were made where an overlapping altimeter profile crossed an eddy feature. Fifty-eight percent of these comparisons between altimeter and IR data correlated favorably. A further 40% of the comparisons showed a partial overlap between the feature as sensed from the two data types. Only 2% of the comparisons did not correlate at all.

These results are in substantial agreement with the results obtained from regional solutions which are subject to slightly higher levels of uncertainty. The analysis of overlapping passes provides the most accurate data for the study of regional variations in the dynamic SST but suffers from limitations in areal coverage. Overlapping pass

solutions contain no non-tidal information on wavelengths greater than $2d$, where d is the average pass length (4000 km in this case) and on periods less than 37.18 days.

6.4.4.3. Regional Sea Surface Model Correlations.

The positions of the eddy features, shown by stippled areas in Figures 6.15 to 6.20, are taken from the NOAA publication, Gulf Stream, and are corroborated by data from Lai & Richardson (1977). Where cruise data has confirmed or located a cyclonic eddy, an asterisk is placed next to the date of observation. Inspection of the figures shows good general agreement between lows in relative SSH and cyclonic eddies observed by ship and IR imagery data. Given the differences between the two types of information compared, none of the comparisons can be classified as being unsatisfactory. Table 6.7 summarises the extent of correlation between the two data types. The correlation distances were obtained using a spherical distance algorithm given the positions of the centres of the eddy feature and SSH minima. For the six monthly solutions analysed, SSH minima occurred within 50 km of the IR sensed eddy features 56% of the time and within 100 km 90% of the time. These statistics ignore those locations where insufficient data were considered available to confirm the existence of a SSH feature (see Table 6.7). These locations are shown in Figures 6.15 to 6.20 by a dagger (\dagger) placed next to the date of eddy observation. The uncertainties occur when the geometry of the passes is grossly irregular and there is an imbalance between the distribution of north-south as compared to south-north passes in the monthly solution. (See Figures 6.15 and 6.20).

The contours shown in Figures 6.15 to 6.20 specifically exclude the quasi-stationary component of the SST. The possibility of recovering this part of the spectrum of SST is discussed in the next sub-section. The contours shown in these figures are based on data on a 0.5 degree grid and thereby reflect wavelengths greater than 100 km. Additional data were plotted at 20 km intervals to enhance local features in areas where IR imagery reported the existence of cyclonic eddies.

Some additional observations can be made from information displayed in the sea surface models:

- (i) the broad high of +80 cm in the solution for July 1975 (Figure

Table 6.7.
 Correlations Between Remote Sensed Cyclonic Eddies and Dynamic SSH's of Regional Models
 of the Sargasso Sea from GEOS-3 Altimetry

Month	Year	Correlations with Cyclonic Eddies as (%) function of distance (km)				Sample Size
		0<d<50	50<d<100	d>100	Insuff. Data	
July	1975		50		50	2
August	1975	100				4
September	1975	40	20	20	20	5
October	1975	33	50		17	6
April	1976	20	20	20	40	5
May	1976	50			50	2
Total		42	25	8	25	24

6.15) poses some doubt on the validity of the solution. This feature is certainly not of oceanographic origin as can be gauged by simply working out the transport implied by its dimensions. The feature is due predominantly to the unstable geometry of this solution, there being no crossover points in the south-east corner of the region, thereby causing biases in the model.

(ii) the feature at about 31.5°N , 285.5°E in the September 1975 solution (Figure 6.17) appears to be correlated with a cyclonic eddy whose position, confirmed by IR data, is further south at 30°N , 284°E in the October 1975 solution (Figure 6.18). The implied rate of eddy movement, assuming an initial date of mid-September for this feature, is about 5 km/day which is in agreement with documented eddy rates (Lai & Richardson 1977). There is, however, not enough evidence in the WALLOPS solutions for September or October (Figures A2.3 and A2.4 in Appendix A2) to prove or disprove this statement.

As shown in Mather et al. (1978a) and evidenced in the results presented in this section, regional sea surface modelling provides a reliable basis for the study of eddies which cause variations in SSH's larger than ± 30 cm. These figures only apply in the immediate vicinity of groundtracks as the precision falls off rapidly with distance from the nearest groundtracks. Much more work is required before complete reliability can be placed in altimeter defined SSH features not confirmed or surveyed by IR or surface ship data. A much improved solution can be obtained if the region is covered with an adequate and balanced network of passes and the tidal signal is eliminated from the SSH data before processing. The use of laser derived orbits from a well distributed tracking station complement will also improve the resolution of the regional monthly models. Unfortunately, this situation seems only possible, at the present time, in the western North Atlantic.

6.4.4.4. Summary.

There is no doubt that the GEOS-3 altimeter data in the short pulse mode is of sufficient precision for oceanographic studies. The analyses described above demonstrate the potential of the satellite altimeter as a tool with which to study the dynamics of the surface layer of the oceans. Sophisticated laser tracking support is not needed to track eddies, provided 30 balanced passes of data are available each month per 10^6 km² in the region of interest. A resolution of ± 20 -

30 cm can be expected in such a case. It should also be possible to recover variations with wavelengths between 150 and 5000 km and amplitudes in excess of 30 cm, provided a reliable ocean tide model is available.

The regional model solutions cannot resolve features with periods shorter than a month and all information in the time varying part of the spectrum of SST with wavelengths greater than twice the dimension of the region studied are also lost (for analyses above, the limiting wavelength is about 2×10^3 km).

For overlapping pass analysis, a higher resolution of the eddy features is obtained but the coverage in both space and time is very much more restricted. Sea surface variability information can only be obtained for wavelengths less than twice the length of the pass (on average about 5000 km) and periods greater than 37.18 days.

The correlation studies indicate a 90% agreement between the altimeter-defined ocean surface feature and the locations of eddies defined by IR and ship data using either overlapping pass or regional sea surface model solutions. The reliability of the correlations suggest that these techniques should be extremely useful for detecting the frequency of formation, movement and distribution of ocean eddies and given a sufficient data coverage provide statistics on the mesoscale variability on monthly/yearly time scales.

6.4.5. Geostrophic Current Estimates.

6.4.5.1. Requirements for Recovering the SST.

The Gulf Stream is an example of a quasi-stationary current system that is well described by its density field alone. The oceanographically determined density distribution defines that portion of the pressure field which is used to measure the geostrophic current. All of the major surface currents in the ocean are, to a first approximation, in geostrophic balance, and their surface pressure gradients can be inferred from the sea surface slopes relative to a datum level surface. Satellite-borne altimeters are capable of providing a direct measure of these sea surface slopes giving a possible supportive approach to estimating surface ocean currents and providing a viable technique for the synoptic monitoring of the dynamic SST, and

ultimately, ocean surface dynamics.

From equation 2.29 the dynamic SST (ζ_s) is defined as

$$\zeta_s = \zeta - N \quad (6.23)$$

where ζ is the SSH above the reference ellipsoid, deduced from the altimeter measurement and N is the geoid height obtained using a specified gravity field model. ζ_s is defined as the radial departure of the sea surface from the geoid where the geoid is that level surface of the Earth's gravity field corresponding to a globally determined MSL.

Geodetic determinations of ζ_s should aim for a minimum resolution of ± 10 cm if they are to play a useful role in defining phenomena of interest for quantifying the dynamics of the air/sea interface. Short period variations of ζ_s associated with eddy formation and seasonal changes in sea level are expected to vary from ± 10 cm to ± 80 cm. Such variations could be studied directly from variations in the radial component of the instantaneous sea surface position provided the geoid can be assumed to change shape in this same time interval by less than $\pm 1-2$ cm. As concluded in Chapter 5, it is not possible to use the BVP approach in determining ζ_s from SSH's (ζ) above the reference figure because no data can be unambiguously related to the geoid at the desired level of precision without making unwarranted assumptions about the magnitude and distribution of ζ_s . The role of purely geodetic techniques in remote sensing ocean dynamics is primarily that of providing values of ζ_s from the radar altimeter data. This section attempts to circumvent the problems previously mentioned and under certain speculative assumptions estimate values of ζ_s for geostrophic current determinations on a regional basis.

The influence of the horizontal gradients of ζ_s on the circulation of the ocean surface layer has been given in equation 4.6. Examining the quantities in equation 6.23, ζ will be subject to altimeter error (the noise level of the GEOS-3 altimeter is assessed at ± 20 cm on a relative basis) and orbital uncertainties. Complications are also introduced because the value of ζ measured by the altimeter contains not only the geostrophic current component, but also other forces influencing the SST such as tides, atmospheric pressure, gravity, etc as set out in sub-section 3.2.1. However, most of these signals (with the exception of gravity variations) are of long wavelength compared to the Gulf Stream features under study and should be

eliminated by an overall tilt to the sea surface over regional extents.

The gravity variations are removed by subtracting out the best available estimate of the geoid surface from the altimeter signal. Thus, the calculations of ocean dynamic information depend critically on the accuracy obtainable for the local independent gravimetric geoid which serves as a datum similar to the assumed level of no motion used in the dynamic method of oceanography. This requires that the accuracy to which the values of N are known must be at the ± 10 cm level through relevant wavelengths. At the present time, the absolute accuracy of the best available gravimetric geoid in the Northwestern Atlantic (Marsh & Chang 1978) is unknown but is certainly a factor of at least 5 higher than that required for synoptic ocean dynamic modelling.

The maximum current velocities reported in the vicinity of the Gulf Stream in the western part of the Sargasso test area are of the order 100 to 250 cm/sec (Stommel 1965). In a geostrophically balanced system, the surface velocity (\dot{x}) is given by

$$\dot{x} = \frac{g}{f} \frac{\partial \zeta_s}{\partial x} \quad (6.24)$$

where g is gravity, f is the Coriolis parameter ($f = 2 \Omega \sin \phi$) and x is the cross-stream horizontal dimension. The SST gradient needed to maintain a 200 cm/sec current at latitude $35^\circ N$ using equation 6.24 is thus, about 170 cm per 100 km orthogonal to the mean direction of flow. In terms of the regional sea surface models with data at 20 km intervals produced in sub-section 6.4.4, a change in SSH of 34 cm is required to produce a 200 cm/sec current. This information on the gradient $\partial \zeta_s / \partial x_\alpha$ can only be obtained from GEOS-3 altimetry, processed in the form of regional models, if the SSH's were referred to an error free geoid. As seen from Figure 6.14, the discrepancies between the altimetry sea surface models after orientation to GEM 9 (Table 6.6), are systematically discrepant with the best available gravimetric geoid in the region.

These discrepancies can be attributed to the following factors:

- (i) differences between the gravimetric geoid and the satellite determined gravity field model,
- (ii) the quasi-stationary component of the dynamic SST.

For example, if it were assumed that the GEM 9 gravity field model were free of error, the differences at (i) are due entirely to errors in the

gravimetric geoid due to the variable quality and distribution of surface gravity data currently available for such computations in the region. Since the gravimetric geoid is computed from a fixed gravity data bank using quadrature techniques, the resulting errors in the geoid are slowly varying functions of position (e.g., see Mather 1968). The pattern of errors is a function of distance from the east coast of North America (Figure 6.14) and as such it is possible to make a very approximate estimate of the quasi-stationary SST using the procedures outlined in Mather et al. (1978a). An alternative technique, which is more successful in estimating the surface current velocities, is proposed in the next paragraph.

6.4.5.2. Data Analysis Procedure.

The Marsh-Chang detailed gravimetric geoid, computed on a 5' x 5' grid (about 9 km x 9 km) using a combination of satellite and surface gravity data, is presently considered the best available geoid for the Northwestern Atlantic Ocean. A conservative estimate of its precision is ± 50 cm. The regional sea surface models, summarised in Table 6.5, were considered as estimates of the sea surface with relative configuration accuracies, as a continuous field of about ± 30 cm, assuming that the long wavelength orbital errors have been eliminated by bias and tilt corrections.

Using equation 6.15, a transformation was made to fit the regional model onto the Marsh-Chang geoid over a portion of the test area away from the Gulf Stream region. The area excluded in the transformation was the northwest section of the test area from latitudes 32° to 37°N and longitudes 282° to 286°E being an area of high eddy energy variability. Column 5 of Table 6.6 gives the percentage area of the total block used in the transformation. Estimates of the transformed ζ values on a 0.2° grid were made and 0.5° means taken for both ζ and the Marsh-Chang geoid (N values).

The values of ζ_s (equation 6.23) were used in equation 4.6 to calculate estimates of the geostrophic component of the surface current. This procedure makes the assumption that the gradients of ζ_s obtained after the surface fitting give a realistic estimate of the "true" gradients, despite the inaccuracies present in either the sea surface model or the detailed geoid. Previous estimates of the quasi-stationary SST by Mather et al. (1978a) considered the pattern of discrepancies

shown in Figure 6.14 and used linear regression techniques along altimetry profiles to eliminate geoid error. Similar regression techniques have been used by Leitao et al. (1977). However, the contours derived by Mather et al. (1978a) underestimated the Gulf Stream velocity by a factor of about 4.

In addition to the Marsh-Chang geoid, the calculations were repeated using geoid height estimates derived from the GEM 9 (Lerch et al. 1977) and GEM 10B (Lerch et al. 1978a) gravity field models evaluated to degree and order 15.

6.4.5.3. Results.

The geostrophic component of the surface current is shown in Eulerian flow form for each monthly solution and for the epoch solution (May 1975 - May 1976) in Figures 6.21 to 6.27. The mean Gulf Stream path for each month, taken from the publication *Gulfstream*, is shown in the figures and corresponds closely to the larger velocity vectors derived from the altimeter sea surface models. The solutions are again weaker towards the peripheries of the region and in areas where the geoid shows steep gradients (i.e., the SW corner of the block). All the current velocities are between 4 and 280 cm/sec and at most 1% of the data, mainly in the areas mentioned above, has been excluded from the solutions. The satellite groundtracks are spaced too far apart to accurately show any of the ring currents and also most of this information is lost in averaging over 50 km squares.

The epoch solutions using the GEM 9 (Figure 6.28) and the GEM 10B (Figure 6.29) geoids give vastly different patterns to the Marsh-Chang solution. As expected, these solutions have a greater signal variance than the Marsh-Chang solution since they are evaluated to only (15,15) and do not contain the higher frequency information available in the detailed gravimetric geoid. Approximately 12% of the 0.5° data were excluded in the GEM solutions (i.e., $\dot{x} > 300$ cm/sec) and as seen from the figures, there is little resemblance to the physical oceanographic system.

The mean current velocities for the epoch solutions, over the $12^\circ \times 12^\circ$ area, using the Marsh-Chang, GEM 9 and GEM 10B geoids were 49 cm/sec, 163 cm/sec and 160 cm/sec respectively. This again gives an indication of the difference between the solutions. As a rough estimate of the average current speed for the area, annual mean current speeds

from Fuglister (1951, Figure 1 and Table 2), give an average current speed of 43 cm/sec. The average was calculated as the mean of segments 4,5 and 8 indicated in Fuglister (1951, Figure 1). The agreement between the two results is surprisingly good. While not being overly optimistic about this result, it does indicate that some useful analyses of ocean dynamic parameters of interest will be obtained in the future using satellite altimetry data.

The problem in comparing Figures 6.21 to 6.27 with oceanographic estimates of dynamic height maps is the tremendous variability created by the Gulf Stream rings and the meanders in the Western Sargasso. Maps of the topography of the 15° isothermal surface produced over yearly intervals (e.g. Richardson et al. 1978, Figure 2) do not look like (as expected) maps produced for monthly periods (e.g. Richardson et al. 1978, Figure 1). These maps may be viewed as having similar patterns to dynamic height contours because of the linear temperature-salinity relation and nearly constant vertical temperature gradient in the main thermocline. Figure 1 of Richardson et al. (1978), for the period March 16-July 9 1978, was converted to a dynamic height chart noting that a 100 m change in 15°C depth is approximately equivalent to a 15 cm change in dynamic height (R.E. Cheney, private communication, 1979). However, comparison with Figure 6.21 (July 1975 solution) showed that there were no similarities and the eddy features seen in Figure 1 of Richardson et al. (1978) were completely lost in the regional model solution. Unfortunately, the July 1975 solution was one of the weakest of the six months analysed so that realistic comparisons could not be made.

The flow patterns in the monthly and yearly solutions presented can distinguish the Gulf Stream and suggest a width of the main current of about 50-100 km. The yearly solution (Figure 6.27) should provide information on the mean ocean circulation but as seen in the Figure, the flow patterns do not seem consistent with the general broad return flow suggested by dynamic height charts (e.g. Sturges 1972, Figure 2). An improvement of these results would be obtained if the full 3.6 year GEOS-3 data set were analysed.

6.4.5.4. Discussion.

It is not possible, at the present time, to recover the quasi-stationary component of the SST in the desired wavelengths unless certain speculative assumptions are made. The limiting factor is the

Geostrophic Current - July 1975

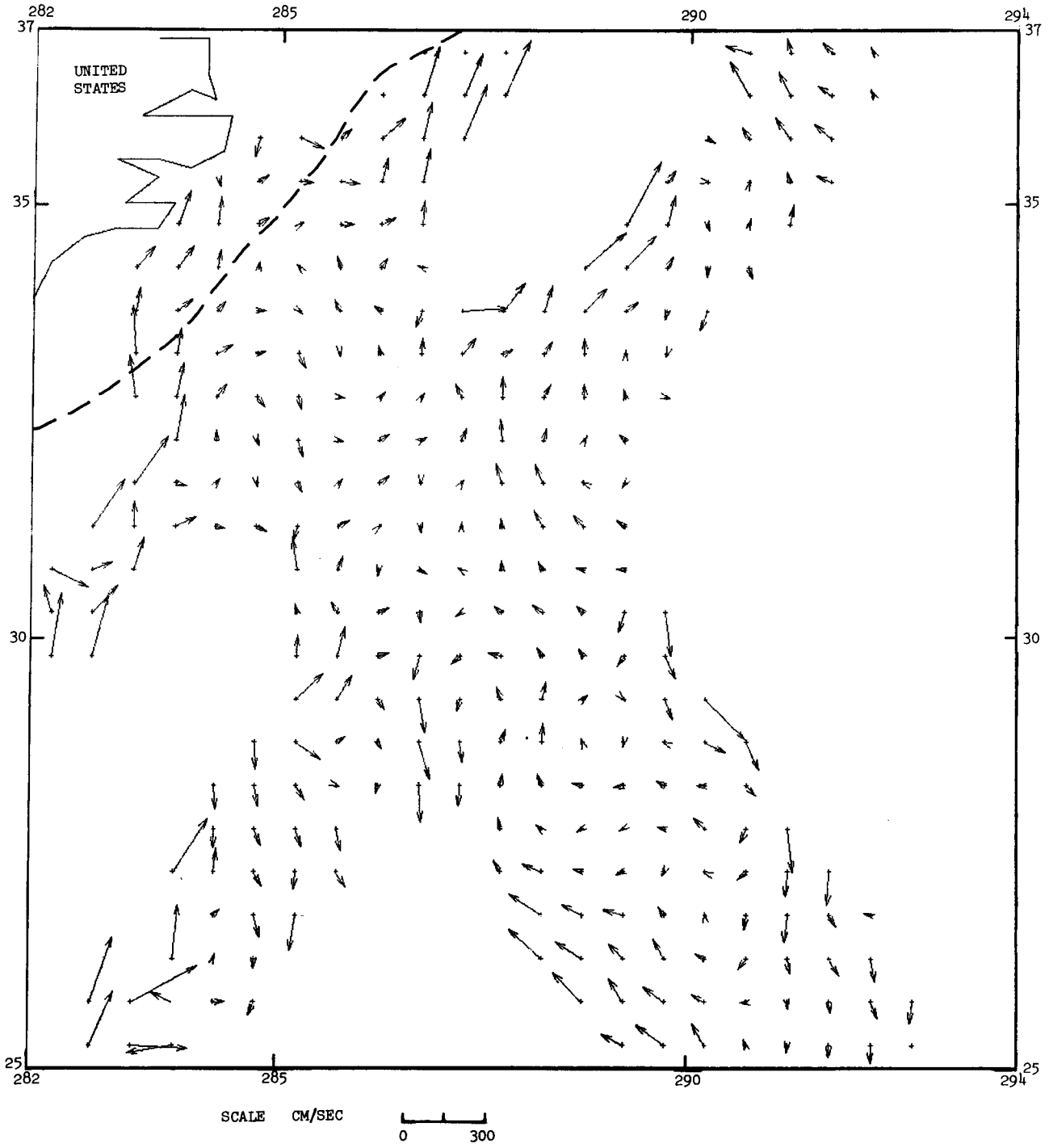


Figure 6.21

Geostrophic Current - August 1975

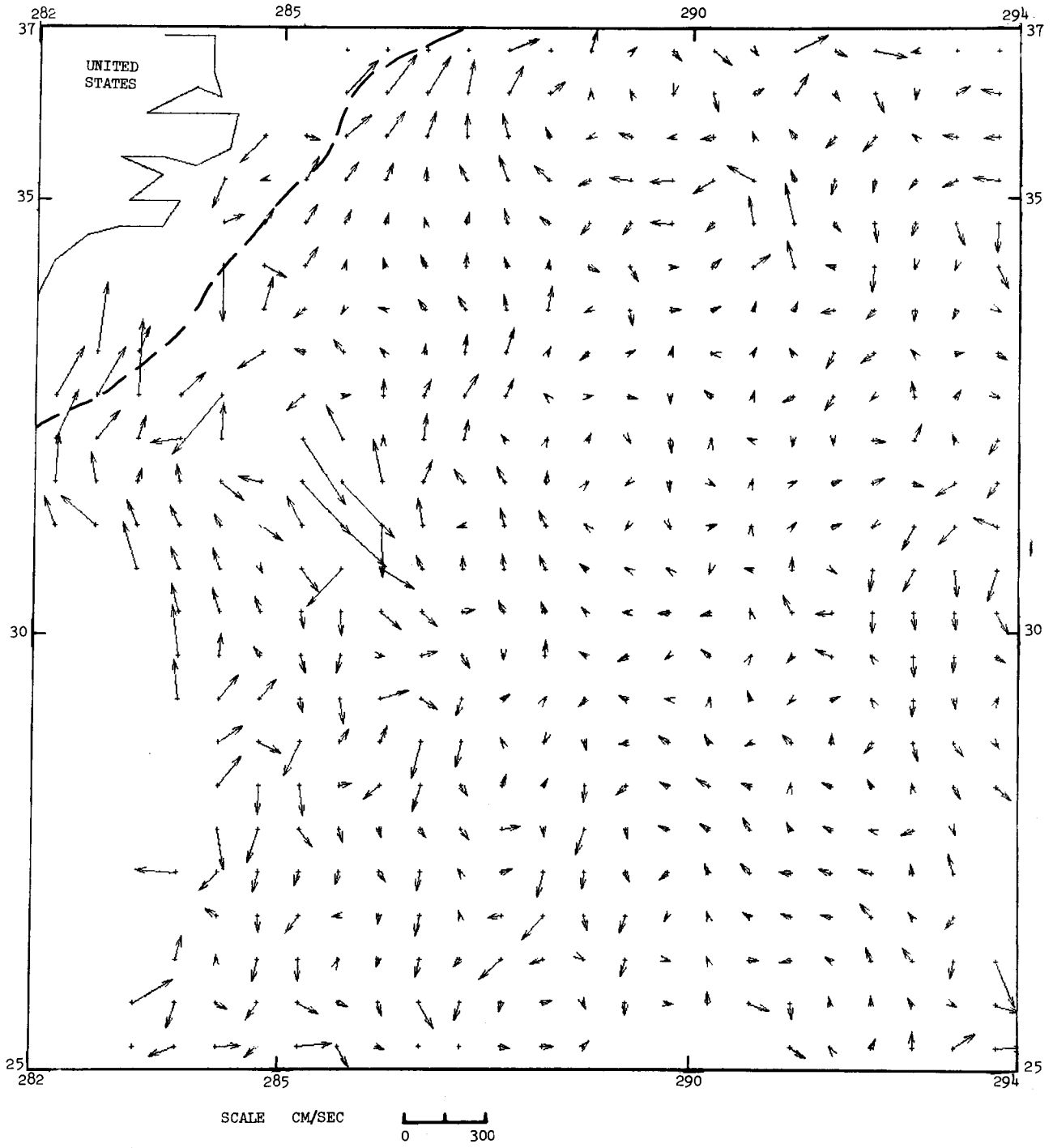


Figure 6.22

Geostrophic Current - September 1975

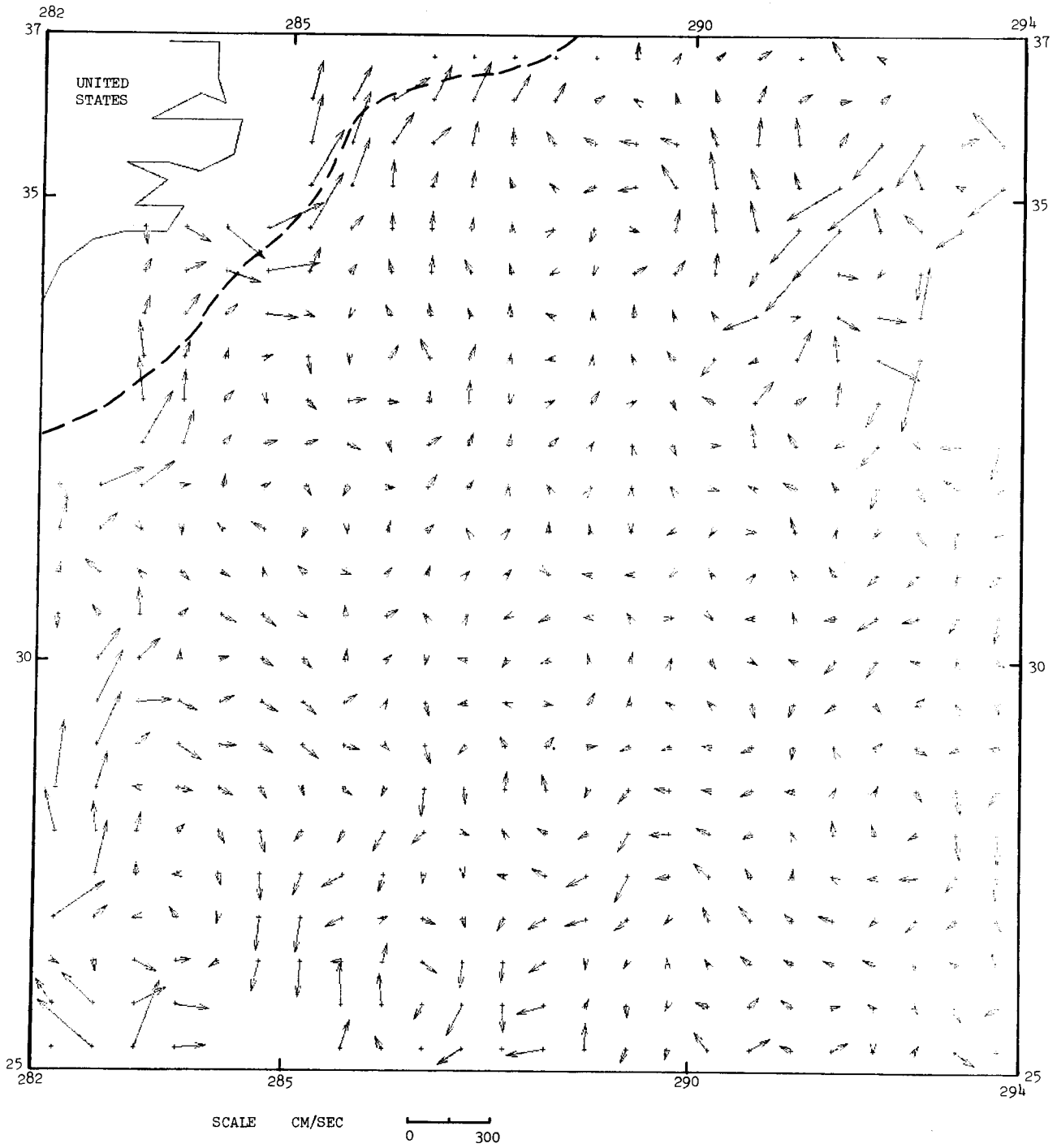


Figure 6.23

Geostrophic Current - October 1975

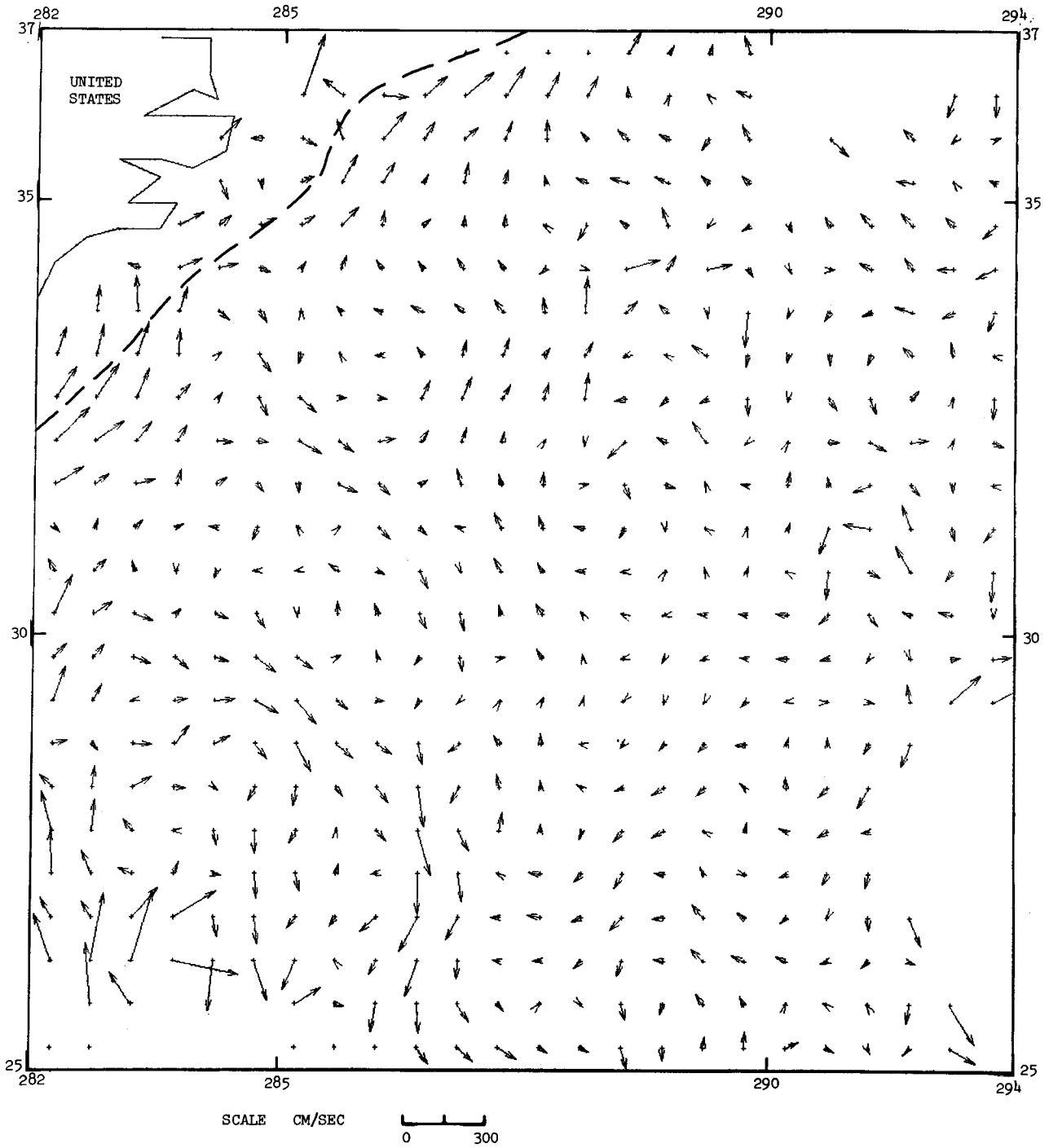


Figure 6.24

Geostrophic Current - April 1976

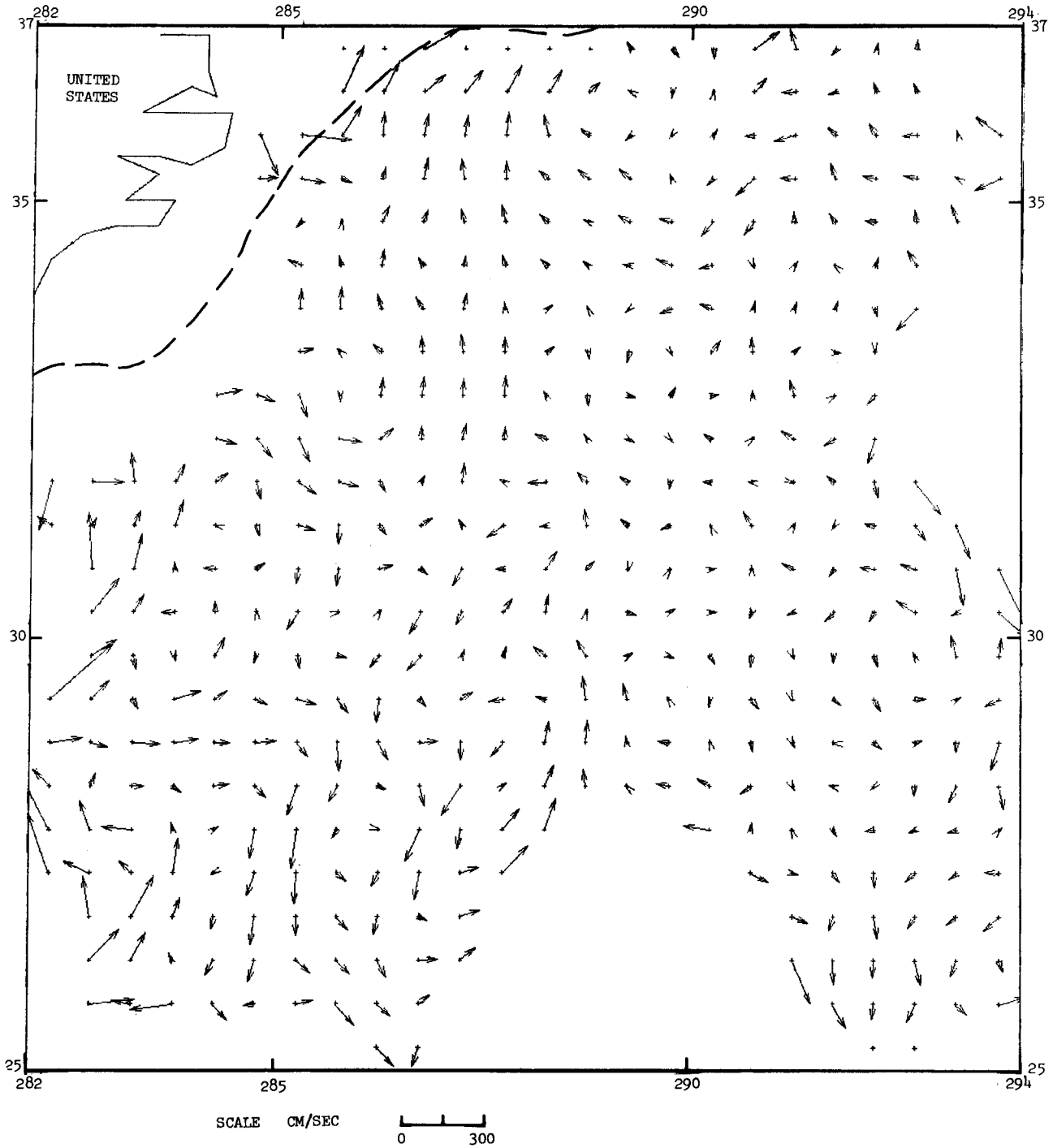


Figure 6.25

Geostrophic Current - May 1976

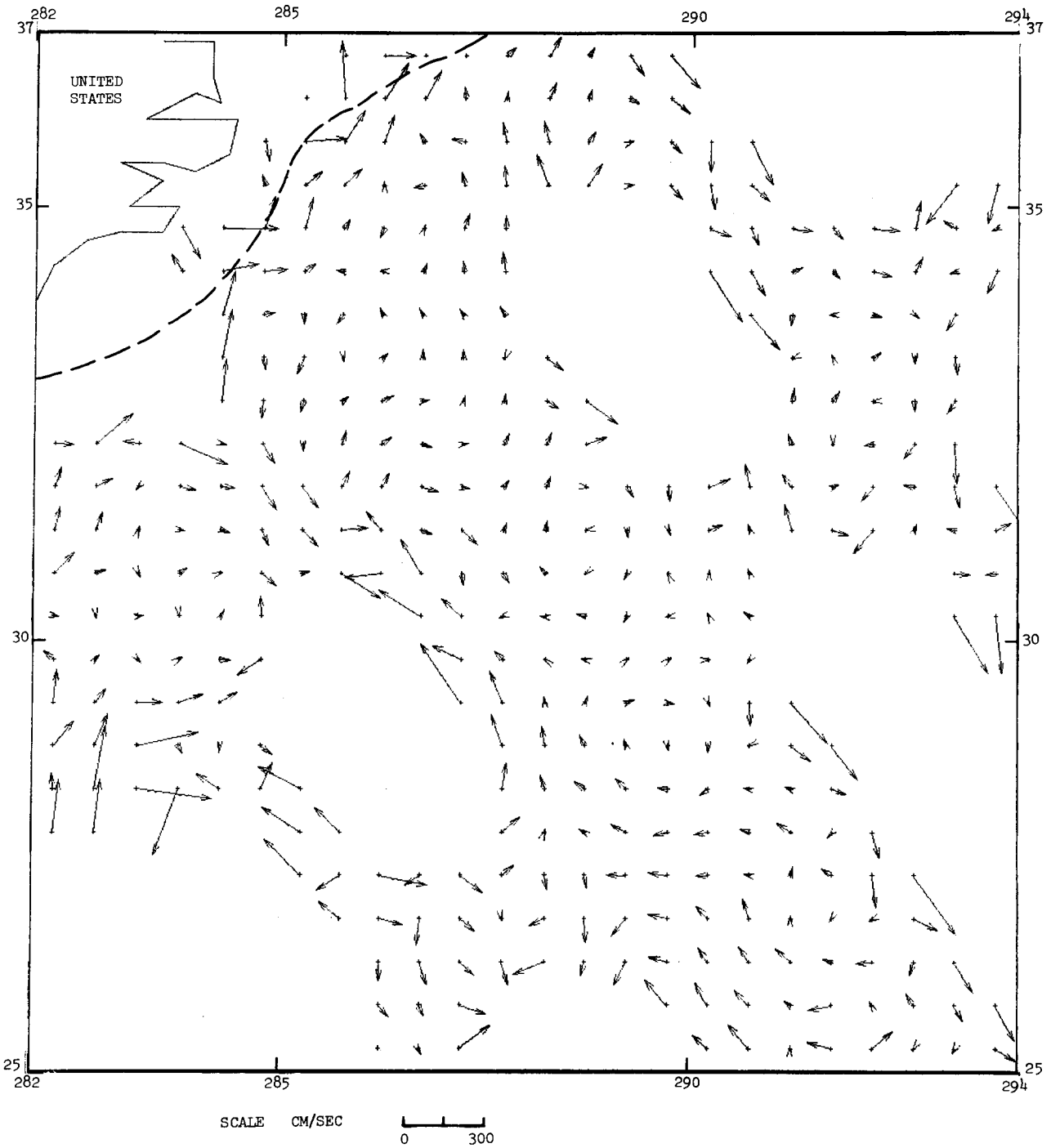


Figure 6.26

Geostrophic Current - Epoch (May 75 - May 76)

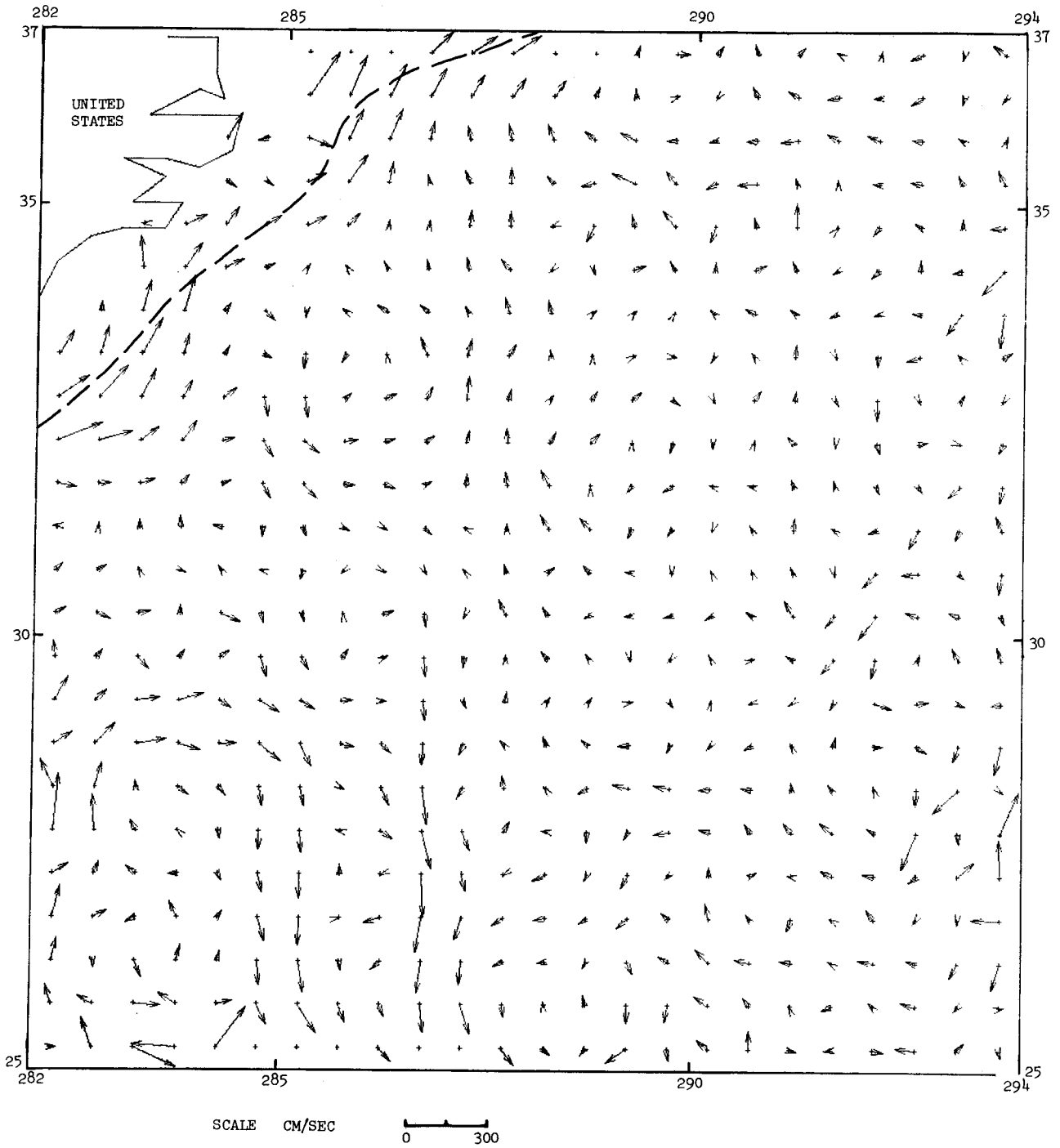


Figure 6.27

Geostrophic Current - Epoch (GEM9)

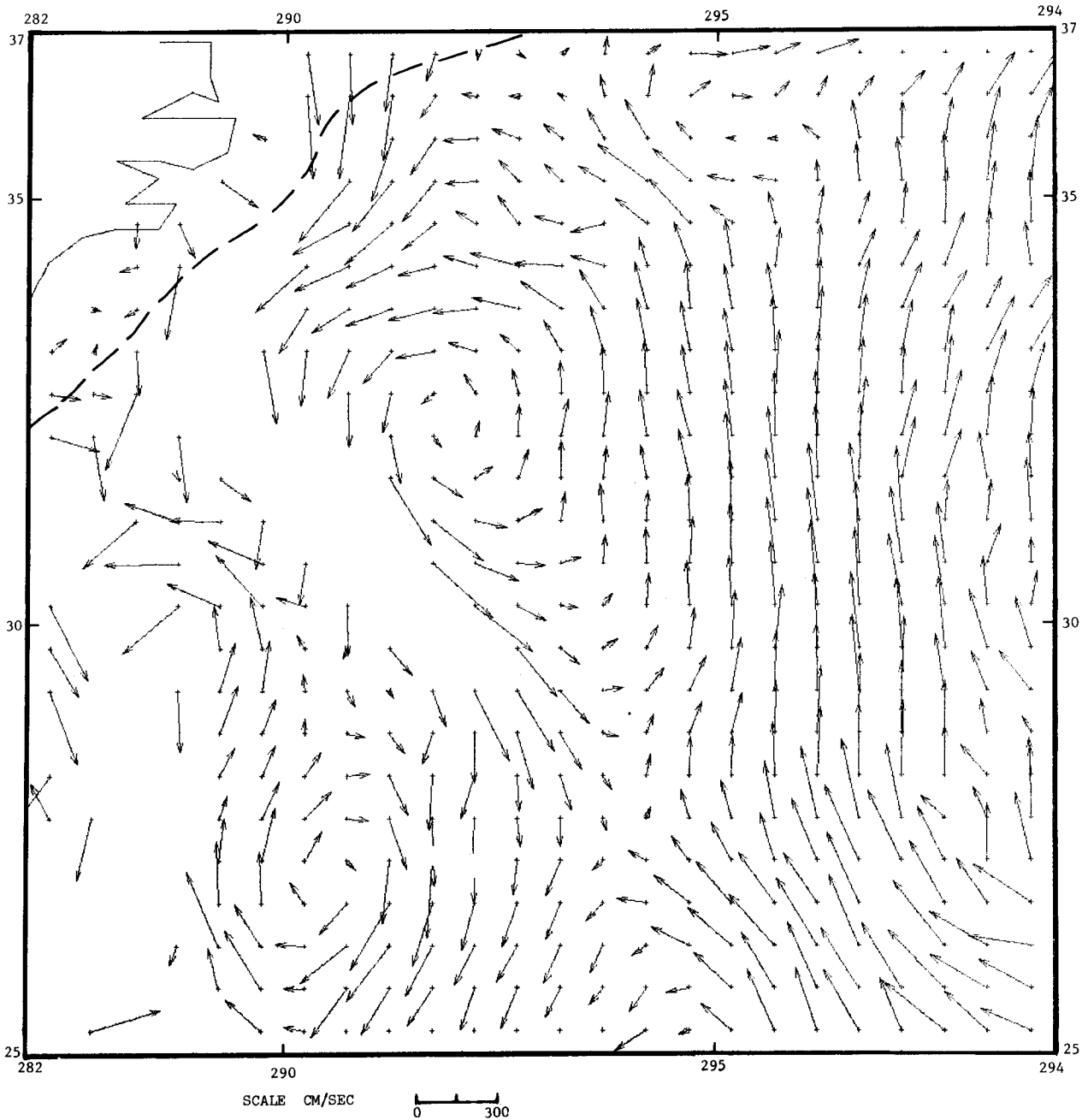


Figure 6.28

Geostrophic Current - Epoch (GEM10B)

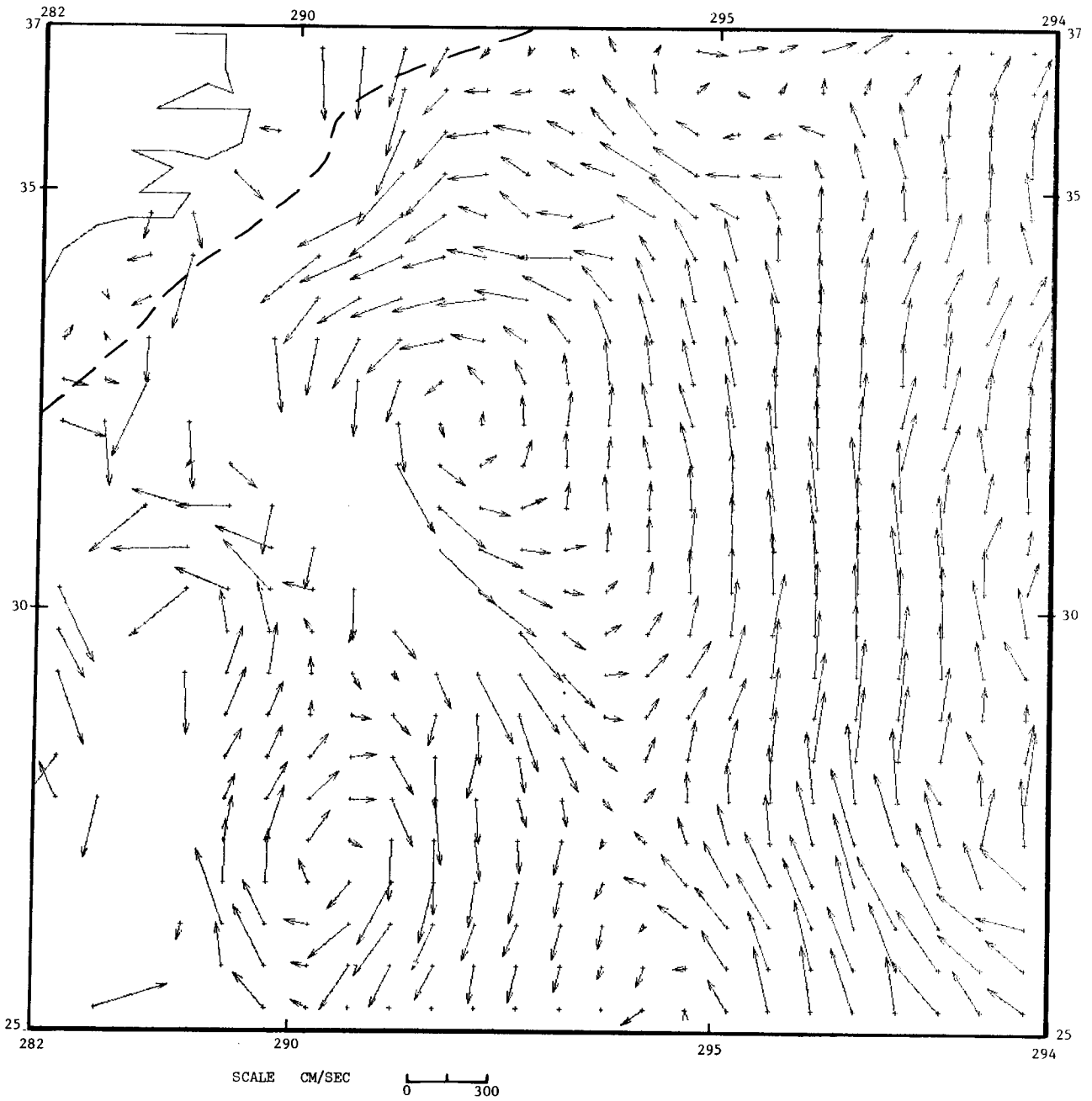


Figure 6.29

accuracy of the gravity field models. Progress in synoptic ocean circulation modelling is likely to be slow until the gravity field models have been improved by at least an order of magnitude, hopefully to 3 parts in 10^9 . Attempts should be made when using GEOS-3 and SEASAT data for circulation studies, to incorporate the existing oceanographic information on the density field of the oceans, as a constraint in linking the two data types to obtain an improved knowledge of the complex circulation patterns. Preliminary ideas on this problem have been given in Wunsch and Gaposchkin (1980).

The results presented here are a first attempt at estimating the geostrophic component of the sea surface current from satellite altimetry data, and demonstrate that possibilities do exist for using altimeter data for definitive ocean circulation studies. The solutions reported above give limited information on the general circulation patterns associated with the Northwestern Atlantic circulation (Worthington 1976) and the eddy dynamics. But it has been shown that the Gulf Stream region is defined with certainty. Much more work remains to be done on the recovery of oceanographic information from satellite altimetry under adverse signal to noise conditions but the potential of utilising these data for synoptic regional oceanography in the near future is a viable proposition.

7. ON THE RECOVERY OF OCEAN TIDE MODELS.

7.1. Ocean Tides.

7.1.1. Introduction.

Until recently, the majority of ocean tide studies have been essentially confined to coastal waters and continental shelf areas. Traditionally, the ocean tide measurements are made at tide gauge sites where these sites are typically located at the mouths of harbours or rivers. It has been noted by Hendershott & Munk (1970) that at various tide gauge locations, anomalous results may arise in the phase and amplitude of the tides due to coastal features dissipating the tides. Thus, the coastal tides that reach amplitudes of more than 5 m are very much influenced by local effects and are not characteristic of the global ocean tide. There are two main factors producing the amplification of the tidal range in the above cases (Fairbridge 1966). Firstly, in shallow water the tidal range rises approximately inversely to the fourth root of the water depth and the square root of the width of the water mass. Secondly, resonance occurs when the free period of the water mass approaches the period of the tide. Thus coastal tide gauge sites give very limited information about the behaviour of the tides in the ocean.

Tide gauge sites at island stations, particularly those on islands that rise up steeply from the ocean floor, give the most unperturbed tidal signal. These records generally show that the ocean tide has an amplitude of the order of 1-2 m. However, due to the limited availability of adequate tide gauge sites, global tidal models cannot be established with any confidence from these measurements alone. Traditionally, the procedure has been to resort to theory for estimating the tides. This technique for tidal modelling is described in Section 7.2 .

The introduction of deep sea tide gauges has done much to alleviate some of the problems mentioned above. These instruments are sensitive to pressure/temperature fluctuations and with in-built recording devices, they can be placed at various locations on the ocean floor and later the data are recovered by acoustic commands from surface

vessels. Basic improvement in the knowledge of regional ocean tides has resulted, as reported in Munk et al. (1970), Filloux (1971), Collar & Cartwright (1972), Luther & Wunsch (1975) and Cartwright et al. (1980) but the distribution obtained is not yet adequate for global tide models.

With the development of NASA'S EODAP program, there is now a need for precise tide predictions on a global scale, as ocean tides represent fluctuating loads on the solid Earth causing tilting of the Earth's crust and disturbances of the Earth's stress and gravity fields. An accurate knowledge of these loads would permit determination of hydrodynamic parameters of the oceans and elastic parameters of the solid Earth. More importantly, in relation to the development of satellite altimetry applications to ocean dynamics, the accurate modelling of the dominant ocean tide components would permit the elimination of this signal, which is present in both the orbit integration procedures and the altimeter ranges themselves. Removing the tidal signal would enable a more complete understanding of the parameters of interest. Similarly, interactions between ocean tides and the atmosphere, which play a vital role in the air/sea interface exchanges and ocean circulation modelling, may be quantified at a higher resolution.

Tidal undulations of the sea surface reach amplitudes of more than 100 cm in the open oceans and generally about 200 cm in coastal waters. Thus, ocean tides need to be determined with an accuracy compatible with the desired geoid accuracy (ie. ± 10 cm) in order to provide effective corrections for altimeter measurements. It should also be noted that the altimeter detects the geocentric tide, being the sum of the oceanic tide, the body tide and the loading tide of the solid Earth. This chapter looks at the possibilities of utilising satellite altimetry data for the determination of open ocean tides, both on a regional and a global basis. Preliminary sections deal with the development of tidal theory and present day representation of the ocean tide models from the solution of Laplace's tidal equations (LTE's). The later sections set out the details of the application of GEOS-3 altimeter measurements to the recovery of ocean tidal constituents.

A basic assumption made in this development is that the effect that the ocean tides may have on the orbits of artificial Earth satellites has been modelled adequately via the Love numbers k and k' (Munk & MacDonald 1960) in the orbit integration procedure, or that the

error is below the noise level of the altimeter data - ie. at the 20 cm level. It was pointed out in Lambeck et al. (1974) that the ocean tides measurably distort the gravitational potential field of the Earth, and that the satellite orbits are sensitive to not only the body tide in the solid Earth, but also the gravitational attraction of the fluid tide in the oceans. Numerous solutions of ocean tide parameters from satellite orbit analyses have been published in recent years; Cazenave et al. (1977), Cazenave & Daillet (1977), Goad & Douglas (1977), and Felsentreger et al. (1978) to mention a few. A recent review of results has been given by Felsentreger et al. (1979). However, in this chapter only the altimeter measurements are assumed to contain any information on the ocean tides and other oceanographic signals such as the dynamic height.

7.1.2. Tidal Potential.

Celestial bodies exert a gravitational force on the Earth. At any point within or on the surface of the Earth, the gravitational force can be divided into two components: a force equal to the gravitational force acting at the centre of mass of the Earth (geocentre), and the remaining deforming force.

Using the law of universal attraction, the magnitude of the tidal acceleration, U_T at a point P is

$$U_T(P) = GM_B \left(\frac{1}{(\rho_B - r_P)^2} - \frac{1}{\rho_B^2} \right) \quad (7.1)$$

where M_B is the mass of the tide producing body, B

G is the gravitational constant,

ρ_B is the distance from the geocentre to the body, B

and r_P is the distance from the geocentre to the point, P.

The tidal potential is evaluated as the difference between the potential of the total force and the potential of the force exerted at the centre of mass. Thus, the attractive potential due to the tide producing body at P is (see Figure 7.1).

$$W_B(P) = \frac{GM_B}{\rho_P} = \frac{GM_B}{(\rho_B^2 + r_P^2 - 2\rho_B r_P \cos \psi_B)^{1/2}} \quad (7.2)$$

where the geocentric angle between the position vectors ρ_P and ρ_B is given by

$$\cos \psi_B = \frac{r_P \cdot \rho_B}{r_P \rho_B} \quad (7.3)$$

With equation 7.3, the potential at equation 7.2 can be expressed by Legendre polynomials, to degree n as

$$W_B(P) = \frac{GM_B}{\rho_B} \sum_{n=0}^{\infty} \left| \frac{r_P}{\rho_B} \right|^n P_n(\cos \psi_B) \quad (7.4)$$

The potential exerted at the geocentre can be written as

$$\begin{aligned} V_B(P) &= \frac{GM_B}{\rho_B} + \frac{GM_B}{\rho_B} \frac{r_P}{\rho_B} \cos \psi_B \\ &= \frac{GM_B}{\rho_B} \sum_{n=0}^1 \left| \frac{r_P}{\rho_B} \right|^n P_n(\cos \psi_B) \end{aligned} \quad (7.5)$$

Thus the tidal potential of the tide producing body is

$$\begin{aligned} U_B(P) &= W_B(P) - V_B(P) \\ &= \frac{GM_B}{\rho_B} \sum_{n=2}^{\infty} \left| \frac{r_P}{\rho_B} \right|^n P_n(\cos \psi_B) [1 + O\{10^{-2}\}] \end{aligned} \quad (7.6)$$

As the term (r_P/ρ_B) is of the order 2×10^{-2} for the Earth-Moon system, the $(n+1)$ th term in equation 7.6 is 0.02 times smaller than the n -th term. Hence, to about 1%, the tidal potential is usually written as

$$U_B(P) = \frac{GM_B}{\rho_B} \left| \frac{r_P}{\rho_B} \right|^2 P_{20}(\cos \psi_B) \quad (7.7)$$

where the Legendre polynomial $P_{20}(\cos \psi_B) = (3 \cos^2 \psi_B - 1)/2$.

It therefore follows that under the above conditions, the tide

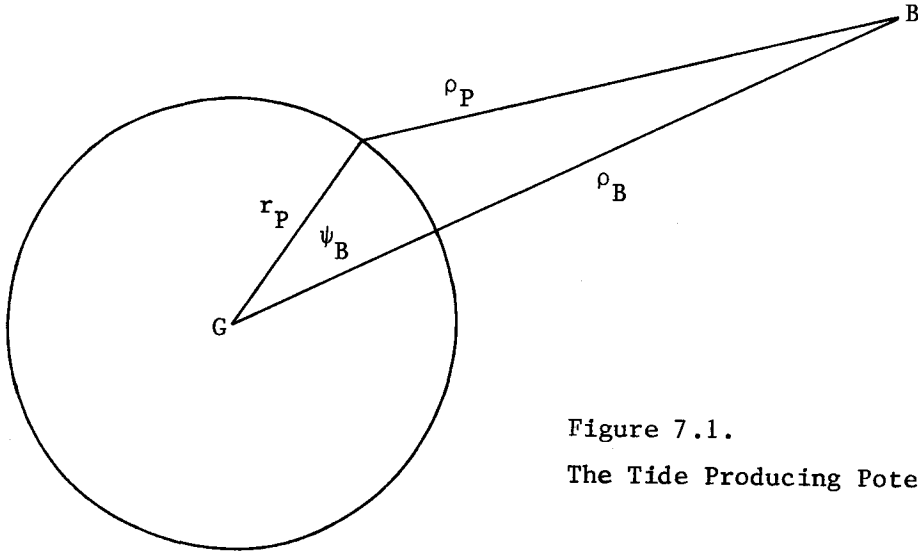


Figure 7.1.
The Tide Producing Potential

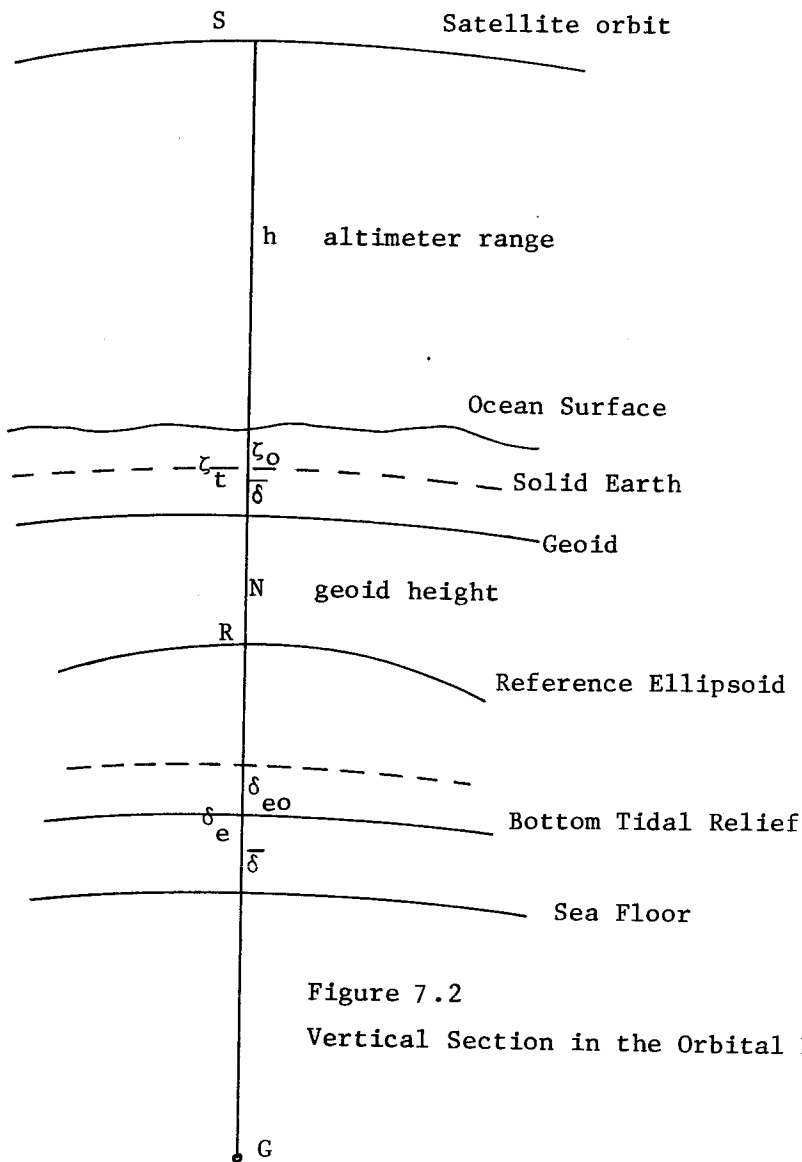


Figure 7.2
Vertical Section in the Orbital Plane

producing potential can be described by a zonal harmonic of the second degree, the pole of the harmonic lying on the line joining the geocentre to the tide producing body. In more general terms, this equation is expressed as

$$U_2 = 2 G_D \left| \frac{a_B}{\rho_B} \right|^3 \left(\cos^2 \psi_B - \frac{1}{3} \right) \quad (7.8)$$

where a_B is the semi-major axis of the disturbing body's orbit, and G_D is the Doodson constant where $G_D = 3/4 GM_B r_p^2 / a_B^3$ (for the lunar constants, $G_D = 2.627723 \text{ m s}^{-2}$).

The potential given by equation 7.8 is in terms of the local coordinate ψ_B of the perturbing body, but can be written as a function of geographic position and the position of the perturbing body using the cosine law of the spherical triangle,

$$\cos \psi_B = \sin \phi \sin \delta + \cos \phi \cos \delta \cos H \quad (7.9)$$

where ϕ is the latitude of the point of observation, P

δ is the declination of the disturbing body, and

H is the hour angle of the disturbing body,

giving equation 7.8, assuming $a_B / \rho_B \approx 1$, as

$$U_2 = G_D \left[3 \left(\sin^2 \delta - \frac{1}{3} \right) \left(\sin^2 \phi - \frac{1}{3} \right) - \sin 2\phi \sin 2\delta \cos H + \cos^2 \phi \cos^2 \delta \cos 2H \right] \quad (7.10)$$

The terms in equation 7.10 represent three types of surface spherical harmonic functions of the second order. The first, a long period term, is a zonal function and is dependent only on latitude. The second, a tesseral function, has diurnal characteristics, with amplitude being maximum at latitude $\pm 45^\circ$ when the declination of the disturbing body is maximum. The third term is maximum at the equator when the declination of the disturbing body is zero.

The summation W_B of lunar and solar potentials, called the luni-solar potential, accounts for almost all of the tide. The largest contribution from other celestial bodies comes from the planet Venus, which amounts to about $5 \times 10^{-5} W_B$. Thus, the other celestial bodies are too distant from the Earth to exert any appreciable effects (Melchior 1978).

For tidal analysis, the astronomical tide generating potential, U_B (or equilibrium tide $\bar{\zeta} = U_B/g$) is expressed as a finite series of harmonic terms with fixed maximum amplitudes and frequencies. The harmonic development is a function of six independent variables, which are linear with time. These variables are :

- τ the mean lunar time,
- s the mean longitude of the Moon,
- h the mean longitude of the Sun,
- p the longitude of the lunar perigee,
- N the longitude of the ascending node of the Moon,
- p_S the longitude of perihelion,

and a combination of these variables can define solar time t , and sidereal time θ .

Decomposed into a series of harmonic partial tides, the equilibrium tide is represented as

$$\bar{\zeta} = \sum_{\nu=0} \bar{\zeta}_{\nu}(\phi, \lambda, t) \quad (7.11)$$

with the following three major species of harmonic partial tides:

(i) Long Period ($\nu=0$)

$$\bar{\zeta} = \frac{1}{2} G_D (3\sin^2\phi - 1) A \cos(\sigma t + \alpha) \quad (7.12)$$

(ii) Diurnal ($\nu=1$)

$$\bar{\zeta} = G_D (\sin 2\phi) A \sin(\sigma t + \alpha + \lambda) \quad (7.13)$$

(iii) Semi-diurnal ($\nu=2$)

$$\bar{\zeta} = G_D (\cos^2\phi) A \cos(\sigma t + \alpha + 2\lambda) \quad (7.14)$$

In these equations, the following notations are used:

- σ frequency of partial equilibrium tide (Table 7.1)
- t universal time, hours
- α astronomical argument of partial equilibrium tide (Table 7.1)
- λ longitude east
- ϕ latitude
- A amplitude factor (Table 7.1)
- G_D Doodson constant
- $\bar{\zeta}$ total or partial equilibrium tide.

A summary for the major tidal waves, taken from Melchior (1973), is given in Table 7.1 .

Every harmonic component of the equilibrium tide (equations 7.12, 7.13 and 7.14) generates, through the ocean's response, a similar oceanic partial tide,

$$\zeta_o = \xi(\phi, \lambda) \cos(\sigma t + \alpha - \chi(\phi, \lambda)) \quad (7.15)$$

of identical frequency σ but differing amplitude $\xi(\phi, \lambda)$ and phase $\chi(\phi, \lambda)$.

Assuming a rigid Earth, the potential Γ of all tide producing forces is given by the astronomical contribution, U_B (equation 7.6). But as stressed in Farrell (1972a, 1972b, 1973), accurate global tidal models must also account for the mutual disturbances exerted by the solid Earth tide on the oceanic tide and vice versa. Consequently, the primary astronomical tide generating potential must be extended to include the two major additional terms representing the yielding of the solid Earth to the direct action of U_B and the yield of the solid Earth to the weight of the overlying ocean tidal column.

The additional potential contributions arising from the yielding of the solid Earth and of the fluid ocean can be decomposed into spherical harmonics, typically denoting the n -th spherical partial potential of U_B as U_{Bn} . The responses of the solid Earth and oceans have been conventionally expressed in terms of the Love numbers k_n, h_n (non-loading) and k'_n, h'_n (loading) of order n , defined by Munk & MacDonald (1960) .

The solid Earth responds to a non-loading potential U_{Bn} by an uplift $h_n U_{Bn}/g$ and to the additional gravitational potential $k_n U_{Bn}$ of U_{Bn} , arising from this redistribution of mass. The n -th degree spherical harmonic constituent (ζ_{on}) of ζ_o gives rise to the ocean self-attraction potential $W_n = g \alpha_n \zeta_{on}$ where $\alpha_n = [3/(2n+1)](\rho_w/\rho_e)$ with ρ_w being the density of sea water and ρ_e being the mean density of the Earth. The surface load $g \rho_w \zeta_{on}$ of the oceanic tidal column at the surface of the solid Earth gives a solid Earth deformation $h'_n W_n/g$. This geocentric displacement defines a redistribution of mass giving an additive augmentation $k'_n W_n$ of the potential W_n due to the surface load.

The n -th spherical harmonic component of the total tide

TABLE 7.1. Principal Tidal Waves

Tidal Symbol	Argument (α)	Frequency (σ) degrees/hour	Amplitude Factor (A)	Origin (L,lunar;S,solar)
Diurnal components				
O_1	$\tau-s$	13.943 036	+0.376 89	L, principal wave
P_1	$\tau-h$	14.958 931	+0.175 54	S, principal wave
S_1	$t-ps$	15.000 002	-0.004 23	S, elliptic wave of S_{K_1}
$^m K_1$	$\tau+s$	15.041 069	-0.362 33	L, declinational wave
$^s K_1$	$t+h$	15.041 069	-0.168 17	S, declinational wave
Semi-diurnal components				
$2N_2$	$2\tau-2s+2p$	27.895 355	+0.023 01	L, elliptic wave of M_2
N_2	$2\tau-s+p$	28.439 730	+0.173 87	L, major elliptic wave of M_2
M_2	2τ	28.984 104	+0.908 12	L, principal wave
S_2	$2t$	30.000 000	+0.422 86	S, principal wave
$^m K_2$	$2\tau+2s$	30.082 137	+0.078 58	L, declinational wave
$^s K_2$	$2t+2h$	30.082 137	+0.036 48	S, declinational wave
Long period components				
M_0	0	0.000 000	+0.504 58	L, constant flattening
S_0	0	0.000 000	+0.234 11	S, constant flattening
S_a	$h-ps$	0.041 067	+0.011 76	S, elliptic wave
Mm	$s-p$	0.544 375	+0.082 54	L, elliptic wave

generating potential can now be defined as

$$\Gamma_n = (1+k_n)U_{Bn} + \sum_n (1+k'_n)W_n \quad (7.16)$$

while that of the geocentric Earth tide (displacement of the sea floor) is given by

$$\bar{\delta}_n = h_n U_{Bn}/g + \sum_n h'_n \alpha_n \zeta_{on} \quad (7.17)$$

Equations 7.16 and 7.17 define, in spherical harmonic components, the total tide generating potential and solid Earth tide in terms of the astronomical potential and the observed ocean tide ζ_o , where

$$\zeta_o = \zeta_t - \bar{\delta} \quad (7.18)$$

and ζ_t is the geocentric ocean tide derived from satellite altimetry measurements.

Predicting the response of the oceans to the tide generating forces is obtained by the integration of Newton's dynamical equations, and approximated by solving the Laplace Tidal Equations (LTE's). Modelling of ocean tides via solutions of the LTE's is discussed in the next section.

7.2. Modelling of Ocean Tides.

7.2.1. Laplace Tidal Equations.

The LTE's, including the total tide generating potential (equation 7.16) and bottom friction relations, may be written as (Zahel 1973) :

$$\frac{\partial u}{\partial t} - (2\Omega \sin \phi)v = \frac{-g}{a \cos \phi} \frac{\partial}{\partial \lambda} (\zeta_t - \Gamma/g) + F_\lambda / (\rho_w D) \quad (7.19)$$

$$\frac{\partial v}{\partial t} + (2\Omega \sin \phi)u = -\frac{g}{a} \frac{\partial}{\partial \phi} (\zeta_t - \Gamma/g) + F_\phi / (\rho_w D) \quad (7.20)$$

$$\frac{\partial \zeta_t}{\partial t} - \frac{\partial \bar{\delta}}{\partial t} + \frac{1}{a \cos \phi} \left(\frac{\partial}{\partial \lambda} (uD) + \frac{\partial}{\partial \phi} (vD \cos \phi) \right) = 0 \quad (7.21)$$

where (ϕ, λ) are latitude and longitude, and (u, v) are the eastward and northward components of the fluid velocity. The mean spherical radius of the Earth is denoted by a , Ω is the Earth's angular rate of rotation, and g is the acceleration of gravity at the surface of the spherical Earth. F_λ and F_ϕ are the meridional and zonal components of the bottom stress and $D(\phi, \lambda)$ is the undisturbed ocean depth. All other quantities have been defined in the previous sections.

Equations 7.19 and 7.20 are derived from the Navier-Stokes equations of momentum conservation, assuming an homogeneous fluid in a hydrostatic pressure field. The equations also neglect all dissipative terms, non-linear terms, variations in gravity g and in the geocentric radius of fluid particles. The third equation (7.21) is a conservation equation for an incompressible, homogeneous fluid, obtained by integrating the conditions of continuity and mass conservation from the sea floor to the ocean surface.

The LTE's are integro-differential equations, as seen above, and are quite complex to solve. Hendershott (1972) published the first solutions including the effects of solid Earth yielding and ocean self-attraction. More recently, Miles (1974) investigated the limiting approximations made in deriving the LTE's. Comprehensive reviews of ocean tides and the nature of solutions of the LTE's have been given in Pekeris & Accad (1969), Hendershott & Munk (1970), Hendershott (1973), Cartwright (1977), Zahel (1978) and Schwiderski (1979a, 1979b).

The latest numerical, global ocean tide models (Estes (1977), Zahel (1978, 1980), Accad & Pekeris (1978), Parke & Hendershott (1980), and Schwiderski (1980)) show some consistent agreement for the M2 tidal constituent, taking into account the differing solution techniques. There are essentially two approaches for obtaining a solution - a formal solution of the LTE's or a solution in which the LTE's are used as an

interpolation device. The latter solution will include loading effects implicitly. It has been claimed that present global tide models are accurate to ± 10 cm (Schwiderski 1980). However, there are still unexplained discrepancies between the models and the physical ocean responses. The application of satellite altimetry data to solutions of ocean tide models may be beneficial for filling in the present gaps in knowledge.

7.2.2. Satellite Altimetry Applications.

To date, ocean tide models have been produced using the procedures outlined in previous sections. With the launching of the GEOS-3 satellite in April 1975, the possibility of using satellite altimetry measurements for recovering ocean tidal information was realised. Prior simulation studies (Zetler & Maul 1971) had confirmed the likelihood of satellite-derived ocean tide models. A more detailed discussion of this study and other simulation studies is given in sub-section 7.3.1.

The geocentric ocean tide, ζ_t is the observable quantity obtained from satellite altimetry measurements, as illustrated in Figure 7.2, where conceptually

$$\zeta_t = SG - h - N - RG \quad (7.22)$$

Here SG is the geocentric distance of the satellite orbit obtained from the computed ephemeris,

h is the measured altimeter range,

N is the geoid height in relation to a specified reference ellipsoid, and

RG is the radial distance to the reference ellipsoid.

The total tide generating potential at the mean sea surface is given in equation 7.16. At satellite altitudes, the orbit is perturbed by both the solid Earth and ocean potentials, $k_n U_n + \sum_n (1+k'_n) W_n$. As mentioned in sub-section 7.1.1, the combined effect of these potentials has been assumed to be adequately modelled in the orbit integration procedure. Thus, consideration is only given to those corrections, at the surface of measurement, embodied in equation 7.17. These secondary tide generating forces are the solid Earth tide $\delta_e (= h_n U_{Bn}/g)$ and the ocean load response, $\delta_{eo} (= \sum_n h'_n \alpha_n \zeta_{on})$ and considering a simple second

order Love number approximation, these responses may be written as

$$\delta_e(\phi, \lambda, t) = \frac{h_2 U_2}{g} \approx 0.612 U_2 \quad (7.23)$$

$$\delta_{eo}(\phi, \lambda, t) = h_2' \alpha_2 \zeta_o \approx -0.108 \zeta_o \quad (7.24)$$

As an order of magnitude estimate for δ_{eo} , a mean amplitude of 40 cm from the Mofjeld model in the Sargasso Sea area (see sub-section 7.3.5) was adopted for ζ_o , giving an estimate for the yielding of the solid Earth in response to the oceanic tidal load of about 4 cm. It was considered that corrections of this magnitude would be neglected in the calculation of the ocean tide models, being an order of magnitude below the noise level of the altimeter data.

Hence, only the solid Earth tide correction (equation 7.23) was calculated at each satellite groundtrack point to correct the geocentric ocean tide measurement according to equation 7.18. In the ocean tide model solutions listed in Table 7.3, not all cases had the solid Earth tide correction applied. This was only because of practical problems of computer time limitations. The next section sets out the procedures for satellite-derived regional, ocean tide models.

7.3. Recovery of Regional Ocean Tide Models.

7.3.1. Preamble.

GEOS-3 radar altimeter measurements for the period May 1975 to May 1976 were analysed in an attempt to obtain a representation of regional ocean tide models in the Sargasso Sea area (in the same location as the ocean dynamic/eddy study of Section 6.4, see Figure 6.12). Two different techniques were investigated for the determination of the tidal signal. Firstly, functional analysis techniques were applied to the altimeter SSH data and to SSH differences at crossover points. This analysis technique had a twofold objective in that the results of the functional analysis were also investigated with the view to eliminating any inherent errors in the derived SSH data caused by systematic orbital errors. A detailed description of this analysis is given in Masters et al. (1979, Section 3) and only a brief summary of the results is given in sub-section 7.3.3 for completeness.

Modelling of the ocean tide in a regional area was also attempted using two-dimensional Fourier solutions on both altimeter profiles and overlapping passes of altimeter data. The altimeter data contains variations due to altimeter errors as well as the desired oceanographic signals (tidal and dynamic height), the problem being the separation of the latter information. The altimeter derived SSH data also contains geoidal model and orbital uncertainties.

Early work by Zetler & Maul (1971) showed that it was possible to retrieve the most dominant tidal constituents (M2 and K2) for both amplitude and phase from simulated satellite altimeter measurements, in the presence of signal-to-noise ratios of up to 1 : 4. They considered, however, only random white noise effects of the altimeter measurements in the recovery of the tidal constituent, and also made the assumption that the tidal height at a given time would be uniform over a 1°-5° area. Simulation studies in the Coral Sea area, off the east coast of Australia, were attempted by Bretreger (1976) using similar procedures to that of Zetler and Maul. Bretreger concluded that the successful recovery of tidal signals was dependent upon the amplitude of the tidal constituent and the resulting signal-to-noise ratio. Over a 5°x 5° area in the Coral Sea, with 40 observations spanning 3 months, only the M2 constituent could be recovered at the 80% reliability level tolerating noise levels of up to 100 cm (equivalent to the M2 amplitude for the area using Zahel's empirical model (Kuznetsov 1972)).

Won et al. (1978) investigated the simultaneous recovery of the geoid and ocean tides in a simulation study in the northeastern Pacific Ocean. Their studies revealed that the four major tides M2, O1, K1 and S2 could be recovered on a regional scale (50° in latitude by 70° in longitude), together with a geoid rigorously corrected for dynamic tides, with random noise levels of up to ± 100 cm in the altimeter data. A suggestion made from their results was that for the separation of the tidal constituents it would be necessary to have an altimeter data span of at least 1 year, consisting of approximately 100-200 altimeter passes distributed uniformly in both space and time. An important point made in their study was the constraining of the ocean tide solution by ocean bottom and/or island tide gauge measurements - this has the effect of directly linking the solution, although somewhat weakly, to conventional tide models derived from empirical relations such as the LTE's (See Section 7.2). Won et al. also pointed out the possible significance of the ocean and solid Earth tide interaction. However, the treatment

adopted by Won et al. for removing the systematic orbit error will also remove part of the spectrum of the tidal signal as pointed out in Mather et al. (1978a). In using low order polynomials to eliminate orbital errors, all long wavelength tidal information with wavelengths equivalent to the orbital periods or wavelengths greater than twice the length of the altimeter pass will be lost. This fact has also been pointed out in Douglas & Goad (1978) and Douglas (1979) where it was shown that in the GEOS-3 calibration area, it is impossible to remove orbit error with a tilt correction applied to the altimeter profiles and yet still retain the dominant tidal signatures.

It is apparent from the results of the investigations mentioned above that random, high-frequency measurement error can be tolerated even when the error amplitude is equivalent to or exceeds the tidal signal. The dominant error source in the successful recovery of ocean tide constituents comes from the systematic, orbital error as any radial error in the satellite orbit enters directly into the SSH data used in the tidal analysis, i.e. the orbital bias error will be aliased into any tidal spectrum. The orbital bias error can best be gauged by studying the discrepancies at crossover points as the error is a function of the tracking complement and geopotential model used in the orbit integration. Further consideration of this problem is given in sub-section 7.3.3.

Recently, GEOS-3 altimeter data have been used in an attempt to obtain ocean tidal models on a regional basis at various locations in the world's oceans. To date, the studies have proved unsuccessful. Maul & Yanaway (1978), Bretreger (1979) and Won & Miller (1979) have attempted a recovery of the tidal signal in the GEOS-3 calibration area in the Sargasso Sea, while Ku (1978) used an area in the Gulf of Alaska.

Maul & Yanaway (1978) analysed altimeter data, averaged over a $5^\circ \times 5^\circ$ area, for an observation period of 18 months. It was found that the signal-to-noise ratio of the data was about 0.1, and that only one observation every four days was available in the 5° square. The assumptions made in their study were that the oceanic tide was considered as the temporal variability of the SSH in an area for the relevant tidal frequencies but the perturbations in the SSH data due to wind waves, swell, quasi-geostrophic currents and eddies, steric effects and orbital errors were considered to be noise. The dominant error neglected by these assumptions would come from systematic orbital errors. The other effects averaged over the $5^\circ \times 5^\circ$ square size in this

region are estimated to contribute a variability of about ± 15 cm.

The results of their research showed that the GEOS-3 data, in the form of global and intensive mode altimetry, could not yield any realistic ocean tide information. The analysis technique used consisted of solving for the tidal signal in an $n^\circ \times n^\circ$ square using equations similar to equation 7.31, with square sizes varying from 1° to 5° . All altimeter measurements within the $n^\circ \times n^\circ$ area were averaged and the resulting averaged value was considered as a measure of the SSH. Thus, each averaged SSH value includes errors due to variations in the tides, geoid slope, and Earth tide effects. In comparing the altimeter-derived tidal constituents with the known tidal constituents from Zetler et al. (1975), Maul and Yanaway have neglected to take into account the effects of the solid Earth tide and oceanic tidal load response. These corrections are required as the tidal constituents derived from altimeter measurements are with respect to a geocentric frame of reference and not the oceanic crust, as implied by the direct comparison of the two results above.

The analyses performed by Bretreger (1979) were based on the use of equation 7.32. The modelling of the regional sea surface was completed using the procedure adopted by Mather et al. (1977b) in which biases and tilts are applied to passes of altimetry data using equations of the form:

$$\zeta = \zeta_{ij} + b_i + c_i(t_{ij} - t_{i1}) \quad (7.25)$$

where ζ_{ij} is the estimate of the SSH from the j -th element of the i -th pass, b_i the bias for the i -th pass, c_i a tilt applied to the i -th pass, t_{ij} and t_{i1} being the times of the j -th and first elements in the i -th pass.

The basis of the analysis is that when two passes intersect at a crossover point, the difference between the two SSH values should contain the tidal information. A crossover point was defined as any two passes intersecting within a $0.2^\circ \times 0.2^\circ$ area. A full description of this adjustment procedure is given in sub-section 6.2.2. Geoid variations within such an area should not significantly affect the analysis since, as pointed out in Mather et al. (1978a), the geoid variations over 0.2° squares in the region studied should not materially mask features in the sea surface with amplitudes greater than ± 25 cm and wavelengths in excess of 40 km.

The study by Bretreger (1979) used 282 passes of altimeter data in a $12^\circ \times 12^\circ$ area, defined by latitude 25°N and longitude 282°E at the southwest corner of the block. The results proved unsuccessful due to the high levels of systematic noise and geometric instabilities introduced by the absence of very long passes of continuous data in the regional sea surface model solution. Theoretical investigations in this study showed that only a small number of Fourier coefficients were required to successfully reproduce the theoretical tidal model in the Sargasso area. The proposed analysis technique could have tolerated a signal-to-noise ratio of 1 : 10, if the noise exhibited a random nature, but only one quarter of this ratio if the noise showed a limited systematic pattern over a given pass length. The solid Earth tide effect was considered negligible, being of the order 5 cm.

Won & Miller (1979) performed an analysis using two narrow strips of altimeter data in the Sargasso Sea, with each strip containing over 25 groundtracks of altimeter data. Profiles for four ocean tide signals were attempted along the two strips based on solutions using fifth-, sixth-, seventh- and eighth-order Chebychev polynomial approximations to the residual altimeter data. Uncertainties caused by the linear orbital bias error proved too large, and the resultant tidal amplitudes and phases gave poor agreement with the MODE deep-sea gauge data in their test area. Corrections for the solid Earth and ocean loading responses should be applied either to the altimeter-derived results or in the opposite sense to the MODE data for valid comparisons to be made.

The latest attempts at ocean tidal model recovery using satellite altimetry data are reported in Brown & Hutchinson (1980), Parke (1980) and Diamante & Nee (1980).

The aim of this section is to develop a tidal analysis technique capable of overcoming the problems of orbital errors aliasing the tidal signal which have been encountered by other investigators. The following sub-section deals with the compilation of the altimetry data sets used in this analysis and the evaluation of orbital errors in the GEOS-3 data bank is discussed in sub-section 7.3.3. The techniques used to recover the ocean tidal signals are outlined in sub-section 7.3.4.

7.3.2. Altimeter Data Sets.

The short pulse (intensive) mode, GEOS-3 altimeter data base available for the analysis covered the period May 1975 to May 1976.

NASA's Wallops Flight Center (WFC) provided the raw GEOS-3 altimeter data, the intensive mode data consisting of 10 or 100 points/sec measurements grouped into variable length (2-3 sec) frames. These data were smoothed over a frame using a quadratic polynomial to provide the approximate 1 point/sec data used in this analysis. Stringent criteria were enforced to exclude the 1% of noisy data encountered in the processing of GEOS-3 data. There is no difficulty in identifying the faulty records. From this data base, three data sets were produced to study the problem of ocean tide model recovery. These global data sets were then sorted into the region of interest, the Sargasso Sea area, for the regional tidal analysis.

7.3.2.1. GEOS-3 Altimetry Data Base - LAS79.

The altimetry data set (LAS79) was prepared by updating the 1977 GEOS-3 altimetry data set reported in Mather et al. (1978b), the latter data set referred to as the WALLOPS data set in this thesis. The orbits necessary to reduce the altimetry data to SSH's were computed using the GEM10 gravity field (Lerch et al. 1977) and all available laser tracking data (Unified S-Band where necessary) and the GEODYN orbit determination program (Martin et al. 1976). The ephemerides were derived using 5-day arcs to estimate state vectors in true of date, inertial Cartesian coordinates at epoch, referenced to the laser tracking station configuration shown in Masters et al. (1979, Figure 1). The 1975 altimetry data were computed at Goddard Space Flight Center and the remaining 1976 data were computed at the University of New South Wales. The orbits give an rms fit to the laser data of about ± 1 m (Lerch et al. 1978b).

The LAS79 data base should have a number of advantages for oceanographic studies over the previous WALLOPS data. Crossover statistics (Masters et al. 1979) and the results of altimeter analysis in the Sargasso Sea (Coleman 1980) suggest that the laser orbits show more internal consistency and give an improvement of approximately a factor of 2 in accuracy. Thus the nature of systematic errors which could affect the recovery of the oceanographic signal may be more apparent.

A number of regional sub-sets were selected from this global data base and are set out below:

- (i) SARG - all altimetry data available in a $12^\circ \times 12^\circ$ block with

- coordinates at the southwest corner of the block of 25°N, 282°E. A total complement of 183 passes were available made up of 99 south-to-north passes and 84 north-to-south, giving a total of 21,676 observation points in this area.
- (ii) FIVSARG - all altimetry data available in a 5°x 5° block with coordinates at the southwest corner of the block of 27°N, 287°E. A total complement of 82 passes were available made up of 42 south-to-north passes and 40 north-to-south passes, giving 4,018 observation points in this area.
- (iii) SARGNS and SARGSN - a split up of the SARG data set into only descending (NS) or ascending (SN) passes.
- (iv) FIVNS and FIVSN - a split up of the FIVSARG data set into only descending or ascending passes.

7.3.2.2. Crossover Data Base - CROSSOVER

The discrepancy between the two estimates of SSH at a crossover point should give information on orbital errors and other time varying features such as tides and currents. The technique used to create the CROSSOVER data base initially involved finding the locations of the intersection points of the descending and ascending passes of GEOS-3 altimetry. Using data extending to 0.2° on either side of the crossover point, a quadratic interpolation was used to obtain the precise time, latitude and longitude of the crossover point. Similarly, values of SSH at the crossover point were evaluated yielding a data set consisting of time, latitude and longitude of the crossover point and the altimeter derived SSH values from the ascending and descending passes.

CROSSOVER data sets were produced using both the WALLOPS and the LAS79 altimetry data sets. In total, 52,333 global crossover points were obtained in the WALLOPS CROSSOVER data set and their distribution is shown in Figure 7.3. Note the high density of crossover points in the tidal model recovery area off the east coast of the United States.

Statistics on the CROSSOVER data sets are given in Table 7.2, taken from Masters et al. (1979). The variance of the data is, for laser orbits with a 10 m cutoff criterion, approximately 6.8 m². This figure compares favourably with a variance of 4.00 m², produced by Lerch et al. (1978b) from a similar data set, in which more stringent preprocessing criterion were applied to the altimetry data. In the

Wallops Global CROSSOVER Data Set

1975 - 1976

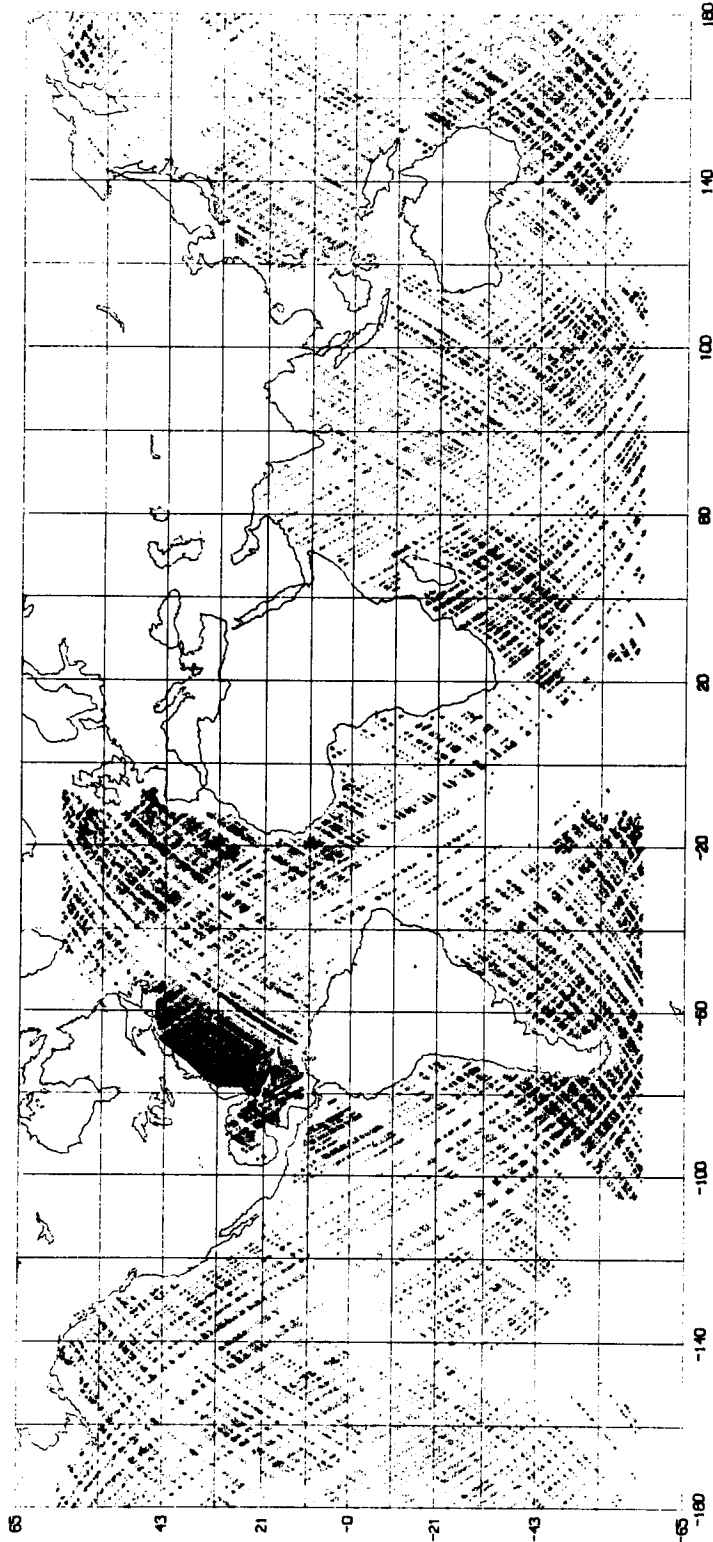


Figure 7.3

northwest Atlantic area chosen for the ocean tide model study, the variance of the LAS79 data is of the order 3.2 m^2 , again using a 10 m cutoff and removing a zero degree bias term.

TABLE 7.2. Crossover Data Bank Statistics.

Cutoff Discrepancy (m)	WALLOPS Crossovers		LAS79 Crossovers	
	Number of Observations	rms (m)	Number of Observations	rms (m)
∞	52333	43	21747	3.6
30	50323	5.6	21744	3.1
20	49772	4.9	21721	3.0
10	46727	3.8	21460	2.6
5	37530	2.4		

7.3.2.3. Overlap Data Base - OVERLAP

The orbital period of the GEOS-3 satellite is approximately 101.79 minutes. The condition for a repeated groundtrack (or overlapping pass) after n revolutions is given by

$$\sum_{i=1}^n (\dot{\Omega}_i t_i - \Omega_i t_i) = 0 \quad (7.26)$$

on suppressing multiples of 2π in the second term, Ω_i is the angular velocity of rotation of the Earth during the i -th revolution of GEOS-3 which is completed in time t_i , and $\dot{\Omega}_i$ is the instantaneous rate of precession of the orbital node. This condition is nearly satisfied every 526 revolutions. The observed drift in longitude ($\delta\lambda$), from an exact repeating groundtrack as a function of time is given in Figure 6.1. Using the multiple of 526 revolutions as a criterion, 189 passes

of GEOS-3, short-pulse mode altimetry were selected in the northwest Atlantic area. Details of the 189 passes are given in Table 6.3.

7.3.3. Problems To Be Considered For Ocean Tide Model Recovery.

7.3.3.1. Introduction.

As outlined above, the dominant error source affecting the recovery of tidal information will be the systematic orbital errors, due mostly to errors in the geopotential model, atmospheric drag and solar radiation pressure models used in the integration of the orbit force functions. The errors from these dynamic models account for about 70% of the total accuracy limitation for precise orbit determination. The procedure used by numerous investigators to filter out long wavelength orbital errors from the altimetry data banks has been to solve for a bias and tilt per pass, where an altimetry pass could extend in length up to 9000 km. Analysis of overlapping passes (Coleman & Mather 1978; Mather et al. 1978a) shows that the altimeter is internally consistent at the ± 20 -30 cm level. However techniques such as this are not valid for tidal model recovery as it has been previously shown that part of the tidal signal is eliminated using these procedures.

Douglas & Gaborski (1979) analysed 17 overlapping pairs of GEOS-3 altimeter profiles in the calibration area and concluded that at the scale of GEOS-3 altimeter pass lengths, the orbit error has negligible power beyond a bias and tilt correction. Anderle & Hoskin (1977), in a simulation study, demonstrated the possible existence of an additional ephemeris error that was a function of geographical position - the orbit errors being correlated over distances of about 500 km normal to the direction of the satellite groundtrack. Such errors would not be apparent in crossover data or overlapping pass information and only detailed surface truth data could resolve the ambiguities of position dependent, systematic orbital errors. Hopefully, these errors will be of longer wavelength than the tidal signal as at the present stage there is no way of correcting for this error. This assumption should be reasonably valid over regional extents.

Anderle et al. (1976) suggested that, to properly analyse orbit errors using crossover differences, the SSH discrepancies should be weighted according to the relative accuracy of the orbit of each

intersecting profile. The orbits produced for this analysis (see sub-section 7.3.2) ~~have all been reduced using laser ranging data and a~~ consistent set of fundamental constants, a and GM , for the GEM10 geopotential model used. There may, however, be differences in the relative accuracy of each orbit set dependent upon the tracking station configuration that was ranging during the 5-day arc period. Despite this fact, there has been no attempt to apply weighting constraints at crossover points in this study.

Under the assumption that orbital errors are highly correlated with the oceanographic signal, the recovery of this information depends significantly on whether the orbital errors can be successfully removed from the altimeter data set in the desired frequency range. In what follows, mention is made of the work in Masters et al. (1979) on GEOS-3 orbital errors.

7.3.3.2. GEOS-3 Orbital Errors.

The effects of geopotential model errors on the radial position vector were investigated using GEODYN, in the orbit generation mode (simulation), over a 1-day arc using the GEM10 geopotential model (Lerch et al. 1977) as a reference. The geopotential models GEM7 (Wagner et al. 1976), GEM9 (Lerch et al. 1977) and GEM10B (Lerch et al. 1978a) were used as test models and the radial differences in the ephemerides (between the test and reference models) were plotted as a function of time and position. The results showed a dominant 1 revolution period (102 minutes) in the radial error as a function of time. Maximum amplitudes of the radial error were of the order of ± 15 m for GEM7, ± 1.5 m for GEM9 and ± 3.5 m for GEM10B.

Plotted as a function of position, the radial error showed that ascending passes would be biased with respect to descending passes over regional areas, whereas if considered on a global basis, the mean bias between ascending and descending passes would tend to zero. Possible factors that could account for these differences would be the different tracking station complement and geopotential model used in the orbit integration of the north-south passes compared to the south-north passes.

The quality of the orbit determination can be partially assessed by looking at the rms residuals for orbit intercomparisons of laser short and long arcs. These discrepancies were of the order of ± 80 cm

(Lerch et al. 1978b). The study of the crossover discrepancies can further verify the quality of the orbits.

The propagation of the radial components of the orbital error as a function of time can be studied using equations of the form (Masters et al. 1979),

$$\Delta\zeta_{lm} + \sum_{i=1}^n \{c_i (F_i(\phi_2, \lambda_2, t_2) - F_i(\phi_1, \lambda_1, t_1))\} = v \quad (7.27)$$

where $\Delta\zeta$ is the SSH difference between the l-th and m-th pass at a crossover point, c_i are the coefficients required in the solution and F_i are functions of position and time. Various functional models have been used in solutions of equation 7.27, for both global and regional crossover data sets, in order to determine any significant features in the crossover data.

A preliminary investigation of crossover discrepancies was done by Mather et al. (1978b) to constrain the satellite ephemeris and reduce the signal-to-noise ratio. The dominant orbital periods modelled had periods of one half revolution, 1 revolution, 14 revolutions, a resonance effect with a period of approximately 4.7 days and terms to account for linear drifts with time. Analysis of the LAS79 CROSSOVER data set, using the procedures adopted in Mather et al. (1978b), revealed no significant harmonic feature with respect to time except for the expected resonance term at 4.68 days and a term at 28 days. In all, the periods of 1/2, 1, 2, 7, and 14 revolutions and 4.68 days could account for only 10% of the total variance of the crossover data.

Examination of the position dependence of the crossover differences was attempted because it had been previously found that the time dependence was insignificant. The crossover differences were block meaned on a $1^\circ \times 1^\circ$ grid and a spherical harmonic analysis to degree and order 5 was calculated. The results were inconclusive. The rms discrepancy of the crossover differences within the 1° blocks was still large (± 1.7 m) compared to the rms of the raw crossover differences on a global basis (± 2.6 m). The only conclusion that could be made from this study was that there is about 1 to 1.5 m of noise in the data which is still unaccounted for.

Analyses of regional data sets showed significant trends in the sea surface spectrum at quite arbitrary periods, which could not be interpreted as any specific phenomenon, except that the 4.68 day resonance term was more pronounced than in the global data set.

Significant features noted at periods between 1 and 2 days were probably a result of the data sampling. Due to the lack of success in determining any significant orbital trends from the crossover data sets, a method of improving the GEOS-3 data for oceanographic work would be to recompute the altimetry data bank with a more recent geopotential model. This model should aim for a resolution of 3 parts in 10^9 and include the use of altimetry data in ocean areas. Thus, any subsequent analysis of the data sets outlined in sub-section 7.3.2 can only be made assuming an unknown correlation exists between orbital errors and oceanographic features, i.e. no corrections were made to these data sets for orbital errors.

7.3.3.3. Sampling Distribution.

The GEOS-3 spacecraft traces out an $n^\circ \times n^\circ$ grid every $25/n$ days. With an orbital inclination of approximately 115° , the minimum time for a crossover to occur will depend on latitude and also on whether the crossover is derived from a north-south pass followed by a south-north pass or vice versa. The criteria for a crossover can be determined from relationships between the appropriate Keplerian orbital elements (Masters et al. 1979) as,

$$\sin(\lambda + \theta - \bar{\Omega}) = \tan\phi_c \cot i \quad (7.28)$$

where ϕ_c is the geocentric latitude
 λ is the longitude,
 θ is the Greenwich sidereal time,
 $\bar{\Omega}$ is the longitude of the ascending node, and
 i is the satellite inclination.

The above equation may be rewritten in terms of the dominant time-varying elements θ and $\bar{\Omega}$, and a solution obtained for the crossover time as a function of latitude (see Masters et al. 1979, Figure 7). A crossover for GEOS-3 will occur every 0.5 days at the equator. It is possible for 4 altimeter measurements to be taken in a $10^\circ \times 10^\circ$ square within 48 hours. For the Sargasso Sea area, the optimum spacing in time of crossovers would occur after periods of 0.4 days for a north-south pass followed by a south-north pass and 0.59 days for the opposite situation. Thus, crossovers occur at times of 0, 0.4, 0.99 and 1.39 days during a 48 hour period and then the cycle is repeated 5 days

later.

In reality, this groundtrack pattern is not reproduced but for the regional area chosen, the sampling pattern is close to optimal for the GEOS-3 altimetry data set (see Figure 6.12 for a distribution of altimetry profiles in the area). The Sargasso area contains 183 altimetry passes with approximately 1200 crossover points. These figures are in agreement with the estimates set out by Won et al. (1978), from their simulation studies, for possible tidal model recovery.

Ordinarily, geophysical phenomena such as tides with frequencies of one and two cycles per day are not readily studied by observations obtained at varying intervals of from 1/2 day to 5 days apart (see Figure 3.4). However, as the tidal frequencies are well determined from astronomical considerations, it is possible to use harmonic analysis or similar techniques to obtain solutions for the amplitude and phase of the tidal constituent. The next sub-section sets out the formulation used for tidal recovery, an approach similar to that suggested by Won et al. (1973). Studies by Zetler & Maul (1971) and Bretreger (1976, 1979) showed that the M2 ocean tide is the most likely tidal constituent to be successfully recovered given the present noise levels in the GEOS-3 altimeter data and this has been corroborated from the findings in previous sections. For these reasons, the following analysis attempts to recover only the M2 tidal constituent.

7.3.4. Method of Analysis.

The ocean tide signal, ζ_T at any point on the globe can be expressed as the sum of the numerous tidal constituents, ζ_{Ti}

$$\zeta_T = \sum_i \zeta_{Ti} \quad (7.29)$$

Any tidal constituent can be expressed as

$$\zeta_{Ti}(\phi, \lambda, t) = \zeta_{ai}(\phi, \lambda) \cos(\theta_i - \alpha_i(\phi, \lambda)) \quad (7.30)$$

where ζ_{ai} is the constituent amplitude of the i -th tidal constituent, θ_i is the time dependent argument of the i -th tidal constituent (see Melchior, 1978, p.27 for a listing of these arguments) taking into account the frequency and Greenwich epoch phase, and α_i is the phase lag

of the i -th tidal constituent at a particular epoch.

Equation 7.30 can also be expressed as

$$\begin{aligned} \zeta_{Ti}(\phi, \lambda, t) = & \zeta_{ai}(\phi, \lambda) \cos \alpha_i(\phi, \lambda) \cos \theta_i + \\ & \zeta_{ai}(\phi, \lambda) \sin \alpha_i(\phi, \lambda) \sin \theta_i \end{aligned} \quad (7.31)$$

which relates observations taken at a specific latitude and longitude, but does not take into consideration the correlation of adjacent observations. To overcome this limitation, and to allow all observations taken within a specified region to be simultaneously analysed, the above equation can be modified so that each tidal constituent is expressed in terms of a Fourier model, such that

$$\zeta_{Ti}(\phi, \lambda, t) = \cos \theta_i \sum_{k=1}^8 \sum_n^{N_k} F_{kn} c_{kn} + \sin \theta_i \sum_{k=1}^8 \sum_n^{N_k} F_{kn} c'_{kn} \quad (7.32)$$

where c_{kn} and c'_{kn} are the Fourier coefficients solved for in solution, and F_{kn} are the position dependent functions, given below

$$\begin{aligned} F_{1n} &= \cos na_{\phi_j} & n=0, \dots N1 \\ F_{2n} &= \sin na_{\phi_j} & n=1, \dots N2 \\ F_{3n} &= \cos na_{\lambda_j} & n=1, \dots N3 \\ F_{4n} &= \sin na_{\lambda_j} & n=1, \dots N4 \\ F_{5n} &= \cos na_{\phi_j} \cos ma_{\lambda_j} & n=1, \dots N5 \quad m=1, \dots N5 \\ F_{6n} &= \cos na_{\phi_j} \sin ma_{\lambda_j} & n=1, \dots N6 \quad m=1, \dots N6 \\ F_{7n} &= \cos na_{\lambda_j} \sin ma_{\phi_j} & n=1, \dots N7 \quad m=1, \dots N7 \\ F_{8n} &= \sin na_{\lambda_j} \sin ma_{\phi_j} & n=1, \dots N8 \quad m=1, \dots N8 \end{aligned}$$

and

$$\begin{aligned} a_{\phi_j} &= \pi(\phi_j - \phi_o) / (\phi_m - \phi_o) \\ a_{\lambda_j} &= \pi(\lambda_j - \lambda_o) / (\lambda_m - \lambda_o) \end{aligned}$$

with (ϕ_o, λ_o) being the coordinates of the southwest corner of the area and (ϕ_m, λ_m) the coordinates of the northeast corner.

Note that when using altimeter data and equations of the form at 7.32, ζ_{Ti} represents the geocentric tide for the i -th constituent.

7.3.5. Theoretical Tidal Model.

A number of theoretical global and regional tidal models have

been developed in recent years. However, for the selected region of the north Atlantic Ocean, an empirical tidal prediction model developed by Mofjeld (1975) was selected. When this model was compared with deep-sea tide gauges within the GEOS-3 calibration area, the discrepancies had an rms of ± 3 cm. The range (difference in elevation between consecutive high and low waters) of the ocean tide in this area is about 60 cm, which predominately consists of the M2, N2, S2, K1, O1 and P1 tidal constituents. The cotidal-coamplitude chart for the M2 tidal constituent is shown in Figure 7.4a. The application of equation 7.32 to Mofjeld's M2 tidal model gave the following values for the significant Fourier coefficients,

$$\begin{array}{ll} c_{10} = 0.403 \text{ m} & c'_{10} = -0.029 \text{ m} \\ c_{11} = -0.064 \text{ m} & c'_{11} = 0.028 \text{ m} \\ c_{31} = 0.043 \text{ m} & c'_{31} = -0.009 \text{ m} \end{array}$$

These coefficients reproduce the M2 Mofjeld tidal signal to ± 2 cm.

7.3.6. Analysis of Data Available in the Sargasso Sea.

7.3.6.1. Introduction.

The Sargasso Sea test area selected for this study was a $12^\circ \times 12^\circ$ area, bounded by the parallels 25°N and 37°N , and meridians 282°E and 294°E . Over 21,000 observations from 183 passes were obtained from the LAS79 data set in this area, covering a time span of 393 days beginning in April 1975. Figure 6.12 shows the distribution of altimetry profiles in the area. Each observation consists of a SSH, latitude, longitude and time. The data were not separated or meaned over smaller blocks, as was done in Bretreger (1979), but observation equations were formed using each individual altimetry profile measurement. Each measurement was referenced to a specific epoch (00 hours GMT, March 29 1975), so that all tidal phases were consistent.

The GEOS-3 data used in these analyses contained no corrections for orbital uncertainties as explained in sub-section 7.3.3. To obtain the tidal signal, an interpolated geoid height value was subtracted from each altimeter derived SSH. Corrections for the solid Earth tide were also computed at each point along the profile, when specified, according to the relations given in sub-section 7.2.2. The analysis used two

different geoid models, one derived from the GEM10 geopotential model (Lerch et al. 1977), and the Marsh-Chang detailed gravimetric geoid (Marsh & Chang 1978) for the calibration area. Due to long wavelength geoid and orbital biases, various zero degree terms (time independent - i.e. only latitude or longitude dependent) were introduced as extra parameters in equation 7.32. These extra parameters were -

- (i) a bias term, coefficient $F_{00} = 1$
- (ii) a latitude term, coefficient $F_{01} = a_{\phi j} / \pi$
- (iii) a longitude term, coefficient $F_{02} = a_{\lambda j} / \pi$
- (iv) a latitude/longitude term, coefficient $F_{03} = a_{\phi j} a_{\lambda j} / \pi^2$

Various combinations of these zero degree terms could be solved for in solutions of the tidal model.

7.3.6.2. Results for SARG Data Set.

The results of numerous solutions showed that not all coefficients listed in sub-section 7.3.5 could be determined with confidence due to aliasing - high correlation coefficients of the order 0.8-0.9 were present between particular c_{kn} and c'_{kn} coefficients and the latitude and/or longitude time independent zero degree terms. Table 7.3 summarizes the results of some of the solutions. It can be seen in this Table that when larger coefficient solutions were attempted, over 55% of the coefficients had cross correlation coefficients of greater than 0.7.

The difference between the Marsh-Chang and GEM10 solutions is somewhat curious. The presumably more precise geoid over the area (Marsh-Chang gravimetric geoid) exhibits more solution instabilities for larger coefficient terms than the GEM10 solutions. This may be due to the higher frequency information present in the Marsh-Chang geoid values although how this affects the solution is hard to assess.

The coefficients obtained in columns 7,8,12 and 13 of Table 7.3 give reasonable representations of the M2 tidal model in the area when compared to the empirical Mofjeld solution. Both the GEM10 solution (column 7) and the Marsh-Chang solution (column 12) are plotted as co-amplitude/cotidal maps in Figures 7.5 and 7.6 respectively. The amplitudes of the GEM10 solution are larger by a factor of about 0.2 (18%) when compared to the Mofjeld model (Figure 7.4a) but exhibit close to the same variation in amplitude over the region - 14 cm for GEM10 solution compared to 20 cm for the Mofjeld model. The phases disagree, on average over the area, by about +20°. For the Marsh-Chang solution,

TABLE 7.3. M_2 Tidal Solutions Using SARG Data Set.

Data Set	SARG (Reference: GEM10)						SARG (Reference: Marsh-Chang)				
	Solution						Solution				
Coefficient	1	2	3	4	5*	6*	1	2	3	4*	5*
C_{10}	0.375 ⁺	0.545 ⁺	0.357 ⁺	0.537	0.444	0.439	-0.012	0.230 ⁺	0.633	0.543	0.541
C'_{10}	-0.109 ⁺	-0.449 ⁺	-0.290 ⁺	0.006	0.074	0.080	0.628 ⁺	-0.249 ⁺	-0.284	-0.216	-0.215
C_{11}	-0.334	-0.320	-0.140	-0.107	-0.117		-0.163	-0.079	-0.052	-0.062	
C'_{11}	0.378	0.327	0.168	0.182	0.189		0.309	-0.055	-0.028	-0.022	
C_{21}	0.123 ⁺	0.011 ⁺	-0.016 ⁺				0.295 ⁺	0.213 ⁺			
C'_{21}	0.152 ⁺	0.377 ⁺	0.528 ⁺				-0.195 ⁺	-0.053 ⁺			
C_{31}	0.415	0.375	0.262				0.340	0.487			
C'_{31}	-0.162	-0.163	-0.128				0.020	-0.337			
C_{41}	0.193 ⁺	0.058 ⁺	0.330 ⁺				0.597 ⁺	0.395 ⁺			
C'_{41}	-0.082 ⁺	0.130 ⁺	-0.123 ⁺				-0.831 ⁺	-0.024 ⁺			
C_{00}	-2.089 ⁺	-4.226 ⁺	-4.885	-4.885	-4.866	-4.865	-0.336 ⁺	-6.394	-6.374	-6.356	-6.354
C_{01}	-8.476 ⁺	-3.844 ⁺					-8.334 ⁺				
C_{02}	-1.698 ⁺	2.310 ⁺					-10.670 ⁺				
C_{03}	8.507 ⁺						13.723 ⁺				

TABLE 7.3 (cont.) M_2 Tidal Solutions Using SARG Data Set.

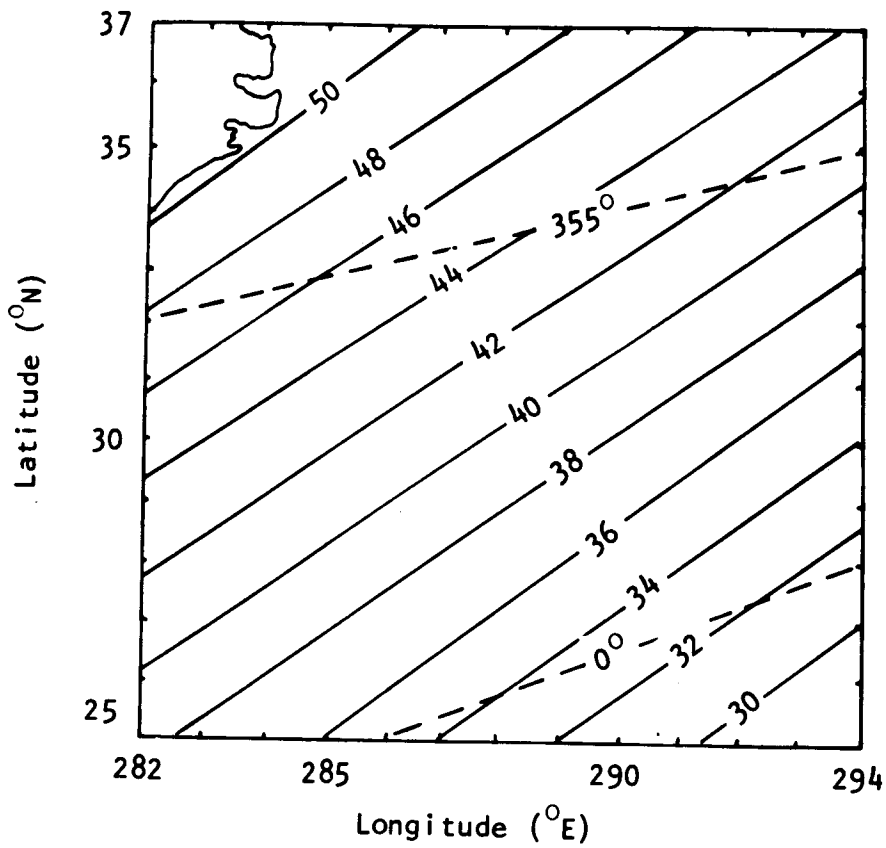
Data Set	SARGNS (Reference: GEM10)			SARGSN		
	1	2	3	1	2	3
Mofjeld M_2 Tidal model [†]	Solution			Solution		
C_{10}	0.436 [†]	0.457 [†]	1.012	0.017 [†]	-0.030 [†]	0.039
C'_{10}	-0.376 [†]	-0.555 [†]	0.005	0.007 [†]	-0.162 [†]	0.050
C_{11}	-0.376	-0.071	-0.361	-0.261	-0.247	-0.204
C'_{11}	0.046	-0.315	0.021	0.505	0.565	0.426
C_{21}	0.321 [†]	0.244 [†]		-0.006 [†]	-0.333 [†]	
C'_{21}	0.128 [†]	0.201 [†]		0.369 [†]	1.186 [†]	
C_{31}	0.496	0.333		0.393	0.315	
C'_{31}	0.060	0.158		-0.417	-0.480	
C_{41}	0.492 [†]	0.576 [†]		0.064 [†]	0.416 [†]	
C'_{41}	0.517 [†]	0.886 [†]		-0.259 [†]	-0.873 [†]	
C_{00}	-0.968 [†]	-4.285	-3.381 [†]	-3.421 [†]	-5.464 [†]	-4.955 [†]
C_{01}	-9.098 [†]		-3.739 [†]	-7.441 [†]		-4.054 [†]
C_{02}	-2.996 [†]		1.758 [†]	-0.120 [†]		2.744 [†]
C_{03}	10.281 [†]			6.136 [†]		

[†] from BRETREGGER (1979)

+ Correlations between coefficients > 0.7

* Solid Earth Tide correction applied.

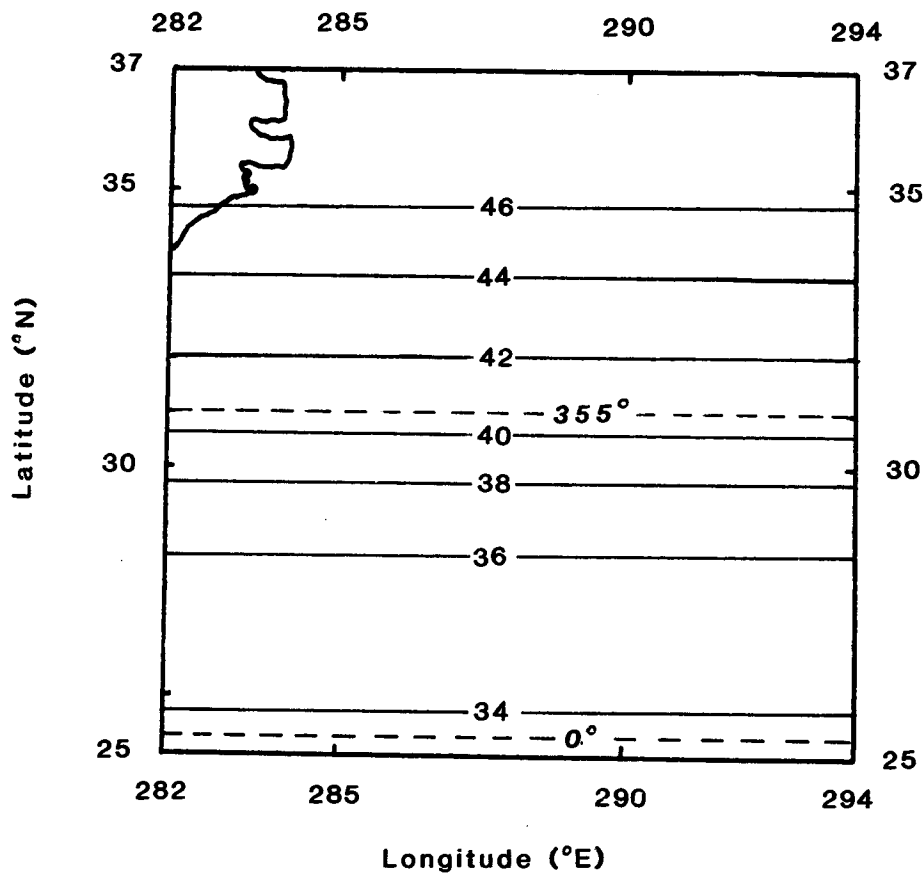
Mofjeld M2 Tide Model



Coamplitude contours in cm.

Cotidal contours in degrees w.r.t. Greenwich

Figure 7.4a

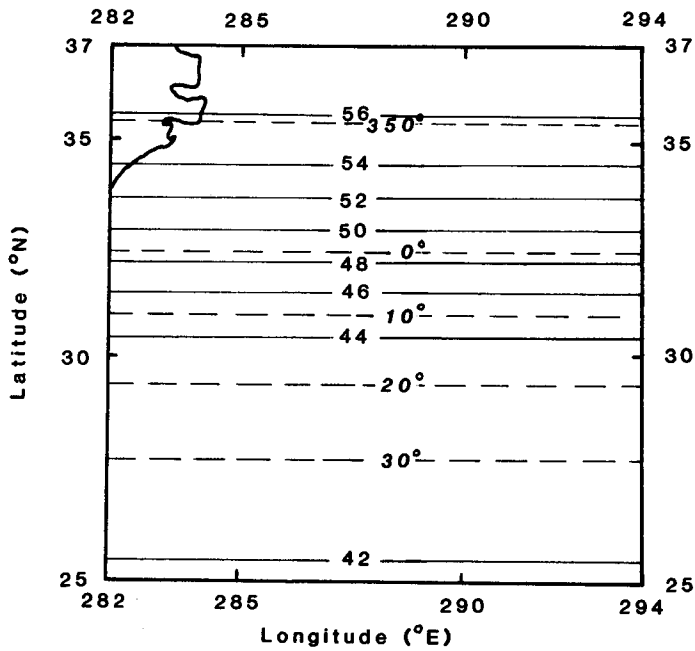
Modified Mofjeld M2 Tide Model

Coamplitude contours in cm.

Cotidal contours in degrees w.r.t. Greenwich

Figure 7.4b

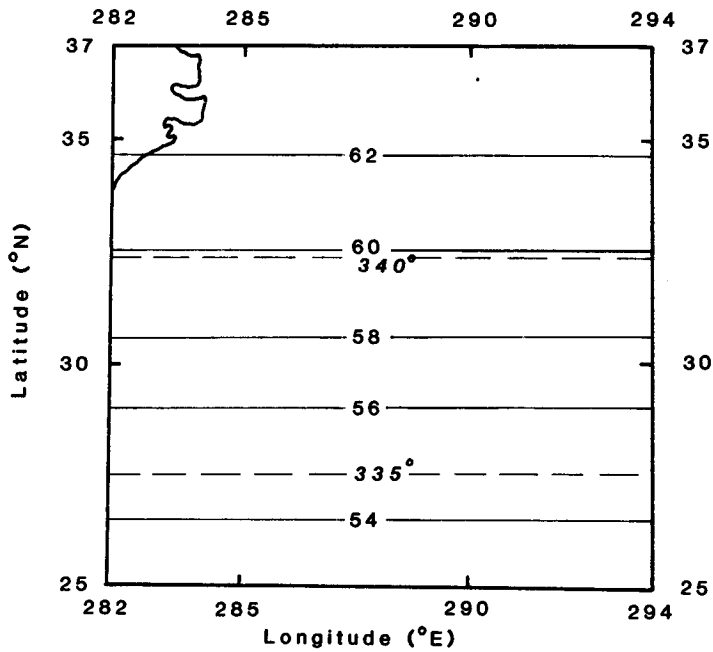
Satellite(GEM 10) M2 Tide Model



Coamplitude contours in cm.
Cotidal contours in degrees w.r.t. Greenwich

Figure 7.5

Satellite(Marsh-Chang) M2 Tide Model



Coamplitude contours in cm.
Cotidal contours in degrees w.r.t. Greenwich

Figure 7.6

the tidal amplitudes when compared to the empirical model are larger by a factor of 0.4 (45%) and the phases disagree, again as an average over the area, by about -19° . These figures suggest that the GEM10 solution gives better agreement with the Mofjeld model but the excessive phase change across the region is disturbing.

A more appreciative view of the satellite results is obtained if a direct comparison is made between the coefficients listed in Table 7.3 (Columns 7 and 12) and the Mofjeld empirical model limited to the same coefficient set. The modified Mofjeld tide model, using coefficients c_{10} , c'_{10} , c_{11} and c'_{11} , is given in Figure 7.4b. Comparison of Figure 7.4b with Figures 7.5 and 7.6 shows that the satellite solutions have adequately modelled the latitudinal variation of the tide model over the area but have somewhat higher amplitudes (about 5-20 cm). The phases again give disagreement by about 20° .

Additional analyses consisted of separating the SARG data set into either descending (SARGNS) or ascending (SARGSN) data sets and solving for the M2 tidal coefficients separately. Both these data sets had interpolated GEM10 geoid values subtracted from the altimeter SSH values. Considerable differences were found in the coefficients between the two analyses, including about a 2 m difference in the zero degree term, c_{00} , supporting the earlier findings of a bias between north-south passes compared to south-north passes. The results are shown in columns 14 to 19 of Table 7.3.

Attempts were also made to extract tidal information by rotating the SARG data set through the satellite inclination (for GEOS-3, the inclination was approximately 115°) so that the satellite groundtracks were orthogonal to the (ϕ, λ) system of the Fourier representation. This procedure also met with limited success.

7.3.6.3. Results for the FIVSARG Data Set.

Studies were carried out using a $5^\circ \times 5^\circ$ area, bounded by parallels 27°N and 32°N , and meridians 287°E and 292°E , which contained over 4000 observations. Only the coefficients c_{10} and c'_{10} plus the c_{00} zero degree term were solved for. These coefficients will give a mean amplitude and phase for the block. Using the GEM10 geoid model, the mean amplitude and phase recovered for the area was 53 cm and 349° respectively. The Mofjeld model gives results of 49 cm and 359° for the amplitude and phase at the centre of the 5° block. Results using the

Marsh-Chang gravimetric geoid gave an amplitude of 65 cm and a phase of 320°. Obtaining these plausible solutions for this area size raises the distinct possibility of dividing an entire oceanic area into, say 5° blocks, and completing successive analyses to obtain regional tidal models. This assumes, however, that the altimetry data coverage is adequate in each block.

In view of the above solutions, further studies were implemented using four adjacent 5° blocks, which covered the area sampled in paragraph 7.3.6.1. The four blocks were bounded by the parallels 26°N and 36°N, and the meridians 283°E and 293°E. The southwest block gave an amplitude of 93 cm and a phase of 5° (41 cm, 357°), the southeast block, 32 cm and 324° (35 cm, 358°), the northwest block, 67 cm and 326° (47 cm, 355°), and the northeast block, 87 cm and 347° (42 cm, 356°). The figures shown in brackets are the Mofjeld values (Figure 7.4a) at the centres of the 5° blocks. These analyses used the Marsh-Chang gravimetric geoid as reference, and consisted of approximately 4,000 observations per block. The southwest block results suffer from errors due to larger variations of the geoid in this region aliasing the ζ_{Ti} values. The remaining results also show disagreements with the Mofjeld model values but the results are still encouraging enough to suggest that, with an increase in both quality and quantity of altimetry data in the future, it will be possible to produce satellite derived tidal models using these techniques.

7.3.6.4. Results of the OVERLAP Data Set.

The results of tidal studies using the overlapping pass data set showed that it was not possible to recover the M2 tidal signal with any confidence. In total, only 23 individual sets of overlapping passes were available in the 12°x 12° area chosen. Each set comprised of between 5 to 9 altimeter passes spaced within 60 km of each other giving a total of about 12,000 observations. The unrealistic results from this study were to be expected, as the 37 day cycle between successive passes severely constrains the ability of the solution procedure to extract any semi-diurnal frequency information. Allied with this is the fact that there was also an inadequate data coverage to model the area. The results, which have been referenced to the Marsh-Chang gravimetric geoid, are summarized in Table 7.4 .

TABLE 7.4. M_2 Tidal Solutions Using OVERLAP Data Set.

Coefficient	Mofjeld Tidal Model	Solution		
		1	2	3
C_{10}	0.403	0.987	1.167	1.161
C'_{10}	-0.029	-0.065	-0.483	-0.499
C_{11}	-0.064	-0.238	0.017	
C'_{11}	0.028	0.254	-0.463	
C_{00}		0.144 ⁺	-5.783	-5.789
C_{01}		-8.846 ⁺		
C_{02}		-10.690 ⁺		
C_{03}		15.022 ⁺		

TABLE 7.5. M_2 Tidal Solutions Using CROSSOVER Data Set.

Block	Amplitude (m)	Phase (degrees)
Model (5° block)	0.33 - 0.43	354 - 359
LAS79 CROSSOVER	0.2 - 0.4	270 - 290
LAS79 SSH	0.3 - 0.6	335 - 353

7.3.6.5. Results for the CROSSOVER Data Set.

The results of functional analyses of the CROSSOVER data set have been reported in Masters et al. (1979) and are summarized in Table 7.5. The results are in general agreement with the empirical model in the area. These analyses were carried out in a $5^\circ \times 5^\circ$ block in the Sargasso area, the same area as in paragraph 7.3.6.2. In Table 7.4, the Mofjeld results are given for comparison, as well as the LAS79 SSH results.

The difference between the CROSSOVER and SSH solutions would suggest some aliasing due to bias terms. More reliable solutions would probably be obtained if the altimetry were reprocessed using improved geopotential models so that the rms of the crossover differences could be reduced to about the 1 m level, as used in the simulation by Bretreger (1979).

7.3.7. Discussion.

The results for the M2 tidal signal presented in previous sections corroborate the earlier simulations of Zetler & Maul (1971) and confirm the possibility of mapping the ocean tides using satellite altimetry data. However, with the GEOS-3 data sets used in this study, it seems that for realistic tidal models it is necessary to restrict the analysis to limited regional areas, where the orbit error is of the same order of magnitude as the tidal signal. At the present time this precludes any analysis of regions other than the northwest Atlantic calibration area. Limited success was also obtained by subdividing the regional area into even smaller blocks. The distribution and amount of data available limited the analyses for each $5^\circ \times 5^\circ$ block to recovering only the mean amplitude and phase for that block. If a sufficient number of such blocks were established with an adequate data coverage, it is foreseeable that a regional tidal model could be produced which would not be inconsistent with many of the cotidal-coamplitude charts presently available.

However, from the results presented, it is evident that the limitations imposed by the nature of the systematic orbital errors needs to be resolved before any time variant studies are undertaken. The importance of the geoid model used is also significant, as shown in the results presented for the GEM10 and the Marsh-Chang geoids. However it may be possible to use the existing global tidal models derived

empirically using LTE's, such as those of Schwiderski (1980) and Parke & Hendershott (1980), to eliminate the signal of the tidal constituents not being solved for in the solution procedure, i.e. solve for only one constituent in the area and remove the tidal information pertaining to the other constituents. A possible limitation may be that this process could remove an unknown percentage of the required tidal constituent from the data. Simulation studies need to be carried out to find a solution to this problem.

The existence of continuous global passes of altimetry will significantly improve the quality of regional and global satellite altimetry derived ocean tide models. This should be possible with the use of the SEASAT altimetry data and the improved tracking complement and groundtrack configuration (Tapley et al. 1979b). Tidal models with better resolution could also be obtained with the full 3.6 year GEOS-3 data set rather than the 393 day span analysed here. With the increase in the signal-to-noise ratio, which is expected from the SEASAT data, as well as the hoped for improvement in gravity field models derived using altimetry data, it should be possible to recover a greater number of coefficients than the mean amplitude and phase found in these studies, leading to the possibility of mapping complex ocean tide patterns encompassing several tidal constituents.

7.4. Recovery of Global Ocean Tide Models.

This section outlines a procedure to obtain a global representation of the ocean tides, given as input the satellite altimetry data and orbital ephemeris.

7.4.1. Altimeter Data Sets.

The input data set required would be similar to that mentioned in paragraph 7.3.2.1, but for a successful global determination of the tidal constituents, the rms fit of the orbits would need to be at least at the ± 50 cm level. The distribution of the altimetry data in both space and time plays a critical role in the separation of the tidal constituents. It is considered, from the solutions obtained on a regional basis, that for recovery of a global, satellite-derived ocean tide model to be viable, at least 2-3 years data should be available and that on average there should be approximately 200-250 passes (balanced

number of north-south and south-north passes) within each $10^\circ \times 10^\circ$ square with over 80% of the total area covered by the altimetry data. Problems will exist at high latitudes where there is no altimetry coverage. These requirements are certainly not met at all levels by the present GEOS-3 data base. For this reason, only an analysis procedure is given below and no global tide model simulations or solutions are attempted.

7.4.2. Modelling the Ocean Tide.

At any given time (GST = θ), the hour angle of the i -th tide producing body is θ_{bi} where

$$\theta_{bi} = RA_i - \theta \quad (7.36)$$

where RA is the right ascension of the tide producing body, and the value of θ is obtained from a conversion of the orbital ephemeris value of U.T.

The tide at the general point $P(\phi, \lambda)$ can be completely represented by a tidal amplitude $\zeta_a(\phi, \lambda)$ and a lag of the tide $\beta(\phi, \lambda)$ in relation to the time of high tide at Greenwich, assumed to have zero lag. However, this step assumes that the tidal characteristics at a point are time invariant.

The tidal height $\zeta_t(\phi, \lambda, \theta)$ at $P(\phi, \lambda)$ and time θ can then be expressed as

$$\begin{aligned} \zeta_t(\phi, \lambda, \theta) &= \sum_{i=1}^N \zeta_{ai}(\phi, \lambda) \cos(\theta_{bi} - \beta_i(\phi, \lambda)) \\ &= \sum_{i=1}^N \zeta_{ai}(\phi, \lambda) \cos \beta_i(\phi, \lambda) \cos \theta_{bi} + \zeta_{ai}(\phi, \lambda) \sin \beta_i(\phi, \lambda) \sin \theta_{bi} \end{aligned} \quad (7.37)$$

where N is the number of tidal constituents being solved for. In this equation the time component has been separated from the positional component.

The global tide is modelled by setting up two surface spherical harmonic series

$$\zeta_i = \zeta_{ai} \cos \beta_i = \sum_{n=1}^{n'} \sum_{m=0}^n \sum_{\alpha=1}^2 \zeta_{i\alpha nm} S_{\alpha nm} \quad (7.38)$$

and

$$\zeta'_i = \zeta_{ai} \sin \beta_i = \sum_{n=1}^{n'} \sum_{m=0}^n \sum_{\alpha=1}^2 \zeta'_{i\alpha nm} S_{\alpha nm}$$

where $S_{\alpha nm}$ are the surface spherical harmonic functions defined by

$$S_{1nm} = P_{nm}(\sin \phi) \cos m\lambda \quad ; \quad S_{2nm} = P_{nm}(\sin \phi) \sin m\lambda \quad (7.39)$$

up to degree n' , and $P_{nm}(\sin \phi)$ are the associated Legendre functions (see H & M 1967, Section 1-11).

Using the same procedure as for the regional analysis, observation equations can be set up at each altimeter measurement such that the residuals

$$v = \zeta_t(\phi, \lambda, \theta) - \left(\sum_{i=1}^N \sum_{n=1}^{n'} \sum_{m=0}^n \sum_{\alpha=1}^2 S_{\alpha nm} (\zeta_{i\alpha nm} \cos \theta_{bi} + \zeta'_{i\alpha nm} \sin \theta_{bi}) \right) \quad (7.40)$$

are minimised over the epoch considered.

The geocentric tidal height $\zeta_t(\phi, \lambda, \theta)$ is related to the altimeter derived SSH (ζ) by the relation

$$\zeta_t = \zeta - N \quad (7.41)$$

where N is the "geoid" height evaluated from the best available geopotential model or is estimated from $n^\circ \times n^\circ$ block mean SSH values derived using techniques outlined in Chapter 6. ζ_t will have values within the range $\pm 1-2$ m.

Equation 7.40 can be rewritten as

$$v = \zeta_t(\phi, \lambda, \theta) - \sum_{i=1}^N (\cos \theta_{bi} \underbrace{\sum_{n=1}^{n'} \sum_{m=0}^n \sum_{\alpha=1}^2 S_{\alpha nm}}_{\text{coefficient}}) \underbrace{\zeta_{i\alpha nm}}_{\text{unknown}} - \sum_{i=1}^N (\sin \theta_{bi} \underbrace{\sum_{n=1}^{n'} \sum_{m=0}^n \sum_{\alpha=1}^2 S_{\alpha nm}}_{\text{coefficient}}) \underbrace{\zeta'_{i\alpha nm}}_{\text{unknown}} \quad (7.42)$$

The total number of coefficients will be $N = (2(n'+1)^2 - 2) \times N$. The solutions for $\zeta_{i\alpha nm}$ and $\zeta'_{i\alpha nm}$ will define the global tide in terms of surface spherical harmonic coefficients. The success of this analysis

procedure awaits evaluation using firstly, simulation studies and then testing the procedures using the available altimetry data sets.

A global simulation study for the ocean tides, considering systematic orbital errors in the altimeter data, was reported in Estes (1979). It was concluded in this investigation that the radial orbit error needed to be less than 1 m, using 10 cm precision altimeter data, to adequately recover the principal tidal constituents. This is the major problem in using the altimeter data for the recovery of tidal information.

7.5. Conclusions.

Despite the difficulties associated with using satellite altimetry techniques for tidal model recovery, the prospects of nearly global coverage without the expense and logistic problems of ocean bottom gauges, tide gauge maintenance etc, makes the use of satellite remote-sensed data a valuable addition for the eventual solution of a world cotidal-coamplitude map at the centimeter level. The two major gaps in the understanding of the tidal system at present (Cartwright 1977) are the mechanism causing the non-tidal acceleration of the Earth and the missing sink of energy in the oceanic tidal dynamics. Improvement of global cotidal maps using satellite altimetry, in conjunction with oceanographic data, will almost certainly lead to improved estimates of the non-Newtonian acceleration caused by tidal deformation with friction (Lambeck 1975) and estimates of power budgets in the oceans.

The results for the Sargasso area (summarized in Section 7.3) show that the techniques proposed do indeed give results that are encouraging. The recovery of an amplitude and phase of the M2 tidal constituent to within 20% or less of the empirical model suggests that, given an improved data coverage and time span, orbital configuration and laser tracking complement, possibilities exist for mapping complex ocean tide patterns covering several dominant tidal constituents. The ocean tide information obtained from satellite altimetry can never replace the solution of ocean models via the LTE's but the altimeter results can act as a useful constraint to the overall system.

The solution technique set out in Section 7.4 gives a procedure whereby a global tide model may be obtained. The question of whether it is better to build up blocks of regional solutions into a global model

or to consider processing the data in a single global solution remains to be answered. However, the conclusion that can be stated, from the development set out in this Chapter, is that satellite altimetry does provide quantitative information on the ocean tide signal. The results obtained show that problems encountered by previous investigators have been overcome and a further step has been achieved in extracting the tidal signal from satellite-remote sensed data.

8. CONCLUSIONS.

8.1. Remote Sensing Capabilities.

The use of measurements from orbiting spacecraft platforms to the ocean surface has the potential to provide information previously unobtainable using conventional oceanographic techniques. It is quite clear that the utilisation of these remote sensed measurements can make some limited but certainly unique and valuable contributions to the study of ocean dynamics. Nevertheless, it should be borne in mind that the use of remote sensed data should not be considered a "stand-alone" system but be used in conjunction with in-situ measurements.

Since the ocean spectrum varies over such a broad and complex time-space continuum and the nature of the satellite time-space scales is fixed by the chosen orbital parameters, only certain portions of the ocean spectrum may be recovered from the satellite measurements. Results for the GEOS-3 and SEASAT-1 satellites (see Figure 3.4) indicates that, generally speaking, the ocean spectrum with wavelengths greater than 30 km and time scales in excess of 0.5 days may be recovered provided the satellite sensors meet the accuracy requirements. This means that ocean phenomena such as ocean eddies, western boundary currents, equatorial currents and tides may be studied with these and future 300 km altitude, oceanographic-dedicated satellite missions.

The present remote sensing instruments available and their contributions or expected contributions to oceanographic information are summarized in Table 8.1. This table indicates the incredible volume of information that will ultimately become available to quantify the surface ocean dynamics provided correct analysis procedures are followed. The geodetic concepts presented in this thesis to obtain oceanographic information using the radar altimeter data are discussed further in the next Sections.

8.2. A 10 cm Marine Geoid.

8.2.1. Preamble.

It has been the aim of this thesis to formulate a geodetic basis

TABLE 8.1 Sensor Capabilities

Sensor Type	Measurement Type	Resolution	Application
Radar Altimeter	Altitude	± 10 cm	<ul style="list-style-type: none"> Monitoring ocean variability associated with western boundary currents and mesoscale eddy features.
	Significant Wave Height	± 50 cm (Range 1-20 m)	<ul style="list-style-type: none"> Mass transport estimates for major current systems.
	Surface Wind Speed	± 3 m/s (Range 1-20 m/s)	<ul style="list-style-type: none"> Surface geostrophic current patterns.
	Ocean Surface Roughness		<ul style="list-style-type: none"> Global circulation models.
Microwave Scatterometer	Surface Wind Speed	± 2 m/s (Range 4-28 m/s)	<ul style="list-style-type: none"> Derive wind stress estimates and thus frictional forces at the air/sea interface.
	Surface Wind Direction	$\pm 20^\circ$	<ul style="list-style-type: none"> When combined with the geostrophic component, total surface velocity field of the ocean is obtained.
Microwave Radiometer	Ocean Surface Temperature	$\pm 1-2^\circ\text{C}$	<ul style="list-style-type: none"> Monitoring movement of ocean currents and eddies.
	Ocean Salinity	1%	<ul style="list-style-type: none"> Surface heat transport.
	Surface Wind Speed	± 2 m/s (Range 7-30 m/s)	<ul style="list-style-type: none"> Wind stress. Detection of cloud patterns and rain cells. Monitoring movement of sea ice boundaries and concentrations.

TABLE 8.1 cont.

Sensor Type	Measurement Type	Resolution	Application
Synthetic Aperature Radar	Deriving Wave Spectra in open oceans and coastal areas	25 m x 25 m cell 15% in wavelength 25° in wave direction	<ul style="list-style-type: none"> Monitor ocean swell and currents, surface wind changes, internal wave patterns, and sea ice conditions.
Visible and Infrared Radiometer	Ocean Surface Temperature Visible and IR emission	± 1-2°C 5 km	<ul style="list-style-type: none"> Monitoring movement of ocean currents and eddies.

for the recovery of ocean dynamic parameters using satellite altimetry data. Satellite altimetry data has the capability of defining the spatial location of the instantaneous ocean surface in relation to a geocentric Cartesian coordinate system rigidly fixed in Earth space to precisions of the order of 10 cm. The problem of using these data for ocean dynamic applications requires an expertise in both orbital dynamics and physical geodesy in which the location of the satellite orbit and the position of a level surface of the Earth's gravity field, in particular the shape of the ocean geoid, needs to be defined at the sub-meter level. If these requirements are met then, in principle, it is a straightforward procedure to determine the SST in ocean areas (see equation 2.29 and Figure 3.2). But at this point, the problem also requires an appreciation of the principles of physical oceanography to correctly interpret the derived SST values.

The insurmountable obstacles at the present time to achieving these objectives are:

- (i) the Earth's disturbing potential, and hence the shape of the geoid, is only known at the 1% level. For ocean circulation studies, it is necessary to have a global gravity field model correct to ± 6 kGal cm through wavelengths of interest.
- (ii) the position of the satellite orbit cannot be defined at the ± 10 cm level.

However, the findings of the study showed that useful information can still be gained by studying the time variations of the SST and also under certain hypothetical assumptions, estimates of the quasi-stationary component of the SST can be made over regional areas of interest. The value of these SST data for quantifying oceanographic information is discussed in Section 8.3. The remaining sub-sections detail the procedures that can be used to extract the SST when the above limitations are overcome.

8.2.2. A Geoid Definition Adequate for Ocean Dynamic Studies.

A conceptual definition of the geoid sufficient for the realisation of a 10 cm marine geoid was discussed in sub-section 2.4.2. This requirement is necessary to ensure the unambiguous definition of the geoid when using a combination of satellite altimetry, surface gravity and satellite tracking data. It was concluded that a suitable

definition acceptable to oceanographers and geodesists is the following:

"The geoid, for a selected epoch of measurement, is that level surface of the Earth's gravity field in relation to which the average non-tidal SST is zero as sampled globally in ocean regions."

Having adopted this definition for the geoid, its validity depends on the maintenance of its stability over geodetic time scales. It was concluded in sub-section 2.4.3 that the phenomena causing secular changes in the shape of the geoid, such as changes in the global MSL and mass redistributions within the Earth, can be considered negligible at the 10 cm level over time scales of about 50 years.

8.2.3. Determinations using the GBVP Approach.

The practicalities for formulating a solution of the GBVP which seeks to define the height anomaly to ± 5 cm are based on the requirements for:

- (i) determining the SST in ocean areas, and
- (ii) unifying the regional levelling datums in the context of a unique datum level surface.

A solution procedure for achieving the above objectives is given in Chapter 5. It is evident that no combination of data collected from satellite altimetry and surface gravity can provide a definition of the SST unless both types of data have global distributions such that error patterns with wavelengths equivalent to those sought in the SST have cumulative magnitudes less than ± 10 cm and ± 30 μ Gal.

It is shown that the three basic equations relating the observed quantities at the Earth's surface to the SST are equivalent (see equations 5.4, 5.42 and 5.52). The choice of one integral over another is merely a matter of convenience. Based on the nature of the available geodetic data, the use of equation 5.4 appears to provide a more promising basis for improving the gravity field model and determining the long wave features of the quasi-stationary SST.

The conclusions reached from this investigation may be summarized as follows:

- (i) Relatively simple techniques are available for determining the long wave features in the quasi-stationary SST from a combination of satellite altimetry and surface gravity anomaly data provided the accuracy of the gravity field model is commensurate with the

determination of the altimeter-equipped spacecraft using a 10 cm global tracking network. This means that the resolution of the disturbing potential should be at the ± 0.1 kGal m level for wavelengths of 1000 km or greater (see Section 5.4).

(ii) Information on the quasi-stationary SST with wavelengths shorter than those in the satellite determined gravity field model cannot be determined unless there is an adequate coverage of sufficiently precise gravity anomaly data (see Section 6.1). An alternate means, in principle, for obtaining an improved definition of the Earth's gravity field for wavelengths shorter than those at (i) is to use the satellite-to-satellite tracking data collected during a mission such as the proposed GRAVSAT mission. It is expected that the minimum wavelength resolved, in the case of GRAVSAT, could be reduced to about 500 km.

(iii) Neither surface gravity information nor satellite altimetry data on their own can provide information on level surfaces to a precision below the magnitude of the SST because none of the data can be unambiguously related to the geoid at the 10 cm level. It is therefore not possible to determine the geoid to a precision adequate for global SST studies from solutions of the GBVP without making unwarranted assumptions about the magnitude and distribution of the SST. The only data source uncontaminated by the SST is the satellite determined gravity field model (see Section 5.4).

(iv) The unification of the world's geodetic levelling datums in relation to a datum equipotential surface can be achieved using equations 5.126 to 5.128. The prerequisite conditions for this technique to be successful are a gravity field model to degree n' (wavelengths greater than 1) which is consistent with the altimeter-equipped satellite orbit at the 10 cm level, and surface gravity data with systematic errors of wavelength greater than 1 being below ± 30 μ Gal (see Section 5.5).

The formulation of the GBVP for the solution of the height anomaly presented in Chapter 5 is entirely satisfactory for determining the SST provided the input data are of adequate quality. However, in recent years alternate formulations of Molodenskii's classical BVP have been proposed by Sanso (1978, 1979) and a solution of Stokes' BVP using variational principles was given by Nakiboglu (1978). Future research may be directed to investigating the potential of these new approaches for determining the geoid/SST under conditions of mixed data sets and

non-global coverages of such data sets.

8.3. Recovering Ocean Dynamic Information.

8.3.1. Overlapping Pass Analysis.

The technique of using overlapping passes allows the detailed examination of the time varying ocean phenomena since the geoid signal in each of the profiles is assumed time-invariant. The analysis procedure developed has been described in paragraph 6.2.1.2. Limitations of this type of analysis procedure are that information with wavelengths greater than twice the length of the pass and periods shorter than the repeat period of the orbit are lost. The technique also suffers from limitations of areal coverage compared to regional sea surface model techniques.

Unfortunately, the analysis of overlapping passes in the EAC area proved unproductive due to the limited data set available at the time of analysis. For the Gulf Stream area, however, studies of 32 sets of overlapping passes over a 5 month period gave valuable information on SSH changes related to ocean eddy features. Correlation studies of the altimeter-defined SSH anomaly with satellite IR and/or ship defined anticyclonic and cyclonic rings indicated a 98% correlation between the individual features if time varying factors were allowed for. This technique thus demonstrates its potential for tracking transient ocean features.

The analysis of overlapping passes provides a better picture of the instantaneous SSH variability through wavelengths greater than 30 km. From the spectral analysis of overlapping pass residuals, the variance of the SSH variability in the Sargasso Sea through wavelengths between 50 and 1500 km is estimated at about 540 cm^2 . This estimate agrees reasonably well with oceanographic estimates of structure functions and intensities of eddy fields in the North Atlantic (Dantzler 1976 a).

If the set of overlapping passes is referred to a detailed geoid, instead of the average profile for the set, it has been demonstrated by Cheney & Marsh (1980b) and Kao & Cheney (1980) that fluctuations in the SST across current boundaries can be used to infer changes in mass transport of the current system above the main thermocline since the SST variations are proportional to the geostrophic surface transport (Kao

1980). Leita0 et al. (1978a) using the same technique of fitting to a detailed geoid, speculated that the spatial changes between the profiles over a 3 month period could be associated with fragmentary flow patterns in the Gulf Stream. Data from oceanographic measurements seems to support this view (Luyten 1977). This provides considerable support for the usefulness of the altimeter as a tool to study the dynamics of the ocean circulation.

Thus, the ocean dynamic information obtainable from the analysis of overlapping passes, given sufficient data coverage, may be summarized as:

(i) transient ring and mesoscale eddy movement (see sub-section 6.4.2 and also Gaborski (1979), Cheney & Marsh (1980b) and Leita0 et al. (1978a).

(ii) current meanders and current boundary position (Leita0 et al. 1979b).

(iii) mass transport variations (Kao & Cheney 1980).

The real value in using overlapping pass techniques is that it can be used for studying ocean features with amplitudes above the noise level of the altimeter (i.e., $\pm 20-30$ cm for GEOS-3 and ± 10 cm for SEASAT) in any ocean area since a precise marine geoid is not required. This opens up the exciting prospects for studying currents such as the Antarctic Circumpolar Current and the Equatorial Current.

8.3.2. Regional Sea Surface Models.

The concept of regional sea surface models has been developed in sub-section 6.2.2. The technique proposed is comparable, if not more flexible, than methods proposed by other investigators. Regional model solutions cannot resolve features with periods shorter than the time period of data analysis and all time varying SST information with wavelengths greater than twice the dimension of the area studied are lost.

The mean ocean surface obtained from this analysis method will contain both oceanographic as well as geoidal uncertainties. But when the time span for the computation of the regional sea surface model is long enough (say, 1 to 3 years - the longer time period is more suitable) the transient phenomena, such as the eddies, are smoothed out in the averaging procedure at the junction point squares. Thus, when taking differences between shorter time period regional sea surface

models and the long period mean surface, the technique is capable of tracking eddy features and giving information on ocean variability.

Results for the EAC area were again not attempted because of the totally inadequate altimetry distribution. In the Gulf Stream area, the results of the correlation studies indicated that the SSH anomalies were located within 100 km (about one half the typical ring diameter) of the IR sensed cold ring about 90% of the time.

It can be concluded from these studies that sophisticated tracking support is not needed to monitor the movement of eddy features, provided 30 balanced passes of altimetry data are available each month per 10^6 km² in the region of interest. Resolutions of the order ± 20 -30 cm can be expected in such cases. It is seen that this technique can be used to monitor transient features on a real-time basis with future planned oceanographic satellite missions.

Regional sea surface modelling concepts can also be used successfully to study the distribution of the eddy kinetic energy in the oceans since this information is available in the variability of the SSH data in the junction point squares over a selected period of analysis (see Figure 6.13). Leitao et al. (1979b) have given results for the variability using the full 3.6 year data set but their solution procedure could not incorporate the complete data set in a unique solution.

The attempts at extracting estimates of the quasi-stationary SST over regional areas for computing the geostrophic flow field has been set out in sub-section 6.4.5. It is apparent that the limiting factor for obtaining estimates of the absolute geostrophic circulation is the accuracy of the gravity field models. At the present time, the only area where realistic attempts can be made at this type of analysis is in the northwest Atlantic Ocean where the precision of the available detailed gravimetric geoids (Marsh & Chang 1978, Mader 1979) is estimated at ± 50 cm. Under the speculative assumptions discussed in paragraph 6.4.5.2, the computed geostrophic velocity gave current speeds in agreement with oceanographic estimates and the signature of the Gulf Stream could be distinguished. These preliminary results indicate that the possibilities exist for using the altimeter data for definitive surface ocean circulation studies over regional areas.

8.3.3. Discussion.

The altimetry data from the GEOS-3 satellite has shown the potential for becoming an important tool for oceanographers in determining time and space scales associated with the variability of the oceans. The GEOS-3 data base used in this thesis was limited in a number of ways :

(1) the data available was a 393 day subset of the full 3.6 year altimetry set. This means that the long period regional sea surface model and its variability could be improved using the extended data set now available.

(2) the GEOS-3 altimetry released in 1977 had been edited by an erroneous land data mask and consequently valuable data on the continental shelf areas was lost. The problem has been rectified in the re-released GEOS-3 data set and this additional data will be of great benefit for analysis in the EAC area and the Gulf Stream area. It means not only is there added data for studying possible ocean dynamic features but the extra data will increase the stability of the regional sea surface models. As seen in Figure 6.13, the peripheries of the regional solutions tend to be noisy and with the shelf data being included, the edges of the solution will be located at the coastal boundaries rather than in the midst of the boundary current signature.

However, at the present time there are still problems with the new GEOS-3 data set that need attention. Problems exist with the derived SSH estimates as the Kalman type filter used to smooth the SSH data produced biased estimates (H.R. Stanley, private communication, 1981). But, the more alarming aspect of the new data set is the discontinuous nature of the altimetry passes, particularly in the southern ocean areas, which was not present in the previous 1977 GEOS-3 data set.

The prospects of utilising the "cleaned-up" GEOS-3 data set and the more accurate SEASAT altimetry data for ocean dynamic studies promises to offer a stimulating challenge to investigators.

8.4. Tide Model Recovery.

It has been traditional to resort to theory for estimating the tides in the open oceans. The introduction of deep sea tide gauges has partly solved this problem (see Cartwright et al. 1980) but the data coverage is still not sufficient to use in global tide models.

The use of satellite altimetry data, with its near global coverage, has the potential to define global tide models with a precision approaching 10 cm. The altimeter detects the geocentric tide, being the sum of the oceanic tide, body tide and the loading tide of the solid Earth (see Figure 7.2). Early simulation studies by among others Zetler & Maul (1971) and Bretreger (1976) indicated that the amplitude and phase of the dominant tidal constituents could be recovered from the altimeter data with random, high frequency noise levels in excess of the tidal signal.

However, the dominant error source affecting the successful recovery of the ocean tide signal comes from the systematic satellite orbital error which will be aliased into the tidal spectrum. This error is largely due to the uncertainties in the geopotential model, atmospheric drag and solar radiation pressure models used in the integration of the orbit force functions. Crossover techniques were used to study the orbital errors of the GEOS-3 altimetry data base used for the tidal analysis. It was found that about 1 to 1.5 m of noise in the data could not be accounted for, being neither position or time dependent (see sub-section 7.3.3).

A solution procedure was given in sub-section 7.3.4 for the recovery of regional ocean tidal information in which the problems of orbital errors aliasing the tidal signal were minimised. Using a number of different data sets - crossover differences, overlapping passes and altimeter profiles - solutions were attempted for the recovery of the M2 tidal constituent in the Sargasso Sea. The available data distribution and the level of the GEOS-3 orbital error, as well as the resolution of the geoid model, restricted the recovered M2 tide information to a limited number of coefficients. The analysis showed that the altimeter-derived tide models agreed to within about 20 cm in amplitude and about 20° in phase compared to the empirical Mofjeld M2 model for the same regional area. It is envisaged that given an improved spatial and time coverage of altimetry data and improved orbital resolution from 10 cm laser tracking data, the procedure proposed should be capable of mapping complex ocean tide patterns covering several dominant tidal constituents over regional areas.

8.5. Discussion.

The analyses described above demonstrate the potential of remote

sensed data to quantify the dynamics of the surface layer of the ocean. In particular, the satellite altimeter data has been shown to be of sufficient precision for the following regional oceanographic studies:

- (i) the study of the temporal variations in the ocean surface,
- (ii) preliminary estimates of the geostrophic current vector associated with western boundary current areas,
- (iii) the recovery of the M2 tidal signal.

Further progress in global ocean dynamic studies cannot be achieved until the following requirements are satisfied:

- (i) Refinement of the Earth's geopotential model to a resolution of 6 kGal cm through all wavelengths of interest,
- (ii) Determination of the radial component of the satellite orbit to accuracies of the order of ± 10 cm on a global basis.

Since these requirements are unlikely to be met in the near future and the prospects of launching an altimeter-equipped satellite within 5 years seems doubtful, the main contribution of the available altimeter data will be in determining the time variations in the SST and hence the variations of the ocean circulation and eddy kinetic energy fields, and the study of the movement of ocean eddy features. This information in itself will be of great value in understanding the ocean environment.

Much more research remains to be done on the recovery of ocean dynamic information from satellite altimetry data under adverse signal-to-noise conditions but the concepts of using geodetic techniques for oceanographic studies will considerably enhance the realisation of real-time ocean monitoring in future years.

REFERENCES.

- Accad, Y. & Pekeris, C.L. 1978. Solution of the Tidal Equations for M2 and S2 tides in the world oceans from a knowledge of the tidal potential alone. *Phil.Trans.Roy.Soc.London, Ser.A*, 290, 235-266.
- Allen, C.P. & Martin, C.F. 1977. SEAHT - A computer program for the use of intersecting arcs of altimeter data for sea surface height refinement. NASA CR 141432, Wallops Flight Center, Wallops Is., Va., 116pp.
- Amorocho, J. & DeVries, J.J. 1980. A New Evaluation of the Wind Stress Coefficient Over Water Surfaces. *J.Geophys.Res.*, 85(C1), 433-442.
- Anderle, R.J. & Hoskin, R. 1977. Correlated errors in satellite altimetry geoids. *Geophys.Res.Lett.*, 4(10), 421-423.
- Anderle, R.J., Beuglass, L.K. & Tanenbaum, M.G. 1976. Accuracy of Computed Orbits of GEOS-3 Satellite. Naval Surface Weapons Center, NSWC/DL TR-3470, 28pp.
- Anderson, E.G. 1979. Are Primary Levelling Networks Useless ? - A Review of Errors in Precise Geodetic Levelling. Paper presented at ASP-ACSM Convention, March 18-24, 1979, Washington, D.C., 13 pp.
- Anderson, E.G., Rizos, C. & Mather, R.S. 1975. Atmospheric Effects in Physical Geodesy. *Unisurv G 23*, Sch. of Surveying, Uni. of New South Wales, Sydney, Australia, 23-41.
- Andrews, J.C. & Scully-Power, P.D. 1976. The Structure of an East Australian Current Anticyclonic Eddy. *J.Phys.Oceanogr.*, 6, 756-765.
- Andrews, J.C., Lawrence, M.W. & Nilsson, C.S. 1979. Observations of the Tasman Front. (to be published).
- Apel, J.R., (ed.). 1972. Sea Surface Topography From Space, Vols I & II. NOAA Tech. Rep., ERL 228-AOML 7.
- Apel, J.R. 1976. Ocean Science From Space. *EOS, Trans.Am.Geophys.Union*, 57, 612-624.
- Apel, J.R. 1980. Satellite Sensing of Ocean Surface Dynamics. *Ann.Rev.Earth Planet.Sci.*, 8, 303-342.
- Apel, J.R. & Apel, J.J. 1976. Gulf Stream meander and eddy dynamics as observed from ship and spacecraft. *Bull.Am.Meteorol.Soc.*, 57, 99.
- Balmino, G., Brossier, C. & Moynot, B. 1977. Pretraitement des mesures altimetriques de GEOS-3 : description du logiciel developpe. Tech. Rep. GB/CB/BM/NS/7.089/CT/GRGS, 83pp.
- Balmino, G., Brossier, C., Cazenave, A., Nouel, F., Dominh, K. & Vales, N. 1979. Geoid of the Kerguelen Islands Area Determined from GEOS-3 Altimeter Data. *J.Geophys.Res.*, 84(B8), 3827-3832.
- Barnett, T.P., Knox, R.A. & Weller, R.A. 1977. Space/time structure of

- the near-surface temperature field during the NORPAX POLE Experiment. *J.Phys.Oceanogr.*, 7, 572-579.
- Barrett, J.R. 1963. Cyclonic eddies in the Western Sargasso Sea. *Trans.Am.Geophys.Union*, 46(1), 99.
- Barrett, J.R. 1971. Available potential energy of Gulf Stream rings. *Deep-Sea Res.*, 18, 1221-1231.
- Barrick, D.E. 1972. Remote Sensing of Sea State by Radar. In: *Remote Sensing of the Troposphere*, V.E.Derr, (ed.), U.S. Govt. Printing Office, 12.1-12.46.
- Bernstein, R.L. & White, W.B. 1974. Time and length scales of baroclinic eddies in the central North Pacific Ocean. *J.Phys.Oceanogr.*, 4, 613-624.
- Bjerhammer, A. 1962. On an explicit solution of the Gravimetric Boundary Problem for an Ellipsoid of Reference. Geodesy Division Publication, Royal Institute of Technology, Stockholm.
- Blume, H-J.C., Kendall, B.M. & Fedors, J.C. 1978. Measurement of Ocean Temperature and Salinity via Microwave Radiometry. *Boundary-Layer Meteorology*, 13, 295-308.
- Boland, F.M. 1973. A monitoring section across the East Australian Current. Technical Paper No.34, CSIRO Aust.Div.Fish. Oceanogr.
- Boland, F.M. 1979. A time series of XBT sections across the East Australian Current. *Aust.J.mar.Freshwat.Res.*, 30, 303-313.
- Boland, F.M. & Hamon, B.V. 1970. The East Australia Current, 1965-1968. *Deep-Sea Res.*, 17, 777-794.
- Bomford, A.G. 1971. *Geodesy* (3rd ed). Oxford Univ. Press, 731 pp.
- Bowie, W. 1929. Tilting of Mean Sea Level. *Gerlands Bertrage zur Geophysik*, Vol. XXIII, 97-98.
- Brace, K.L. 1978. Analysis/Evaluation of the Preliminary Gridded DOD GEOS-3 Geoid. Paper presented at AGU Spring Meeting, Miami Beach, Florida, April 1978.
- Brammer, R.F. 1979. Estimation of the Ocean Geoid Near the Blake Escarpment Using GEOS-3 Satellite Altimetry Data. *J.Geophys.Res.*, 84(B8), 3843-3852.
- Brammer, R.F. & Sailor, R.V. 1980. Preliminary Estimates of the Resolution Capability of the SEASAT Radar Altimeter. *Geophys.Res.Lett.*, 7(3), 193-196.
- Bretreger, K. 1976. On Recovering the Ocean Tide Signal from Satellite Altimetry. Unisurv G25, Sch. of Surveying, Univ. of New South Wales, Sydney, Australia, 85-94.
- Bretreger, K. 1979. Ocean Tide Models from GEOS-3 Altimetry in the

- Sargasso Sea. *Aust.J.Geod.Photo.Surv.*, 30, 1-14.
- Brooks, R.L. 1979. Monitoring of Thickness Changes of the Continental Ice Sheets by Satellite Altimetry. *J.Geophys.Res.*, 84(B8), 3965-3968.
- Brown, G.S. 1979. Estimation of Surface Wind Speeds Using Satellite Borne Radar Measurements at Normal Incidence. *J.Geophys.Res.*, 84(B8), 3974-3978.
- Brown, G.S. & Curry, W.J. 1977. The estimation of pointing angle and σ_0 from GEOS-3 radar altimeter measurements. NASA CR 141426, Wallops Flight Center, Wallops Is., Va., 101pp.
- Brown, N.L. & Hamon, B.V. 1961. An inductive salinometer. *Deep-Sea Res.*, 8, 65-75.
- Brown, R.D. & Hutchinson, M.K. 1980. Ocean Tide Determination from Satellite Altimetry. Presented at COSPAR/SCOR/IUCRM Symposium Oceanography From Space, Venice, Italy, May 26-30 1980.
- Brown, Jr., W.E., Elachi, C. & Thompson, T.W. 1976. Radar Imaging of Ocean Surface Patterns. *J.Geophys.Res.*, 81(15), 2657-2667.
- Bryan, K. & Cox, M.D. 1968a. A nonlinear model of an ocean driven by wind and differential heating: Part I. Description of three-dimensional velocity and density fields. *J.Met.*, 25, 945-967.
- Bryan, K. & Cox, M.D. 1968b. A nonlinear model of an ocean driven by wind and differential heating: Part II. An analysis of the heat, energy, and vorticity balance. *J.Met.*, 25, 968-978.
- Busch, N.E. 1977. Fluxes in the Surface Boundary Layer over the Sea. In: *Modelling and Prediction of the Upper Layers of the Ocean*, E.B. Krauss, (ed.), Pergamon Press, 72-91.
- Cartwright, D.E. 1977. Oceanic Tides. *Rep. Progr. Phys.*, 40, 665-708.
- Cartwright, D.E., Edden, A.C., Spencer, R. & Vassie, J.M. 1980. The Tides of the Northeast Atlantic Ocean. *Phil.Trans.R.Soc.Lond.*, A1436, 87-139.
- Cazenave, A. & Daillet, S. 1977. Determination de la maree oceanique M2 avec STARLETTE. Internal Report of the Groupe de Recherches de Geodesie Spatiale, Centre Nationale d'Etudes Spatiales, Toulouse, 39pp.
- Cazenave, A., Daillet, S. & Lambeck, K. 1977. Tidal Studies from the perturbations in satellite orbits. *Trans.R.Soc.Lond.*, A284, 595-606.
- Cheney, R.E. 1975. A Comparison of Various Gulf Stream Ring Structures. NOAA/NWS, *Gulfstream*, 1(7), July 1975.
- Cheney, R.E. 1977. Synoptic Observations of the Oceanic Frontal System East of Japan. *J.Geophys.Res.*, 82(34), 5459-5468.
- Cheney, R.E. & Marsh, J.G. 1980a. Oceanographic Evaluation of Geoid Surfaces in the western North Atlantic. Paper presented at Symposium on Oceanography from Space, Venice, Italy, May 26-30 1980.

- Cheney, R.E. & Marsh, J.G. 1980b. SEASAT Altimeter Observations of Dynamic Topography in the Gulf Stream Region. *J.Geophys.Res.*, 86(C1), 473-483.
- Cheney, R.E. & Richardson, P.L. 1976. Observed Decay of a cyclonic Gulf Stream ring. *Deep-Sea Res.*, 23, 143-155.
- Cheney, R.E., Richardson, P.L. & Nagasaka, K. 1980. Tracking a Kuroshio cold ring with a free-drifting surface buoy. *Deep-Sea Res.*, 27A, 641-654.
- Cheney, R.E., Gemmill, W.H., Shank, M.K., Richardson, P.L. & Webb, D. 1976. Tracking a Gulf Stream Ring with SOFAR floats. *J.Phys.Oceanogr.*, 6, 741-749.
- Coleman, R. 1980. On the Recovery of Ocean Dynamic Information from Satellite Altimetry. *Marine Geodesy*, 4(4), 351-386.
- Coleman, R. 1981. East Australian Current Study using Satellite Altimetry. (in prep.)
- Coleman, R. & Mather, R.S. 1978. On the determination of Time Varying Features in the Sea Surface Topography using GEOS-3 Altimetry. *EOS Trans.Am.Geophys.Union*, 59(4), 259.
- Coleman, R., Rizos, C., Masters, E.G. & Hirsch, B. 1979. The Investigation of the Sea Surface Slope Along the North Eastern Coast of Australia. *Aust.J.Geod.Photo.Surv.*, 31, 65-99.
- Collar, P.G. & Cartwright, D.E. 1972. Open sea tidal measurements near the edge of the northwest European continental shelf. *Deep-Sea Res.*, 19, 673-689.
- Colombo, O.L. 1980a. A World Vertical Network. Rep. No. 296, Dept. of Geodetic Science, Ohio State Univ., 63pp.
- Colombo, O.L. 1980b. Transoceanic Vertical Datum Connections. Paper presented at the NAD Symposium on Problems Related to the Redefinition of North American Vertical Geodetic Networks, Ottawa, May 26-30, 1980.
- Crepon, M. 1973. Sea Level, Atmospheric pressure and geostrophic adjustment. Woods Hole Oceanographic Institute Contribution 3208, Woods Hole Oceanographic Institute, Mass., 30pp.
- Cresswell, G.R. 1973. The French-Australian satellite buoy experiment. *Aust.Meteor.Mag.* 21, 1-17.
- Cresswell, G.R. 1976. A Drifting Buoy Tracked by Satellite in the Tasman Sea. *Aust.J.mar.Freshwat.Res.*, 27, 251-262.
- Cresswell, G.R. 1977. The trapping of two drifting buoys by an ocean eddy. *Deep-Sea Res.*, 24, 1203-1209.
- Cresswell, G.R. 1979. Techniques For Ocean Current Studies in the 200 Mile Economic Zone. Presented at Aust.Symp.on Ship Technology - The Impact of 200 Mile Economic Zones, Univ.of New South Wales, Sydney, 5-7

November, 1979.

Cresswell, G.R. & Garrett, J. 1980. The Response of Drogued and Undrogued Drifting Buoys to Eddies and the Wind. CSIRO Division of Fisheries and Oceanography Report 115, Cronulla, Australia.

Cresswell, G.R. & Golding, T.J. 1979. Satellite-tracked buoy data report III. Indian Ocean 1977. Tasman Sea July-December 1977. CSIRO Division of Fisheries and Oceanography Report 101, Cronulla, Australia.

Cresswell, G.R. & Grieg, M.A. 1979. Satellite tracked buoy report IV. South west Pacific Ocean January-June 1978. CSIRO Division of Fisheries and Oceanography Report 104, Cronulla, Australia.

Cresswell, G.R. & Nilsson, C.S. 1979. The Formation and Evolution of Eddy "B" 1977/78. CSIRO Aust.Div.Fish.Oceanogr.Internal Report - May 1979.

Cresswell, G.R. & Wood, J.E. 1977. Satellite-Tracked Buoy Data Report II. Tasman Sea Releases November 1976-July 1977. CSIRO Aust.Div.Fish. Oceanogr.Rep.No.91.

Cresswell, G.R., Richardson, G.T., Wood, J.E. & Watts, R. 1978. The CSIRO Satellite-Tracked "Torpedo" Buoy. CSIRO Aust.Div.Fish. Oceanogr.Rep.No.82.

CSIRO Aust. 1962. Oceanographical observations in the Pacific Ocean in 1960. H.M.A.S. Gascoyne Cruises G1/60 and G2/60. Oceanogr.Cruise Report. CSIRO Aust., 5, 255pp.

Dantzler, Jr., H.L. 1976a. Geographic variations in intensity of the North Atlantic and North Pacific oceanic eddy fields. Deep-Sea Res., 23, 783-794.

Dantzler, Jr., H.L. 1976b. 13° Isotherm Displacement Statistics. Polymode News, 5, March 19 1976.

Diamante, J.M. & Nee, T. 1980. Application of satellite radar altimeter data to the determination of regional tidal constituents and the mean sea surface. Presented at the COSPAR/SCOR/IUCRM Symposium Oceanography from Space, Venice, Italy, May 26-30 1980.

Dickinson, D.F., Grossi, M.D. & Pearlman, M.R. 1970. Refractive corrections in high-accuracy radio interferometry. J.Geophys.Res., 75, 1619-1621.

Doblar, R.A. & Cheney, R.E. 1977. Observed Formation of a Gulf Stream Cold Core Ring. J.Phys.Oceanogr., 7, 944-946.

Douglas, B.C. 1979. Comment on 'Mapping ocean tides with satellites: A Computer Simulation' by I.J.Won, J.T.Kuo & R.C.Jackens. J.Geophys.Res., 84(B12), 6909-6910.

Douglas, B.C. & Gaborski, P.D. 1979. Observation of Sea Surface Topography with GEOS-3 Data. J.Geophys.Res., 84(B8), 3893-3896.

- Douglas, B.C. & Goad, C.C. 1978. The role of orbit determination in satellite altimeter data analysis. *Boundary-Layer Meteorology*, 13, 245-251.
- Düing, W. 1978. Spatial and Temporal Variability of Major Ocean Currents and Mesoscale Eddies. *Boundary-Layer Meteorology*, 13, 7-22.
- Eaton, W.T. & Munster, A.C. 1977. Application of Satellite-Borne Synthetic Aperture Radar to Marine Operations. AIAA/AGU/AMS/IEEE/MTS/SEG Conference on Satellite Applications to Marine Technology, New Orleans, La., November 15-17, 1977, Paper 77-1610, 11pp.
- Estes, R.H. 1977. A Computer Software System for the Generation of Global Ocean Tides Including Self-Gravitation and Crustal Loading Effects. NASA/GSFC Rep. X-920-77-82, Goddard Space Flight Center, Greenbelt, Md., 59pp.
- Estes, R.H. 1979. A Simulation of Global Ocean Tide Recovery Using Altimeter Data with Systematic Orbit Error. *Marine Geodesy*, 3, 75-139.
- Fairbridge, R.W. 1966. *The Encyclopedia of Oceanography*. Vol 1. Reinhold Pub. Co., New York.
- Farrell, W.E. 1972a. Deformation of the earth by surface loads. *Rev. Geophys. Space Phys.*, 10(3), 761-797.
- Farrell, W.E. 1972b. Global calculations of tidal loading. *Nature*, 238, 43-44.
- Farrell, W.E. 1973. Earth tides, ocean tides, and tidal loading. *Phil. Trans. Roy. Soc. London, Ser. A*, 274, 253-259.
- Fedor, L.S., Godbey, T.W., Gower, J.F.R., Guptill, R., Hayne, G.S., Rufenach, C.L. & Walsh, E.J. 1979. Satellite Altimeter Measurements of Sea State - An Algorithm Comparison. *J. Geophys. Res.*, 84(B8), 3991-4002.
- Felsentreger, T.L., Marsh, J.G. & Williamson, R.G. 1978. Tidal Perturbations on the Satellite 1967-92A. *J. Geophys. Res.*, 83, 1837-1842.
- Felsentreger, T.L., Marsh, J.G. & Williamson, R.G. 1979. M2 Ocean Tide Parameters and the Deceleration of the Moon's Mean Longitude from Satellite Orbit Data. *J. Geophys. Res.*, 84(B9), 4675-4679.
- Filloux, J.H. 1971. Deep sea tide observations from the north-eastern Pacific. *Deep-Sea Res.*, 18, 275-284.
- Fornshell, J. 1977. XBT transect through a warm core eddy. NOAA/NWS, Gulfstream, III(9), September 1977.
- Fomin, L.M. 1964. *The Dynamic Method in Oceanography*. Elsevier, Amsterdam, 212 pp.
- Freeland, H.J. & Gould, W.J. 1976. Objective analysis of mesoscale ocean circulation features. *Deep-Sea Res.*, 23, 915-923.
- Freeland, H.J., Rhines, P.B. & Rossby, H.T. 1975. Statistical

observations of the trajectories of neutrally buoyant floats in the North Atlantic. *J.Mar.Res.*, 33, 383-404.

Fuglister, F.C. 1947. Hydrography of the western North Atlantic, hydrography of the Northwestern Sargasso Sea. Woods Hole Oceanographic Institute Tech. Rep. No. 4, Woods Hole, Ma.

Fuglister, F.C. 1951. Annual variations in current speeds in the Gulf Stream System. *J.Mar.Res.*, 10(1), 119-127.

Fuglister, F.C. 1963. Gulf Stream '60. *Progr.Oceanogr.*, 1, 265-385.

Fuglister, F.C. 1972. Cyclonic rings formed by the Gulf Stream, 1965-1966. In: *Studies in Physical Oceanography, a tribute to Georg Wunst on his 80th birthday*, A.L.Gordan, (ed.), Gordan & Breach, Vol I, 137-168.

Fuglister, F.C. 1977. A cyclonic ring formed by the Gulf Stream 1967. In: *A Voyage of Discovery*, Pergamon Press, 177-198.

Fuglister, F.C. & Worthington, L.V. 1951. Some Results of a multiple ship survey of the Gulf Stream. *Tellus*, 3(1), 1-14.

Gaborski, P. 1979. Observations of mesoscale circulation phenomena using Seasat altimeter data and digital infrared imagery. *EOS Trans.Amer.Geophys.Union*, 60(18), 232.

Gaposchkin, E.M. 1974. Earth's gravity field to the eighteenth degree and geocentric coordinates for 104 stations from satellite and terrestrial data. *J.Geophys.Res.*, 76, 5377-5411.

Gaposchkin, E.M. 1978. Recent Advances in Analytical Satellite Theory. Proc. of the 9th GEOP Conference, Symp. on the Applications of Geodesy to Geodynamics, October 2-5, 1978, Rep. No. 280, Dept. of Geodetic Science, Ohio State Univ., Columbus, Ohio.

Gaposchkin, E.M. 1980. Global gravity field from GEOS-3 satellite altimetry and other data. *J.Geophys.Res.*, 85(B12), 7221-7234.

Gaposchkin, E.M. & Lambeck, K. 1971. Earth's gravity field to the sixteenth degree and station coordinates from satellite and terrestrial data. *J.Geophys.Res.*, 76, 4855-4883.

Garrett, C. 1979. Topographic Rossby Waves off East Australia: Identification and Role in Shelf Circulation. *J.Phys.Oceanogr.*, 9, 244-253.

GEOS-C. 1972. GEOS-C Mission: Proposal Briefing Information, December 13, 1972. NASA/Wallops Flight Center, Wallops Island, Va.

Gloersen, P. & Barath, F.T. 1976. The SEASAT-A Scanning Multichannel Microwave Radiometer. *Oceans 76 Conference Record*, MTS-IEEE, 10C.1-10C.8.

Goad, C.C. & Douglas, B.C. 1977. Determination of M2 ocean tide parameters from satellite orbit perturbations. *J.Geophys.Res.*, 82,

898-900.

Goad, C.C. & Martin, C.F. 1977. Effects of Tropospheric and Ionospheric Refraction Errors in the Utilisation of GEOS-C Altimeter Data. NASA CR 141427, Wallops Flight Center, Wallops Is., Va., 55pp.

Godbey, T.W. 1965. Oceanographic satellite radar altimeter and wind sea sensor. Oceanography in Space, Ref. 65-10, Woods Hole Oceanographic Institute, Woods Hole, Ma., 21-26.

Godfrey, J.S. 1973a. On the dynamics of the western boundary current in Bryan and Cox's (1968) numerical ocean model. Deep-Sea Res. 20, 1043-1058.

Godfrey, J.S. 1973b. Comparison of the East Australian Current with the western boundary flow in Bryan and Cox's (1968) numerical model ocean. Deep-Sea Res., 20, 1059-1076.

Godfrey, J.S. & Robinson, A.R. 1971. The East Australian Current as a Free Inertial Jet. J.mar.Res., 29, 256-280.

Godfrey, J.S., Cresswell, G.R. & Boland, F.M. 1980a. Observations of Low Richardson Numbers and Undercurrents near a Front in the East Australian Current. J.Phys.Oceanogr., 10, 301-307.

Godfrey, J.S., Cresswell, G.R., Golding, T.J., Pearce, A.F. & Boyd, R. 1980b. The Separation of the East Australian Current. J.Phys.Oceanogr., 10, 430-440.

Gonzalez, F.I., Beal, R.C., Brown, W.E., DeLeonibus, P.S., Sherman III, J.W., Gower, J.F.R., Lichy, D., Ross, D.B., Rufenach, C.L. & Shuchman, R.A. 1979. Seasat Synthetic Aperture Radar: Ocean Wave Detection Capabilities. Science, 204(4400), 1418-1421.

Gordon, A.L. & Baker, T.N. 1980. Ocean Transients as Observed by GEOS-3 Coincident Orbits. J.Geophys.Res., 85(C1), 502-506.

Gotthardt, G.A. 1973. Observed Formation of a Gulfstream Anticyclonic Ring. J.Phys.Oceanogr., 3, 237-238.

Gotthardt, G.A. & Potocsky, G.J. 1974. Life Cycle of a Gulf Stream Anticyclonic Eddy Observed from Several Oceanographic Platforms. J.Phys.Oceanogr., 4, 131-134.

Gower, J.F.R. 1979. The Computation of Ocean Wave Heights from GEOS-3 Satellite Radar Altimeter Data. Remote Sensing of Environment, 8, 97-114.

Gower, J.F.R., (ed.). 1980. Boundary-Layer Meteorology, 18, Nos. 1, 2 & 3.

Grantham, W.L., Bracalente, E.M. & Jones, W.L. 1976. The Seasat-A Satellite Scatterometer. Oceans 76 Conference Record, MTS-IEEE, 10D.1-10D.9.

Grantham, W.L., Bracalente, E.M., Jones, W.L., Shrader, J.H., Schroeder,

L.C. & Mitchell, J.L. 1975. An Operational Satellite Scatterometer for Wind Vector Measurements over the Ocean. NASA TM X-72672, Goddard Space Flight Center, Greenbelt, Md.

Greenwood, J.A., Nathan, A., Neumann, G., Pierson, W.J., Jackson, F.C. & Pease, T.E. 1969a. Radar Altimetry from a Spacecraft and Its Potential Applications to Geodesy. *Remote Sensing of Environment*, 1, 59-70.

Greenwood, J.A., Nathan, A., Neumann, G., Pierson, W.J., Jackson, F.C. & Pease, T.E. 1969b. Oceanographic Applications of Radar Altimetry from a Spacecraft. *Remote Sensing of Environment*, 1, 71-80.

Hagan, D.E., Olson, D.B., Schmitz, J.E. & Vastano, A.C. 1978. A Comparison of Cyclonic Ring Structures in the Northern Sargasso Sea. *J.Phys.Oceanogr.*, 8, 997-1008.

Halliwell, Jr., G.R. & Mooers, C.N.K. 1979. The space-time structure and variability of the shelf water-slope water and Gulf Stream surface temperature fronts and associated warm core eddies. *J.Geophys.Res.*, 84(C12), 7707-7725.

Hammond, D.L. Mennalla, R.A. & Walsh, E.J. 1977. Short pulse radar used to measure sea surface wind speed and SWH. *IEEE Trans.*, AP-25, 61-65.

Hamon, B.V. 1961. The Structure of the East Australian Current. Technical Paper No.11, CSIRO Aust.Div.Fish.Oceanogr.

Hamon, B.V. 1962a. Current, temperature and salinity measurements in physical oceanography. *Navigation*, 1(4), 27-34.

Hamon, B.V. 1962b. The spectrums of mean sea level at Sydney, Coffs Harbour and Lord Howe Island. *J.Geophys.Res.*, 67, 5147-5155.

Hamon, B.V. 1965. The East Australian Current, 1960-1964. *Deep-Sea Res.*, 12, 899-921.

Hamon, B.V. 1966. Continental Shelf Waves and the Effects of Atmospheric Pressure and Wind Stress on Sea Level. *J.Geophys.Res.*, 71(12), 2883-2893.

Hamon, B.V. 1968a. Spectrum of sea level at Lord Howe Island in relation to circulation. *J.Geophys.Res.*, 73, 6925-6927.

Hamon, B.V. 1968b. Temperature structure in the upper 250 meters in the East Australian Current area. *Aust.J.mar.Freshwat.Res.*, 19, 91-99.

Hamon, B.V. 1969. A review of "current effect" on sea level. Report No.46, CSIRO Aust.Div.Fish.Oceanogr.

Hamon, B.V. 1970. Western boundary currents in the South Pacific. Proceedings SCOR Symposium on the South Pacific, National Academy of Sciences, U.S.A., 50-59.

Hamon, B.V. & Cresswell, G.R. 1972. Structure functions and intensities off east and west Australia. *Aust.J.mar.Freshwat.Res.*, 23, 99-103.

- Hamon, B.V. & Grieg, M.A. 1972. Mean Sea Level in Relation to Geodetic Land Leveling around Australia. *J.Geophys.Res.*, 77(36), 7157-7162.
- Hamon, B.V. & Kerr, J.D. 1968. Time and space scales of variations in the East Australian Current, from merchant ship data. *Aust.J.mar.Freshwat.Res.*, 19, 101-106.
- Hamon, B.V. & Stacey, F.D. 1960. Sea-levels around Australia during the International Geophysical Year. *Aust.J.mar.Freshwat.Res.*, 11, 269-281.
- Hamon, B.V., Godfrey, J.S. & Grieg, M.A. 1975. Relation between mean sea level, current and wind stress on the East coast of Australia. *Aust.J.mar.Freshwat.Res.*, 26, 389-403.
- Hansen, D.V. 1970. Gulf Stream meanders between Cape Hatteras and the Grand Banks. *Deep-Sea Res.*, 17, 495-511.
- Hanson, K.J. 1972. Remote Sensing of the Ocean. In: Remote Sensing of the Troposphere, V.E. Derr, (ed.), U.S. Govt. Printing Office, Washington, D.C., 22.1-22.56.
- Hayne, G.S. 1980. Wallops Waveform Analysis of SEASAT-1 Radar Altimeter Data. NASA CR 156869, Wallops Flight Center, Wallops Is., Va., 43pp.
- Hayne, G.S., Miller, L.S. & Brown, G.S. 1977. Altimeter Waveform Software Design. NASA CR 141419, Wallops Flight Center, Wallops Is., Va., 128pp.
- Heiskanen, W.A. & Moritz, H. 1967. Physical Geodesy. W.H.Freeman & Co., San Francisco, 364 pp.
- Hendershott, M.C. 1972. The effects of solid earth deformation on global ocean tides. *Geophys.J.Roy.astr.Soc.*, 29, 389-402.
- Hendershott, M.C. 1973. Ocean Tides. *EOS, Trans.Am.Geophys. Union*, 54(2), 76-86.
- Hendershott, M.C. & Munk, W.H. 1970. Tides. *Annu.Rev.Fluid Mech.*, 2, 205-224.
- Hirvonen, R.A. 1960. New Theory of the Gravimetric Geodesy. *Publ.Inst.Geod.,Photogramm. and Cartography*, No. 9, Ohio State Univ., Columbus, Ohio.
- Huang, N.E. 1979. New Developments in Satellite Oceanography and Current Measurements. *Rev.Geophys.Space Phys.*, 17(7), 1558-1568.
- Huang, N.E., Leitao, C.D. & Parra, C.G. 1978. Large-Scale Gulf Stream Frontal Study using GEOS-3 Radar Altimeter Data. *J.Geophys.Res.*, 83(C9), 4673-4682.
- Hynd, J.S. 1969. Isotherm maps for tuna fisherman. *Australian Fisheries*, 28(7), 13-22.
- IAG. 1971. Geodetic Reference System 1967, Special Publication. International Association of Geodesy, Paris.

- Iselin, C.O'D. 1936. A study of the circulation of the western North Atlantic. *Pap.Phys.Oceanogr.Met.*, 4(4), 101pp.
- Iselin, C.O'D. 1940. Preliminary report on long period variations in the transport of the Gulf Stream. *Pap.Phys.Oceanogr.Met.*, 8(1), 39pp.
- Iselin, C.O'D. & Fuglister, F.C. 1948. Some recent developments in the study of the Gulf Stream. *J.Mar.Res.*, 7, 317-329.
- Jackson, F.C. 1979. The Reflection of Impulses from a Non-Linear Random Sea. *J.Geophys.Res.*, 84(C8), 4939-4943.
- Kao, T.W. 1980. The dynamics of oceanic fronts, I, The Gulf Stream. *J.Phys.Oceanogr.*, 10, 483-492.
- Kao, T.W. & Cheney, R.E. 1980. The Gulf Stream Front: A Comparison between SEASAT altimeter observations and theory. *J.Phys.Oceanogr.*, (in press).
- Kaula, W.M. 1966. *Theory of Satellite Geodesy*. Blaisdell Publ. Co., Waltham, Ma., 124pp.
- Kaula, W.M.(ed.). 1970. *The Terrestrial Environment: Solid Earth and Ocean Physics*. NASA CR 1579, National Aeronautics and Space Administration, Washington, D.C.
- Kearsley, A.H.W. 1977. The Prediction and Mapping of Geoid Undulations from GEOS-3 Altimetry. Rep. No. 267, Dept. of Geodetic Science, Ohio State Univ., Columbus, Ohio, 68pp.
- Kirwan, Jr., A.D., McNally, G. & Coehlo, J. 1976. Gulf Stream Kinematics inferred from satellite tracked drifters. *J.Phys.Oceanogr.*, 6, 750-755.
- Kirwan, Jr., A.D., McNally, G., Chang, M.S. & Molinari, R. 1975. The effect of wind and surface currents on drifters. *J.Phys.Oceanogr.*, 5, 361-368.
- Krarup, T. 1969. A contribution to the mathematical foundation of physical geodesy. Danish Geodetic Institute, Rep. No. 44, Copenhagen, Denmark.
- Kraus, E.B., (ed.). 1977. *Modelling and prediction of the upper layers of the ocean*. Pergamon Press, 325pp.
- Ku, L. 1978. The Computation of Tides, Satellite and Geoidal Heights from Altimeter Data. EOS, *Trans.Am.Geophys. Union*, 59(4), 261.
- Kumar, M. & Soler, T. 1981. 1978 Southern Californian Releveling and Its Implications with respect to the Sea Surface Slope Problem. Submitted to *Marine Geodesy*.
- Kundu, P.K. 1980. A Numerical Investigation of Mixed-Layer Dynamics. *J.Phys.Oceanogr.*, 10, 220-236.
- Kuznetsov, M.V. 1972. Calculation of the Secular Retardation of the Earth's Rotation from up-to-date Cotidal Charts. *Izv.Acad.Sci.USSR*

Phy.Solid Earth, 779-784.

Lai, D.Y. & Richardson, P.L. 1977. Distribution and Movement of Gulf Stream Rings. *J.Phys.Oceanogr.*, 7, 670-683.

Lambeck, K. 1975. Effects of Tidal Dissipation in the Oceans on the Moon's Orbit and the Earth's Rotation. *J.Geophys.Res.*, 80, 2917-2925.

Lambeck, K. 1980. *The Earth's Variable Rotation: Geophysical Causes and Consequences.* Cambridge Univ. Press, Cambridge, 449pp.

Lambeck, K., Cazenave, A. & Balmino, G. 1974. Solid Earth and Ocean Tides Estimated from Satellite Orbit Analyses. *Rev. Geophys. Space Phys.*, 12, 421-434.

Lambeck, K., Coleman, R. & Hirsch, B. 1980. A Geophysical Discussion of the Oceanic Geoid for the Southwest Pacific. Paper presented at Second Int. Workshop on Geology, Mineral Resources and Geophysics of the South Pacific, Noumea, New Caledonia, 9-15 October 1980.

Lambeck, K., Coleman, R. & Nakiboglu, S.M. 1981. Isostatic response of the Tasman Seamounts. (in prep.)

Larden, D.R. & Bender, P.L. 1980. Expected Accuracy of geodetic baseline determinations using the GPS reconstructed carrier phase method. *Bull.Geod.* (in prep).

Lawrence, M.W. 1979. The Prospect of Ocean Current Forecasting on the East Australian Coast. Presented at Aust.Symp. on Ship Technology - The Impact of 200 Mile Economic Zones, Univ. of New South Wales, Sydney, 5-7 November, 1979.

Legeckis, R. 1975. Application of synchronous meteorological satellite data to the study of time dependent sea surface temperature change along the boundary of the Gulf Stream. *Geophys.Res.Lett.*, 2(10), 435-438.

Legeckis, R. 1977. Oceanic polar front in the Drake Passage - Satellite observations during 1976. *Deep-Sea Res.*, 24, 701-704.

Legeckis, R. 1978. A Survey of Worldwide Sea Surface Temperature Fronts Detected by Environmental Satellites. *J.Geophys.Res.*, 83(C9), 4501-4522.

Legeckis, R. 1979. Satellite Observations of the Influence of Bottom Topography on the Seaward Deflection of the Gulf Stream off Charleston, South Carolina. *J.Phys.Oceanogr.*, 9, 483-497.

Leitao, C.D., Huang, N.E. & Parra, C.G. 1977. Ocean Current Surface Measurement using Dynamic Elevations Obtained by the GEOS-3 Altimeter. Proc. AIAA Symposium on Satellite Applications to Marine Technology, New Orleans, November 15-17 1977, 43-49.

Leitao, C.D., Huang, N.E. & Parra, C.G. 1978a. Remote Sensing of Gulf Stream Using GEOS-3 Radar Altimeter. NASA Tech. Paper 1209, NASA/Wallops Flight Center, Wallops Is., Va., 31pp.

Leitao, C.D., Huang, N.E. & Parra, C.G. 1978b. Final Report of GEOS-3 Ocean Current Investigation Using Radar Altimeter Profiling. NASA TM 73280, Wallops Flight Center, Wallops Is., Va., 31pp.

Leitao, C.D., Huang, N.E. & Parra, C.G. 1979a. A Note on the Comparison of Radar Altimetry with IR and In Situ Data for the Detection of the Gulf Stream Surface Boundaries. *J.Geophys.Res.*, 84(B8), 3969-3973.

Leitao, C.D., Huang, N.E. & Parra, C.G. 1979b. The Variation of Geostrophic Kinetic Energy over the Northwestern Atlantic Ocean. Paper presented at Interdisciplinary Symp. No. 19, Geodetic Applications to Oceanography, Canberra, Australia, Dec 3-15, 1979.

Lelgemann, D. 1976. Some Problems Concerned with the Geodetic Use of High Precision Altimeter Data. Rep. No. 237, Dept. of Geodetic Science, Ohio State Univ., 62 pp.

Lerch, F.J., Belott, R.P., Klosko, S.M. & Litkowski, E.M. 1978b. Laser Reference Orbits and Altimeter Validation for GEOS-3. Presented at the Marine Geodesy Symposium, Univ. of Miami, Miami, Florida, September, 1978.

Lerch, F.J., Klosko, S.M., Laubscher, R.S. & Wagner, C.A. 1977. Gravity Model Improvement Using GEOS-3 (GEM9 and GEM10). NASA/GSFC Rep. X-921-77-246, Goddard Space Flight Center, Greenbelt, Md., 121pp.

Lerch, F.J., Marsh, J.G., Klosko, S.M. & Williamson, R.G. 1980. Gravity Model Improvement for SEASAT. Submitted to *J.Geophys.Res.*

Lerch, F.J., Wagner, C.A., Richardson, J.A. & Brown, J.E. 1974. Goddard Earth Models (5 and 6). Rep. X-921-74-145, NASA/Goddard Space Flight Center, Greenbelt, Md., 100pp + App.

Lerch, F.J., Wagner, C.A., Klosko, S.M., Belott, R.P., Laubscher, R.E. & Taylor, W.A. 1978a. Gravity Model Improvement Using GEOS-3 Altimetry (GEM10A and 10B). Presented at AGU Spring Meeting, Miami Beach, Florida, April, 1978.

Levitus, S. & Dort, A.H. 1977. Global Analysis of Oceanographic Data. *Bull.Ameri.Met.Soc.*, 58(12), 1270-1284.

Linwood Jones, W., Black, P.G., Boggs, D.M., Bracalente, E.M., Brown, R.A., Dome, G., Ernst, J.A., Halberstam, I.M., Overland, J.E., Peteherych, S., Pierson, W.J., Wentz, F.J., Woiceshyn, P.M. & Wurtele, M.G. 1979. Seasat Scatterometer: Results of the Gulf of Alaska Workshop. *Science*, 204(4400), 1413-1415.

Lipes, R.G., Bernstein, R.L., Cardone, V.J., Katsaros, K.B., Njoku, E.G., Riley, A.L., Ross, D.B., Swift, C.T. & Wentz, F.J. 1979. Seasat Scanning Multichannel Microwave Radiometer: Results of the Gulf of Alaska Workshop. *Science*, 204(4400), 1415-1417.

Lisitzin, E. 1974. *Sea Level Changes*. Elsevier, Amsterdam, 286pp.

Luther, D.S. & Wunsch, C. 1975. Tidal charts of the Central Pacific Ocean. *J.Phys.Oceanogr.*, 5, 222-230.

Luyten, J.R. 1977. Scales of motion in the deep Gulf Stream and across the continental rise. *J.Mar.Res.*, 35, 49-74.

Mader, G.L. A Revised 5' gravimetric geoid and associated errors for the North Atlantic calibration area. NASA CR 156851, Wallops Flight Center, Wallops Is., Va., 28pp.

Malkus, J.S. 1957. Trade cumulus cloud groups: Some observations suggesting a mechanism of their origin. *Tellus*, 9, 33-44.

Mameyev, O.I. 1975. Temperature-Salinity Analysis of World Ocean Waters. Elsevier, Amsterdam, 374pp.

Marsh, J.G. & Chang, E.S. 1976. Global Detailed Gravimetric Geoid. Paper presented at AGU Fall Meeting, San Francisco, California, December 1976.

Marsh, J.G. & Chang, E.S. 1978. Five Minute Detailed Gravimetric Geoid in the North Western Atlantic Ocean. *Marine Geodesy*, 1(3), 253-261.

Marsh, J.G., Martin, T.V., McCarthy, J.J. & Chovitz, P.S. 1979. Estimation of Mean Sea Surfaces in the North Atlantic, the Pacific and the Indian Ocean using GEOS-3 Altimeter Data. NASA TM 79074, Goddard Space Flight Center, Greenbelt, Md., 33pp.

Marsh, J.G., Munteanu, M-J., Martin, T.V., McCarthy, J.J. & Chovitz, P.S. 1978. Estimation of the Mean Sea Surface in the North Atlantic using GEOS-3 Altimeter Data. Paper presented at AGU Spring Meeting, Miami Beach, Florida, April 1978.

Martin, C.F. & Butler, M.L. 1977. Calibration Results for the GEOS-3 Altimeter. NASA CR 141430, Wallops Flight Center, Wallops Is., Va., 123pp.

Martin, T.V., Eddy, W.F., Oh, I.H. & Kogut, J.A. 1976. GEODYN System Description. EG&G Washington Analytical Services Center, Contract No. NAS 5-22849, August 1976.

Masters, E.G., Coleman, R. & Bretreger, K. 1979. On Orbital Errors and the Recovery of Regional Ocean Tide Models Using Satellite Altimetry. *Aust.J.Geod.Photo.Surv.*, 31, 127-152.

Mather, R.S. 1968. The Free Air Geoid for Australia. *Geophys.J.Roy.astr.Soc.*, 16, 515-530.

Mather, R.S. 1971. The Analysis of the Earth's Gravity Field. Monograph 2, Sch. of Surveying, Univ. of New South Wales, Sydney, Australia, 172 pp.

Mather, R.S. 1973a. A Solution of the Geodetic Boundary Problem to order e^3 . Doc. X-592-73-11, NASA/Goddard Space Flight Center, Greenbelt, Md., 128 pp.

Mather, R.S. 1973b. The Gravity Field and the Definition of the Sea Surface Topography. *Veroff.Zentralinst.f.Physik der Erde*, 30(2), 381-414.

Mather, R.S. 1974a. Geoid Definitions for the Study of Sea Surface Topography from Satellite Altimetry. Proc.Symp. Applications of Marine Geodesy, Marine Technology Society, Washington, D.C., 279-289.

Mather, R.S. 1974b. On the Solution of the Geodetic Boundary Value Problem for the Definition of Sea Surface Topography. Geophys.J.Roy.astr.Soc., 39, 87-109.

Mather, R.S. 1974c. Geodetic Coordinates in Four Dimensions. Canadian Surveyor, 28, 574-581.

Mather, R.S. 1974d. Quasi-Stationary Sea Surface Topography and Variations of Mean Sea Level with Time. Unisurv G 21, Sch. of Surveying, Univ. of New South Wales, Sydney, Australia, 18-72.

Mather, R.S. 1975a. Reference Coordinate System Requirements for Geodesy and Ocean Dynamics. In (Kolaczek, B. & Weiffenbach, G.C., (eds.)) Proceedings, International Astronomical Union Colloquium No. 26, Polish Academy of Sciences, Warsaw, 93-114.

Mather, R.S. 1975b. On the Evaluation of Stationary Sea Surface Topography Using Geodetic Techniques. Bull.Geod., 115, 65-82.

Mather, R.S. 1975c. Mean Sea Level and the Definition of the Geoid. Unisurv G 23, Sch. of Surveying, Univ. of New South Wales, Sydney, Australia, 68-79.

Mather, R.S. 1976. Some Possibilities for Recovering Oceanographic Information from the SEASAT Mission. Unisurv G 24, Sch. of Surveying, Univ. of New South Wales, Sydney, Australia, 103-122.

Mather, R.S. 1977. The Analysis of GEOS-3 Altimeter Data in the Tasman and Coral Seas. NASA TM 78032, Goddard Space Flight Center, Greenbelt, Md., 32pp.

Mather, R.S. 1978a. On the Realization of a System of Reference in Four Dimensions for Ocean Dynamics. Boundary-Layer Meteorology, 13, 231-244.

Mather, R.S. 1978b. The Earth's Gravity Field and Ocean Dynamics. NASA TM 79540, Goddard Space Flight Center, Greenbelt, Md., 33pp.

Mather, R.S. 1978c. The Role of the Geoid in Four Dimensional Geodesy. Marine Geodesy, 1(3), 217-252.

Mather, R.S. 1978d. A Geodetic Basis for Ocean Dynamics. Bolletino di Geodesia e Scienze Affini (Marrussi Septennial issue), XXXVII(2-3), 285-308.

Mather, R.S. & Coleman, R. 1977. The Role Of Geodetic Techniques in Remote Sensing the Surface Dynamics of the Ocean. In: Using Space Today and Tomorrow, Napolitano, L.G., (ed.), Pergamon Press, Oxford, 163pp.

Mather, R.S. & Larden, D.R. 1978. On the Recovery of Geodynamic Information from Secular Gravity Changes. Unisurv G 29, Univ. of New South Wales, Sydney, Australia, 11-23.

Mather, R.S. & Rizos, C. 1979. The Shape of the Global Mean Sea Level from GEOS-3 Altimetry. *Aust.J.Geod.Photo.Surv.*, 31, 153-159.

Mather, R.S., Coleman, R. & Hirsch, B. 1978a. The Analysis of Temporal Variations in Regional Models of the Sargasso Sea from GEOS-3 Altimetry. NASA TM 79549, Goddard Space Flight Center, Md., 52pp.

Mather, R.S., Coleman, R. & Hirsch, B. 1980. Temporal Variations in Regional Models of the Sargasso Sea from GEOS-3 Altimetry. *J.Phys.Oceanogr.*, 10, 171-185.

Mather, R.S., Masters, E.G. & Coleman, R. 1977a. The Role of Non-Tidal Gravity Variations in the Maintenance of Reference Systems for Secular Geodynamics. Unisurv G 26, Sch. of Surveying, Univ. of New South Wales, Sydney, Australia, 1-25.

Mather, R.S., Rizos, C. & Coleman, R. 1979b. Remote Sensing of Surface Ocean Circulation with Satellite Altimetry. *Science*, 205(4401), 11-17.

Mather, R.S., Rizos, C. & Morrison, T.S. 1978c. On the Unification of Geodetic Levelling Datums Using Satellite Altimetry. NASA TM 79533, Goddard Space Flight Center, Greenbelt, Md., 30 pp.

Mather, R.S., Coleman, R., Rizos, C. & Hirsch, B. 1977b. A Preliminary Analysis of GEOS-3 Altimeter Data in the Tasman and Coral Seas. Unisurv G26, Sch. of Surveying, Univ. of New South Wales, Sydney, Australia, 27-46.

Mather, R.S., Rizos, C., Coleman, R. & Masters, E.G. 1979a. Geodetic Reference Systems for Crustal Motion Studies. *Tectonophysics*, 52, 15-37.

Mather, R.S., Rizos, C., Hirsch, B. & Barlow, B.C. 1976. An Australian Gravity Data Bank for Sea Surface Topography Determinations (AUSGAD 76). Unisurv G25, Sch. of Surveying, Univ. of New South Wales, Sydney, Australia, 54-84.

Mather, R.S., Lerch, F.J., Rizos, C., Masters, E.G. & Hirsch, B. 1978b. Determination of Some Dominant Parameters of the Global Dynamic Sea Surface Topography from GEOS-3 Altimetry. NASA TM 79558, Goddard Space Flight Center, Greenbelt, Md., 39pp.

Maul, G.A. 1977. Recent Progress in the remote sensing of ocean surface currents. *MTS Journal*, 11, 5-13.

Maul, G.A. & Yanaway, A. 1978. Deep Sea Tides Determination From GEOS-3. NASA CR 141435, Wallops Flight Center, Wallops Is., Va., 26pp.

Maul, G.A., deWitt, P.W., Yanaway, A. & Baig, S.R. 1978. Geostationary Satellite Observations of Gulf Stream Meanders: Infrared Measurements and Time Series Analysis. *J.Geophys.Res.*, 83(C12), 6123-6135.

McAlister, E.D. & McLeish, W. 1969. Heat Transfer in the Top Millimeter of the Ocean. *J.Geophys.Res.*, 74(13), 3408-3414.

McCartney, M.S. 1975. Big babies in the northern Sargasso Sea. *MODE*

- Hotline News, 74, 1-4.
- McCartney, M.S., Worthington, L.V. & Schmitz, Jr., W.J. 1978. Large Cyclonic Rings from the Northeast Sargasso Sea. *J.Geophys.Res.*, 83(C2), 901-914.
- McClain, E.P. & Marks, R.A. 1979. Seasat Visible and Infrared Radiometer. *Science*, 204(4400), 1421-1424.
- McGoogan, J.T., Miller, L.S., Brown, G.S. & Hayne, G.S. 1974. The S-193 Radar Altimeter Experiment. *Proc. IEEE*, 62(6), 795-803.
- Melchior, P. 1978. *The Tides of the Planet Earth*. Pergamon Press, Oxford, 609pp.
- Miles, J. 1974. On Laplace's tidal equations. *J.Fluid Mech.*, 66, 241-260.
- Miller, L.S. 1977. Investigation of the Applications of GEOS-3 Radar Altimeter Data in Remote Sensing of Land and Sea Features. NASA CR 141428, Wallops Flight Center, Wallops Is., Va., 93pp.
- Miller, L.S. & Hayne, G.S. 1972. Characteristics of Ocean-Reflected Short Radar Pulses with Application to Altimetry and Surface Roughness Determination. In: *Sea Surface Topography From Space, Vol I*, J.R. Apel, (ed.), NOAA Tech. Rep., ERL 228-AOML 7, 12.1-12.32.
- Miller, L.S. & Priester, R.W. 1978. An Investigation of the Observability of Ocean Surface Parameters Using GEOS-3 Backscatter Data. NASA CR 156846, Wallops Flight Center, Wallops Is., Va., 109pp.
- MODE Group. 1978. The Mid-Ocean Dynamics Experiment. *Deep-Sea Res.*, 25, 859-910.
- Mofjeld, H.O. 1975. Empirical Models for Tides in the Western North Atlantic Ocean. NOAA Technical Report ERL 340-AOML 19, Boulder, Co., 27pp.
- Molodenskii, M.S., Eremeev, V.F. & Yurkina, M.I. 1962. Methods for the Study of the External Gravitational Field and Figure of the Earth. Israel Program for Scientific Translations, Jerusalem, 248pp.
- Monin, A.S., Kamenkovich, V.M. & Kort, V.G. 1977. Variability of the oceans. John Wiley & Sons, New York, 241pp.
- Montgomery, R.B. 1969. Comments on Oceanic Levelling. *Deep-Sea Res.*, 16, 147-152.
- Moore, R.K. & Williams, Jr., C.S. 1957. Radar Terrain at near vertical incidence. *Proc. IRE*, 45(2), 228-238.
- Morelli, C., Gantar, C., Honkasalo, T., McConnell, R.K., Szabo, B., Tanner, S.G., Uotila, U.A. & Whalen, C.T. 1971. International Gravity Standardisation Network 1971 (IGSN71). Special publication, International Association of Geodesy, Paris, 194pp.

- Moritz, H. 1966. Linear solutions of the geodetic boundary-value problem. Rep. No. 11, Dept. of Geodetic Science, Ohio State Univ.
- Moritz, H. 1969. Non-linear solutions of the geodetic boundary value problem. Rep. No. 126, Dept. of Geodetic Science, Columbus, Ohio.
- Moritz, H. 1974. Precise Gravimetric Geodesy. Rep. No. 219, Dept. of Geodetic Science, Ohio State Univ.
- Moritz, H. 1979. Fundamental Geodetic Constants. Report of Special Study Group No. 5.39 of IAG, XVII General Assembly IUGG, Canberra, Australia, December, 1979.
- Munk, W.H. & MacDonald, G.J.F. 1960. The Rotation of the Earth. London, Cambridge Univ. Press, 323pp.
- Munk, W.H. & Wunsch, C. 1979. Ocean acoustic tomography: a scheme for large scale monitoring. Deep-Sea Res., 26A, 123-161.
- Munk, W.H., Snodgrass, F. & Wimbush, M. 1970. Tides offshore : transition from California coastal to Deep-sea Waters. Geophys.Fluid Dyn., 1, 161-235.
- Nakiboglu, S.M. 1978. Variational Formulation of the Geodetic Boundary Value Problem. Bull.Geod., 52, 93-100.
- NASA. 1972. The Earth and Ocean Physics Applications Program: Vol. 2 Rationale and Program Plans. National Aeronautics and Space Administration, Washington, D.C.
- Neumann, G. 1968. Ocean Currents. Elsevier Oceanography Series. Vol.4, 352pp.
- Neumann, G. & Pierson, W.J. 1966. Principles of Physical Oceanography. Prentice-Hall, Englewood Cliffs, N.J.
- Newell, B.S. 1966. Seasonal changes in the hydrological and biological environments off Port Hacking, Sydney. Aust.J.mar.Freshwat. Res., 17, 77-91.
- Newton, C.W. 1961. Estimates of vertical motions and meridional heat exchange in Gulf Stream eddies and a comparison with atmospheric disturbances. J.Geophys.Res., 66, 853-870.
- Niell, A.E., Ong, K.M., MacDoran, P.F., Resch, G.M., Morabito, D.D., Claflin, E.S. & Dracup, J.F. 1979. Comparison of a radio interferometric differential baseline measurement with conventional geodesy. Tectonophysics, 52, 49-58.
- Nilsson, C.S. & Cresswell, G.R. 1980. The Evolution of East Australian Eddies. (to appear in Progress in Oceanography.)
- Nilsson, C.S., Andrews, J.C. & Scully-Power, P.D. 1977. Observations of Eddy formation off East Australia. J.Phys.Oceanogr., 7(5), 659-669.
- NOAA/National Weather Service. 1975. Gulfstream. Vol. 1(8-12), U.S.

Govt. Printing Office, Washington, D.C.

NOAA/National Weather Service. 1976. Gulfstream. Vol. 2(4-8), U.S. Govt. Printing Office, Washington, D.C.

NOAA/National Weather Service. 1979. Gulfstream, Vol V. United States Govt. Printing Office, Washington, D.C.

Njoku, E.G., Stacey, J.M. & Ross, D. 1978. Preliminary Results from the SEASAT-A Scanning Multichannel Microwave Radiometer. EOS Trans.Amer.Geophys. Union, 59(12), 1092.

Parke, M.E. 1980. Tides on the Patagonian Shelf from SEASAT radar altimeter. Presented at COSPAR/SCOR/IUCRM Symposium Oceanography from Space, Venice, Italy, May 26-30 1980.

Parke, M.E. & Hendershott, M.C. 1980. M2, S2, K1 Models of the Global Ocean Tide on an Elastic Earth. Marine Geodesy, 3, 379-408.

Parker, C.E. 1971. Gulf Stream Rings in the Sargasso Sea. Deep-Sea Res., 18, 981-993.

Parsons, C.L. 1976. Total attenuation measurements of the intertropical convergence zone by satellite altimeter. Bull.Amer.Meteorol.Soc., 57, 1151-1152.

Parsons, C.L. 1979. GEOS-3 Wave Height Measurements: An Assessment during High Sea State Conditions in the North Atlantic. J.Geophys.Res., 84(B8), 4011-4020.

Pekeris, C.L. & Accad, Y. 1969. Solution of Laplace's equation for the M2 tide in the world oceans. Phil.Trans.Roy.Soc.London, Ser.A, 265, 413-436.

Perchal, R.J. 1975. Satellite Imagery of an Anticyclonic Eddy. NOAA/NWS, Gulfstream, I(12), December 1975.

Phillips, O.M. 1977. The dynamics of the upper ocean. Cambridge Univ. Press, Cambridge, 336pp.

Pickard, G.L. 1963. Descriptive Physical Oceanography. Pergamon Press, 200pp.

Pond, S. & Pickard, G.L. 1978. Introductory Dynamic Oceanography. Pergamon Press, 241pp.

Priester, R.W. & Miller, L.S. 1979. Estimation of Significant Wave Height and Wave Height Density Function Using Satellite Altimeter Data. J.Geophys.Res., 84(B8), 4021-4026.

Rapp, R.H. 1975. Comparison of the Potential Coefficient Models of the Standard Earth (II & III) and the GEM5 and GEM6. Bull.Geod., 118, 443-445.

Rapp, R.H. 1979. The Oceanic Geoid. Paper presented at XVII IUGG General Assembly, Canberra, Australia, Dec 3-15 1979.

- Reed, R.K., Ryan, T.V., Hamon, B.V. & Boland, F.M. 1968. New Feature of the East Australian Current. *Nature*, 218, 557-558.
- Reid, Jr., J.L. 1961. On the Geostrophic Flow at the Surface of the Pacific Ocean with Respect to the 1000-Decibar Surface. *Tellus*, 13(4), 489-502.
- Richardson, P.L. 1980. Gulf Stream Ring Trajectories. *J.Phys.Oceanogr.*, 10, 90-104.
- Richardson, P.L., Cheney, R.E. & Mantini, L.A. 1977. Tracking a Gulf Stream Ring with a Free Drifting Buoy. *J.Phys.Oceanogr.*, 7, 580-590.
- Richardson, P.L., Cheney, R.E. & Worthington, L.V. 1978. A Census of Gulf Stream Rings, Spring 1975. *J.Geophys.Res.*, 83(C12), 6136-6144.
- Richardson, P.L., Strong, A.E. & Krauss, J.A. 1973. Gulf Stream eddies: recent observations in the western Sargasso Sea. *J.Phys.Oceanogr.*, 3, 297-301.
- Richman, J.G., Wunsch, C. & Hogg, N.G. 1977. Space and Time Scales of Mesoscale Motion in the Western North Atlantic. *Rev.Geophys.Space Phys.*, 15(4), 385-420.
- Rizos, C. 1980. The Role of the Gravity Field in Sea Surface Topography Studies. *Unisurv S 17*, Sch. of Surveying, Univ. of New South Wales, Sydney, Australia, 299 pp.
- Robinson, A.R. 1964. Continental Shelf Waves and the Response of the Sea Level to Weather Systems. *J.Geophys.Res.*, 69, 367-368.
- Robinson, A.R. & Baker, D.J., (eds.) 1979. Ocean Models and Climate Models. *Dynamics of Atmospheres and Oceans*, Special Issue, 3, 81-523.
- Robinson, A.R. & Niiler, P.P. 1967. The theory of free inertial jets. I: Path and structure. *Tellus*, 19(2), 269-291.
- Robinson, A.R., Harrison, D.E. & Haidvogel, D.B. 1979. Mesoscale Eddies and General Ocean Circulation Models. *Dynamics of Atmospheres and Oceans*, Special Issue, 3, 143-180.
- Rockford, D.J. 1968. The continuity of water masses along the western boundary of the Tasman and Coral Seas. *Aust.J.mar.Freshwat.Res.*, 19, 77-90.
- Ross, D.B. & Cardone, V. 1974. Observations of Oceanic Whitecaps and their Relation to Remote Measurements of Surface Wind Speed. *J.Geophys.Res.*, 79(3), 444-452.
- Rossby, T. & Webb, D. 1970. Observing abyssal motions by tracking Swallow floats in the SOFAR channel. *Deep-Sea Res.*, 15, 359-365.
- Rossby, T. & Webb, D. 1971. The four month drift of a Swallow float. *Deep-Sea Res.*, 18, 1035-1039.
- Rossby, T., Voorhis, A.D. & Webb, D. 1975. A Quasi-Lagrangian study of

mid-ocean variability using long range SOFAR floats. *J.Mar.Res.*, 33, 355-382.

Rufenach, C.L. & Alpers, W.R. 1978. Measurement of Ocean Wave Heights Using the GEOS-3 Altimeter. *J.Geophys.Res.*, 83(C10), 5011-5018.

Sanso, F. 1978. Molodensky's problem in gravity space: A review of the first results. *Bull.Geod.*, 52, 59-70.

Sanso, F. 1979. The Boundary Value Problems in the Representation of the Gravity Field. Paper presented at XVII IUGG General Assembly, Canberra, Australia, Dec 3-15, 1979.

Saunders, P.M. 1970. Corrections for airborne radiation thermometry. *J.Geophys.Res.*, 75(36), 7596-7601.

Saunders, P.M. 1971. Anticyclonic eddies formed from shoreward meanders of the Gulf Stream. *Deep-Sea Res.*, 18, 1207-1219.

Schanda, E., (ed.). 1976. Remote Sensing for environmental sciences. Springer-Verlag, Berlin, 367pp.

Schmitz, Jr., W.J. 1976. Eddy Kinetic Energy in the Deep Western North Atlantic. *J.Geophys.Res.*, 81(27), 4981-4982.

Schmitz, Jr., W.J. 1978. Observations of the vertical distribution of low frequency kinetic energy in the western North Atlantic. *J.Mar.Res.*, 36, 295-310.

Schmitz, Jr., W.J. & Owens, W.B. 1980. Observed and Numerically Simulated Kinetic Energies for MODE Eddies. *J.Phys.Oceanogr.*, 10

Schott, F. & Stommel, H. 1978. Beta spirals and absolute velocities in different oceans. *Deep-Sea Res.*, 25, 961-1010.

Schott, F. & Zantopp, R. 1979. Calculation of Absolute Velocities from Different Parameters in the Western North Atlantic. *J.Geophys.Res.*, 84(C11), 6990-6994.

Schwiderski, E.W. 1979a. Ocean Tides, Part I : Global Ocean Tidal Equations. *Marine Geodesy*, 3, 161-217.

Schwiderski, E.W. 1979b. Ocean Tides, Part II : A Hydrodynamical Interpolation Method. *Marine Geodesy*, 3, 219-255.

Schwiderski, E.W. 1980. On Charting Global Ocean Tides. *Rev.Geophys.Space Phys.*, 18(1), 243-268.

Scully-Power, P.D. 1973. Coral sea flow budgets in winter. *Aust.J.mar.Freshwat.Res.*, 24, 203-215.

Scully-Power, P.D. & Twitchell, P. 1975. Satellite observations of cloud patterns over East Australian Current Anticyclonic Eddies. *Geophys. Res. Lett.*, 2(3), 117-119.

Sessions, M.H., Barnett, T.P. & Wilson, W.S. 1976. The airborne

- expendable bathythermograph. *Deep-Sea Res.*, 23, 779-782.
- Shapiro, A., Uliana, E.A. & Yaplee, B.S. 1972. Radar Pulse Shape Versus Ocean Wave Height. In: *Sea Surface Topography From Space, Vol I*, J.R.Apel, (ed.), NOAA Tech. Rep., ERL 228-AOML 7, 11.1-11.29.
- Silverberg, E.C. 1978. Mobile Satellite Ranging. (In) *Applications of Geodesy to Geodynamics*, Report No. 280, Dept. of Geodetic Science, Ohio State Univ., Columbus, Ohio, 41-46.
- Smith, D.E. 1979. Dynamic Satellite Geodesy. *Rev.Geophys.Space Phys.*, 17(6), 1411-1418.
- Smith, III, S.L. & Chappell, A.C. 1977. Preliminary Eastern Indian Ocean Geoid from GEOS-3 Data. Naval Surface Weapons Center/DLT, Rep., Warfare Analysis Department, 25pp.
- Staelin, D.H., Barrett, A.H., Rosenkranz, P.W., Barath, F.T., Johnson, E.J., Waters, J.W., Wouters, A. & Lenoir, W.B. 1975. The scanning microwave spectrometer (SCAMS) experiment. *The NIMBUS-6 User's Guide*. Goddard Space Flight Center, Greenbelt, Md., 59-86.
- Stanley, H.R. & Dwyer, R.E. 1980. NASA Wallops Flight Center GEOS-3 Altimeter Data Processing Report. NASA Wallops Flight Center, Wallops Is., Va., 128pp.
- Stanton, B.R. 1976. An oceanic frontal jet near the Norfolk Ridge north-west of New Zealand. *Deep-Sea Res.*, 23, 821-829.
- Stengel, K.C. 1979. An Inverse Technique for Obtaining Geostrophic Ocean Currents Independent of Reference Level. *J.Phys.Oceanogr.*, 9, 856-857.
- Stern, M.E. 1975. *Ocean circulation physics*. Academic Press, New York, 246pp.
- Stewart, R.H., (ed.). 1978. *Boundary-Layer Meteorology*, 13, Nos. 1,2,3 & 4, 428pp.
- Stolz, A. 1976a. Changes in the Position of the Geocentre due to Variation in Sea Level. *Bull.Geod.*, 50, 159-168.
- Stolz, A. 1976b. Changes in the Position of the Geocentre due to Seasonal Variations in Air Mass and Groundwater. *Geophys.J.Roy.astr.Soc.*, 44, 19-26.
- Stolz, A. & Larden, D.R. 1979. Seasonal Displacement and Deformation of the Earth by the Atmosphere. *J.Geophys.Res.*, 84(B11), 6185-6194.
- Stommel, H. 1964. Summary charts of the mean dynamic topography and current field at the surface of the ocean, and related functions of the mean wind stress. In: *Studies on Oceanography, dedicated to Prof. Hidaka*, 53-58.
- Stommel, H. 1965. *The Gulf Stream: A Physical and Dynamical Description*. Univ. of California Press, Berkeley, California, 248pp.

- Stommel, H. & Schott, F. 1977. The beta spiral and the determination of the absolute velocity field from hydrographic station data. *Deep-Sea Res.*, 24, 325-329.
- Stumpf, H.G. & Rao, P.K. 1975. Evolution of Gulf Stream eddies as seen in satellite infrared imagery. *J.Phys.Oceanogr.*, 5, 388-393.
- Stumpf, H.G., Strong, A.E. & Pritchard, J. 1973. Large cyclonic eddies of the Sargasso Sea. *Mariners Weather Log*, 17, 208-210.
- Sturges, W. 1967. Slope of sea level along the Pacific coast of the United States. *J.Geophys.Res.*, 72(14), 3627-3637.
- Sturges, W. 1972. Comments on Ocean Circulation with regard to Satellite Altimetry. In: *Sea Surface Topography from Space, Vol II*, J.R. Apel, (ed.), NOAA Tech. Rep., ERL 228-AOML 7, 24.1-24.17.
- Sverdrup, H.U., Johnson, M.W. & Fleming, R.H. 1942. *The Oceans, their Physics, Chemistry and General Biology*. Prentice-Hall, N.J., 1087pp.
- Swallow, J.C. 1955. A neutrally buoyant float for measuring deep currents. *Deep-Sea Res.*, 3, 74-81.
- Szekielda, K. 1976. *Spacecraft Oceanography*. *Oceanogr.Mar.Biol.Ann.Rev.*, 14, 99-166.
- Tapley, B.D., Schutz, B.E., Marsh, J.G., Townsend, W.F. & Born, G.H. 1979a. Accuracy Assessment of the SEASAT Orbit and Altimeter Height Measurement. Phase II Calibration Workshop, Univ. of Texas, TR.79-5, 120pp.
- Tapley, B.D., Born, G.H., Hagar, H.H., Lorell, J., Parke, M.E., Diamante, J.M., Douglas, B.C., Goad, C.C., Kolenkiewicz, R., Marsh, J.G., Martin, C.F., Smith III, S.L., Townsend, W.F., Whitehead, J.A., Byrne, H.M., Fedor, L.S., Hammond, D.C. & Mognard, N.M. 1979b. SEASAT Altimeter Calibration : Initial Results. *Science*, 204(4400), 1410-1412.
- Thompson, T.W. & Laderman, A. 1976. Seasat-A Synthetic Aperture Radar: Radar System Implementation. *Oceans 76 Conference Record, MTS-IEEE*, 10E.1-10E.5.
- Thrane, L. 1978. Evaluation of multi-frequency microwave radiometer system performance for oceanography. *Boundary-Layer Meteorology*, 13, 373-392.
- Townsend, W.F. 1980. An Initial Assessment of the Performance Achieved by the SEASAT-1 Radar Altimeter. NASA TM 73279, Wallops Flight Center, Wallops Is., Va., 31pp.
- Vastano, C.A. & Hagan, D.E. 1977. Observational evidence for transformation of tropospheric waters within cyclonic rings. *J.Phys.Oceanogr.*, 7, 938-943.
- Vukovich, F.M. 1976. An Investigation of a Cold Eddy on the Eastern Side of the Gulf Stream using NOAA-2 and NOAA-3 Satellite Data and Ship Data. *J.Phys.Oceanogr.*, 6, 605-612.

- Vukovich, F.M. & Crissman, B.W. 1978. Further Studies of a Cold Eddy on the Eastern Side of the Gulf Stream Using Satellite and Ship Data. *J.Phys.Oceanogr.*, 8, 838-845.
- Wagner, C.A., Lerch, F.J., Brownd, J.E. & Richardson, J.A. 1976. Improvement in the Geopotential Derived from Satellite and Surface Data (GEM7 and 8). NASA/GSFC Rep. X-921-76-20, Goddard Space Flight Center, Greenbelt, Md., 11pp.
- Walsh, E.J. 1974. Analysis of experimental NRL radar altimeter data. *Radio Sci.*, 9(8,9), 711-722.
- Walsh, E.J. 1979. Extraction of Ocean Wave Height and Dominant Wavelength from GEOS-3 Altimeter Data. *J.Geophys.Res.*, 84(B8), 4003-4010.
- Walsh, E.J., Uliana, E.A. & Yaplee, B.S. 1978. Ocean Wave Heights Measured by a High Resolution Pulse-Limited Radar Altimeter. *Boundary-Layer Meteorology*, 13, 263-276.
- Warren, B.A. 1963. Topographical influences on the path of the Gulf Stream. *Tellus*, 15(2), 167-183.
- Warren, B.A. 1967. Notes on translatory movement of rings of current in the Sargasso Sea. *Deep-Sea Res.*, 14, 505-524.
- Watts, A.B. 1978. Present Status of Marine Gravity. Proc. of the 9th GEOP Conference, Symp. on the Applications of Geodesy to Geodynamics, October 2-5, 1978, Rep. No. 280, Dept. of Geodetic Science, Ohio State Univ., Columbus, Ohio.
- Watts, D.R. & Olson, D.B. 1978. Gulf Stream Ring Coalescence with the Gulf Stream off Cape Hatteras. *Science*, 202, 971-972.
- Wilheit, Jr., T.T. 1978. A Review of Applications of Microwave Radiometry to Oceanography. *Boundary-Layer Meteorology*, 13, 277-293.
- Wilson, U.S. & Dugan, J.P. 1977. Mesoscale Thermal Variability in the vicinity of the Kuroshio extension. *J.Phys.Oceanogr.*, 8, 537-540.
- Won, I.J. & Miller, L.S. 1979. Oceanic Geoid and Tides from GEOS-3 Satellite Data in the Northwestern Atlantic Ocean. *J.Geophys.Res.*, 84, 3833-3842.
- Won, I.J., Kuo, J.T. & Jachens, R.C. 1978. Mapping Ocean Tides with Satellites : A Computer Simulation. *J.Geophys.Res.*, 83, 5947-5960.
- Worthington, L.V. 1976. On the North Atlantic Circulation. Johns Hopkins Oceanographic Ser., Vol. 6, Johns Hopkins Univ. Press, Baltimore, Md., 110pp.
- Wunsch, C. 1972. Bermuda sea level in relation to tides, weather, and baroclinic fluctuations. *Rev.Geophys.Space Phys.*, 10, 1-49.
- Wunsch, C. 1978. The North Atlantic General Circulation West of 50°W Determined by Inverse Methods. *Rev.Geophys.Space Phys.*, 16(4), 583-620.

- Wunsch, C. & Gaposchkin, E.M. 1980. On Using Satellite Altimetry to Determine the General Circulation of the Oceans with Application to Geoid Improvement. *Rev.Geophys.Space Phys.*, 18(4), 725-745.
- Wyrтки, K. 1960. The surface circulation in the Coral and Tasman Sea. Technical Paper No.8, CSIRO Aust.Div.Fish.Oceanogr.
- Wyrтки, K. 1962. Geopotential topographies and associated circulation in the western South Pacific Ocean. *Aust.J.mar.Freshwat. Res.*, 13, 89-105.
- Wyrтки, K. 1975. Fluctuations of the Dynamic Topography in the Pacific Ocean. *J.Phys.Oceanogr.*, 5, 450-459.
- Wyrтки, K., Magaard, L. & Hager, J. 1976. Eddy Energy in the Oceans. *J.Geophys.Res.*, 81(15), 2641-2646.
- Zahel, W. 1978. The influence of solid earth deformations on semidiurnal and diurnal oceanic tides. (In) *Tidal Friction and Earth's Rotation*, (eds.) Brosche, P. & Sundermann, J., Springer, New York, 98-124.
- Zahel, W. 1980. Mathematical Modelling of Global Interaction between Ocean Tides and Earth Tides. *Phys.Earth Planet.Int.*, 21, 202-217.
- Zetler, B.D. & Maul, G.A. 1971. Precision Requirements for a Spacecraft Tide Program. *J.Geophys.Res.*, 76, 6601-6605.

APPENDIX A1.

Results of Overlapping Pass Analyses.

Correlation of IR Imagery with GEOS-3 Altimetry Profiles - September 1975

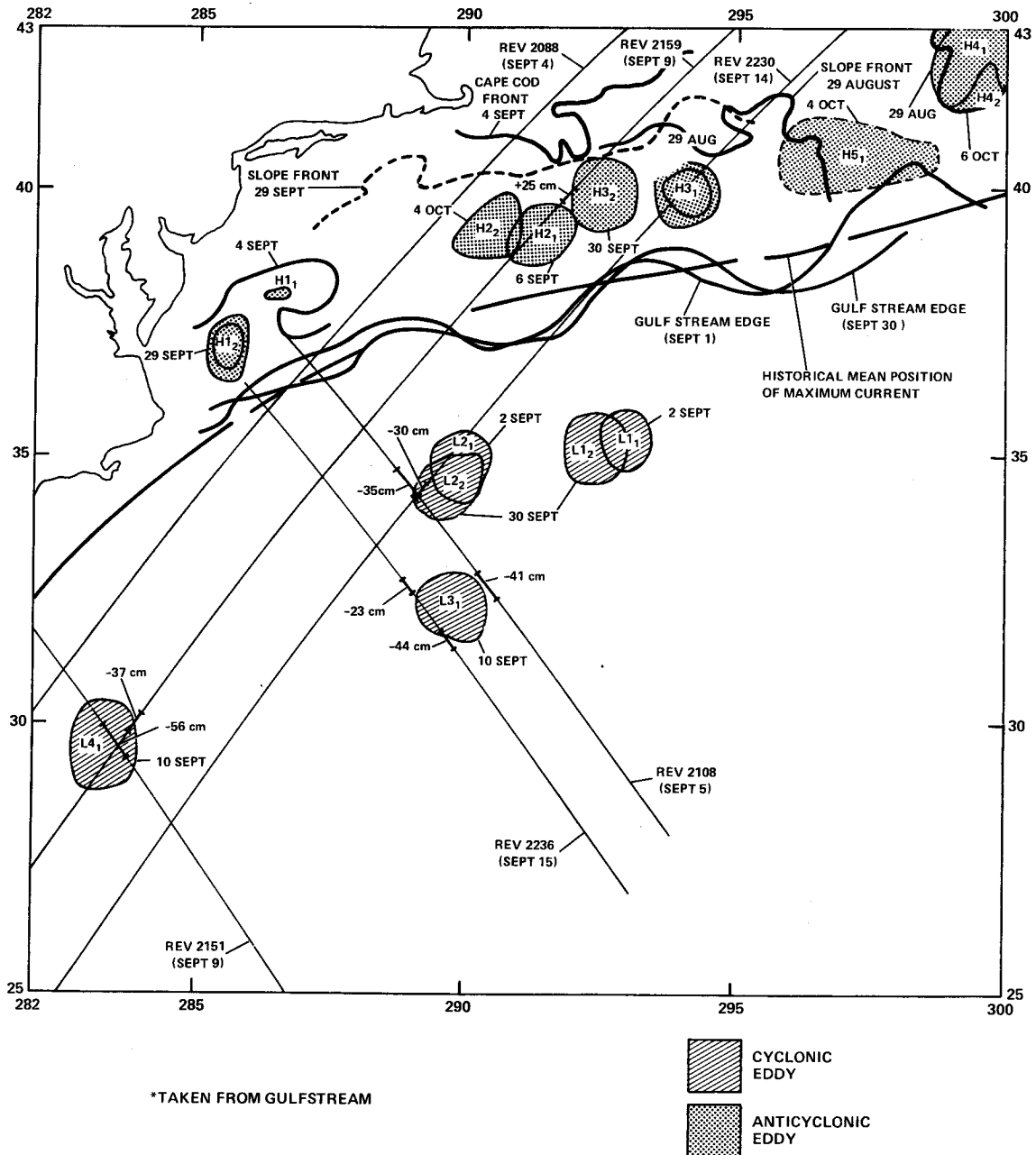


Figure A1.1

Correlation of IR Imagery with GEOS-3 Altimetry Profiles - November 1975

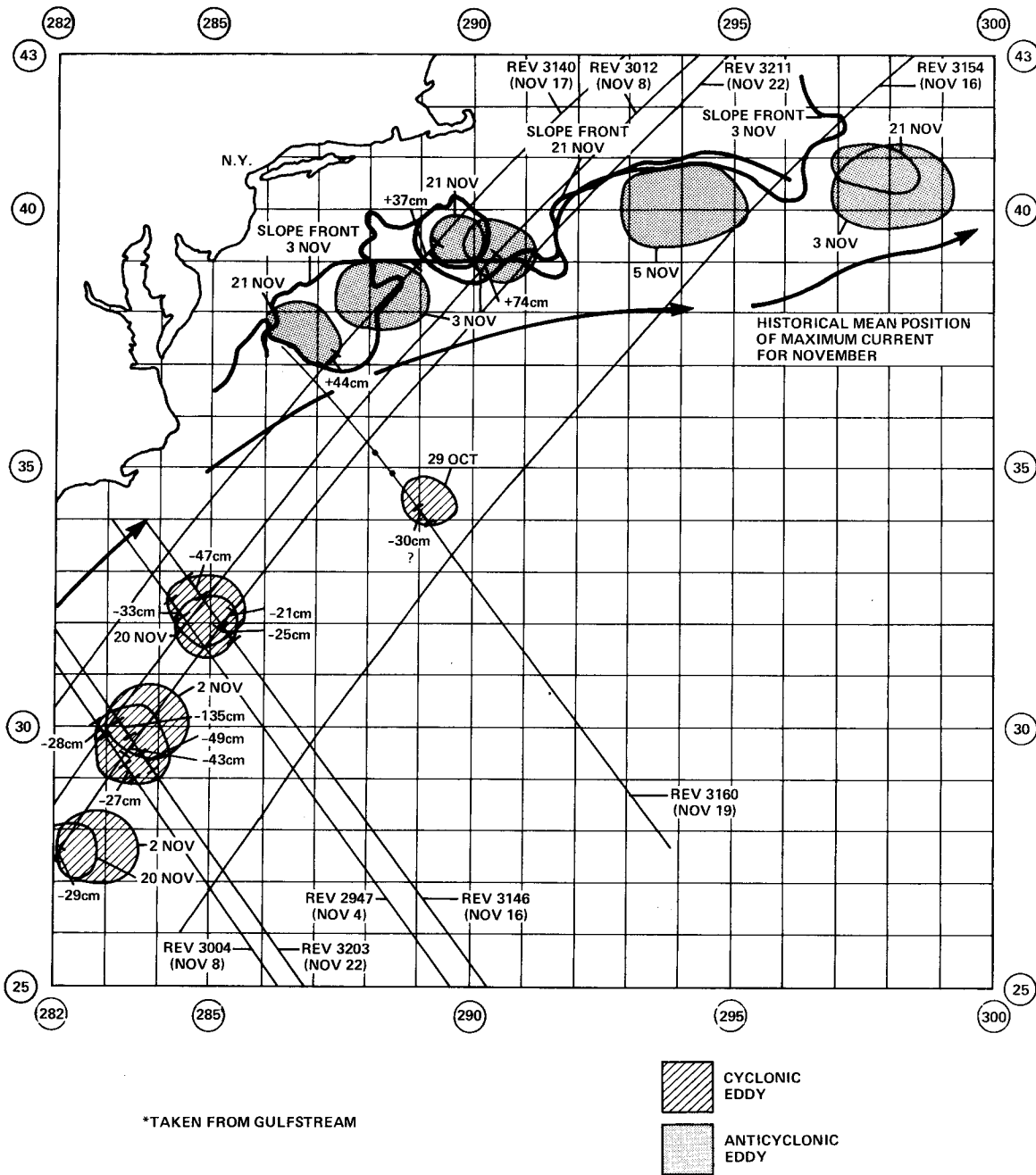


Figure A1.2

Correlation of IR Imagery with GEOS-3 Altimetry Profiles - December 1975

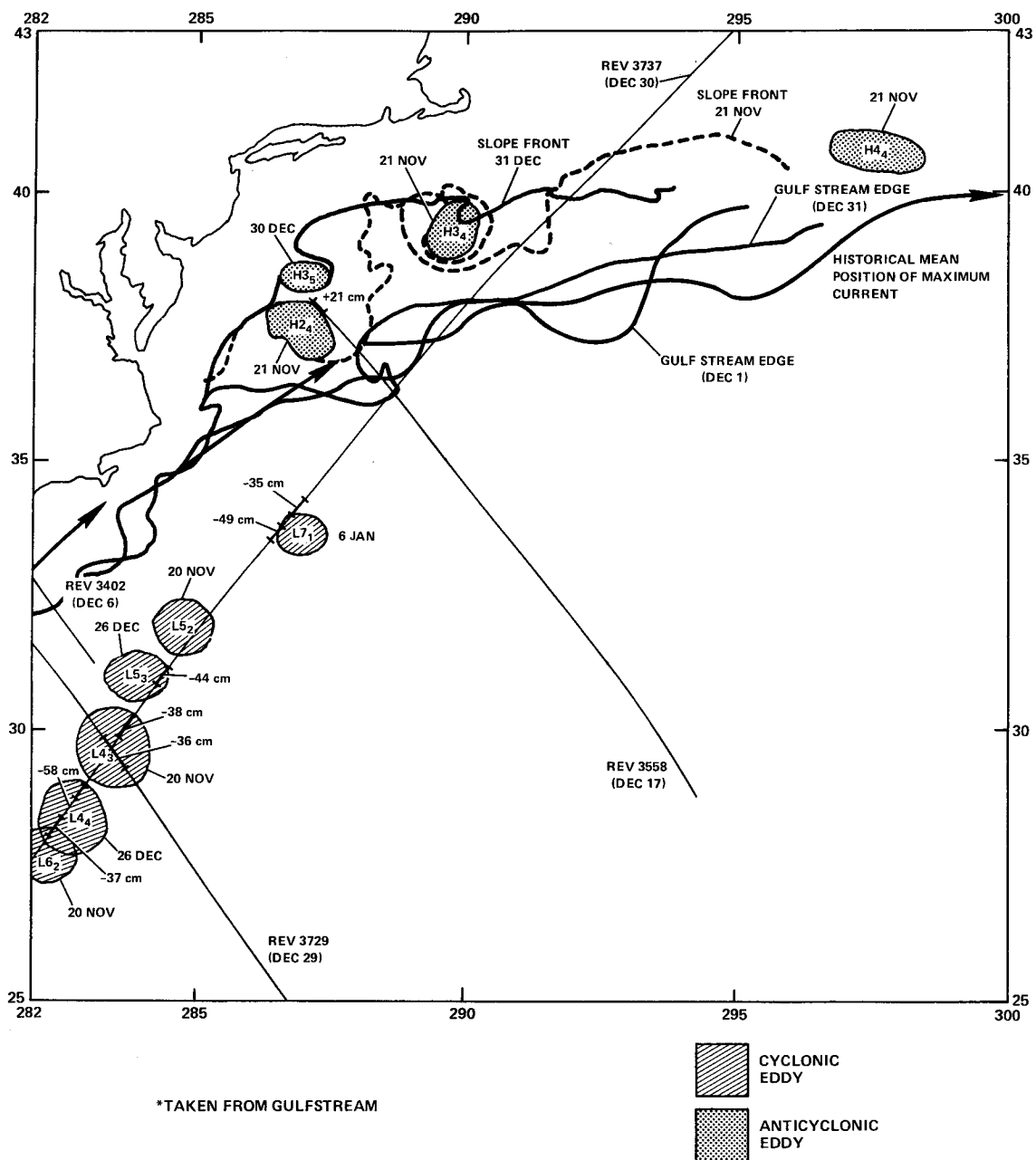
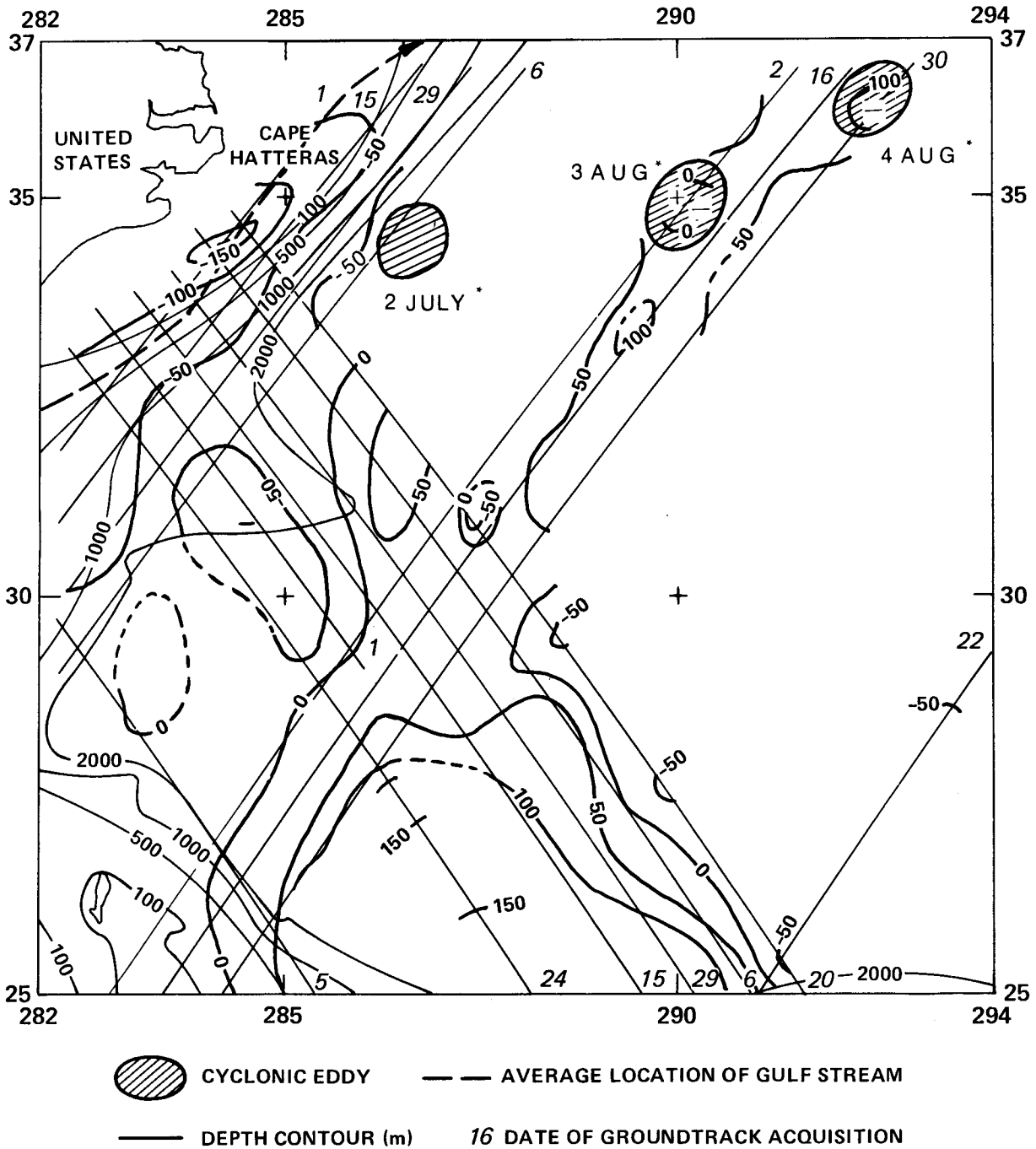


Figure A1.3

APPENDIX A2.

Results of Regional Sea Surface Model Analyses
Using the WALLOPS Altimetry Data Set.

**Regional Model of Dynamic Sea Surface Topography Variations –
Sargasso Sea – July 1975**



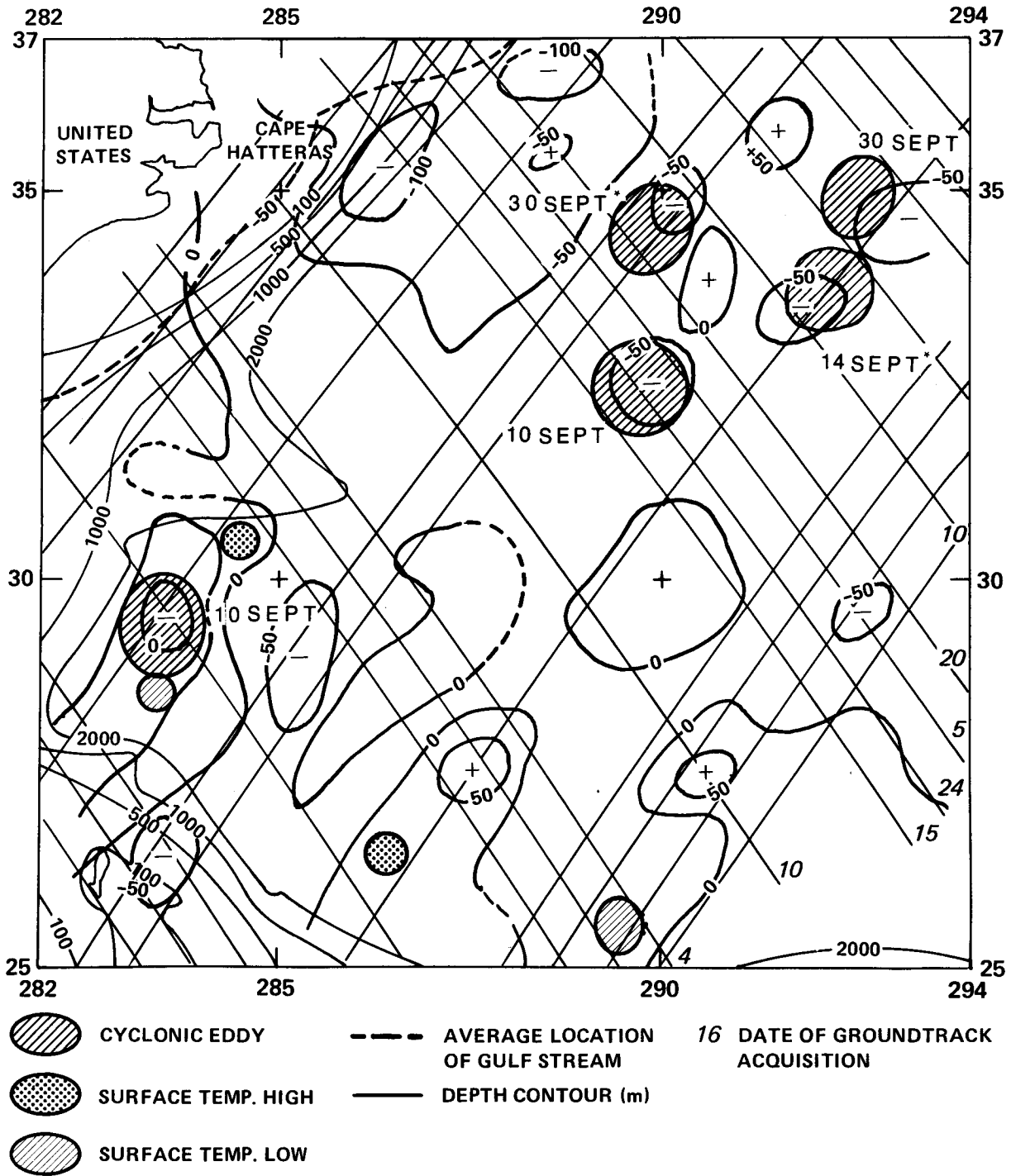
VARIATIONS – SARGASSO SEA – JULY 1975

DATUM – AVERAGE SEA SURFACE FOR JULY 1975 – AUGUST 1976

WAVELENGTHS >200 Km CONTOUR INTERVAL 50 cm

Figure A2.1

**Regional Model of Dynamic Sea Surface Topography Variations —
Sargasso Sea — September 1975**

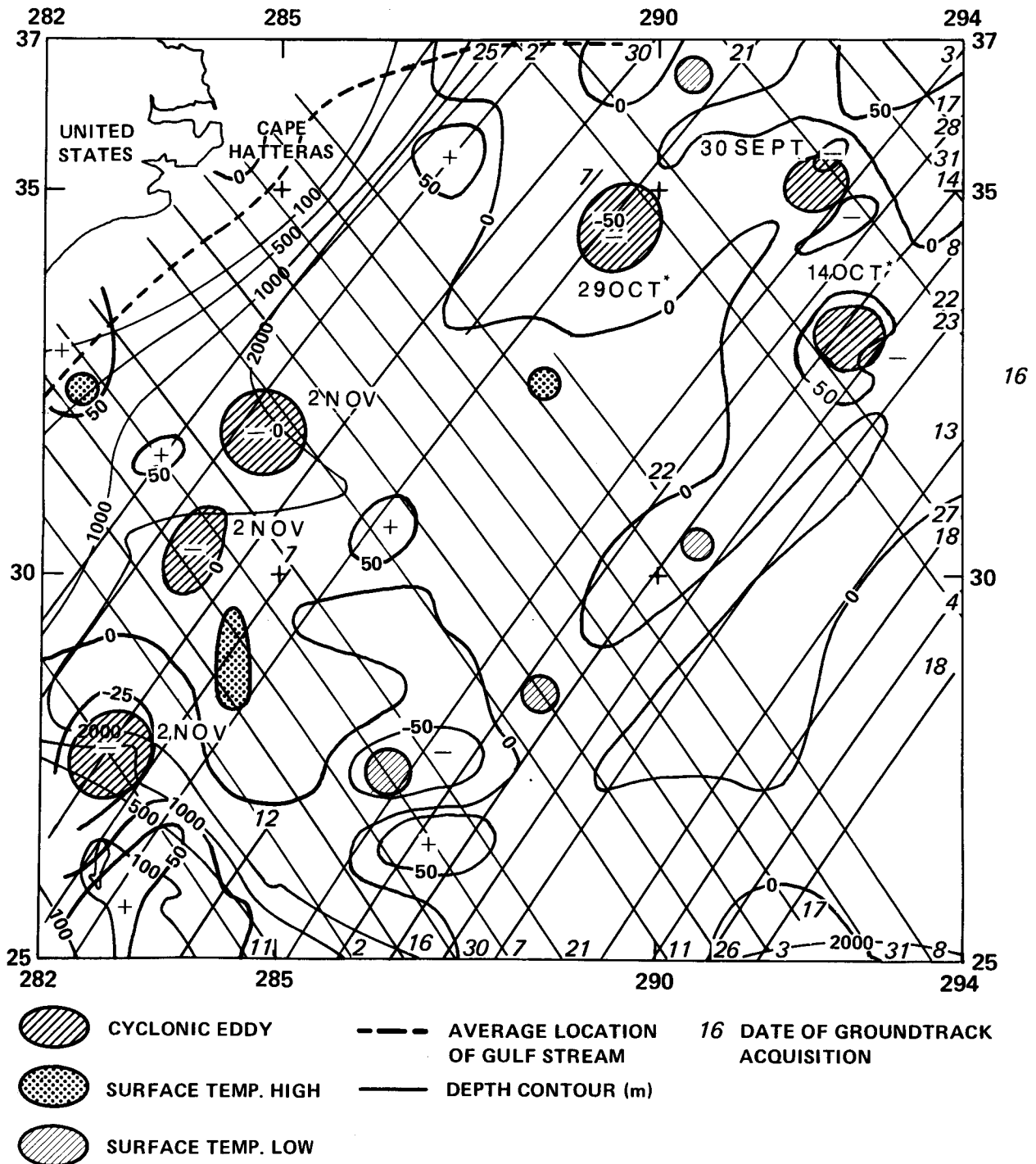


DATUM — AVERAGE SEA SURFACE FOR JULY 1975 — AUGUST 1976

CONTOUR INTERVAL 50 cm WAVELENGTHS >200 km

Figure A2.3

**Regional Model of Dynamic Sea Surface Topography Variations –
Sargasso Sea – October 1975**



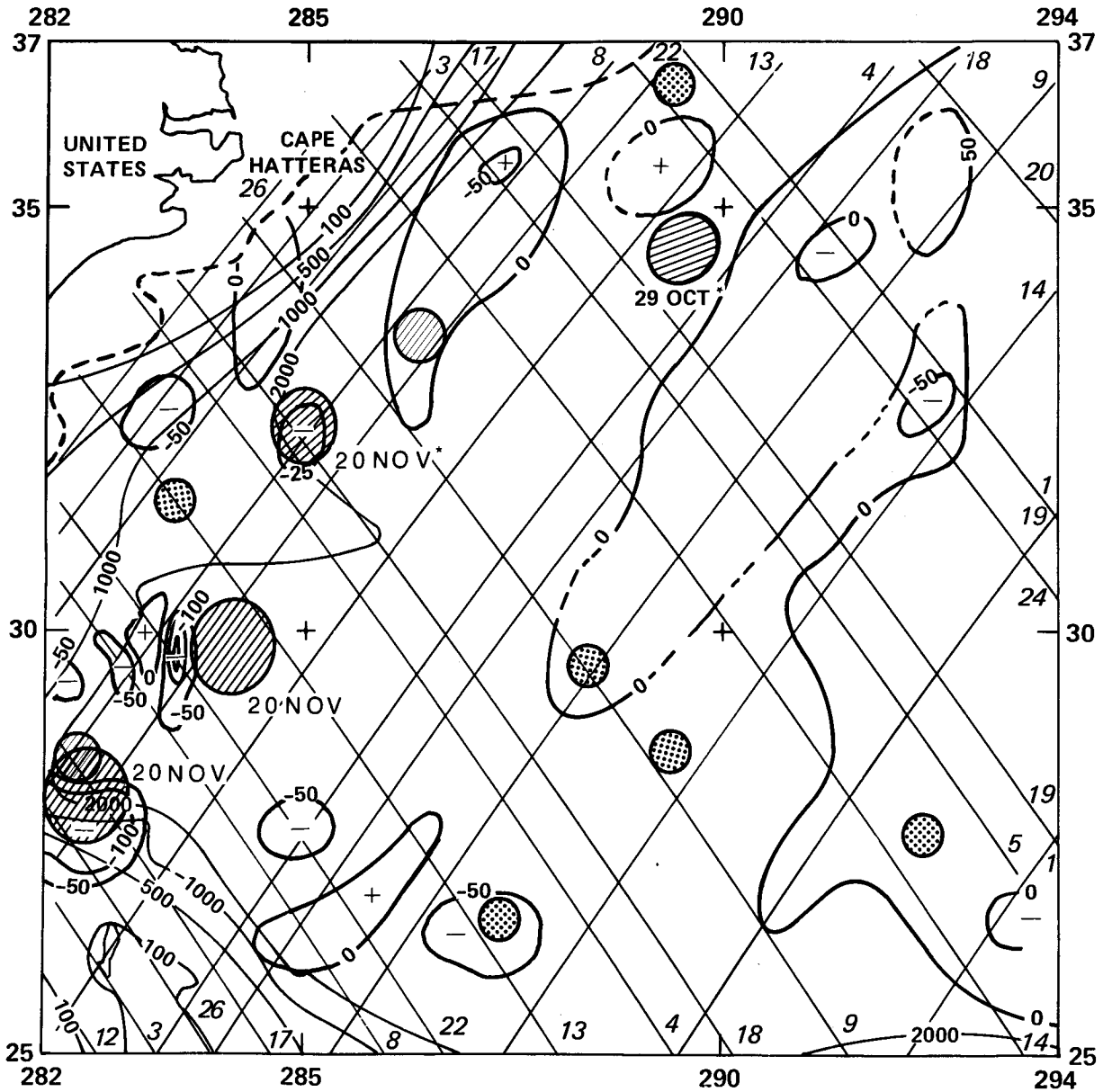
DATUM – AVERAGE SEA SURFACE FOR JULY 1975 – AUGUST 1976






CONTOUR INTERVAL 50 cm

WAVELENGTHS >200 km

Figure A2.4

**Regional Model of Dynamic Sea Surface Topography Variations –
Sargasso Sea – November 1975**



- | | | | | | |
|---|--------------------|---|---------------------------------|----|---------------------------------|
|  | CYCLONIC EDDY |  | AVERAGE LOCATION OF GULF STREAM | 16 | DATE OF GROUNDTRACK ACQUISITION |
|  | SURFACE TEMP. HIGH |  | DEPTH CONTOUR (m) | | |
|  | SURFACE TEMP. LOW | | | | |

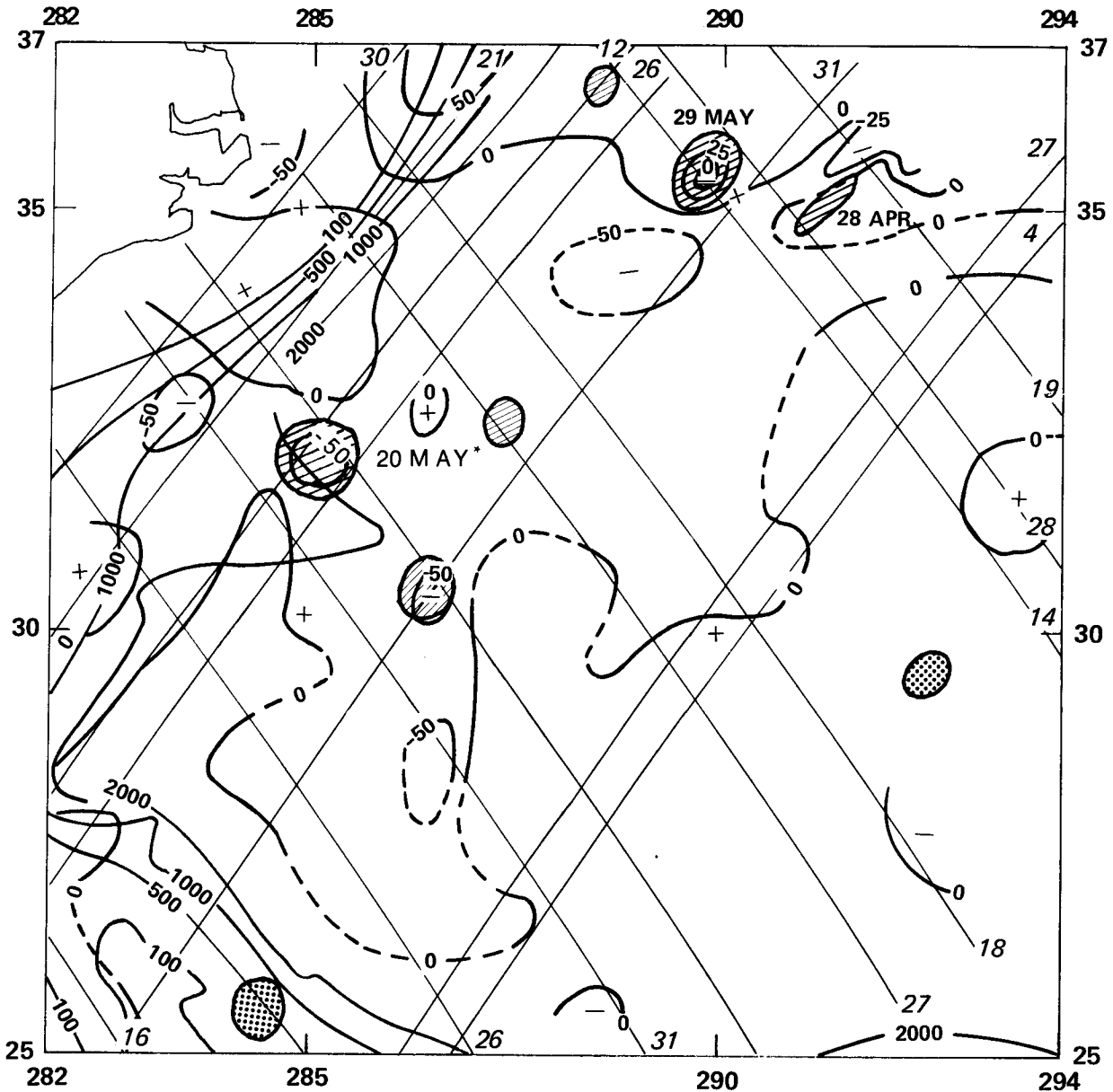
DATUM – AVERAGE SEA SURFACE FOR JULY 1975 – AUGUST 1976






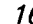
CONTOUR INTERVAL 50 cm

WAVELENGTHS >200 km

Figure A2.5

**Regional Model of Dynamic Sea Surface Topography Variations –
Sargasso Sea – May 1976**



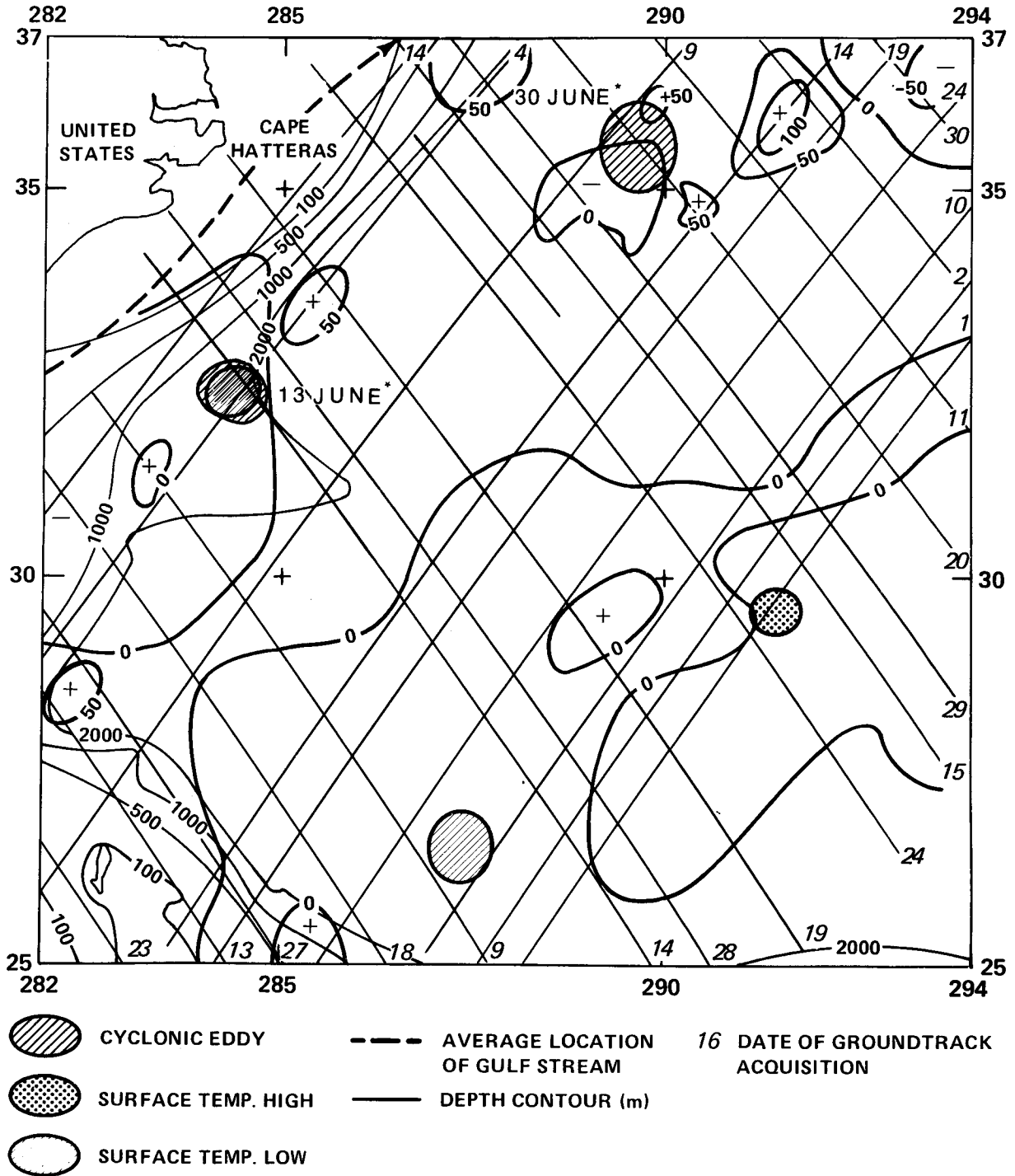
-  CYCLONIC EDDY
-  SURFACE TEMP. HIGH
-  SURFACE TEMP. LOW
-  AVERAGE LOCATION OF GULF STREAM
-  DEPTH CONTOUR (m)
-  DATE OF GROUNDTRACK ACQUISITION

DATUM – AVERAGE SEA SURFACE FOR JULY 1975 – AUGUST 1976

CONTOUR INTERVAL 50 cm WAVELENGTHS >200 km

Figure A2.7

Regional Model of Dynamic Sea Surface Topography Variations — Sargasso Sea — June 1976

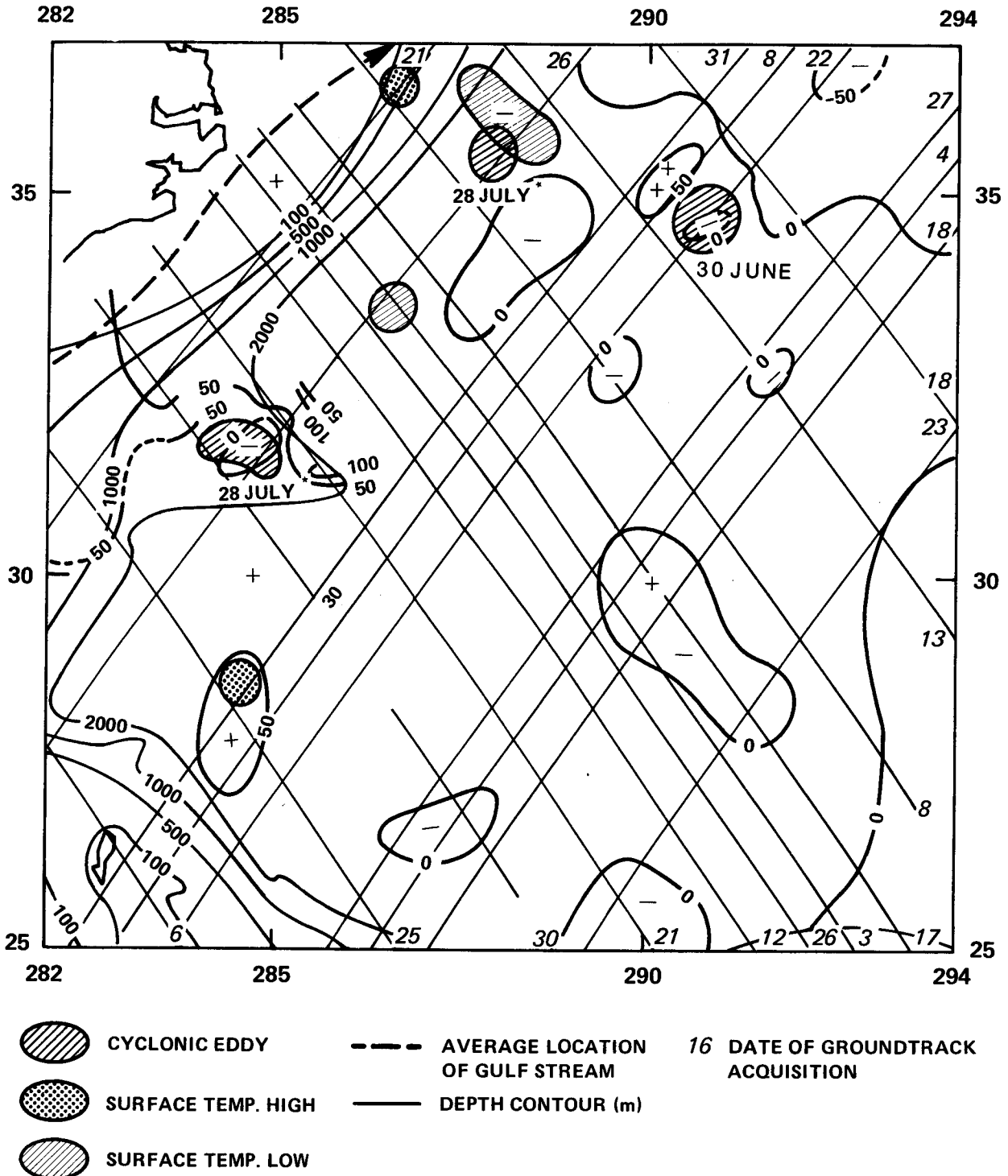


DATUM — AVERAGE SEA SURFACE FOR JULY 1975 — AUGUST 1976

CONTOUR INTERVAL 50 cm WAVELENGTHS >200 km

Figure A2.8

**Regional Model of Dynamic Sea Surface Topography Variations –
Sargasso Sea – July 1976**



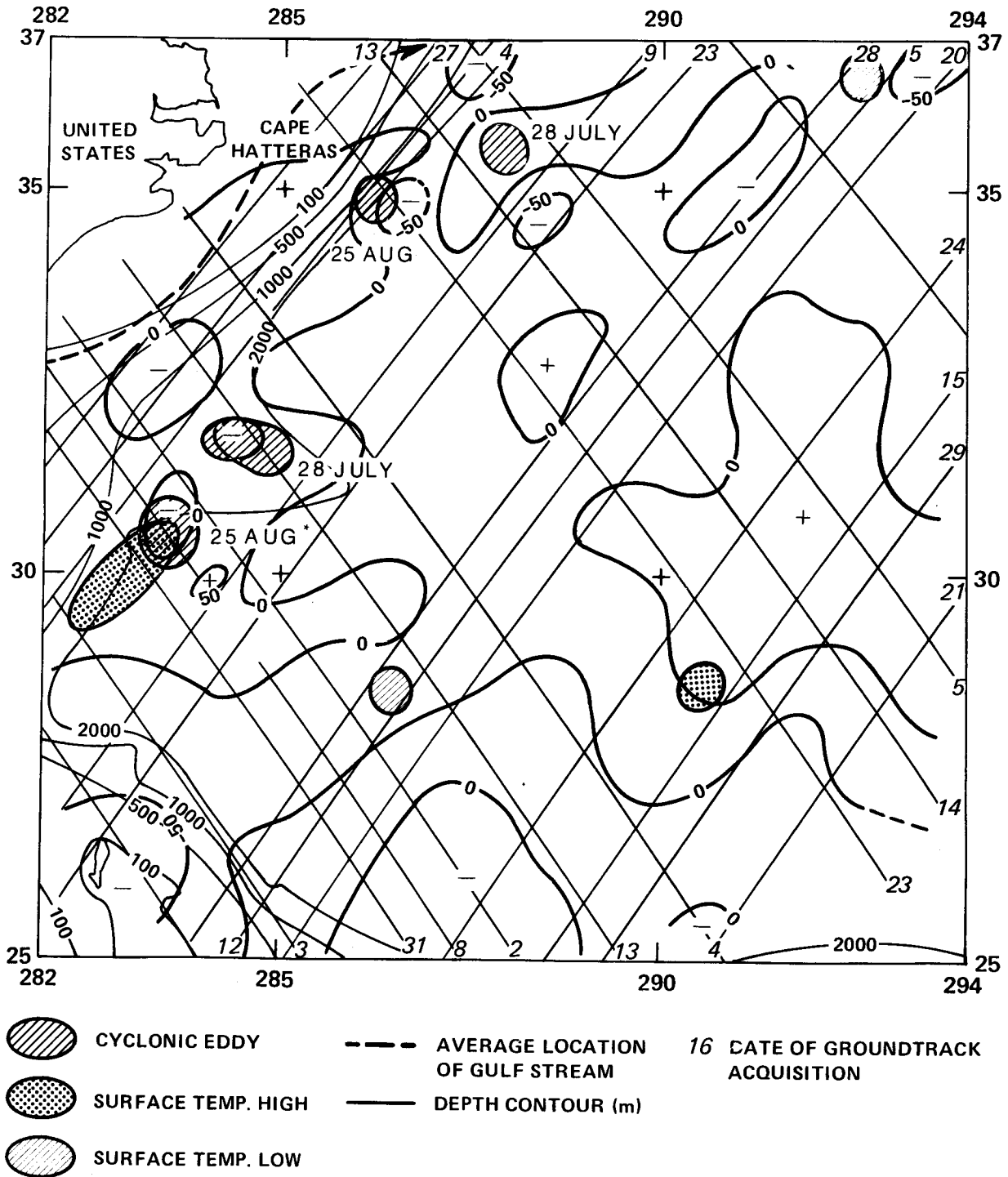
DATUM – AVERAGE SEA SURFACE FOR JULY 1975 – AUGUST 1976

CONTOUR INTERVAL 50 cm

WAVELENGTHS >200 km

Figure A2.9

**Regional Model of Dynamic Sea Surface Topography Variations —
Sargasso Sea — August 1976**



DATUM — AVERAGE SEA SURFACE FOR JULY 1975 — AUGUST 1976

CONTOUR INTERVAL 50 cm

WAVELENGTHS >200 km

Figure A2.10

Publications from
THE SCHOOL OF SURVEYING, THE UNIVERSITY OF NEW SOUTH WALES
P.O. Box 1, Kensington, N.S.W. 2033
AUSTRALIA

Reports

- 1.* G.G. Bennett, "The discrimination of radio time signals in Australia", Uniciv Rep. D1, 88 pp. (G 1)
- 2.* J.S. Allman, "A comparator for the accurate measurement of differential barometric pressure", Uniciv Rep. D3, 9 pp. (G 2)
3. R.S. Mather, "The establishment of geodetic gravity networks in South Australia", Uniciv Rep. R-17, 26 pp. (G 3)
- 4.* R.S. Mather, "The extension of the gravity field in South Australia", Uniciv Rep. R-19, 26 pp. (G 4)
- 5.* J.S. Allman, "An analysis of the reliability of barometric elevations", Unisurv Rep. 5, 335 pp. (S 1)
- 6.* R.S. Mather, "The free air geoid for South Australia and its relation to the equipotential surfaces of the earth's gravitational field", Unisurv Rep. 6, 491 pp. (S 2)
- 7.* P.V. Angus-Leppan, (Editor), "Control for mapping" (Proceedings of Conference, May 1967), Unisurv Rep. 7, 329 pp. (G 5)
- 8.* G.G. Bennett & J.G. Freislich, "The teaching of field astronomy", Unisurv Rep. 8, 30 pp. (G 6)
- 9.* J.C. Trinder, "Photogrammetric pointing accuracy as a function of properties of the visual image", Unisurv Rep. 9, 64 pp. (G 7)
- 10.* P.V. Angus-Leppan, "An experimental determination of refraction over an icefield", Unisurv Rep. 10, 23 pp. (G 8)
- 11.* R.S. Mather, "The non-regularised geoid and its relation to the telluroid and regularised geoids", Unisurv Rep. 11, 49 pp. (G 9)
- 12.* G.G. Bennett, "The least squares adjustment of gyro-theodolite observations", Unisurv Rep. 12, 53pp. (G 10)
- 13.* R.S. Mather, "The free air geoid for Australia from gravity data available in 1968", Unisurv Rep. 13, 38 pp. (G 11)

* OUT OF PRINT

- 14.* R.S. Mather, "Verification of geoidal solutions by the adjustment of control networks using geocentric Cartesian co-ordinate systems", Unisurv Rep. 14, 42 pp. (G 12)
- 15.* G.G. Bennett, "New methods of observation with the Wild GAKI gyrotheodolite", Unisurv Rep. 15, 68 pp. (G 13)
- 16.* G.G. Bennett, "Theoretical and practical study of a gyroscopic attachment for a theodolite", Unisurv Rep. 16, 343 pp. (S 3)
- 17.* J.C. Trinder, "Accuracy of monocular pointing to blurred photogrammetric signals", Unisurv Rep. 17, 231 pp. (S 4)
18. A. Stolz, "The computation of three dimensional Cartesian co-ordinates of terrestrial networks by the use of local astronomic vector systems", Unisurv Rep. 18, 47 pp. (G 14)
19. R.S. Mather, "The Australian geodetic datum in earth space", Unisurv Rep. 19, 130 pp. (G 15)
- 20.* J.G. Fryer, "The effect of the geoid on the Australian geodetic network", Unisurv Rep. 20, 221 pp. (S 5)
- 21.* G.F. Toft, "The registration and cadastral survey of native-held rural land in the Territory of Papua and New Guinea", Unisurv Rep. 21, 441 pp. (S 6)
22. R.S. Mather et al, "Communications from Australia to Section V, International Association of Geodesy, XV General Assembly, International Union of Geodesy and Geophysics, Moscow 1971", Unisurv Rep. 22, 72 pp. (G 16)
- 23.* A.H. Campbell, "The dynamics of temperature in surveying steel and invar measuring bands", Unisurv Rep. S 7, 195 pp.
24. A. Stolz, "Three-D Cartesian co-ordinates of part of the Australian geodetic network by the use of local astronomic vector systems", Unisurv Rep. S 8, 182 pp.
25. Papers by R.S. Mather, H.L. Mitchell & A. Stolz on the following topics:- Four-dimensional geodesy, Network adjustment and Sea surface topography, Unisurv G 17, 73 pp.
26. Papers by L. Berlin, G.J.F. Holden, P.V. Angus-Leppan, H.L. Mitchell & A.H. Campbell on the following topics:- Photogrammetry co-ordinate systems for surveying integration, Geopotential networks and Linear measurement, Unisurv G 18, 80 pp.
27. R.S. Mather, P.V. Angus-Leppan, A. Stolz & I. Lloyd, "Aspects of four-dimensional geodesy", Unisurv G 19, 100 pp.
28. H.L. Mitchell, "Relations between MSL & geodetic levelling in Australia", Unisurv Rep. S 9, 264 pp.

29. A.J. Robinson, "Study of zero error & ground swing of the model MRA101 tellurometer", Unisurv Rep. S 10, 200 pp.
30. Papers by J.S. Allman, R.C. Lister, J.C. Trinder & R.S. Mather on the following topics:- Network adjustments, Photogrammetry, and 4-Dimensional geodesy, Unisurv G 20, 133 pp.
31. G.J.F. Holden, "An evaluation of orthophotography in an integrated mapping system", Unisurv Rep. S 12, 232 pp.
32. G.J. Hoar, "The analysis precision and optimization of control surveys", Unisurv Rep. S 13, 200 pp.
33. Papers by E. Grafarend, R.S. Mather & P.V. Angus-Leppan on the following topics:- Mathematical geodesy, Coastal geodesy and Refraction, Unisurv G 21, 100 pp.
34. Papers by R.S. Mather, J.R. Gilliland, F.K. Brunner, J.C. Trinder, K. Bretreger & G. Halsey on the following topics:- Gravity, Levelling, Refraction, ERTS imagery, Tidal effects on satellite orbits and Photogrammetry, Unisurv G 22, 96 pp.
35. Papers by R.S. Mather, E.G. Anderson, C. Rizos, K. Bretreger, K. Leppert, B.V. Hamon & P.V. Angus-Leppan on the following topics:- Earth tides, Sea surface topography, Atmospheric effects in physical geodesy, Mean sea level and Systematic errors in levelling, Unisurv G 23, 96 pp.
36. Papers by R.C. Patterson, R.S. Mather, R. Coleman, O.L. Colombo, J.C. Trinder, S.U. Nasca, T.L. Duyet & K. Bretreger on the following topics:- Adjustment theory, Sea surface topography determinations, Applications of LANDSAT imagery, Ocean loading of Earth tides, Physical geodesy, Photogrammetry and Oceanographic applications of satellites, Unisurv G 24.
37. E.G. Anderson, "The Effect of Topography on Solutions of Stokes' Problem", Unisurv Rep. S 14, 252 pp.
38. A.H.W. Kearsley, "The Computation of Deflections of the Vertical from Gravity Anomalies", Unisurv Rep. S 15, 181 pp.
39. Papers by S.M. Nakiboglu, B. Ducarme, P. Melchior, R.S. Mather, B.C. Barlow, C. Rizos, B. Hirsch, K. Bretreger, F.K. Brunner & P.V. Angus-Leppan on the following topics:- Hydrostatic equilibrium figures of the Earth, Earth tides, Gravity anomaly data banks for Australia, Recovery of tidal signals from satellite altimetry, Meteorological parameters for modelling terrestrial refraction and Crustal motion studies in Australia, Unisurv G 25.
40. Papers by R.S. Mather, E.G. Masters, R. Coleman, C. Rizos, B. Hirsch, C.S. Fraser, F.K. Brunner, P.V. Angus-Leppan, A.J. McCarthy & C. Wardrop on the following topics:- Four-dimensional geodesy, GEOS-3 altimetry data analysis, Analysis of meteorological measurements for microwave EDM and Meteorological data logging system for geodetic refraction research, Unisurv G 26, 113 pp.

41. Papers by F.K. Brunner, C.S. Fraser, S.U. Nasca, J.C. Trinder, L. Berlin, R.S. Mather, O.L. Colombo & P.V. Angus-Leppan on the following topics:- Micrometeorology in geodetic refraction, LANDSAT imagery in topographic mapping, Adjustment of large systems, GEOS-3 data analysis, Kernel functions and EDM reductions over sea, Unisurv G 27, 101 pp.
42. K. Bretreger, "Earth Tide Effects on Geodetic Observations", Unisurv S 16, 173 pp.
43. Papers by S.M. Nakiboglu, H.L. Mitchell, K. Bretreger, T.A. Herring, J.M. Rueger, K.R. Bullock, R.S. Mather, B.C. Forster, I.P. Williamson & T.S. Morrison on the following topics:- Variations in gravity, Oceanographic and geodetic levelling, Ocean loading effects on Earth tides, Deflections of the vertical, Frequencies of EDM instruments, Land information systems, Sea surface topography, Accuracy of Aerial Triangulation and Questionnaire to Surveyors, Unisurv G 28, 124 pp.
44. Papers by F.L. Clarke, R.S. Mather, D.R. Larden & J.R. Gilliland on the following topics:- Three dimensional network adjustment incorporating ξ , η and N , Geoid determinations with satellite altimetry, Geodynamic information from secular gravity changes and Height and free-air anomaly correlation, Unisurv G 29, 87 pp.
- From June 1979 Unisurv G's name was changed to Australian Journal of Geodesy, Photogrammetry and Surveying (Aust.J.Geod.Photo.Surv.).
45. Aust.J.Geod.Photo.Surv. No. 30, (June, 1979), 127 pp.:
Bretreger, "Ocean tide models from GEOS-3 altimetry";
Trinder & Smith, "Rectification of LANDSAT data";
Nakiboglu & Lim, "Numerical test of initial value method";
Herring, "The accuracy of deflections of vertical";
Angus-Leppan, "Radiation effects on temperature of metal tape";
Covell, "Errors of short range distance meters", and
Nasca, "Contour lines in engineering".
- 46.* Aust.J.Geod.Photo.Surv. No. 31, (December 1979) 177 pp.
(contributions to the XVII General Meeting of the IUGG, Canberra, 3-15 December, 1979):
Allman et al., "Readjustment of Australian geodetic survey";
Angus-Leppan, "Ratio method and meteorology" and
"Refraction in levelling",
Berlin, "Adjustment of continental networks",
Brunner, "Limiting factor to geodetic precision";
Coleman et al., "Sea surface slope along NE Australia",
Kahar and Kearsley, "Jawa geoid from altimetry and gravity",
Kearsley & van Gysen, "Outer zone effects on the Australian geoid",
Masters et al., "Tide models from GEOS-3 altimetry", and
Mather & Rizos, "Global mean sea level from altimetry".
47. C. Rizos, "The role of the gravity field in sea surface topography studies", Unisurv S 17 (February, 1980), 299 pp.

48. Aust.J.Geod.Photo.Surv. No. 32, (June,1980) 121 pp.:
 van Gysen, "Gravimetric deflections of the vertical",
 Fraser, "Self calibration of non-metric camera",
 Rizos, "Ocean circulation from SST studies",
 Trinder, "Film granularity and visual performance".

49. Aust.J.Geod.Photo.Surv. No. 33, (December,1980) 85 pp.:
 Burford, "Controlling geodetic networks";
 Masters & Stolz, "Crustal motion from LAGEOS";
 Fraser, "Variance analysis of adjustments", and
 Brunner et al., "Incremental strain near Palmdale".

50. B.C. Forster, "Some measures of urban residual quality from LANDSAT
 multi-spectral data", Unisurv S 18, (January,1981) 223 pp.

51. Aust.J.Geod.Photo.Surv. No. 34, (June,1981) 94 pp.:
 Welsch, "Variances of geodetic observations";
 Gilliland, "Outer zones effects on geoid", and
 Khalid, "Models of vertical refraction".

52. Richard Coleman, "A Geodetic Basis for recovering Ocean Dynamic
 Information from Satellite Altimetry", Unisurv S 19, (October,1981)
 332 pp.

53. Aust.J.Geod.Photo.Surv. No.35 (December 1981):
 Kahar, "Geoid in Indonesia",
 Morgan, "Crustal Motion in Papua New Guinea",
 Masters et al, "LAGEOS Range Filter",
 Stolz et al, "Baseline Values from LAGEOS",
 Bishop, "Digital Elevation Models".

* Out of print

Proceedings

P.V. Angus-Leppan (Editor), "Proceedings of conference on refraction effects in geodesy & electronic distance measurement", 264 pp.

Price: \$10.00

R.S. Mather & P.V. Angus-Leppan (Eds.), "Australian Academy of Science/International Association of Geodesy Symposium on Earth's Gravitational Field & Secular Variations in Position", 740 pp.

Price: \$20.00

Monographs

1. R.S. Mather, "The theory and geodetic use of some common projections", (2nd edition), 125 pp. Price: \$ 5.00
2. R.S. Mather, "The analysis of the earth's gravity field", 172 pp. Price: \$ 5.00
3. G.G. Bennett, "Tables for prediction of daylight stars", 24 pp. Price: \$ 2.50
4. G.G. Bennett, J.G. Freislich & M. Maughan, "Star prediction tables for the fixing of position", 200 pp. Price: \$ 8.00
5. M. Maughan, "Survey computations", 98 pp. Price: \$ 5.00
6. M. Maughan, "Adjustment of Observations by Least Squares", 61 pp. Price: \$ 4.00
7. J.M. Rieger, "Introduction to Electronic Distance Measurement", (2nd Edition), 140 pp. Price: \$ 7.00

OTHER PRICES (Surface Mail Postage Inclusive)

1. Aust.J.Geod.Photo.Surv. (formerly Unisurv G), 2 issues annually of approximately 100 pages each issue.

Subscription for 1981

To Libraries \$18

To Individuals \$12

2. Special Series (Unisurv S)
Research reports of 200 to 300 pages, published annually (on average).

To Libraries \$25 per copy

To Individuals \$18 per copy

